

JUSTUS-LIEBIG-



UNIVERSITÄT
GIESSEN

II. Physikalisches Institut

Dielectron reconstruction in Ag+Ag collisions at $\sqrt{s_{NN}} = 2.55 \text{ GeV}$ with HADES

zur Erlangung des Grades
eines Doktors der Naturwissenschaften (Dr. rer. nat.)

genehmigte Dissertation von

M.Sc. Jan-Hendrik Otto

Gießen 2022

1. Supervisor : Prof. Dr. Claudia Höhne
2. Supervisor : Prof. Dr. Lorenz von Smekal

DANKSAGUNG

An dieser Stelle möchte ich mich bei all jenen bedanken, die mich nicht nur während meiner Promotion, sondern dem gesamten Physik Studium begleitet haben. An erster Stelle sind hier natürlich meine Familie, meine Freundin und meine Freunde zu nennen, die mich zu jedem Zeitpunkt voll unterstützt und motiviert haben.

Der gesamten Arbeitsgruppe Höhne und insbesondere Prof. Claudia Höhne selbst bin ich ebenfalls zu besonderem Dank verpflichtet. Seit meiner Bachelor Arbeit im Jahr 2015 ist die Arbeitsgruppe mein wissenschaftliches Zuhause. Die herrschende wissenschaftliche Expertise gepaart mit einer sehr angenehmen und gleichzeitig produktiven Arbeitsatmosphäre haben diese Jahre maßgeblich geprägt. Insbesondere letzteres ist zu großen Teilen auch Marten Becker, Adrian Weber, Leonard Koch, Clemens Lauterbach und Christopher Jung zu verdanken, die nicht nur außergewöhnliche Kollegen, sondern auch sehr gute Freunde sind. Dies gilt ebenso für Jörg Förtsch dem ich für die hervorragende Zusammenarbeit und die zahlreichen Telefonate zu wissenschaftlichem Austausch und Diskussionen sehr dankbar bin.

Ebenfalls ganz besonders danken möchte ich Prof. Lorenz v. Smekal. Er hat mich während des Master Studiums durch seine Vorlesungen für die theoretische Physik begeistert und insbesondere zum zweiten Teil der Arbeit durch seine Expertise entscheidend beigetragen.

Ein weiterer Dank gebührt Prof. Tetyana Galatyuk, Dr. Jürgen Friese, Dr. Arno Tripolt und Dr. Kai Gallmeister, die durch Diskussionen und Ratschläge maßgeblich zum Gelingen dieser Arbeit beigetragen haben.

Eine ganz besondere Freude während der letzten Jahre waren die zahlreichen Konferenzen, wobei hier insbesondere die HADES Kollaborationstreffen zu nennen sind.

DECLARATION

Ich erkläre: Ich habe die vorgelegte Dissertation selbstständig und ohne unerlaubte fremde Hilfe und nur mit den Hilfen angefertigt, die ich in der Dissertation angegeben habe. Alle Textstellen, die wörtlich oder sinngemäß aus veröffentlichten Schriften entnommen sind, und alle Angaben, die auf mündlichen Auskünften beruhen, sind als solche kenntlich gemacht. Ich stimme einer evtl. Überprüfung meiner Dissertation durch eine Antiplagiat-Software zu. Bei den von mir durchgeführten und in der Dissertation erwähnten Untersuchungen habe ich die Grundsätze guter wissenschaftlicher Praxis, wie sie in der "Satzung der Justus-Liebig-Universität Gießen zur Sicherung guter wissenschaftlicher Praxis" niedergelegt sind, eingehalten

Ort, Datum

Unterschrift

ABSTRACT

The study of strongly interacting matter under extreme conditions in terms of temperature and pressure has moved more and more in the focus of high energy physics over the last decades. These conditions can be created in the collision of heavy-ions at various facilities around the world, together covering a broad range of collision energies starting in the GeV region and ranging up to energies of several TeV . In order to study the medium created in such collisions and get an insight in the underlying processes, dileptons are ideal messengers as they do not interact strongly and can therefore leave the medium unharmed carrying their initial properties to the particle detectors. They thus reveal the thermal conditions and the lifetime of the medium but also give insights into meson properties at high densities.

One of the experiments dedicated to the investigation of strongly interacting matter is the **High Acceptance DiElectron Spectrometer (HADES)**. It is a versatile detector with particular focus on dielectron measurements in pion, proton, deuteron and (heavy-) ion-induced reactions using proton or nucleus targets in the SIS-18 energy range (1-2 $GeV/nucleon$). Its excellent particle identification capabilities also allow for the investigation of hadronic observables. The analysis of a high statistics sample of $Ag + Ag$ collisions (4.5 billion events for 0 – 40% centrality) at $\sqrt{s_{NN}} = 2.55 GeV$ measured by HADES is presented with respect to dielectron production in this work. The recently upgraded HADES RICH detector leads to an unprecedented quality and signal-to-background ratio in the detection of these extremely rare probes. Due to the large number of reconstructed Cherenkov photons it is possible for the first time ever, to efficiently identify and reject electrons produced in conversion processes by a simple count of measured photons.

The obtained dielectron spectrum shows a signal up to the ϕ meson mass region and is compared to simulated hadronic cocktail and nucleon-nucleon reference spectra revealing a strong contribution from the hot and dense phase quantified by the dielectron excess ratio R_{AA} . The multiplicities of the hadrons are estimated in an analysis of the decay channels $\pi^0/\eta \rightarrow \gamma\gamma^* \rightarrow 4e$ and $\omega \rightarrow e^+e^-$ in the same data set. The slope of the in-medium contribution allows for the extraction of the mean medium temperature. A differential analysis in bins of centrality enables the study of these observables in dependence on the system size. Furthermore, a differential analysis in pair momentum is performed showing a significant change in the line-shape of the spectrum in the $\rho - \omega$ mass region with increasing (transverse) pair-momentum which suggests a substantial modification of the meson properties in the medium.

Previous HADES measurements of $Au + Au$ collisions at $\sqrt{s_{NN}} = 2.42 GeV$ and $Ar + KCl$ at $\sqrt{s_{NN}} = 3.18 GeV$ provide data for comparison and to study

energy and system-size dependence of the obtained results.

In the second part of this work the calculation of spectral functions with the **Functional Renormalization Group (FRG)** including one-loop self-energies in a self consistent way is presented. Spectral functions are defined as the imaginary part of the electromagnetic current-current correlation function and provide direct access to thermal photon and dilepton rates. The calculations are performed for the pion and the sigma meson in the $O(4)$ model at vanishing temperature in the chirally broken phase. Comparing the results with those from previous analytically continued FRG calculations, it is demonstrated, how self-consistency at all momenta fixes the relation between particle masses and decay thresholds.

ZUSAMMENFASSUNG

Die Studie stark wechselwirkender Materie unter extremen Bedingungen in Bezug auf Druck und Temperatur ist in den vergangenen Jahrzehnten mehr und mehr ins Zentrum der Forschung in der Hochenergiephysik gerückt. Die Kollision beschleunigter Schwerionen bietet die Möglichkeit, derartige Bedingungen im Labor zu erzeugen. Hierfür existieren Forschungseinrichtungen auf der ganzen Welt, welche gemeinsam einen Energiebereich von der GeV Region bis hin zu mehreren TeV abdecken. Dielektronen sind ideale Sonden, um das so in Schwerionenkollisionen erzeugte Medium zu untersuchen und einen Einblick in die zu Grunde liegenden Prozesse zu erhalten, da sie nicht an der starken Wechselwirkung teilnehmen und ihre Eigenschaften daher ungehindert zu den Teilchendetektoren transportieren können. Sie sind daher in der Lage, die thermischen Eigenschaften und die Lebensdauer des Mediums zu enthüllen. Zudem kann ein Einblick in die Eigenschaften der Mesonen unter den entsprechenden Bedingungen erlangt werden.

Eines der Experimente, welches stark wechselwirkende Materie erforscht ist das **High Acceptance DiElectron Spectrometer (HADES)**. Der vielseitige Detektor ist speziell auf die Messung von Dielektronen in Pion, Proton, Deuteron und (Schwer-) Ionen induzierten Reaktionen unter Verwendung von Targets aus Wasserstoff oder schwereren Kernen ausgelegt. Die exzellente Fähigkeit zur Identifikation von Teilchen erlaubt des Weiteren auch eine Erforschung hadronischer Observablen. In dieser Arbeit wird die Dielektronen Analyse von $4.5 \cdot 10^9 Ag + Ag$ Kollisionen bei einer Strahlenergie von $\sqrt{s_{NN}} = 2.55 GeV$ präsentiert. Hierbei wird durch den verbesserten HADES RICH Detektor eine bislang unerreichte Qualität in Form von Effizienz, Pion-Unterdrückung und Signal-zu-Untergrund Verhältnis erzielt. Aufgrund der hohen Anzahl an Cherenkov Photonen ist es erstmalig möglich, Elektronen aus Konversionsprozessen durch die Anzahl gemessener Cherenkov Photonen effizient zu identifizieren.

Die resultierenden Dielektronen Spektren enthalten ein Signal bis in die Massenregion des ϕ Mesons und werden mit simulierten hadronischen Cocktail und Nukleon-Nukleon Referenzspektren verglichen, wobei ein starker Beitrag der heißen und Dichten Phasen der Kollision deutlich wird, der im Dielektronen-Überschuss-Verhältnis R_{AA} quantifiziert wird. Die hierfür benötigten Multiplizitäten der Hadronen werden über Analysen der Zerfallskanäle $\pi^0/\eta \rightarrow \gamma\gamma^* \rightarrow 4e$ und $\omega \rightarrow e^+e^-$ in demselben Datensatz bestimmt. Aus der Steigung des in-medium Beitrags kann eine mittlere Temperatur des erzeugten Mediums bestimmt werden. In einer differentiellen Analyse in Abhängigkeit der Zentralität der Kollision werden diese Observablen als Funktion der Systemgröße untersucht. In einer Analyse in Abhängigkeit des Paar-Impulses werden signifikante Unterschiede in der Form des Spektrums in der $\rho - \omega$ Massenregion deutlich, welche eine substantielle Modifikation

der Eigenschaften von Mesonen im Medium nahelegen.

Vorherige Messungen mit HADES an $Au + Au$ Kollisionen bei $\sqrt{s_{NN}} = 2.42 \text{ GeV}$ und $Ar + KCl$ bei $\sqrt{s_{NN}} = 3.18 \text{ GeV}$ liefern Vergleichsdaten um die Abhängigkeit der Ergebnisse von Systemgröße und Energie zu untersuchen.

In dem zweiten Teil dieser Arbeit wird die Berechnung von Spektralfunktionen auf Basis der **Functional Renormalization Group (FRG)** unter Einbeziehung von Ein-Loop Selbstenergien in einem selbstkonsistenten Konzept vorgestellt. Spektralfunktionen sind durch den imaginären Teil der elektromagnetischen Strom-Strom Korrelationsfunktion definiert und erlauben die direkte Berechnung von thermischen Photon- und Dileptonen-Raten. Die Berechnungen werden im $O(4)$ Modell bei verschwindender Temperatur in der chiral gebrochenen Phase durchgeführt. Ein Vergleich mit Ergebnissen mit früheren Rechnungen demonstriert, wie die eingeführte Selbstkonsistenz bei allen Impulsen die Beziehung zwischen Teilchenmassen und Zerfallsschwellen fixt.

CONTENTS

I	DIELECTRON ANALYSIS IN AG+AG COLLISIONS WITH HADES	
1	INTRODUCTION	3
1.1	The standard model of particles physics	3
1.1.1	Spontaneous symmetry breaking	7
1.1.2	Electroweak interaction	8
1.1.3	Quantum Chromodynamics	10
1.2	The QCD phase diagram	12
1.3	Experimental exploration of the QCD phase diagram with heavy-ion collisions	14
1.4	Observables in heavy-ion collisions	16
1.5	Virtual photons in heavy-ion collisions	20
2	THE HADES EXPERIMENT	27
2.1	The target	28
2.2	The START and VETO detector in HADES	28
2.3	The HADES tracking system	29
2.3.1	The HADES magnet	29
2.3.2	Multiwire Drift Chambers (MDCs)	30
2.4	The META system	31
2.4.1	Time-of-Flight (TOF) wall	31
2.4.2	Resistive Plate Chamber (RPC) wall	32
2.5	Electromagnetic calorimeter	33
2.6	HADES trigger	33
2.7	HADES simulation	33
3	THE RICH DETECTOR AT HADES	37
3.1	Cherenkov radiation	37
3.2	Setup of the HADES RICH detector	38
3.3	Signatures in the HADES RICH detector	40
4	DATA ANALYSIS TECHNIQUE	49
4.1	Track reconstruction in HADES	49
4.2	Event selection and centrality estimation	51
4.3	Electron identification	54
4.3.1	Pre-selection of tracks	54
4.3.2	Single track vertex	57
4.3.3	RICH detector observables	59
4.3.4	The effective mass	67
4.4	Physical background rejection using the RICH detector	72
4.4.1	Conversion identification based on the opening angle between RICH rings	72
4.4.2	Conversion identification on the level of calibrated objects (Cals) in the RICH	72
4.5	Overview on the effect of all electron selection criteria	79

4.6	Possible improvements in conversion recognition	80
4.7	Electron-pair formation	83
4.8	Background estimation using UrQMD simulation	89
4.9	Efficiency and acceptance correction	91
4.10	Combinatorial background estimation	102
4.11	Estimation of systematic errors	105
5	ESTIMATION OF HADRON MULTIPLICITIES	109
5.1	η multiplicity estimation	109
5.2	π^0 multiplicity estimation	112
5.3	Recent improvements with four lepton event-mixing	115
5.4	ω multiplicity estimation	119
5.5	Comparison to TAPS measurements	121
6	EXPERIMENTAL RESULTS	123
6.1	The dielectron signal	123
6.2	Hadronic cocktail simulation	125
6.3	NN reference	128
6.4	Estimation of the medium temperature	132
6.5	The dielectron excess	134
6.6	(Transverse) Momentum-differential analysis	139
7	SUMMARY	151
II ONE-LOOP SELF-CONSISTENT SPECTRAL FUNCTIONS WITH THE FRG		
8	DILEPTONS IN THEORY	155
9	CONCEPTUAL BASELINE	159
9.1	Introduction to the Functional Renormalization Group	159
9.2	Flow equation for the average effective action in the $O(4)$ model	160
9.2.1	Analytically continued LPA flows	161
9.2.2	Self-consistent one-loop (SC1L) flows	163
9.2.3	Numerical Implementation	165
10	RESULTS	167
10.1	Masses, couplings and the effective potential	167
10.2	Two-point functions and spectral functions	171
10.3	Summary and discussion	173
A	DERIVATION OF COMBINATORIAL BACKGROUND FORMULAS	175
B	ADDITIONAL FIGURES TO CHAPTER 5	179
B.1	π^0 and η reconstruction in centrality classes	179
B.2	π^0 and η reconstruction in bins of $p_t - y$	183
C	GIBUU JOBCARDS FOR NN REFERENCE SIMULATION	187
C.1	Jobcard for p+n collisions	187
C.2	Jobcard for p+p collisions	190
D	ADDITIONAL FIGURES TO CHAPTER 6	193
D.1	Hadronic cocktail and NN contribution simulation	193
D.2	Medium temperature estimation	195
D.3	Transverse momentum dependent ω multiplicity analysis	197
D.4	Acceptance corrected spectra for theory comparison	200

E DERIVATION OF THE ONE-LOOP SELF ENERGY	205
BIBLIOGRAPHY	207

LIST OF FIGURES

Figure 1.1	Particles included in the <i>Standard Model of Particle Physics</i>	3
Figure 1.2	Feynman diagrams of the electroweak and the strong interaction	5
Figure 1.3	Spontaneous symmetry breaking in the model of an $O(4)$ potential.	7
Figure 1.4	Couplings of all known interactions at various energy scales	11
Figure 1.5	A schematic view of the QCD phase diagram	13
Figure 1.6	Schematics of a heavy-ion collision.	14
Figure 1.7	Space-time evolution of a heavy-ion collision at LHC and RHIC energies.	16
Figure 1.8	J/Ψ suppression in heavy-ion collisions.	17
Figure 1.9	Di-jet correlation in different systems measured with STAR	18
Figure 1.10	Energy dependence of the elliptic flow v_2	18
Figure 1.11	The CM energy dependence of the $\langle K \rangle / \langle \pi \rangle$ ratio in Pb+Pb (Au+Au) and inelastic p+p collisions	19
Figure 1.12	Enhancement of multi-strange hadron production in A+A collision relative to p+p.	19
Figure 1.13	Measured dielectron spectra with CERES at CERN SPS in Pb+Au collisions at $\sqrt{s} = 200 \text{ AGeV}$	21
Figure 1.14	Dimuon measurements with the NA60 CERN SPS experiment in In+In collisions at $\sqrt{s} = 17.3 \text{ AGeV}$	22
Figure 1.15	Dielectron measurements at different CM energies in Au+Au with STAR	23
Figure 1.16	Dielectron excess yield as a function of \sqrt{s} in Au+Au measured with STAR	24
Figure 1.17	Dielectron excess yield in Au+Au collisions at $\sqrt{s} = 2.42 \text{ AGeV}$ measured with HADES	24
Figure 1.18	System size dependence of the dielectron excess radiation measured with HADES.	25
Figure 2.1	Schematic view of HADES	27
Figure 2.2	Segmented Ag target of HADES	28
Figure 2.3	START and VETO detector of HADES	29
Figure 2.4	Side and back view of the HADES magnet	29
Figure 2.5	Magnetic field maps of HADES at different positions.	30
Figure 2.6	Arrangement of the HADES drift chambers and internal wire structure.	31
Figure 2.7	Photo of the HADES TOF detector.	32
Figure 2.8	Schematics of one sector of the HADES RPC.	32
Figure 2.9	Schematic view of the HADES ECal detector setup.	33

Figure 3.1	Schematic explanation of Cherenkov radiation	38
Figure 3.2	Setup of the HADES RICH detector - side view and MAPMT plane	39
Figure 3.3	Quantum efficiency of WLS coated and uncoated MAPMTs	40
Figure 3.4	Detected Cals per Pixel and event on the HADES RICH MAPMT plane.	41
Figure 3.5	<i>Leading Edge</i> and <i>Time over Threshold</i> distributions for a single MAPMT pixel	42
Figure 3.6	Reconstructed ring centres per event per detector pixel in the HADES RICH.	43
Figure 3.7	Single event display of the HADES RICH MAPMT plane	44
Figure 3.8	Dependence of N_{Cals} assigned to a fitted RICH ring and the ring radius on the polar angle Θ	45
Figure 3.9	Event display zoom-in views of the HADES RICH MAPMT plane	47
Figure 4.1	β vs. p/q for all reconstructed tracks after the track finding procedure	50
Figure 4.2	Event and cluster vertex distributions before cuts.	51
Figure 4.3	Effect of all event selection criteria on the whole event sample and classification in centrality bins.	52
Figure 4.4	Centrality classification in HADES	53
Figure 4.5	Origin of fake hits in the MDCs	55
Figure 4.6	β vs. p/q of tracks after HADES standard pre-selection	56
Figure 4.7	Conversion map of HADES from UrQMD simulation .	58
Figure 4.8	Vertex cut on reconstructed tracks	58
Figure 4.9	$N_{Cals}(\Theta)$ comparison between two types of simulations and experiment.	59
Figure 4.10	$r_{ring}(\Theta)$ comparison between two types of simulations and experiment.	60
Figure 4.11	Fitted radius distribution of identified rings in the RICH detector	60
Figure 4.12	Cuts applied on N_{Cals} and ring radius	61
Figure 4.13	β vs. p/q of tracks after RICH ring quality requirements.	61
Figure 4.14	Schematic explanation of the scattering correction applied.	62
Figure 4.15	Ring to track displacement in the azimuth angle Φ before and after applying the multiple scattering correction.	63
Figure 4.16	Ring to track displacement in the polar angle Θ before and after applying the multiple scattering correction. .	64
Figure 4.17	Momentum dependence of angular displacements between rings and tracks.	65
Figure 4.18	Ring to track matching selection window in the $d\Phi - d\Theta$ plane.	66
Figure 4.19	β vs. p/q of tracks after the ring-track requirements. .	67

Figure 4.20	β vs. p/q of reconstructed tracks separated in both META systems, RPC and TOF.	68
Figure 4.21	RICH rotation technique	69
Figure 4.22	β vs. p/q of reconstructed tracks separated in both META systems, RPC and TOF using a rotated RICH geometry.	69
Figure 4.23	Purity of the track sample separated in both META systems, RPC and TOF.	70
Figure 4.24	$m(p)$ selection function in β vs. p/q in both META systems, RPC and TOF.	71
Figure 4.25	Opening angle cut on single leptons	73
Figure 4.26	Double ring reconstruction efficiency	73
Figure 4.27	Identification procedure of unfitted double rings in the RICH detector	75
Figure 4.28	Fitted Distribution of close-to-ring Cals	75
Figure 4.29	Fitted Distribution of close-to-ring Cals in Θ bins	76
Figure 4.30	Efficiency and purity of the Cal dependent conversion rejection	77
Figure 4.31	Comparison of N_{Cal} of isolated rings in experiment and electron-only simulation.	78
Figure 4.32	β vs. $q \cdot p$ of tracks after applying conversion rejection cuts.	79
Figure 4.33	Effect of the individual lepton selection criteria on the track sample	80
Figure 4.34	Impact of all selection cuts on the track sample in $q \cdot p$ and β	80
Figure 4.35	Identification of double rings by summing ToT values of close-by Cals	83
Figure 4.36	Invariant mass spectrum of unlike-sign pairs.	84
Figure 4.37	Reconstructed dielectron pairs in specific bins of invariant mass per event and day.	85
Figure 4.38	$\Theta - \Phi$ map of single leptons forming pairs in four invariant mass bins.	86
Figure 4.39	$\Theta - \Phi$ map of reconstructed dielectrons in specific invariant mass bins.	87
Figure 4.40	Dielectron invariant mass spectra excluding a specific HADES sector from the analysis.	88
Figure 4.41	PID of reconstructed tracks and corresponding parent-PID in UrQMD simulation	89
Figure 4.42	Momentum dependent pion suppression in UrQMD simulations applying the lepton selection criteria.	90
Figure 4.43	e^+e^- invariant mass spectrum in UrQMD simulations.	90
Figure 4.44	Decomposition of the UrQMD MC-true background in its different sources.	91
Figure 4.45	Different ways of efficiency correction tested in simulation.	92

Figure 4.46	Electron efficiency extracted from simulations.	94
Figure 4.47	Positron efficiency extracted from simulations.	95
Figure 4.48	Centrality dependence of the electron efficiency.	96
Figure 4.49	Electron acceptance extracted from simulation.	98
Figure 4.50	Positron acceptance extracted from simulation.	99
Figure 4.51	Comparison of dielectron spectra corrected for efficiency and acceptance in different sets of kinematic variables.	100
Figure 4.52	Comparison of the efficiency and acceptance corrected reconstructed dielectron spectrum with the input data for $\eta \rightarrow \gamma e^+ e^-$	101
Figure 4.53	Pair correction factor	102
Figure 4.54	Same-event like-sign and mixed-event dielectron spectra for background estimation.	103
Figure 4.55	Geometrical mean from mixed-event and same-event like sign spectra together with the k-factor and resulting combinatorial background.	104
Figure 4.56	Systematic error calculation of the combinatorial background estimation and the lepton selection criteria.	107
Figure 4.57	Relative systematic error of the dielectron signal spectrum.	108
Figure 5.1	Reconstruction of the η in the $\eta \rightarrow e^+ e^- e^+ e^-$ channel.	110
Figure 5.2	Reconstruction of the π^0 in the $\pi^0 \rightarrow e^+ e^- e^+ e^-$ channel.	113
Figure 5.3	Background in the $4e$ invariant mass spectrum calculated from $2e+2e$ event-mixing only.	116
Figure 5.4	Contributions to the four particle event mixing.	116
Figure 5.5	Four electron invariant mass spectrum with the BG calculated from event-mixing.	117
Figure 5.6	Reconstructed π^0 in bins of $p_t - y$ and the fitted mean value of the signal.	118
Figure 5.7	ω -meson analysis with hard cuts.	120
Figure 5.8	ω -meson analysis with soft cuts.	120
Figure 5.9	Comparison of the extracted π^0 and η multiplicity with TAPS measurements.	122
Figure 6.1	Centrality integrated, efficiency corrected dielectron spectrum and the corresponding signal-to-background ratio.	124
Figure 6.2	Simulated signal-to-background ratio as published in the beam-time proposal for the AgAg data run.	125
Figure 6.3	Invariant mass distribution of the $\omega \rightarrow e^+ e^-$ channel at different analysis steps.	126
Figure 6.4	Hadronic cocktail simulation in 0 – 40% centrality.	127
Figure 6.5	Invariant mass spectra for elementary pp and pn collisions simulated with GiBUU.	128
Figure 6.6	Momentum smearing applied to GiBUU simulation.	129

Figure 6.7	Acceptance filtered and momentum smeared dielectron spectrum in p+p GiBUU simulation.	129
Figure 6.8	Acceptance filtered and momentum smeared dielectron spectrum in p+n GiBUU simulation.	130
Figure 6.9	NN reference simulated with GiBUU.	130
Figure 6.10	Hadronic cocktail and relevant NN channels from GiBUU simulation.	131
Figure 6.11	Acceptance correction obtained from PLUTO $\rho \rightarrow e^+e^-$ simulation.	132
Figure 6.12	Temperatur estimation in 0 – 40% centrality.	133
Figure 6.13	Dependence of the medium temperature on the centrality of the collision.	134
Figure 6.14	NN reference measured at $\sqrt{s} = 2.42 \text{ GeV}$ together with the $\eta \rightarrow \gamma e^+e^-$ PLUTO cocktail component for $\sqrt{s_{NN}} = 2.55 \text{ GeV}$ and the dielectron signal in Ag+Ag collisions at $\sqrt{s_{NN}} = 2.55 \text{ GeV}$	135
Figure 6.15	Relative acceptance correction for $\sqrt{s_{NN}} = 2.55 \text{ GeV}$ data wrt. $\sqrt{s_{NN}} = 2.42 \text{ GeV}$	135
Figure 6.16	The dielectron excess ratio R_{AA}	136
Figure 6.17	Centrality dependence of the dielectron excess ratio.	137
Figure 6.18	Centrality dependence of the integrated dielectron excess yield.	138
Figure 6.19	Dielectron spectra in $p + Nb$ collisions at $\sqrt{s_{NN}} = 3.18 \text{ GeV}$ and comparison to $p + p$ data measured by HADES	139
Figure 6.20	Pair momentum p_{ee} vs. invariant mass M_{ee} for same-event dielectrons.	140
Figure 6.21	Comparison of same-event and mixed-event combinatorial background in momentum bins.	141
Figure 6.22	Efficiency corrected same-event, combinatorial background and signal spectra in three bins of pair momentum.	142
Figure 6.23	Dielectron signal spectra in three bins of pair momentum.	143
Figure 6.24	Dielectron signal spectra in five bins of pair momentum.	144
Figure 6.25	Momentum dependent dielectron signal in five bins of invariant mass.	146
Figure 6.26	ω multiplicity as a function of pair momentum	146
Figure 6.27	Dielectron signal spectra in three bins of transverse pair momentum.	147
Figure 6.28	Detailed studies of the observed peak structure at $M_{ee} \sim 550 \text{ MeV}/c^2$ in the high p_t data.	148
Figure 6.29	Dielectron signal spectra in three bins of transverse pair momentum.	149
Figure 6.30	High pair p_t invariant mass spectrum corrected for acceptance within the geometric HADES acceptance.	150

Figure 8.1	Compilation of measured data for $\sigma_{tot}(e^+e^- \rightarrow hadrons)$ normalized to $\sigma_{tot}(e^+e^- \rightarrow \mu^+\mu^-)$	156
Figure 8.2	Spectral functions of the ρ and a_1	157
Figure 9.1	One-loop diagrams of the sigma and the pion.	163
Figure 10.1	$Z_{\pi,k}$ and $Z_{\sigma,k}$ as a function of the RG scale k	167
Figure 10.2	The effective potential $U_k(\rho)$ obtained from the LPA and the SC1L flow in the UV and in the IR.	168
Figure 10.3	The scale-dependent minimum of the effective potential.	169
Figure 10.4	Flow of the three-point coupling constants $g_{\sigma\pi\pi,k}$ and $g_{\sigma\sigma\sigma,k}$	169
Figure 10.5	Euclidean curvature masses and pole masses with the LPA setup.	170
Figure 10.6	Euclidean curvature masses and pole masses with the SC1L setup	170
Figure 10.7	Real part of the pion and sigma two-point functions.	171
Figure 10.8	Imaginary part of the pion and sigma two-point functions.	172
Figure 10.9	The pion and sigma spectral functions in the IR for $\varepsilon = 0.1 MeV$	172
Figure 10.10	The pion and sigma spectral functions in the IR for $\varepsilon = 0 MeV$	173

LIST OF TABLES

Table 1.1	Interactions between elementary particles	4
Table 2.1	PLUTO temperatures used for simulation of dielectrons originating from meson decays.	35
Table 2.2	Overview on the HADES simulations used in this work.	35
Table 4.1	Definition of centrality bins and corresponding amount of events left for analysis after cuts.	53
Table 4.2	Number of reconstructed e^+e^- pairs in bins of M_{ee} . .	84
Table 4.3	Reconstructed electrons per sector in bins of the pair invariant mass.	86
Table 4.4	Reconstructed dielectrons per sector in bins of the pair invariant mass.	87
Table 4.5	Cut parameter variation to test efficiency correction. . .	106
Table 5.1	η multiplicity in different centrality classes.	112
Table 5.2	π^0 multiplicity in different centrality classes.	114
Table 5.3	ω multiplicity in different centrality classes.	121
Table 6.1	Dielectron signal pairs in specific invariant mass bins. .	124
Table 6.2	Hadronic cocktail components at freeze-out together with according multiplicity, branching fraction and effective temperature used for PLUTO simulation. . . .	125
Table 6.3	The R_{AA} measured in different systems at different energies.	137
Table 6.4	The R_{AA} measured in different centralities for Ag+Ag collisions at $\sqrt{s_{nn}} = 2.55 \text{ GeV}$	138
Table 6.5	Reconstructed and efficiency corrected number of pairs in bins of momentum and invariant mass.	143
Table 9.1	Parameters of the effective potential in the UV and resulting physical values.	165
Table 10.1	Numerical values for the coupling constants, the curvature masses, the renormalized curvature masses, and the pole masses in the LPA and SC1L setup.	171

Part I

DIELECTRON ANALYSIS IN AG+AG COLLISIONS
WITH HADES

INTRODUCTION

1.1 THE STANDARD MODEL OF PARTICLES PHYSICS

The baseline of modern hadron and particle physics is drawn by the so-called *Standard Model of Particle Physics* (SM) that has been continuously developed in the latter half of the 20th century based on theoretical prediction and subsequent experimental verification of the particles it contains. The formulation we are nowadays used to is established since the experimental confirmation of the existence of quarks in the mid-1970s based on studies of deep-inelastic scattering experiments (e.g. $ep \rightarrow ep^*$) at the Stanford Linear Accelerator Center SLAC [1] [2]. Murray Gell-Mann and George Zweig previously suggested the existence of quarks [3] [4] to classify the large variety of experimentally observed hadrons.

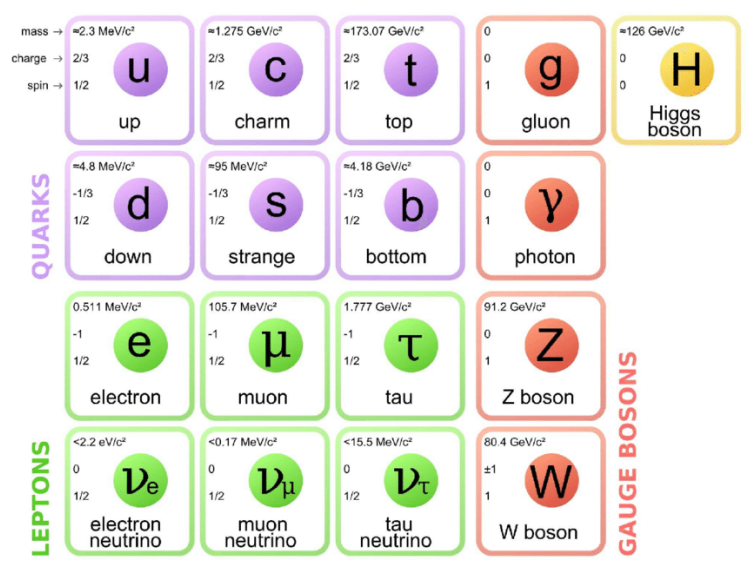


Figure 1.1: Particles included in the *Standard Model of Particle Physics*. See text for details. Taken from [5].

In total, six different types of quarks exist, that are divided into three generations. The first generation of quarks consists of the *up*- (u) and *down*- (d) quarks that form nucleons ($p \sim \{uud\}$, $n \sim \{udd\}$) which are themselves bound together in nuclei and therefore present in the matter that is daily observed. As protons are slightly lighter than neutrons, unbound neutrons are unstable and decay with a mean life time of $\tau_n = 880.2 \pm 1.0 s$ ($n \rightarrow pe^- \bar{\nu}_e$) [6]. Protons are stable within the SM which holds in the limit of experimental measurements ($\tau_p > 3.6 \cdot 10^{29} y$) [6]. The second generation of quarks is

Interaction	Gauge theory	Gauge Boson	charge	range [m]	relative strength
Electromagnetism	QED	photon (γ)	e	∞	$\sim 10^{36}$
Strong	QCD	gluon	color	10^{-15}	$\sim 10^{38}$
Weak	/	Z^0, W^\pm	weak charge	10^{-18}	$\sim 10^{25}$
Gravitation	general relativity	Graviton (*)	mass	∞	1

Table 1.1: Interactions between elementary particles and their properties. The electromagnetic and weak interaction are listed separately although being unified within the SM to point out effects arising from the massive gauge bosons mediating weak forces. Experimentally unconfirmed particles are marked with (*).

composed of the *strange-* (s) and the *charm-* (c) quark. Both are significantly heavier than the first-generation-quarks and can therefore only be observed in unstable hadrons. The same applies to the even more heavy *top-* (t) and *bottom-* (b) quarks that form the third generation of quarks. Within the SM, all quarks are elementary particles being point-like and therefore appear without any inner structure. Having a spin of $s = 1/2$ they are classified as fermions.

Besides the quarks, three generations of leptons are included in the SM as elementary particles. They are formed by the electron (e), the myon (μ) and the tau (τ) together with their corresponding neutrino each. There exist anti-particles to all elementary particles (e.g. \bar{u} as the anti-u quark, e^+ and e^- as anti-particles) that show the exact same behaviour in all respects within the SM but having opposite charges. An overview on all particles and their properties included in the SM is given in fig. 1.1.

As fundamental interactions the SM includes two quantum-field gauge theories, the strong interaction (compare chapter 1.1.3) with the massless gluon (g) as gauge boson and the electro-weak interaction (chapter 1.1.2) with three massive gauge bosons ($m(Z^0) = 91.19 \text{ GeV}/v^2$, $m(W^\pm) = 80.38 \text{ GeV}/c^2$) and one massless, the photon (γ). Gravitation is not yet included into the SM as it misses a formulation as quantum-field-theory. The so-called graviton is proposed to serve as gauge boson but has not been experimentally observed so far. Although gravitation is the dominant force in the macroscopic picture of our daily live its microscopic impact in the picture of elementary particles is neglectable. All known interactions as well as their relative strength and range are shown in table 1.1. The basically unlimited range of these interactions ($1/r$ dependence of the potential) is restricted to very small distances in case of the strong and weak interaction due to *Confinement* and the bare mass of the gauge bosons, respectively. The strength of an interaction can easily be studied applying *Fermis Golden-Rule* [7] [8],

which gives a probability for a transition from an initial quantum state $|i\rangle$ to a final state $\langle f|$

$$\lambda_{i \rightarrow f} \sim \rho(E_f) |\langle f|V|i\rangle|^2 \tag{1.1}$$

where the density of final states is denoted by $\rho(E_f)$ and $|\langle f|V|i\rangle|$ represents the corresponding transition matrix element including the potential V . The matrix element M is basically given by a product of the coupling constant α and the propagator of the gauge boson mediating the interaction and therefore reads

$$M \sim \alpha \cdot \frac{1}{q^2 - m^2 c^2} \cdot \alpha \tag{1.2}$$

with the 4-momentum transfer q and the gauge bosons pole mass m . Obviously not only a strong coupling, but also light gauge bosons increase the strength of an interaction. As a result the weak interaction lives up to its name although the couplings are comparable to the ones of the strong interaction. Following from this, weakly decaying particles have a significantly longer lifetime as those, that are capable of strong decays.

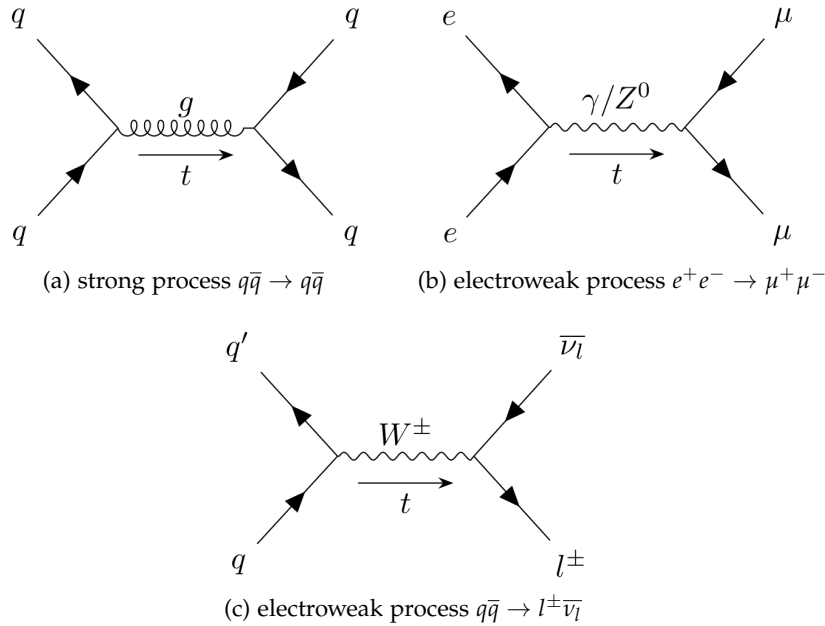


Figure 1.2: Feynman diagrams of the electroweak and the strong interaction.

A coupling between a particle and a gauge boson and therefore an interaction between particles within the corresponding force is possible in case a particle carries the interaction specific charge. This limits the strong interaction to quarks and gluons, whereas the gluons as gauge bosons themselves carry a strong charge enabling self-interaction as a key feature of the

strong interaction. As symbolization for the strong charge, colors are commonly used. In total, there exist three different strong charges (usually denoted as **blue**, **red** and **green**) and their corresponding anti-charges. First experimental hints to the amount of colors were the discovery of the Δ^{++} baryon and the comparison of branching ratios in the channels $e^+e^- \rightarrow q\bar{q}$ and $e^+e^- \rightarrow \mu^+\mu^-$ [9]. All particles included in the standard model carry a weak charge and can therefore couple to the Z^0 and W^\pm bosons. The electric charge is defined within the electroweak unification as the sum of weak hypercharge and third component of weak Isospin to

$$Q = 1/2 \cdot Y_w + T_3 \quad (1.3)$$

Interaction processes are commonly visualized using *Feynman diagrams* [10]. These diagrams furthermore provide a clear mathematical instruction to calculate corresponding matrix elements. Typical first order Feynman diagrams are shown in fig. 1.2. 1.2a shows $q\bar{q}$ annihilation with subsequent formation of a new quark-pair mediated by a gluon. The transition of an electron pair into a myon pair is shown in 1.2b and can either be mediated by a photon or a Z^0 -boson. Annihilation of quarks of different flavor results in an intermediate W^- boson that might decay into a lepton with the corresponding anti-neutrino as shown in 1.2c. It has to be noted, that all mediator particles are off-shell like and therefore not necessarily share the pole mass of a real gauge boson. Particles that move towards negative times indicate anti-particles.

The latest addition to the standard model is the Higgs-Boson that has been discovered in 2012 by the **A Toroidal LHC ApparatuS** (ATLAS) and the **Compact Muon Solenoid** (CMS) experiments [11] [12] after being proposed almost 50 years earlier [13] [14] [15] [16]. The Higgs-boson is the associated particle to the Higgs field which gives mass to particles interacting with it. It plays a crucial role in the electroweak unification and therefore the SM itself making its prediction to the biggest success so far. Despite the general success in many fields, the SM can only be seen as an effective field theory, as there are several observations that verify so called *beyond-Standard-model-physics*: The most obvious is that gravitation is not included. Furthermore, from astrophysical observations, it is also well known, that the matter described by the SM makes up only a small part of the total known matter in the universe (about 5%). The major part of our universe consists of dark matter ($\sim 27\%$) and dark energy ($\sim 68\%$) that at maximum barely interacts with SM matter [17]. The stated values can be extracted from e.g. gravitational lensing effects [18] and galactic rotation curves[19].

Another unsolved question in physics is the present matter-antimatter asymmetry. In the Big Bang equal amounts of matter and anti-matter should have been created but today only matter can be observed [20] [21]. Although the SM includes and explains CP violation in the sector of Kaons and B-mesons [22], the arising effect is by far too small to serve as an explanation for the

astrophysical observations [23].

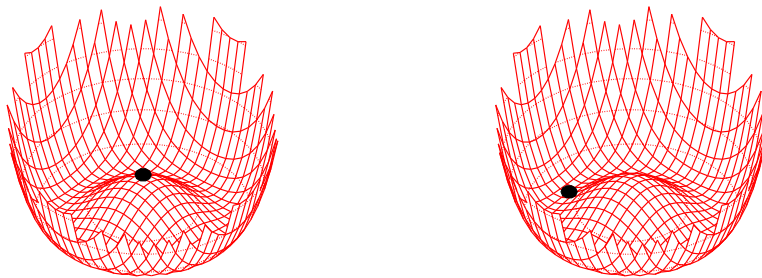
The theoretical formulation of the SM is mathematically based on symmetry groups. There are two main purposes of these groups: At first, they are used as transformation groups under which a theory is invariant (local symmetries). Second, group representations are used for classification of all the different particles and resonances that are observed (global symmetries). In this group-theoretical picture, the SM is a gauge quantum field theory that contains the internal symmetries of the unitary product group $SU(3) \times SU(2) \times U(1)$. The following chapters give a deeper insight into the acquisition of mass within the Higgs-mechanism and the electroweak and strong interactions itself based on the group-theoretical formulation of the SM.

1.1.1 Spontaneous symmetry breaking

The spontaneous breaking of symmetries is an important feature within the SM, that is essential in the understanding of the Higgs mechanism and chiral symmetry and is therefore briefly illustrating in the following in a simple model of a scalar field Φ . The behaviour of any system is determined by the describing Lagrangian \mathcal{L} , which can be split into a kinetic and a potential component and reads

$$\mathcal{L} = \partial^\mu \Phi \partial_\mu \Phi - V(\Phi) \quad (1.4)$$

Breaking of the symmetry of the system refers to the potential $V(\Phi)$. As example, an $O(4)$ potential is chosen ($V(\Phi) \sim a \cdot \Phi^2 + b \cdot \Phi^4$). In this potential, an infinite amount of minima can be observed, that surround the centre



- (a) With a particle located in the vacuum state of the potential, the system is symmetric. (b) The particle moves into a minimum and therefore spontaneously breaks the symmetry of the system.

Figure 1.3: Spontaneous symmetry breaking in the model of an $O(4)$ potential.

symmetrically as shown in fig. 1.3. Here, it is important to note, that the vacuum state of the potential is located in the centre at $\Phi = 0$ which is symmetric under $U(1)$ transformations. This vacuum state is unstable and the system will therefore move into an arbitrary minimum and spontaneously break the present symmetry.

As a consequence of spontaneous symmetry breaking, so-called Goldstone bosons can be observed in accordance to the Goldstone theorem [24] [25]. These are massless, scalar particles that appear in the spectrum of possible excitation for each generator of the symmetry that is broken. In case the corresponding symmetry is not exact, thus explicitly broken, the according Goldstone-bosons appear to have non-zero mass.

1.1.2 Electroweak interaction

The electroweak interaction is mathematically described by an unification of the electromagnetic and the weak interaction to a *Yang-Mills field* with an $SU(2) \times U(1)$ gauge group. This formalism has been developed in the late 1970s by Sheldon Glashow, Abdus Salam and Steven Weinberg [26] [27]. The $SU(2)$ symmetry is generated by the weak isospin T whereas the $U(1)$ symmetry arises from the weak hypercharge Y . As corresponding fields, there is a triplet ($N^2 - 1$) of weak isospin fields W_1, W_2, W_3 and the weak hypercharge field B . The related gauge bosons that mediate the electroweak interaction are the elementary excitation of these underlying fields and equally labeled. Initially these gauge bosons have to be massless in order to preserve gauge invariance. Mass is acquired by the interaction with the Higgs-field and associated spontaneous symmetry breaking of the electroweak symmetry within the Higgs mechanism. This spontaneous symmetry breaking produces the physical SM γ and Z^0 Boson as a consequence of mixing of the W_3 and B boson. This mixing is mathematically described as a rotation of the corresponding eigenstates by the weak mixing angle Θ_W giving also rise to the differences in the W^\pm and Z^0 masses ($M_Z = M_W / \cos\Theta_W$).

$$\begin{pmatrix} \gamma \\ Z^0 \end{pmatrix} = \begin{pmatrix} \cos\Theta_W & \sin\Theta_W \\ -\sin\Theta_W & \cos\Theta_W \end{pmatrix} \begin{pmatrix} B \\ W_3 \end{pmatrix} \quad (1.5)$$

The physical W^\pm states are given as a linear combination of $W_{1,2}$ which reads

$$W^\pm = \frac{1}{\sqrt{2}}(W_1 \mp iW_2) \quad (1.6)$$

This leads to the electroweak Lagrangian, that consists of several parts, which will be shortly discussed in the following.

$$\mathcal{L}_{EW} = \mathcal{L}_K + \mathcal{L}_N + \mathcal{L}_C + \mathcal{L}_H + \mathcal{L}_{HV} + \mathcal{L}_{WWV} + \mathcal{L}_{WWVV} + \mathcal{L}_Y \quad (1.7)$$

\mathcal{L}_K (kinetic part) is composed of the dynamic terms and the mass terms of the W^\pm , Z^0 and the Higgs boson (H). The included mass terms explicitly arise from symmetry breaking. \mathcal{L}_K reads

$$\begin{aligned} \mathcal{L}_K = \sum_f \bar{f}(i\partial - m_f)f - \frac{1}{4}A_{\mu\nu}A^{\mu\nu} - \frac{1}{2}W_{\mu\nu}^+W^{-\mu\nu} + m_W^2W_\mu^+W^{-\mu} \\ - \frac{1}{4}Z_{\mu\nu}Z^{\mu\nu} + \frac{1}{2}m_Z^2Z_\mu Z^\mu + \frac{1}{2}(\partial^\mu H)(\partial_\mu H) - \frac{1}{2}m_H^2H^2 \end{aligned} \quad (1.8)$$

with a summation over all fermions, quarks and leptons. The fields ($A_{\mu\nu}$ denotes the photon field) are given by, e.g.

$$A_{\mu\nu} = \partial_\mu A_\nu - \partial_\nu A_\mu + gf^{abc}A_\mu A_\nu \quad (1.9)$$

with corresponding coupling g and the gauge groups structure constant f^{abc} , which is zero for the photon field, as no first order self interaction is possible. The same applies for $Z_{\mu\nu}$ and $W_{\mu\nu}$ that are identified with the identically labeled gauge bosons.

The neutral current \mathcal{L}_N of the Lagrangian contains the interaction between the fermions and the neutral charged gauge bosons, namely the γ and the Z^0 . Inserting the electromagnetic current J_μ^{em} and the neutral weak current J_μ^3 it reads

$$\mathcal{L}_N = eJ_\mu^{em}A^\mu + \frac{g}{\cos\Theta_W}(J_\mu^3 - \sin^2\Theta_W J_\mu^{em})Z^\mu \quad (1.10)$$

where the first term can be identified as the QED Lagrangian. The couplings to the γ and the Z^0 are related by the relation $e = g \sin\Theta_W$.

The charged current term \mathcal{L}_C represents interaction of fermions with the W^\pm boson. It reads for the W^+ (the W^- term is analogue)

$$\mathcal{L}_C = -\frac{g}{\sqrt{2}} \left[\bar{u}_i \gamma^\mu \frac{1 - \gamma^5}{2} M_{ij}^{CKM} d_j + \bar{\nu}_i \gamma^\mu \frac{1 - \gamma^5}{2} l_i \right] W_\mu^+ + h.c. \quad (1.11)$$

The CKM matrix M_{ij}^{CKM} determines the mixing between the mass and the weak eigenstates of the quarks and thus enables flavor changing within charged weak currents. The second term features lepton number conservation in each family connecting a lepton with the corresponding anti-neutrino. The factor of $(1 - \gamma^5)/2$ is of special interest, as it projects out the left handed components of the spinor fields, which the weak gauge bosons only couple to. Therefore the electroweak theory is a chiral theory maximally violating parity.

As the Higgs boson itself carries a mass, it can self-interact. The corresponding three- and four-point terms are included in \mathcal{L}_H

$$\mathcal{L}_H = -\frac{gm_H^2}{4m_W}H^3 - \frac{g^2m_H^2}{32m_W^2}H^4 \quad (1.12)$$

The same applies to the interaction of the Higgs with the gauge vector bosons:

$$\mathcal{L}_{HV} = \left(gm_W H + \frac{g^2}{4} H^2 \right) \left(W_\mu^+ W^{+\mu} + \frac{1}{2\cos^2\Theta_W} Z_\mu Z^\mu \right) \quad (1.13)$$

Self-interaction of the gauge vector bosons is only possible involving at least two W^\pm bosons. The three- (\mathcal{L}_{WWV}) and four-point (\mathcal{L}_{WWVV}) contributions read

$$\begin{aligned} \mathcal{L}_{WWV} = -ig \left[\left(W_{\mu\nu}^+ W^{-\mu} - W^{+\mu} W_{\mu\nu}^- \right) (A^\nu \sin\Theta_W - Z^\nu \cos\Theta_W) \right. \\ \left. + W_\nu^- W_\mu^+ (A^{\nu\mu} \sin\Theta_W - Z^{\nu\mu} \cos\Theta_W) \right] \quad (1.14) \end{aligned}$$

$$\begin{aligned} \mathcal{L}_{WWVV} = -\frac{g^2}{4} \left(\left[2W_\mu^+ W^{-\mu} + (A_\mu \sin\Theta_W - Z^\mu \cos\Theta_W)^2 \right]^2 \right. \\ \left. - \left[W_\mu^+ W_\nu^- + W_\nu^+ W_\mu^- + (A_\mu \sin\Theta_W - Z^\mu \cos\Theta_W) \right. \right. \\ \left. \left. (A_\nu \sin\Theta_W - Z^\nu \cos\Theta_W) \right]^2 \right) \quad (1.15) \end{aligned}$$

Finally, \mathcal{L}_Y denotes the Yukawa interaction of fermions with the Higgs field

$$\mathcal{L}_Y = -\sum_f \frac{gm_f}{2m_W} \bar{f} f H \quad (1.16)$$

1.1.3 Quantum Chromodynamics

Quantum ChromoDynamics (QCD) is based on the SU(3) gauge group. There are eight generators ($N^2 - 1$) that are identified with eight different gluons that arise from all possible color - anti-color combinations, that do not create a colorless object. The Lagrangian of QCD is given by

$$\mathcal{L}_{QCD} = \bar{\Psi}_q^i (i(\gamma^\mu D_\mu)_{ij} - m\delta_{ij}) \Psi_q^j - \frac{1}{4} G_{\mu\nu}^a G_a^{\mu\nu} \quad (1.17)$$

with the quark field Ψ_q^i with flavor q and color index i ($\Psi_q = (\Psi_{qR}, \Psi_{qG}, \Psi_{qB})$). The gluon field is denoted by $G_{\mu\nu}^a$ with the color index $a \in \{1, \dots, 8\}$ and D_μ represents the covariant derivative in QCD which depends on the strong coupling α_s . This coupling is by far not a constant, but strongly depends on the 4-momentum transfer in a given reaction. Its value is usually numerically specified starting at the reference scale $Q^2 = M_Z^2$ with $\alpha_s(M_Z) \approx 0.12$ by

$$\alpha_s(Q^2) = \alpha_s(M_Z^2) \frac{1}{1 + b_0 \alpha_s(M_Z^2) \ln \frac{Q^2}{M_Z^2} + \mathcal{O}(\alpha_s^2)}. \tag{1.18}$$

Contributions that exceed a first order approximation are specified in $\mathcal{O}(\alpha_s^2)$. Corresponding relations are available e.g. in [28]. However, higher order effects become significant only for $Q^2 \ll M_Z$ [29]. b_0 depends on the amount of flavors which changes at various thresholds ($n_f = 3$ below charm threshold, up to $n_f = 6$ at scales exceeding the top-threshold). As a direct consequence, the slope of α_s changes at specific values of Q^2 . The overall behaviour of α_s leads to the result, that the QCD coupling decreases with energy. This phenomenon is known as asymptotic freedom. As a direct consequence, the most powerful theoretic tool to access QCD, perturbation theory [30], is limited to high energies, where quarks appear to be quasi-free. On the other hand, quarks are confined within colorless objects, hadrons, at low energy scales. A deeper insight on this topic and its experimental assessment will be given in the following sections. A detailed discussion on α_s and recent theoretical calculations is available in [31]. Experimental results are shown e.g. in [32]. The overall behaviour of the strong coupling at various energy scales is shown in fig. 10.4 together with the electromagnetic and the weak coupling. Within the *Standard Model of Particle Physics* the couplings approach each other at high energies but do not meet all in a specific point. This happens in so-called **SUPER-SYMMETRIC** (SUSY) theories [33] [34], where electroweak and strong interaction unify at some high energy scale (typically of about $\sim 10^{15} \text{ GeV}$) to a **Grand Unified Theory** (GUT) in $SU(5)$ [34]. At even higher energies a unification also with gravity seems possible, resulting in a **Theory Of Everything** (TOE) [35]. However, so far no evidence for any SUSY theory has been experimentally found, but the search is ongoing, especially at the **Large Hadron Collider** (LHC) [36][37].

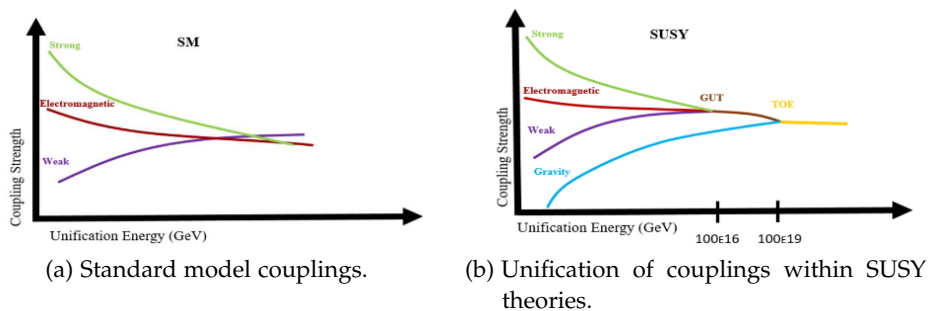


Figure 1.4: Couplings of all known interactions at various energy scales within the *Standard Model of Particle Physics* and SUSY theories. Taken from [35]

An important feature of QCD is the *chiral symmetry* as it is almost perfectly realized in nature and can therefore be well studied to obtain a better understanding of the interaction between quarks and gluons and the strong interaction itself. Generally spoken, *chiral symmetry* is realized in case the quark-part of the QCD Lagrangian can be decomposed into a left-handed and a

right-handed part, which implies both to be transformed independently of each other. Introducing

$$\Psi_L = \frac{\mathbb{1} - \gamma_5}{2} \Psi = \mathcal{P}_L \Psi \quad , \quad \Psi_R = \frac{\mathbb{1} + \gamma_5}{2} \Psi = \mathcal{P}_R \Psi \quad (1.19)$$

and using $\not{D} = (\gamma^\mu D_\mu)_{ij}$ to shorten the notation, the quark part of the QCD Lagrangian reads

$$\mathcal{L}_{QCD} = \bar{\Psi}_L i \not{D} \Psi_L + \bar{\Psi}_R i \not{D} \Psi_R - \bar{\Psi} M \Psi \quad (1.20)$$

Chiral symmetry is obviously explicitly broken by non-zero quark masses and therefore by far not realized in the heavy quark sector. Regarding the light quark sector with only u and d (and in a bit worse approximation also the s) quarks, chiral symmetry is close to be exact. In this case, the Lagrangian in eq. 1.20 is capable of independent phase-changes of the left- and right-handed part (e.g. $\Psi_L \rightarrow \exp(-i\Phi_L)\Psi_L$) which are identified with a global $U(1)_L \times U(1)_R$ symmetry. Furthermore, independent isospin rotations can be applied (e.g. $\Psi_L \rightarrow \exp(-i\vec{\alpha}_L \vec{T})\Psi_L$) as $SU(2)_L \times SU(2)_R$ symmetry is present. In terms of the unprojected quark field Ψ these symmetries write as scalar and pseudoscalar phases and isospin rotations. Among them one finds the $U(1)_s$ and $SU(2)_V$ subgroups, that are **not** explicitly broken by finite quark masses (for $m_u \approx m_d$) and can be identified with Heisenbergs isospin symmetry [38]. As a direct consequence of each global symmetry one encounters a conserved current in accordance with the Noether-Theorem [39][40]. The corresponding Lorentz-invariant objects with according quantum numbers are well known as all different kinds of mesons. As chiral symmetry is explicitly broken by non-zero quark masses, these are not massless. However, one would expect scalar- and pseudoscalar mesons (σ and π) and vector and axialvector (ρ and a) mesons to have the same mass, which is not observed in experiment. The reason being is the non-symmetric and therefore spontaneously broken ground state of QCD which manifests in a non-zero vacuum expectation value of the quark-fields ($\langle vac | \bar{\Psi} \Psi | vac \rangle \neq 0$) and is equivalent to a spontaneous breaking of chiral symmetry. In three flavors (including the strange sector), the Goldstone bosons linked to spontaneous symmetry breaking are the π , K , η and η' mesons.

1.2 THE QCD PHASE DIAGRAM

Similar to molecular matter (e.g. water), QCD matter (composed of quarks and gluons) can be classified in a phase diagram pointing out different states the matter can adopt. The proper variables for this classification are temperature and baryon chemical potential μ_B [41]. A first proposal of such a phase diagram has been made in 1975 by Cabibo and Parisi [42]. The investigation of the QCD phase diagram is experimentally (and also in theory) a major challenge, as free quarks and gluons can not be observed in our surroundings due to confinement, but are bound within colorless objects (hadrons).

However, lattice calculations indicate a continuous transition in terms of a cross over of phases towards free quarks and gluons at high temperatures (the *Quark-Gluon-Plasma*, QGP) and $\mu_B = 0$ [43], which is believed to be the early state of our universe after the big bang. The transition temperature from a hadron gas towards a QGP at vanishing baryon chemical potential has been measured to be in the order of $T_{trans} \sim 160 \text{ MeV}/c$ [44] which agrees with theoretical calculations [45] [46] [47] [48]. A sketch of the QCD phase diagram as it is believed to look like nowadays is shown in fig. 1.5. The matter in its vacuum state, where quarks are bound together to protons and neutrons is located at rather small temperatures and medium densities, whereas the QGP state is located at high temperature and baryochemical potential. The experimental tool to access and study various regions in the phase diagram are collisions of accelerated heavy ions which will be discussed in the following chapter in detail (1.3). Besides the mentioned lattice calculations various other theoretical frameworks have been developed, as lattice is restricted to small baryon density regions [49], see e.g. [50], [51]. Several QCD based models predict, that the transition towards the QGP is realized as a first order phase transition at high baryon densities [52]. Combined with mentioned lattice calculations at zero baryon chemical potential, the existence of a critical endpoint follows [53], [54].

Star remnants that underwent a supernova and were that heavy, that the gravitational pressure exceeded the Fermi pressure of electrons are called neutron stars. They are formed out of dense neutron matter, with the details of the composition still being unclear. If these stars would be slightly heavier, such that the gravitational pressure also exceeds the Fermi pressure of the neutrons, a black hole would be formed. Neutron stars are well known from astronomic observations and the medium present in their cores is thought to be located in the transition region from hadrons to a QGP at low tempera-

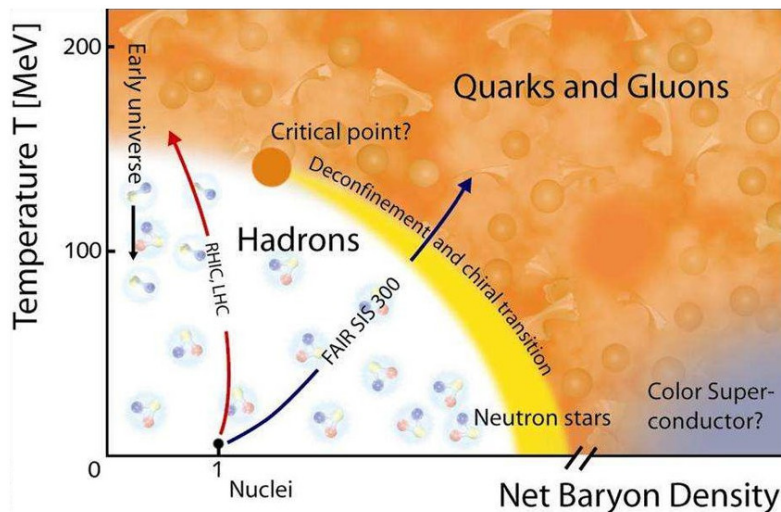


Figure 1.5: A schematic view of the QCD phase diagram. Taken from [55].

tures and high baryon densities [56]. At even higher densities, the existence of a color superconducting phase is postulated, in which no gluons would be needed for color exchange between quarks due to the formation of a diquark condensate similar to Cooper pairs in electromagnetic superconductivity [57]. However, it is unclear how such a kind of matter could be realized in nature.

The QGP is characterized by a restoration of the zero vacuum expectation value of the quark fields ($\langle vac | \bar{\Psi}\Psi | vac \rangle_{QGP} \sim 0$). As a direct consequence, chiral symmetry is restored (not spontaneously broken any longer) which leads to plenty of phenomena that are aimed to be measured in experiment. A detailed discussion on how the existence of a QGP can be experimentally confirmed is given in section 1.4.

1.3 EXPERIMENTAL EXPLORATION OF THE QCD PHASE DIAGRAM WITH HEAVY-ION COLLISIONS

The experimental tool to investigate the various phases of baryonic matter are collisions of heavy ions. They provide a unique possibility to heat and compress the matter of interest. The use of heavy and thus comparably large nuclei ensures a system size that provides a reasonable definition of thermodynamical quantities such as temperature and pressure.

The phenomenology of a heavy-ion collision is determined by three main parameters. At first, the system size is given by the nuclei accelerated and used for collision and the impact parameter b which measures the centrality of the collision in terms of the minimal distance between the centers of the colliding nuclei (compare fig. 1.6 for a schematic view).

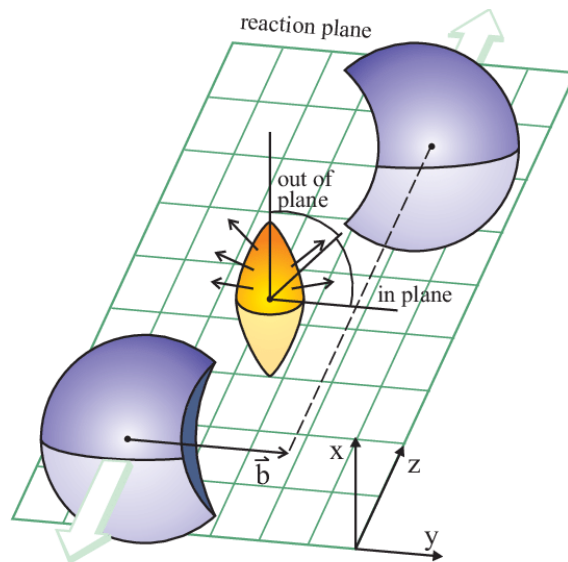


Figure 1.6: Schematics of a heavy-ion collision. Two accelerated nuclei collide with an impact parameter b that together with the given beam axis defines the reaction plane. Taken from [58].

Second, the centre-of-mass (CMS) energy of the system \sqrt{s} regulates the collision dynamics as it defines temperature and baryon chemical potential of the medium created. \sqrt{s} heavily depends on the experimental setup. In case of a fixed target experiment it scales with $\sqrt{s} \sim \sqrt{E_{beam}}$, whereas in collider experiments $\sqrt{s} \sim E_{beam}$ holds. On the other hand a lot higher collision rates can be achieved in fixed target experiments as the amount of target nuclei can be chosen much higher than in a collider, where space charge effects limit the focus and multiplicity of nuclei in a bunch. The *luminosity* is the common variable defining the interaction rate of an experiment and the corresponding accelerator.

At moderate energies as e.g. present at the SIS-18 accelerator at GSI, Darmstadt, where the **H**igh **A**cceptance **D**i**E**lectron **S**pectrometer (HADES) is located, the approaching nuclei merge to a fireball reaching temperatures of about $T \approx 70 \text{ MeV}$ [59] at baryon densities up to three times the normal matter nuclear density [60] with a centre of mass energy of $\sqrt{s} \sim 1 - 2 \text{ AGeV}$. At these medium properties no QGP is present, but a dense hadron gas is formed. At the future FAIR facility at GSI with the SIS-100 and SIS-300 accelerators which will be operated at up to $\sqrt{s} \sim 10 \text{ AGeV}$ and are currently under construction, the chiral transition could be passed in accordance with theoretic calculations and investigated by the **C**ompressed **B**aryonic **M**atter (CBM) experiment [61], [62] and HADES. At other experiments with even higher beam energies (and thus increased \sqrt{s}) the accelerated nuclei are strongly Lorentz-contracted and thus appear in a saucer like shape. In such collisions almost no stopping of the nuclei happens, but color strings are stretched between the nucleons passing each other which leads to extremely high temperatures and the production of $q\bar{q}$ pairs as the strings rip. This enormous production of matter and anti-matter results in a vanishing net baryon density and thus a baryon chemical potential close to zero, which reproduces the conditions that are commonly believed to be present shortly after the Big Bang. This type of collision dynamics is investigated at the **C**onseil **e**uropeén **p**our **l**a **r**echerche **n**ucléaire (CERN) with the **A** **L**arge **I**on **C**ollider **E**xperiment (ALICE) detector [63] measuring $Pb + Pb$ at up to $\sqrt{s} = 2.76 \text{ TeV}$ CMS energy provided by the **L**arge **H**adron **C**ollider (LHC). The **R**elativistic **H**eavy **I**on **C**ollider (RHIC) at Brookhaven National Laboratory offers $Au + Au$ collisions at up to $\sqrt{s} = 200 \text{ AGeV}$ that are measured with the **P**ioneering **H**igh **E**nergy **N**uclear **I**nteraction **e**Xperiment (PHENIX, until 2016) [64] and the **S**olenoidal **T**racker **A**t **R**HIC (STAR) [65].

The space-time evolution of an heavy-ion collision at LHC and RHIC energies is schematically shown in fig. 1.7. A short formation time of $\tau_0 < 1 \text{ fm}/c$ where the matter is heated and compressed is the beginning of the collision. This step is dominated by inelastic, hard processes, where longitudinal momentum of the beam nucleons is converted into new internal and transverse degrees of freedom breaking up the initial baryon structure. At this point of the collision, the system is far away from thermal equilibrium. This is reached, when the longitudinal partonic showers decelerate themselves via

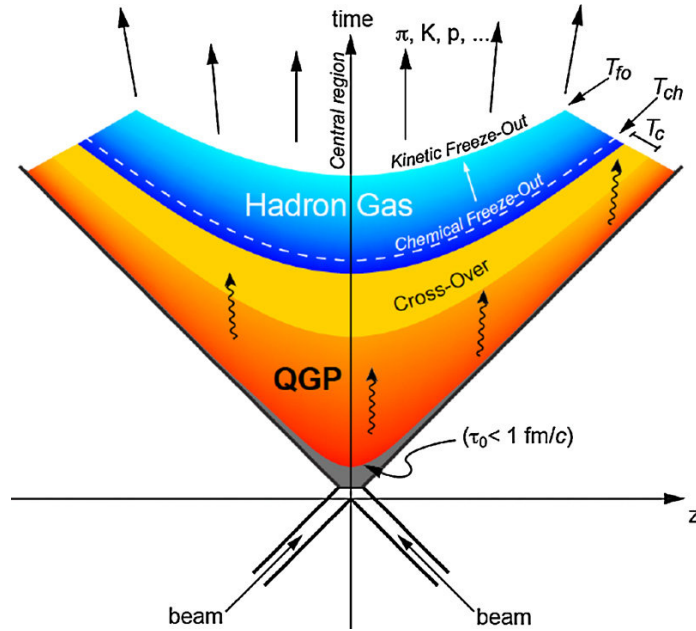


Figure 1.7: Space-time evolution of a heavy-ion collision at LHC and RHIC energies. For details see *text*. Taken from [66].

interaction and form a QGP. In the following, the system quickly expands due to high pressure gradients and thus cools down. With temperature and baryon chemical potential dropping below the parton-hadron boundary, hadrons and hadronic resonances are formed and the system transforms into a hadron gas. This process is called *Chemical Freeze Out*. As particles move away from each other they stop interacting inelastically at some point, which is called the *Kinetic Freeze Out*. As collision products, kaon (K), pions (π), nucleons (n, p), electrons (e), myons (μ), neutrinos (ν) and photons are present. These serve as probes to reconstruct the collision dynamics as it will be discussed in the following chapter.

1.4 OBSERVABLES IN HEAVY-ION COLLISIONS

For verification of model predictions and to get a deeper understanding and insight into the various predicted states of QCD matter, measured particle properties have to be translated into physics observables. Such observables ideally give an insight into a distinct stage of the dynamical evolution of the collision not being overlaid and thus 'washed out' in subsequent stages. The most prominent are shortly discussed in the following.

- **Vector meson and virtual photon production:** Vector mesons such as the J/Ψ and the Y originate from $c\bar{c}$ and $b\bar{b}$ pairs produced in hard inelastic qq interactions in the early stages of the collision. In elementary collisions (e.g. pp or πp) these pairs would directly form a J/Ψ or Y with a certain probability, whereas they are distracted from each other in a potential QGP due to Debye screening effects leading to

an overall suppression of J/Ψ and Y . Data on the J/Ψ production measured in SPS experiments at $\sqrt{s} = 17.3 \text{ AGeV}$ in S+U, Pb+Pb and In+In collisions is shown in fig. 1.8. The data is scaled by a *normal nuclear absorption* factor extracted from p+A collisions accounting for re-scattering dissociation of the pre-hadronic $c\bar{c}$ system traveling through cold nuclear matter [67]. The additional suppression visible in the data in fig. 1.8 is called *anomalous suppression*. Up to a system size of about $N_{part} \sim 100$ the data meets the expected Charmonium production from p+A. With increasing number of participants, J/Ψ production drops to values of about 0.8 and is rather stable up to $N_{part} \sim 200$ followed by a continuous decrease for even larger systems. Interpretation of the step-like reduction in J/Ψ production is a Ψ' suppression occurring at medium system size followed by a χ_c dissociation in even larger systems as these are the main J/Ψ production channels [68] [69]. Virtual photons as penetrating probes of a heavy-ion collision are the topic of this work and are therefore discussed in a separated chapter.

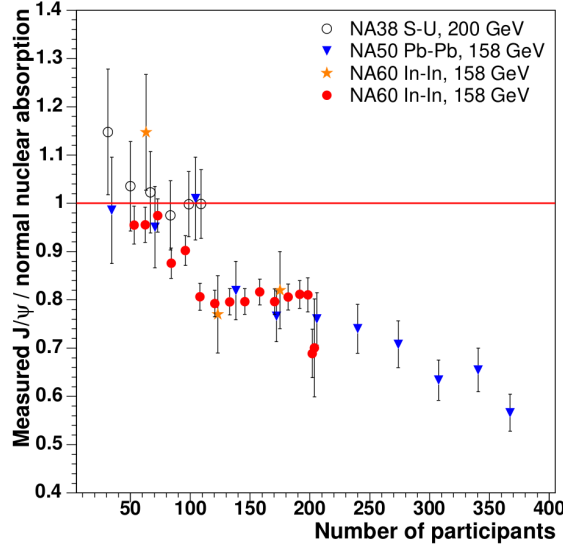


Figure 1.8: Measured J/Ψ production as a function of N_{part} measured in SPS experiments. The yield is scaled by the normal nuclear absorption, thus only anomalous suppression effects are visible. See *text* for details. Taken from [70].

- **Jet-quenching:** High momentum particles are also mainly produced in the very early stages of the collision. Traveling through a unconfined medium as the QGP, they lose a major fraction of their momentum in gluonic bremsstrahlung processes, leading to an overall suppression of high momentum particles compared to elementary reactions. A typical observation is the suppression of Di-Jets, being called *Jet-quenching* in A+A collisions. STAR data on Di-jet correlations in Au+Au collisions at $\sqrt{s} = 200 \text{ AGeV}$ compared to d+Au and p+p data as reference is shown in fig. 1.9. The trigger particle is observed at $\Phi = 0$ with a

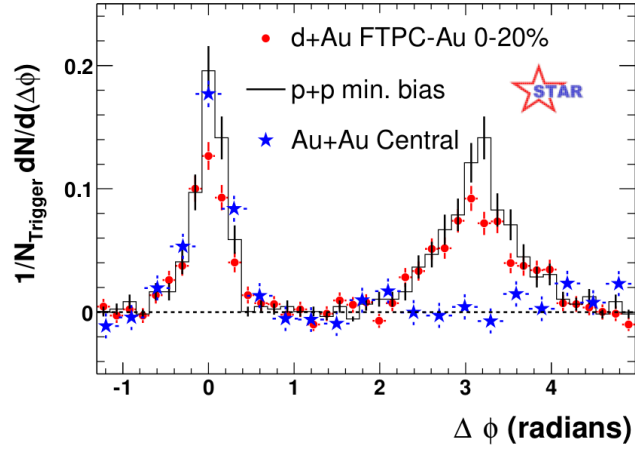


Figure 1.9: Di-jet correlation in different systems measured with STAR. See *text* for details. Taken from [71].

threshold in transverse momentum of $p_t > 4 \text{ GeV}$. In all systems the trigger signal shows the same shape and thus implies, that there is no significant medium impact on the Au+Au trigger jets which therefore mainly originate from primordial jet production on the surface of the collision system. The corresponding opposite jet consequently has to transverse the whole medium. As a result, no correlated signal is observed at $\Delta\Phi = \pi$ in Au+Au, whereas the reference systems shows a clear correlated peak.

- **Collective flow:** The asymmetry in the initial collision geometry results in pressure gradients that lead to a non isotropic particle emission. The coefficients v_i in a Fourier-Propagation of the azimuth particle emis-

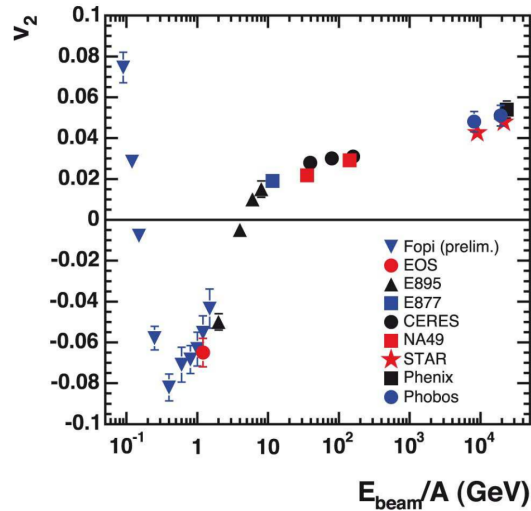


Figure 1.10: Energy dependence of the elliptic flow v_2 . Taken from [72].

sion mirror these pressure gradients and reveal information about the *direct* (v_1) and the *elliptic flow* (v_2) of the medium. As flow is a property of a fluid, it gives an estimate on the level of (local) thermal equilibrium reached. The elliptic flow in dependence of the beam energy is shown in fig. 1.10. It is on a small overall level, but a rise towards top RHIC energies is observed.

- **Hadron yields:** With the hadronisation of a QGP, hadron abundances get fixed (*Chemical Freeze Out*) and reveal conclusions on critical values in $[T, \mu_B]$ along the dynamical evolution path of the medium. A significant enhancement in strangeness production (a factor of 2 ~ 20 depending on the energy and the s -content of the hadrons) in A+A

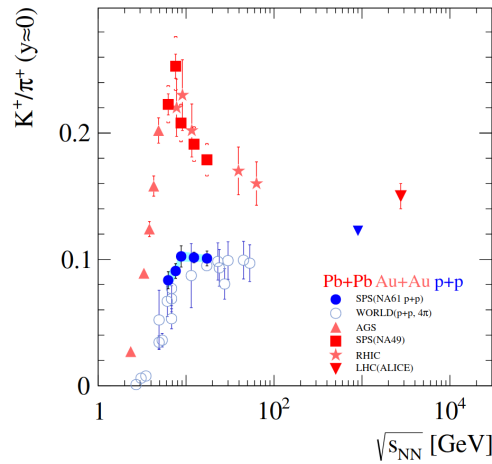


Figure 1.11: The CM energy dependence of the $\langle K \rangle / \langle \pi \rangle$ ratio in Pb+Pb (Au+Au) and inelastic p+p collisions in a world data compilation [73], [74]. Taken from [75].

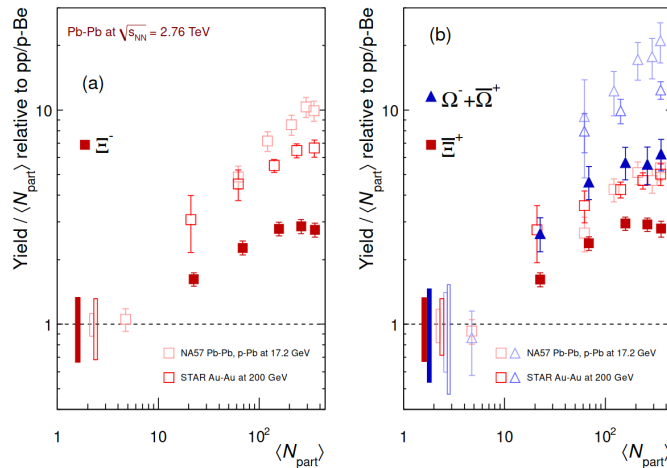


Figure 1.12: Enhancement of multi-strange hadron production in A+A collision relative to p+p in LHC (left), RHIC and SPS (right) data. Taken from [76].

compared to elementary collisions is observed being in agreement with theoretical predictions for the onset of the deconfinement phase transition [77]. A well suited observable is the $\langle K \rangle / \langle \pi \rangle$ ratio which mirrors the fraction of strange quarks produced to the amount of up and down quarks, as shown in fig. 1.11. On top of an overall increase in strangeness production, the A+A data shows a horn-like structure which peaks at values of $\sqrt{s} \sim 7 - 8 \text{ AGeV}$, whereas the p+p reference data smoothly rise with increasing energy. Measurements of multi-strange hadron production as a function of system size in heavy-ion collisions at the LHC [78], [79], [80], the RHIC [81], [82] and the SPS are shown in fig. 1.12 relative to p+p collisions. The data shows a steady rise with the system size reaching up to values of 20 for the most central collisions clearly indicating that different processes account for strangeness production.

- **Fluctuations:** The high multiplicities of charged hadrons in high energy A+A collisions enable the analysis of event-by-event fluctuations in terms of e.g. pion phase space coverage or even strangeness production. Such fluctuations may reveal the existence and position of the potential critical point in the QCD phase diagram as shown in fig. 1.5 [69].

1.5 VIRTUAL PHOTONS IN HEAVY-ION COLLISIONS

Dileptons are emitted throughout the whole evolution of the created medium and therefore deliver a unique picture also of the hot and dense phases. Furthermore electrons and photons do not take part in the strong interaction and leave the medium without further modification thus carrying information that can not be accessed studying hadrons. With modern experiments being more and more capable of a clean detection of these rare probes and handling the enormous background coming along, the field of (virtual) photons has gained a lot in attention over the past years.

The first successful try of measuring dileptons as observable emitted in high-energy heavy-ion collisions was taken by the CERES experiment at CERN SPS in the end of the last century. S+Au data at $\sqrt{s} = 200 \text{ AGeV}$ [83] and Pb+Au data at $\sqrt{s} = 156 \text{ AGeV}$ [84] showed an enhanced dielectron production for $M_{ee} > 0.2 \text{ GeV}/c$ which is not observed in p+A reference data [85]. The observed excess could only be explained by in-medium modifications of vector mesons (especially the ρ), namely a drop in mass and/or a broadening [86]. With the addition of a Time Projection Chamber (TPC) to CERES [87], the experimental performance in terms of particle identification increased such, that in an additional high statistics Pb+Au run in 2000 the observed excess of dielectron pairs could be confirmed and its origin addressed in more detail. The resulting dielectron spectrum is shown in fig. 1.13. A comparison to all relevant hadronic cocktail sources is shown on the left, where a clear excess of $2.56 \pm 0.22 \text{ (stat)} \pm 0.31 \text{ (syst)} \pm 0.83 \text{ (decays)}$ beyond the π^0 Dalitz signal region is visible. A signal to background ratio of

about $1/22$ in this region results in large statistical uncertainties. The stated value are taken from [88]. On the right hand side of fig. 1.13 a comparison of the data to the cocktail sum including a ρ signal derived from the dropping mass scenario (blue) [89] and a broadening of the ρ (red) [90] is shown. The broadening scenario is favored by the data, however, the dropping mass can not be ruled out here.

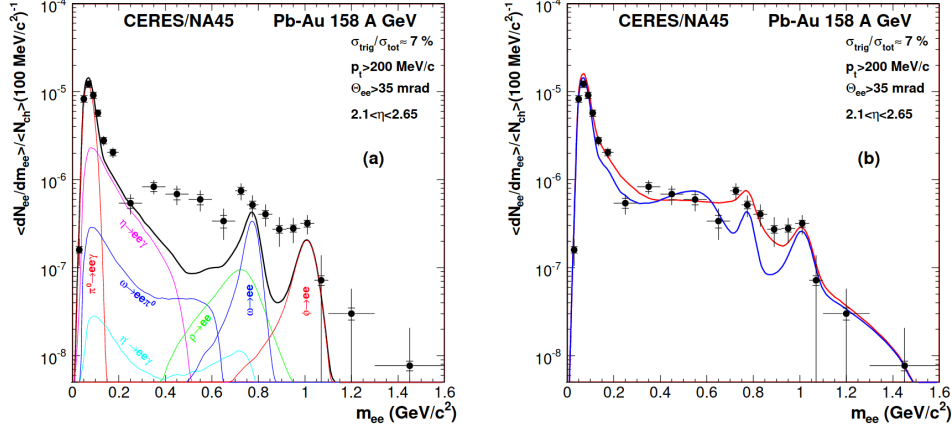


Figure 1.13: Measured dielectron spectra with CERES at CERN SPS in Pb+Au at $\sqrt{s} = 200 \text{ AGeV}$. (a): Decomposition of the measured spectrum into hadronic cocktail components. (b): Comparison to model predictions assuming a dropping ρ mass (blue) or a broadening of the ρ (red). See *text* for details. Taken from [88].

Following up the CERES results and first observations on the invariant mass region $M_{inv} > 1 \text{ GeV}$ measuring dimuons with the HELIOS/3 spectrometer at CERN SPS [91] the NA60 experiment was built, dedicated to measure dimuons reaching up to $M_{\mu\mu} = 1.4 \text{ GeV}$ [92] at $\sqrt{s} = 17.3 \text{ AGeV}$. The extracted invariant mass spectrum is shown in fig. 1.14, left. Narrow signals of the ω and ϕ are well resolved and identified. After subtraction of the cocktail components (except the ρ) a continuous excess is observed showing a broad peak at the nominal ρ vacuum mass. This excess yield is compared to various theoretical predictions on possible in-medium modifications of the ρ spectral function [93] in fig. 1.14, right. The scenario of an unmodified ρ can be excluded from the data, as well as a dropping of the ρ mass (shown in green), which described the previously measured CERES data reasonably well (compare fig. 1.13, right), but completely fails reproducing the more precise NA60 measurement. The theoretical calculations assuming a broadening of the ρ get close describing the data. More recent theoretical developments show an even more improved agreement on the broadening scenario, especially in the high invariant mass region [94] [95] [96]. Not only the ρ but also the ω is expected to show in-medium modifications as at least the low p_t fraction of the ω produced partially decays in-medium. However, due to the short lifetime of the ρ and continuous regeneration via $\pi\pi \rightarrow \rho$

in the medium the ρ is that dominant, that hardly any modification on the ω spectral function can be accessed in ultra-relativistic heavy-ion collisions.

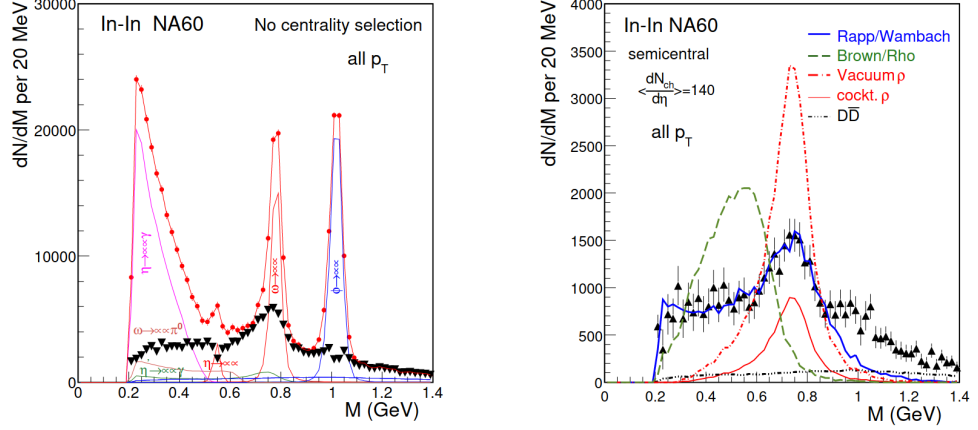


Figure 1.14: Left: Dimuon invariant mass spectrum measured by the NA60 CERN SPS experiment in In+In collisions at $\sqrt{s} = 17.3 A\text{GeV}$ (red dots) decomposed into hadronic cocktail components. The excess yield is shown in black triangles. Right: Comparison of the excess yield to various theoretical models on in-medium modifications of the ρ spectral function [93]. See *text* for details. Taken from [96].

With the PHENIX and STAR experiments starting operation at RHIC, new data at even higher energies became available. However, it also became clear once more, that dileptons are indeed a rare probe and it is hard work to understand the background [97], [98], [99]. While PHENIX used a RICH detector for electron-pion separation [100], the STAR performance was mainly based on the TPC and TOF detectors [101]. Furthermore the RHIC accelerator provided a broad range of energies thus enabling the study of the previously observed dielectron excess at different scales. Both experimental results on dielectrons agree well [98] [102]. The efficiency (but not acceptance) corrected STAR results are shown in fig. 1.15 [102]. The left figure shows the e^+e^- signal in blue data points for various CM energies and the corresponding cocktail sum which does not include any ρ contribution in grey. Note, that the spectra have been scaled individually for a better representation. The excess yield is represented as the data-to-cocktail ratio on the right hand side with the ω and ϕ signal being subtracted from both. This excess ratio is compared to different models that all assume a broadening of the ρ meson. The calculation by Rapp et al. is based on an effective many-body model for vector mesons in a QGP where interactions with hadrons cause the ρ broadening [103]. Endres et al. uses a coarse grained transport approach [104] whereas PHSD is a microscopic transport model including collisional broadening of the ρ [105]. All models successfully describe the high statistics $\sqrt{s} = 200 A\text{GeV}$ data [106] and the dimuon spectrum measured by NA60 presented earlier (fig. 1.14 [96]) [103] [104] [105] and are also in

agreement with the lower energy STAR data shown in fig. 1.15, right, within errors.

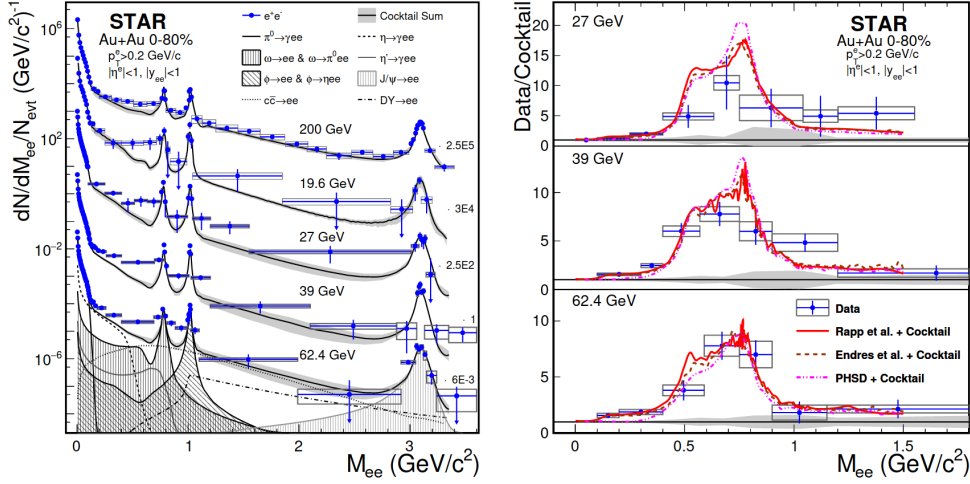


Figure 1.15: Left: Dielectron signal and hadronic cocktail contribution at different CM energies in Au+Au collisions measured by STAR. Right: Comparison of the dielectron excess yield to theoretical predictions [103], [104], [105]. See *text* for details. Taken from [102].

For a more detailed look, the acceptance and efficiency corrected dielectron yields are integrated in the range $0.4 \text{ GeV} < M_{ee} < 0.75 \text{ GeV}$ and compared to the previously mentioned model predictions as well as the In+In data taken by NA60 in fig. 1.16. The experimental data from NA60 and STAR agree well and show no significant dependence on the CM energy. This might be related to the dominant production of the dielectron excess yield due to ρ -baryon coupling [107] where the total baryon density stays almost constant for $\sqrt{s} > 20 \text{ AGeV}$ [108]. In all theoretical models a slight energy dependence is visible but they are statistically still in agreement with the data. All in all the STAR data and all previously discussed measurements are in agreement with a broadening of the ρ with chiral symmetry restoration.

The HADES experiment (compare chapter 2 and 3 for a detailed overview) has measured the production of dielectrons in a dense hadron gas in Au+Au collisions at a CM energy of $\sqrt{s} = 2.42 \text{ AGeV}$ [59], C+C at $\sqrt{s} = 2.35 \text{ AGeV}$ [109] and Ar+KCl at $\sqrt{s} = 2.25 \text{ AGeV}$ [110] allowing a system size dependent study of the excess yield. The dielectron invariant mass spectrum with the highest statistics, Au+Au, is shown in fig. 1.17. Black data points show the same-event unlike-sign pairs reconstructed above the vacuum pion mass, where the η and ω signal have been subtracted as well as the NN reference derived from measured p+p and p+n data [111]. The resulting distribution mirrors the in-medium ρ which is compared to various theory approaches. As previously discussed, an unmodified (vacuum) ρ can not account for the observed excess. Coarse-grained approaches [112], [113], [114] and HSD

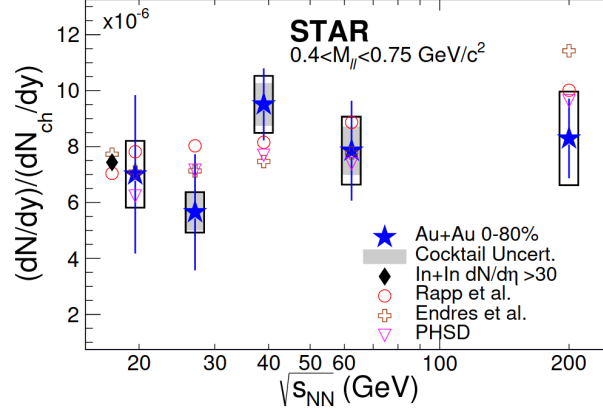


Figure 1.16: Integrated, efficiency and acceptance corrected dielectron excess yield measured in the region $0.4 \text{ GeV} < M_{ee} < 0.75 \text{ GeV}$ with STAR in comparison to theory [103], [104], [105] at various collision energies. See *text* for details. Taken from [102].

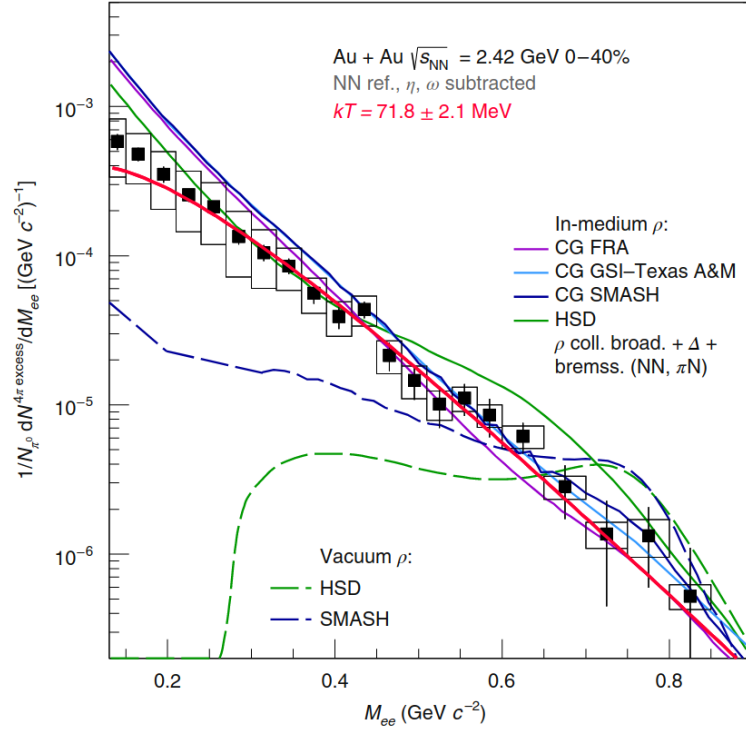


Figure 1.17: The excess yield of dielectrons in Au+Au collisions at $\sqrt{s} = 2.42 \text{ AGeV}$ measured with HADES compared to theory approaches on the ρ spectral function and fitted for a temperature estimate. See *text* for details. Taken from [59].

[115] calculations assuming a broadening of the in-medium ρ are in good agreement with the data. The slope of the in-medium ρ mirrors the temperature of the dense phases of the fireball and therefore allows to locate

the collision system in the QCD phase diagram [59], where the according baryochemical potential μ_B is taken from a statistical model fit. Applying a Boltzman-like fit ($dN/dM_{ee} \sim (M_{ee})^{3/2} \exp(-M_{ee}/T)$) to the data a medium temperature of $kT = 71.8 \pm 2.1 \text{ MeV}$ is obtained.

For a system size dependent analysis, the dielectron excess radiation is compared for all systems measured with HADES relating them to elementary collisions [111] introducing

$$R_{AA} = \frac{1}{\langle A_{part}^{AA} \rangle} \frac{dN^{AA}}{dM_{ee}} \left(\frac{dN^{NN^{-1}}}{dM_{ee}} \right). \quad (1.21)$$

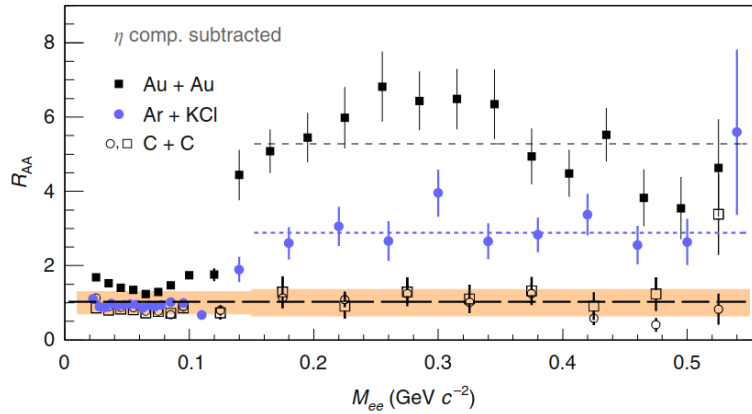


Figure 1.18: Dielectron excess radiation relative to elementary systems [111]. A system-size dependence is observed. See *text* for details. Taken from [59].

The excess ratio for C+C, Ar+KCl and Au+Au is shown in fig. 1.18. For invariant masses beyond the π^0 Dalitz region, an excess is observed in the large systems Au+Au and Ar+KCl, whereas the dilepton radiation in C+C is in agreement with a sum of elementary reactions. The excess yield appears to depend on the system size resulting in an almost twice as high value in Au+Au compared to Ar+KCl. However the exact scaling of R_{AA} to the system size stays unclear. A more detailed view on the dilepton excess ratio and its scale dependence is given in this work adding Ag+Ag data to fig. 1.18.

THE HADES EXPERIMENT

The **H**igh **A**cceptance **D**i**E**lectron **S**pectrometer (HADES) is located at the SIS 18 accelerator at the GSI Helmholtzzentrum für Schwerionenforschung in Darmstadt, Germany and was designed for the investigation of possible in-medium modifications of light vector mesons [116]. To provide measurements of their rare decays into dileptons, HADES is equipped with a hadron blind RICH detector that has been recently upgraded (compare chapter 3). HADES is composed of six sectors each covering $\Delta\Phi = 60^\circ$ in azimuth angle, with the sectors being defined by the superconducting magnet coils producing a toroidal field. For particle tracking and momentum measurement two layers of **M**ini-**D**rift-**C**hambers (MDCs) are located in front of and behind the magnetic field. For time-of-flight measurement a **M**ultiplicity and **E**lectron **T**rigger **A**rray (META) system is installed. A detailed description of HADES in its original design can be found in [117]. The up-to-date version of HADES additionally includes an electromagnetic calorimeter, that covers 2.5 sectors and has first been operated in 2019 and will be further extended to full HADES coverage being 85 % azimuthal acceptance ranging from $\Theta_{min} = 18^\circ$ to $\Theta_{max} = 85^\circ$. A schematic view of HADES including all its sub-detectors in an exploded depiction is shown in fig. 2.1.

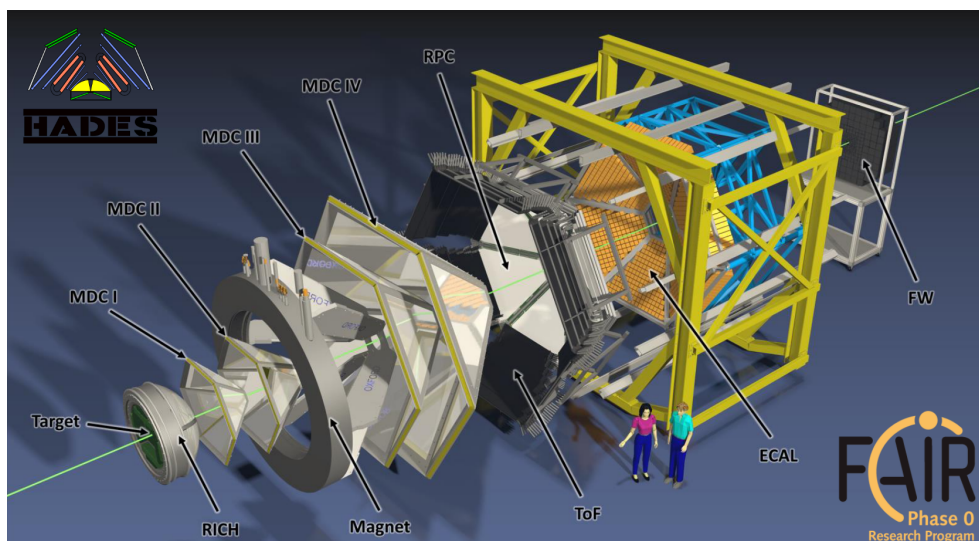


Figure 2.1: Schematic view of HADES including all sub-detectors. Taken from [118]

2.1 THE TARGET

The Ag target used in the march 2019 beamtime consists of 15 foils of $d_{foil} = 42 \mu m$ thickness. A photo is shown in fig. 2.2. All foils are arranged in a staggered way, such that there is only one overlaying point in beam direction, where the beam hits the target. The target is chosen to be segmented and is constructed in the explained way to reduce the interaction and therefore conversion probability of photons in the target.

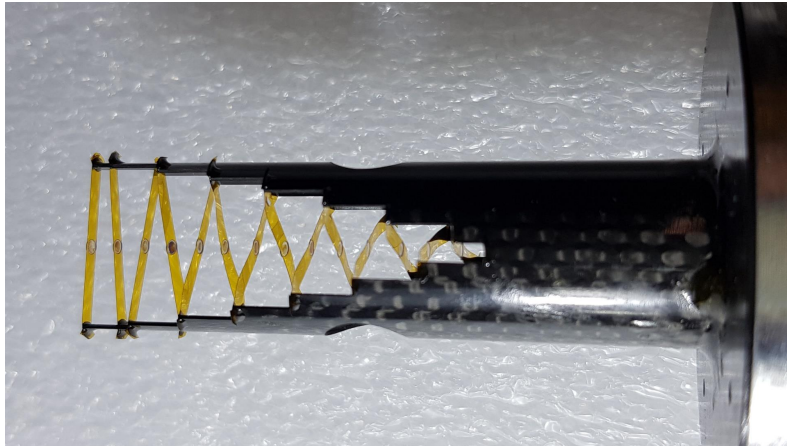


Figure 2.2: Photo of the segmented Ag target of HADES used in the march 2019 beamtime.

2.2 THE START AND VETO DETECTOR IN HADES

The measurement of any particles velocity is based on measuring the time it takes the particle to travel between two detector points. The start signal for this time measurement is provided by the START detector [119] measuring the arrival time of incoming beam particles. The detector is based on a single-crystal diamond allowing for high rate capability paired with low interaction probability and precise time measurement due to fast electron drift times. Furthermore it is capable of a precise position measurement in order to monitor the beam alignment. It is located 2 cm in front of the target, covers an active area of $4.7 mm \times 4.7 mm$ having a thickness of $70 \mu m$. A picture of the sensor is shown in fig. 2.3. 70 cm downstream the target a second diamond based beam detector is located (VETO detector, see fig. 2.3, upper right) for fragment identification to exclude events in the trigger where no reaction took place in the target.

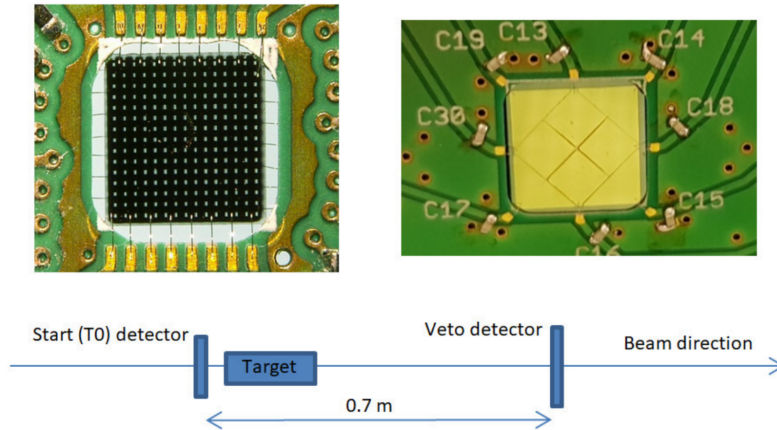


Figure 2.3: START (upper left) and VETO (upper right) detector of HADES. Taken from [120].

2.3 THE HADES TRACKING SYSTEM

2.3.1 The HADES magnet

The purpose of the HADES magnet is to provide a transverse kick to charged particles in order to measure their momentum with a resolution of $\sigma_p/p_e = 1.5 - 2\%$ for electrons. Electron identification based on a RICH detector requires a field free region which is provided by the toroidal geometry around the target, where the RICH is located to have as little as possible conversion signals. The acceptance in terms of electron momentum ranges from $p_{min} = 0.1 \text{ GeV}/c$ up to $p_{max} = 2 \text{ GeV}/c$ combined with a polar acceptance ranging from $\Theta_{min} = 18^\circ$ to $\Theta_{max} = 85^\circ$.

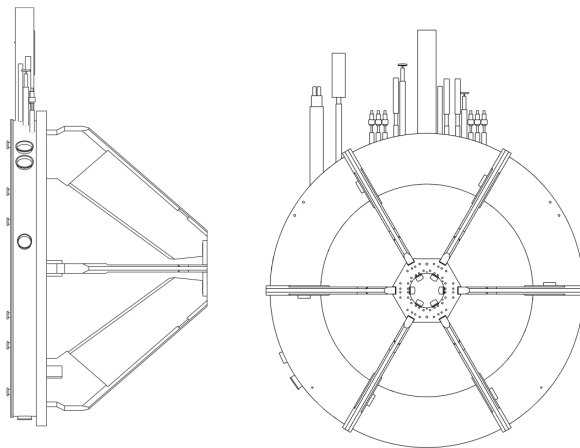


Figure 2.4: Side (left) view, the beam is coming from the left, and back (right) view of the HADES magnet. Taken from [117].

A schematic view of the HADES magnet is shown in fig. 2.4. It is formed by six coils located in vacuum chambers surrounding the beam axis that are connected to a support ring having an outer diameter of $d = 3.56\text{ m}$. The close downstream end of the coils is connected by a hexagonal plate having a circle shaped hole for the beam pipe in the middle. Fig. 2.5 shows magnetic field maps of the HADES magnet at different positions (in-/outside coils). The strongly inhomogeneous field reaches its maximum value downstream with a value of almost $B = 3.6\text{ T}$ (fig. 2.5a) whereas only a peak field strength of $B = 0.87\text{ T}$ is measured between two coils (fig. 2.5b).

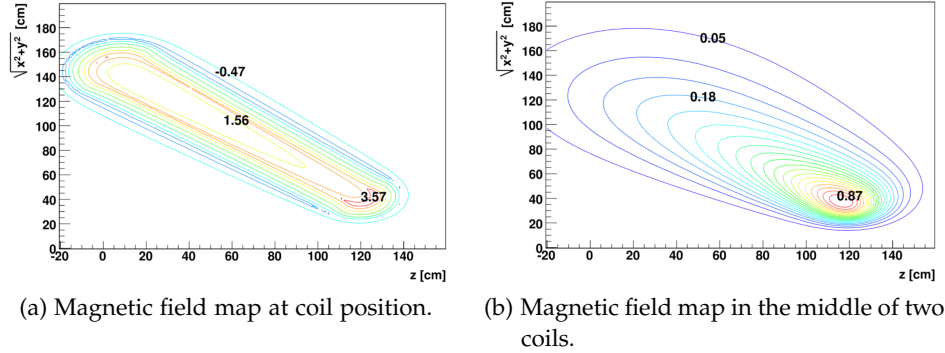


Figure 2.5: Magnetic field maps as a function of z and r of HADES at different positions. The contour lines visualize a step size of $\Delta B = 0.24\text{ T}$. The HADES target region is at z -position of -7 cm to -1 cm . Taken from [117].

2.3.2 Multiwire Drift Chambers (MDCs)

In order to track the particles trajectories within the detector, 24 trapezoidal planar **M**ultiwire **D**rift **C**hambers (MDCs) are symmetrically arranged in six identical sectors [121] [122]. The polar angle coverage matches the magnet opening ($\Theta_{min} = 18^\circ$ to $\Theta_{max} = 85^\circ$) and the active area in azimuth direction is defined by the magnet coils. Two of the four tracking planes are located in front of and the other two behind the magnet. A schematic view of the arrangement of the HADES MDCs is shown in fig. 2.6, left. All chambers are composed of six layers in which the sense and field wires are orientated in different angles each, as indicated in fig. 2.6, right. The choice of angles provides a maximum of polar angle resolution in which the momentum kick from the magnetic field happens. The chambers are filled with an Ar/CO_2 gas mixture (70/30, most inner plane) and Ar/C_4H_{10} (84/16, three outer planes) which is ionized by crossing particles. The resulting electrons and positively charged gas ions drift to the sense and field wires, respectively. Gas amplification of the electrons leads to the detected signal.

The construction is optimized to reach the desired mass resolution of di-electrons ($\sigma_{M_{ee}}/M_{ee} = 2.5\%$ [117]) which implies a single track momentum resolution of $\sigma_p/p = 1.5\% - 2\%$. To reach this goal multiple scattering in

the detector has to be avoided at its best. A radiation length of 0.2% only is reached within the chambers and of 0.3% in the air between the chambers. The spatial resolution of track crossing points is about $60 - 100 \mu\text{m}$ in polar direction and $120 - 200 \mu\text{m}$ in azimuth.

Besides the main purpose of tracking, a measurement of the particles energy loss dE/dx mainly originating from inelastic scattering at electrons, ionization, [123] is also performed (proportional to the signal strength) providing additional information for particle identification.

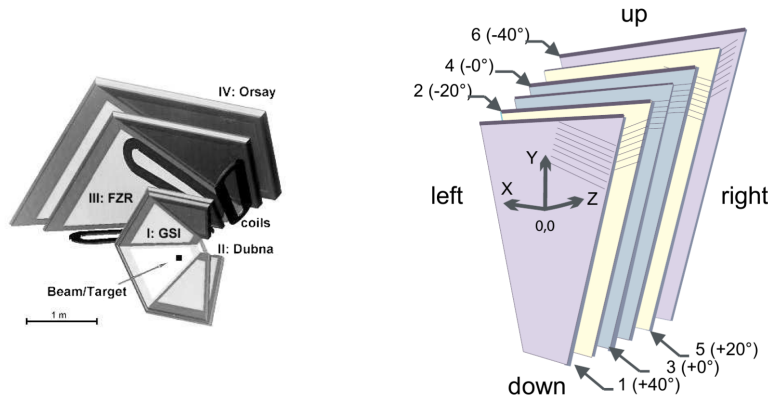


Figure 2.6: Arrangement of the HADES drift chambers around the magnet coils (left, taken from [121]) and the wire structure within one sector of a drift chamber (right, taken from [117]).

2.4 THE META SYSTEM

The purpose of the HADES META system is to provide a time-of-flight measurement of particles which is related to the initial measurement in the START detector. It consists of two scintillator arrays covering different polar angles: The Time Of Flight (TOF) wall [124] from $\Theta_{min} = 44^\circ$ to $\Theta_{max} = 88^\circ$ and the Resistive Plate Chamber (RPC) wall [125] [126] (previously TOFINO) from $\Theta_{min} = 18^\circ$ to $\Theta_{max} = 44^\circ$.

2.4.1 Time-of-Flight (TOF) wall

The HADES TOF wall [124] follows the overall HADES geometry of six sectors of trapezoidal shape. Each sector consists of eight modules with each containing eight scintillator strips themselves. The length varies between $l_{inner} = 1475 \text{ cm}$ and $l_{outer} = 2365 \text{ cm}$. A photo of the TOF detector taken before installation clearly showing its structure is shown in fig. 2.7. For readout purposes, PhotoMultiplier Tubes (PMTs) are attached at both ends of the scintillator strips. From the time difference in the signal detection in both PMTs a position resolution is possible with a timing resolution

of $\sigma = 150 \text{ ps}$ [127]. From the signal amplitude conclusions on the specific energy loss dE/dx of a specific particle can be drawn.



Figure 2.7: Photo of the HADES TOF detector before its installation. In the central part of the photo two sectors of the Pre-Shower detector [128] can be seen. The Pre-Shower detector was replaced by an electromagnetic calorimeter in the $AgAg$ data run.

2.4.2 Resistive Plate Chamber (RPC) wall

The HADES RPC wall [125] [126] has been installed within a detector upgrade in 2010 in order to prepare the HADES for the high particle multiplicities coming along with the first upcoming heavy-ion run in 2012. Following the six sector design of HADES, each RPC sector consists of two layers. These are formed by 93 strip-like cells arranged in three columns as shown in fig. 2.8. The size of the cells changes with the polar angle Θ ranging from $(12 - 52) \text{ cm}$ in width and $(2.2 - 5) \text{ cm}$ in height. The cells are filled with a mixture of $C_2H_2F_4$ (90%) and SF_4 (10%) and have an individual shielding to reduce possible crosstalk.

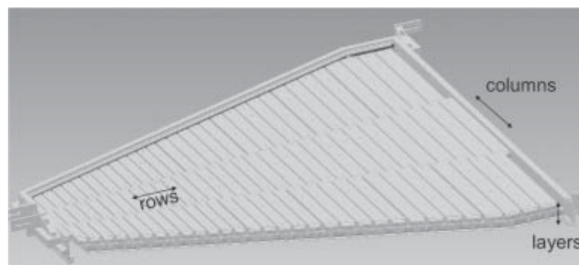


Figure 2.8: Schematics of one sector of the HADES RPC. Taken from [125]

2.5 ELECTROMAGNETIC CALORIMETER

Besides the HADES RICH upgrade, the Electromagnetic Calorimeter (ECal) [129] [130] is the latest addition to the HADES. It replaced the previously installed Pre-Shower detector [128] in 2018. By design, it covers almost full azimuth and polar angles from $\Theta_{min} = 12^\circ$ to $\Theta_{max} = 45^\circ$ in the HADES specific six sectors. It consists of 978 lead glass moduls, giving the ECal a total weight of more than 16 t. The overall structure is shown in fig. 2.9. During the $AgAg$ data run in march 2019, only 2.5 sectors of the ECal were operational.

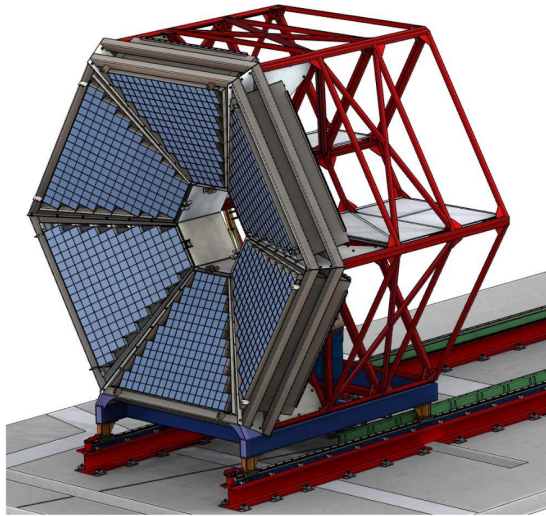


Figure 2.9: Schematic view of the HADES ECal detector setup. Taken from [131].

2.6 HADES TRIGGER

The HADES detector runs in a triggered readout setup, meaning that each collision measured by the detector system has to pass a soft pre-selection in order to be recorded. For this purpose sub-detector data is used. The trigger selection that is used in this thesis is the so-called *Physics Trigger 3* (PT3). It requires a hit in the START detector correlated to at least 20 hits in the META system, namely the RPC and TOF detectors. Besides, other triggers exist, such as the PT2 requiring five hits in the META only, leading to enhanced statistics but worse data quality. General information on the HADES trigger system can be found in [132] and its specific setting in the $Ag + Ag$ data run in March 2019 are available in the corresponding logbook [133].

2.7 HADES SIMULATION

In experimental physics simulations are an important tool in many aspects ranging from the planning of an experiment to the understanding and cor-

rection of physics results.

Therefore, the HADES detector geometry is implemented using the *HADES Geometry and tracking* (HGeant) framework, that utilises Monte Carlo methods. HGeant is based on the Cern software Geant 3.21 [134]. Within HGeant, particles are propagated through the detector volume and their interaction with the material is simulated. The particle input distributions are obtained from event generators such as the Monte Carlo based simulation packages *Ultra relativistic Quantum Molecular Dynamics* (UrQMD) [135] and PLUTO [136] depending on the simulation goal. In case of UrQMD, a centrality distribution according to the experimental observation is simulated.

In this work simulation is used for the following two main purposes:

1. **Verification of data interpretation:** Especially as the upgraded RICH detector has been operated for the first time in the analysed data run, its signals need to be fully understood in order to properly instrumentalize the detector for physics analysis. Here, simulation provides a valuable insight as any detector information can be traced back to its origin.
2. **Efficiency (and acceptance) correction of results:** Physics spectra obtained from experiment are at first limited to active detector areas. Each detector has dead regions, where no particles can be observed and so does HADES. Also within the active detector area not every single particle can be reconstructed due to dead times in the various detector components, limits in detector resolution and the statistical interaction processes of particles with the detector material. Furthermore the identification of a specific species of particles requires a selection based on detector observables characterizing the specific track. Such a selection always comes along with losses in the desired particle species as detector observables are governed by statistical distributions. The corresponding width is given by the detector resolution leading to overlapping distributions for different particle species.

The detector acceptance is defined as the amount of particles traveling through active detector volume relative to all particles produced. The efficiency of a specific particle is not only detector, but also analysis related. It is given by the amount of reconstructed particles in relation to all particles crossing active parts of the detector.

From the physics point, the fully corrected particle distributions are relevant to compare experiment and theory. Based on a highly accurate detector implementation, efficiency corrections can be derived using simulation. Acceptance corrections usually depend on the input particle distribution and are therefore model dependent. Thus, depending on the specific analysis, it might be more reasonable to apply a common, experiment related acceptance filter on theoretic calculations than to derive an acceptance correction based on different models.

In general, commonly used HADES simulations for Ag + Ag collisions using UrQMD are produced. To study the behaviour of rare signals, such

as dielectrons originating from vector meson decays, UrQMD simulation are enriched with these signals, one per collision. The embedded signal distributions are of thermal nature and produced using PLUTO. A compilation of the PLUTO temperatures used is provided in tab. 2.1. These temperature determining the inverse slope of the particle energy distributions serving as input to the *PFireball* class.

meson	T_1 [MeV/k]	T_2 [MeV/k]	f
Φ	100	0	1
ω	100	0	1
π^0	49	93	0.98
η	93	0	1

Table 2.1: PLUTO temperatures used for simulation of dielectrons originating from meson decays. In case of the π^0 two temperatures account for different production mechanisms, which are weighted as $dN/dE = f \cdot dN/dE(T_1) + (1 - f)dN/dE(T_2)$.

For the purpose of efficiency correction and acceptance filtering so-called white simulation (embedding e^+ or e^- only) are used. To ensure a statistically sufficient particle coverage in all detector and kinematical regions, homogeneous electron and positron distributions are embedded into real data. Embedding into real data is important as the single particle efficiency depends on various detector effects as dead times of electronics, that are only present in real data, resulting in a centrality dependence of the efficiency. An overview on all simulations with according statistics and purpose used in this work is given in tab. 2.2.

system	embedded (PLUTO)	N_{events} [Mio.]	purpose
Ag + Ag UrQMD	/	100	study detector effects
Ag + Ag UrQMD	$\Phi \rightarrow e^+e^-$ $\omega \rightarrow e^+e^-$ $\omega \rightarrow e^+e^-\pi^0$ $\pi^0 \rightarrow e^+e^-\gamma$ $\eta \rightarrow e^+e^-\gamma$	100 each	study (rare) e^+e^- signals
Ag + Ag real data	e^- or e^+	50	efficiency and acceptance studies

Table 2.2: Overview on the HADES simulations used in this work.

THE RICH DETECTOR AT HADES

The newly upgraded state of the art *Ring Imaging CHerenkov* (RICH) detector at HADES is the most essential detector component used in this analysis. Therefore the detailed understanding is of key importance to push the performance of this analysis to its limits. In this chapter the basic functionality of a RICH detector is explained and observables of the HADES RICH detector are discussed.

3.1 CHERENKOV RADIATION

Cherenkov radiation (photons) is emitted, when a charged particle travels through a medium with a higher velocity than light does. This phenomenon is generally known as *Cherenkov effect*. It is possible, as the phase velocity of light scales with the refraction index n of the medium it travels through ($\sim 300,000$ km/s in vacuum, but e.g. only 225,000 km/s in water).

Whenever a particle travels through a dielectric medium, atoms are polarized along the trajectory of the particle and emit electromagnetic radiation. In case of a particle velocity that is smaller than the one of light in the medium, the electromagnetic waves of neighbouring atoms interfere destructively. Therefore no radiation can be detected in the macroscopic system. The case of a particle traveling faster than light through a medium is shown in fig. 3.1: The electromagnetic waves of neighbouring atoms do not cancel themselves any longer but together form a cone like wave front. The resulting electromagnetic radiation is called *Cherenkov radiation* and is emitted similar as a *Mach-cone*. It is the optics analogue to the supersonic cone produced by airplanes.

The angle α under which *Cherenkov radiation* is emitted can be calculated by the fraction of the particles velocity and the velocity of light in the medium to

$$\cos(\alpha) = \frac{v_{light}}{v_{particle}} = \frac{c/n}{\beta c} = \frac{1}{\beta n} \quad (3.1)$$

The energy dE emitted by a particle via Cherenkov radiation per unit length traveled dx and per frequency interval $d\omega$ is given by the Frank-Tamm formula [137]

$$\frac{d^2E}{dx d\omega} = \frac{q^2}{4\pi} \mu(\omega) \omega \left(1 - \frac{c^2}{v^2 n^2(\omega)} \right) \quad (3.2)$$

depending on the permeability $\mu(\omega)$ that itself depends on the frequency ω . Assuming constant values for the permeability and the refraction index

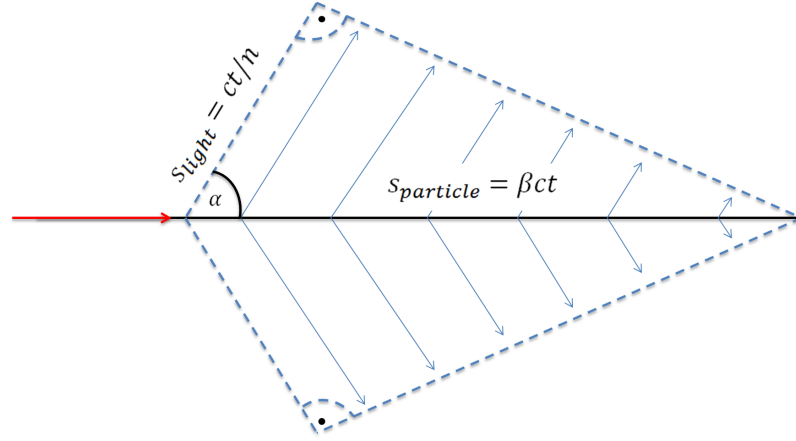


Figure 3.1: *Cherenkov radiation* is emitted under an angle α , when a charged particle travels through a medium faster than light does. The direction of the *Cherenkov radiation* describes a *Mach-cone*.

and inserting $\lambda = 2\pi c/\omega$ one derives for the amount of Cherenkov photons emitted per path-length dx and wave-length $d\lambda$ interval

$$\frac{d^2E}{dx d\lambda} = \frac{\pi e^4}{c\epsilon_0 h \lambda^2 \sin^2(\alpha)} \sim \frac{1}{\lambda^2} \quad (3.3)$$

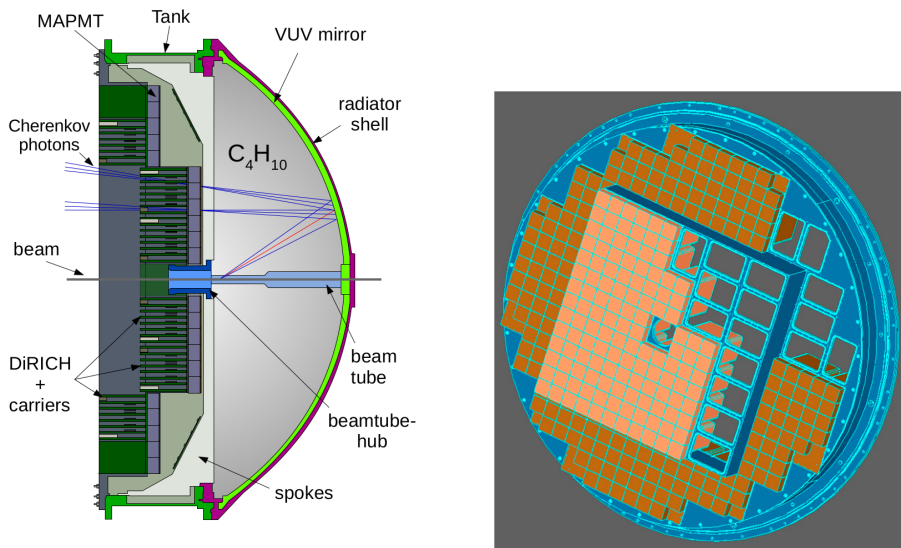
Following equation 3.1, each particle produced in a specific reaction that fulfills $\beta \geq 1/n$ emits *Cherenkov radiation*. Choosing the refractive index in a way, that only a certain kind of particles reaches the threshold value in β , one can select those particles. Another possibility besides this operation as a threshold detector to distinguish for example between electrons and pions (as it is the case at HADES), is the operation over a wide range of velocities and separation of different particle species based on their *Cherenkov angle* α . At the LHCb experiment, dedicated to the study of CP violation and the rare decays of heavy flavors, a RICH detector is run in this way to identify myons, pions, kaons and protons [138].

3.2 SETUP OF THE HADES RICH DETECTOR

The HADES RICH detector has been upgraded within two years from 2016 to 2018. The recent beam time, that is analysed in this work was the first data run of this detector. A side-view of the RICH detector is shown in fig. 3.2a. It surrounds the beam pipe and the Ag target is located right at the beginning of the gas radiator volume filled with C_4H_{10} . The refractive index $n_{C_4H_{10}} = 1.0014$ is optimized to separate electrons and pions. The threshold in electron momentum according to formula 3.1 is calculated to be $p_{thresh,e} = 9.65 MeV$, whereas pions have to reach a momentum of at least $p_{thresh,\pi} = 2636.70 MeV$. At HADES energies particles with

$p_{thresh,track}(B_{Ag+Ag}) \gtrsim 60 \text{ MeV}/c^1$ are detected by the tracking system, which implies all relevant electrons to easily exceed the Cherenkov threshold momentum. With a beam energy of $E_{beam} = 1.56 \text{ AGeV}$ in the analyzed data set, it can be excluded that pions reach their corresponding Cherenkov threshold.

Cherenkov photons produced by electrons in the radiator volume are reflected and focused by a *Vacuum Ultra-Violet* VUV mirror to form rings on the *PhotoMultiplifier* (PMT) plane located behind the target to prevent it from radiation. The PMT plane, shown in fig.3.2b, is built out of 428 H12700 *Multi-Anode PMTs* (MAPMTs) [139] each having 64 channels being read out individually. Usually six MAPMTs are grouped together on back-planes and have a common power supply. At the detector edges also back-planes consisting of four MAPMTs are installed. Each MAPMT is read out by two FPGA based DiRICH boards (32 channels each).



(a) Side view of the HADES RICH detector (b) MAPMT plane of the HADES RICH detector

Figure 3.2: Left: Side view of the HADES RICH detector. Electrons produced in the target emit Cherenkov radiation on their trajectory through the C_4H_{10} gas volume. The Cherenkov photons are reflected and focused by the VUV mirror to form rings on the MAPMT plane. The readout of all individual MAPMT channels is performed by DiRICH boards. Right: Front view on the MAPMT plane of the HADES RICH detector consisting of 428 H12700 MAPMTs. MAPMTs are grouped to pairs of six (sometimes four) on back-planes which are read out by 12 DiRICH boards in total. The MAPMT plane is splitted into an inner and an outer part, that is shifted backwards in order to approximate the curved focal plane. Figures are taken from [140] (left) and [141] (right).

Particles traveling close to the beam axis (small polar angle Θ) fly a comparable short distance in the radiator volume and therefore produce way

¹ This value mainly depends on the strength of the magnetic field in the tracking system, the value given here holds for the analyzed data run

less photons than particles leaving the target under large Θ angles. To counteract this lack of Cherenkov photons, the glass window of the 48 MAPMTs located on the inner most six back-planes is coated with a thin layer of the wavelength shifting p-terphenyl [142] [143]. Formula 3.3 states, that most of the Cherenkov photons are emitted in the UV regime, but the quantum efficiency of the MAPMTs starts to drop at values of $\lambda < 300 \text{ nm}$ and reaches values lower than 10% for $\lambda < 200 \text{ nm}$ as it is shown in fig. 3.3 by the blue circled data points. The p-terphenyl layer on the glass window absorbs a fraction of the Cherenkov photons emitted in the UV regime that would have been detected by the MAPMT with very low efficiency. They are re-emitted within a few ns at higher wave lengths. Compare the inset in fig. 3.3 showing absorption and re-emission spectra of p-terphenyl. This results in a modified quantum efficiency of the coated MAPMTs represented by red data points. Within a proton test-beam at the COSY accelerator an enhancement of 15 – 20% in integrated quantum efficiency has been observed for the H12700 MAPMT [144].

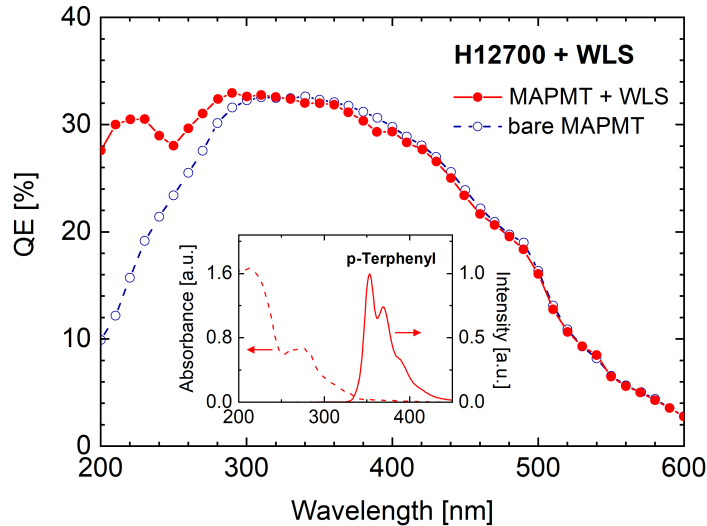


Figure 3.3: Quantum Efficiency (QE) of H12700 MAPMTs that are used to equip the HADES RICH MAPMT plane. Blue data points represent the bare MAPMT QE, red data points show the modified QE after the glass window of the MAPMT is coated with a thin layer of p-terphenyl. Absorption and re-emission spectra of p-terphenyl are shown in the inset in arbitrary units. Figure taken from [144].

3.3 SIGNATURES IN THE HADES RICH DETECTOR

Cherenkov photons that were detected by the MAPMTs are called *CALibrated objects* (Cal) in HADES jargon. Fig. 3.4 shows the position dependence of the amount of Cals reconstructed per event on each pixel of the HADES MAPMT plane. The acceptance gap in the middle of the detector where the

beam pipe crosses the RICH detector is clearly visible as well as the overall two step design of the MAPMT plane. White areas within the equipped MAPMT plane correspond to not operational DiRICH boards due to wrong threshold settings. The holding structure of the RICH mirror (six spokes) is identified as shadow structures on the MAPMT plane. However, these do not lead to additional acceptance losses of the HADES, as in these areas the border regions of the MDC sectors are located where no tracking is possible anyway.

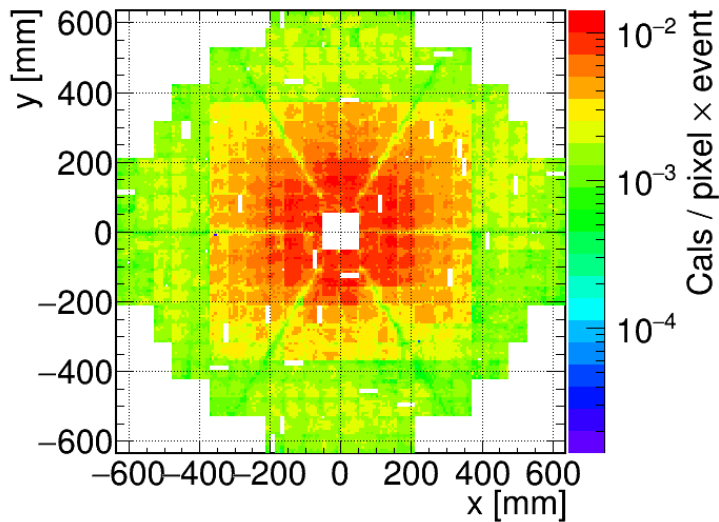


Figure 3.4: Detected Cals per Pixel and event on the HADES RICH MAPMT plane. The data shown is based on day 86 of the Ag+Ag data run. For details see *text*.

Beside its position on the MAPMT plane a Cal also carries timing information. The *Leading Edge* (LE, shown for a single channel in fig. 3.5a) provides a time stamp when the Cal was recorded. It is of particular interest in the rejection of detector noise. An information on the signal strength is given by the *Time over Threshold* (ToT, shown for a single channel in fig. 3.5b), measuring the time span, a signal exceeds the threshold setting in a MAPMT channel.

The cut window on both observables is based on the mean value of the distribution for each individual MAPMT channel. For the LE, the cut reads $t_{LE,mean} - 25 \text{ ns} < t_{LE} < t_{LE,mean} + 35 \text{ ns}$, for the ToT a window of $t_{ToT,mean} - 4\sigma_{fit} < t_{ToT} < 15 \text{ ns}$ is chosen. In the given example (fig. 3.5) the cut values read $-588.7 \text{ ns} < t_{LE} < -528.7 \text{ ns}$ and $2 \text{ ns} < t_{ToT} < 15 \text{ ns}$, respectively. The cuts are based on an analysis performed with data of day 80 only. As the LE denotes a time difference to the corresponding hit in the START detector it is valid to choose a cut window constant in time. The double-peak shape of the LE distribution is not fully understood, however, it seems reasonable that the first peak originates from backwards emitted particles. A time difference of about 2 ns between both peaks supports this argumentation as

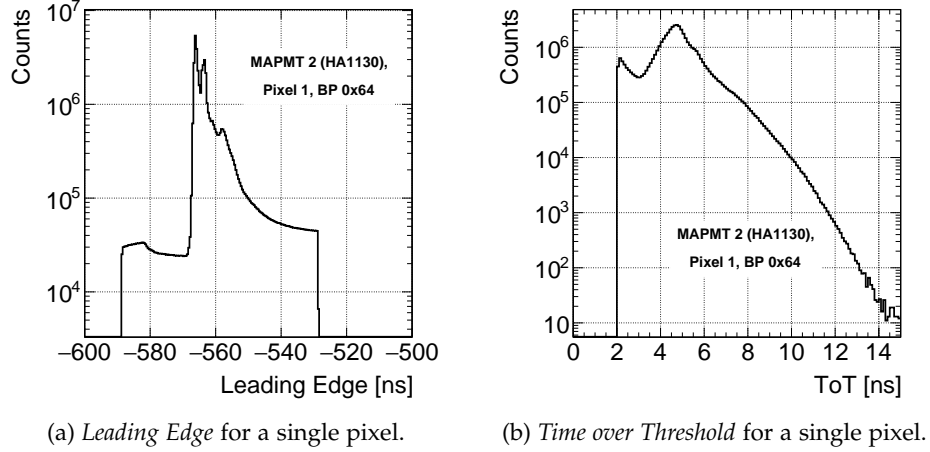


Figure 3.5: *Leading Edge* (a) and *Time over Threshold* (b) distributions for pixel one of MAPMT 2 on BP 0x84 (HA 1130) of the HADES RICH. Cuts on the *Leading Edge* are applied at $t_{LE} > -588.7 \text{ ns}$ and $t_{LE} < -528.7 \text{ ns}$. Only Cals with *Time over Threshold* values of $2 \text{ ns} < t_{ToT} < 15 \text{ ns}$ are accepted. Purpose of the cuts is the rejection of noise hits and cross talk from neighbouring pixels.

it corresponds to the time it takes Cherenkov photons to reach the mirrors and after reflection the MAPMT plane. The ToT spectrum is dominated by a peak at about 5 ns corresponding to a single Cherenkov photon hitting the MAPMT pixel. The rise at low ToT values is explained by detector noise and cross talk caused by neighbouring pixels.

In theory it is possible to distinguish between Cals produced by a single Cherenkov photon and those produced by multiple ones based on the measured ToT. The resolution of the used MAPMTs is not high enough, however, using **S**ilicon **P**hoto**M**ultipliers (SiPMs) would enable this additional feature. A For a brief discussion on this topic see chapter 4.6.

Cals are fitted to rings based on an *Hough-Transformation* [145] [146] and a subsequent ring fitter. Data are transformed to a three dimensional Hough-space (parameters are $x_{Cal}, y_{Cal}, r_{ring}$, whereas rings are searched for. To simplify the search, the radius is restricted to the expected range. After grouping Cals to a ring, the ring is fitted. In HADES terminology, rings are denoted as hits. Fig. 3.6 shows the position dependence of the amount of rings reconstructed per event on the HADES MAPMT plane for each pixel. The ring density obviously scales with the Cal density previously shown in fig. 3.4. However, small area effects, such as the not operational DiRICH boards and the shadows from the mirror holding structure do not lead to a significant loss in rings despite the missing Cals. Especially in the WLS coated regime of the MAPMT plane this lack of Cals is compensated by the overall high amount of Cherenkov photons produced. Due to acceptance gaps of $\Delta r = 1.5 \text{ mm}$ [139] in between the pixels of neighbouring MAPMTs and the fact that the ring radius is about half a MAPMT width, ring centres are

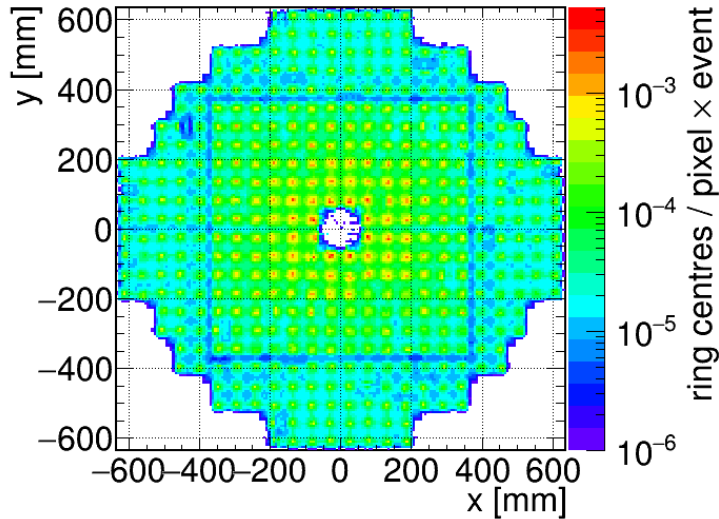


Figure 3.6: Reconstructed ring centres per event per detector pixel in the HADES RICH. The data shown is based on day 86 of the Ag+Ag data run. For details see *text*.

more likely to be reconstructed in the middle of MAPMTs, leading to the chess board like pattern which is observed.

An event display of the HADES MAPMT plane is shown in fig. 3.7. Cals are represented by red squares, reconstructed rings and the corresponding ring centre, visualized by a cross, are colored in blue and the MAPMTs themselves are indicated by black lines. The gap in the origin of the figure corresponds to the opening in the MAPMT plane, where the beam enters. The background, consisting of Cals mainly originating from detector noise, is at a very low level. A detailed analysis results in a fraction of 30% of the Cals per event originating from Cherenkov photons. It has to be noted, that on average less than 0.5% of the whole MAPMT plane is covered by those Cals. The enhancement in $Cals/area$ comparing regions where Cherenkov photons hit the MAPMT plane and areas where only noise Cals are present can therefore be estimated to exceed a factor of 70. In absolute numbers, there are on average about 80 background Cals per event. As these are randomly distributed over the whole MAPMT plane it is very unlikely that five² of them are located in a circular shape in an area that meets the ring radius requirements. To take care of the unlikely case, that rings are formed by noise Cals, cuts on the ring sample are applied in the presented analysis.

With increasing polar angle Θ , a particles trajectory length in the RICH radiator volume increases. The amount of emitted Cherenkov photons in-

² The minimum amount of Cals needed to reconstruct a ring is given by the dimension of the Hough-space. For circles it is three, but for background rejection purpose at least 5 Cals are required.

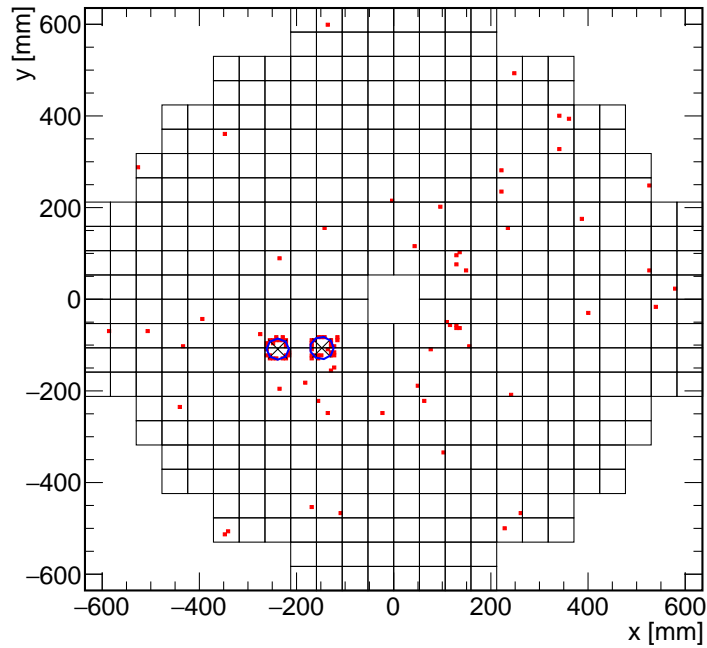


Figure 3.7: A single event display of the HADES RICH MAPMT plane. MAPMTs are indicated by black squares. Cals are shown in red, fitted rings in blue. Ring centres found by Hough-transformation are marked with a blue cross. The enhancement in Cal-density in regions, where the MAPMT plane is hit by Cherenkov photons compared to noise-only regions is estimated to be above 70.

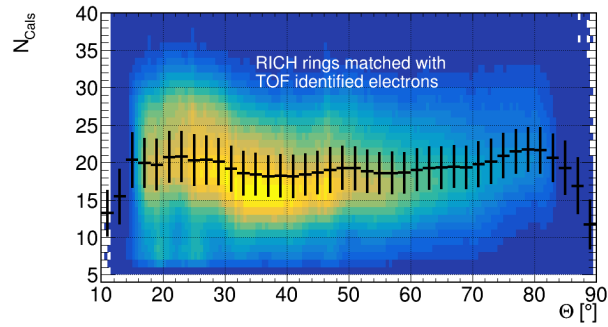
creases linearly with the path length which thus also holds to first order³ for the amount of Cals. The WLS coating of the inner most MAPMTs results in an increase in the amount of Cals for small values in Θ , although the trajectory in radiator volume of the original particle is relatively small. The dependence of N_{Cal} on Θ over the full RICH acceptance is shown in fig. 3.8a. Only such rings are used, that are matched with tracks identified as electrons by time-of-flight methods (see chapter 4.3.4). Mean values and the corresponding standard deviation are shown in black bands.

Due to the RICH detector geometry also the radius of reconstructed rings varies with the polar angle Θ (compare fig. 3.8b). The ring radius is a function of the distance between the VUV mirror and the MAPMT plane⁴. Therefore it decreases with increasing Θ with a sudden rise in between related to the two-step design of the MAPMT plane. This step is not resolved perfectly as the MAPMT plane has cartesian symmetries whereas the VUV mirror is radial symmetric leading to an additional dependence on the azimuth angle

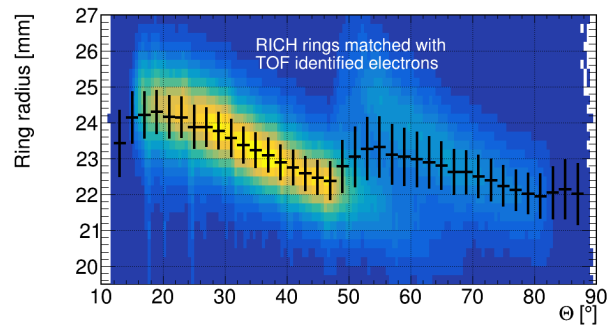
³ This proportionality only holds if the possibility of multiple hits on a single pixel is neglected as well as possible absorption of Cherenkov photons in the radiator gas.

⁴ The relation is linear in very good approximation.

Φ for $50^\circ \leq \Theta \leq 60^\circ$.



(a) Dependence of N_{Cals} on the polar angle Θ .



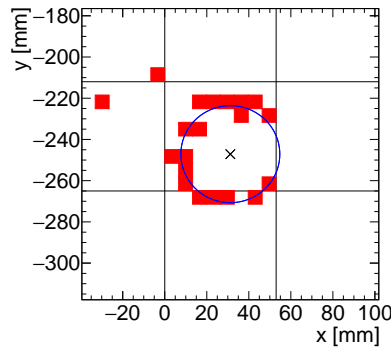
(b) Dependence of the radius of fitted RICH rings on the polar angle Θ .

Figure 3.8: Dependence of N_{Cals} assigned to a fitted RICH ring and the ring radius on the polar angle Θ over the full RICH acceptance. Mean values and the corresponding standard deviation are indicated. Only rings matched to tracks that passed TOF electron requirements are plotted.

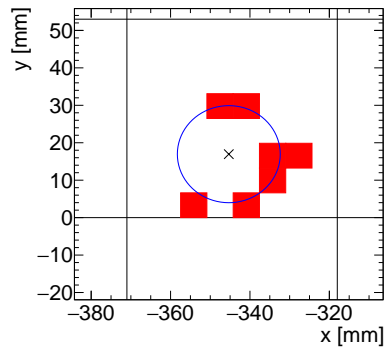
In the data sample one finds different Cal patterns on the MAPMT plane that are fitted to rings. In fig. 3.9 typical event displays of detector regions where these have been observed are shown. Besides rings, that meet the expected values in radius and N_{Cals} (compare fig. 3.9a),

- there is a small fraction of rings that is made up from detector noise only. These rings typically consist of few Cals only and their radius is smaller than the expected value. Such a ring is shown in fig. 3.9b
- close by rings are denoted as double-rings, when they at least partially overlap. Examples with different distance between two rings are shown in fig. 3.9c and 3.9d. For very close rings it is not any longer possible for the ring finding algorithm to separate both rings which results in only one ring being fitted. Such an event is shown in fig. 3.8e. Unidentified double-rings are usually built out of more Cals than a typical ring.

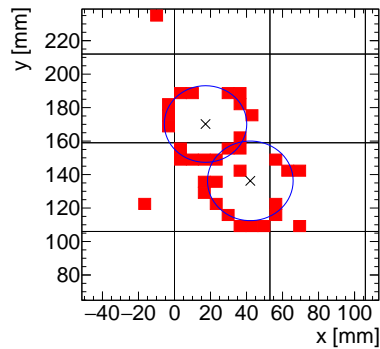
- there are events, where Cals in almost all channels of a MAPMT are detected. The origin of these blob-like structures is not fully understood and still under discussion [147]. A possible explanation that has been investigated by simulation are backwards emitted particles (mainly electrons) flying through the glass window of the MAPMT and generating Cherenkov radiation therein. Also low energy electrons that are significantly influenced by the residual magnetic field in the RICH do not have a straight trajectory and thus produce smeared out rings. Most probably those blob-like structures are caused by backwards flying electrons for which the Cherenkov cone hits the MAPMT surface without being focused. If many pixels see a true signal in the MAPMT, through cross-talk even more pixels give a signal. A blob-like structure is shown in fig. 3.9f. In most cases multiple rings are fitted into such a blob. Besides the high ring density in this area, those rings can easily be identified by an extremely high amount of Cals forming and surrounding them.



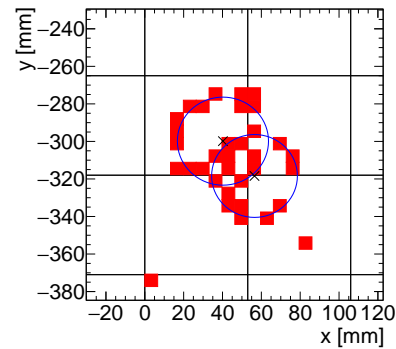
(a) Isolated RICH ring.



(b) Fake-ring built from detector noise.



(c) Near by RICH rings.



(d) Near by RICH rings.

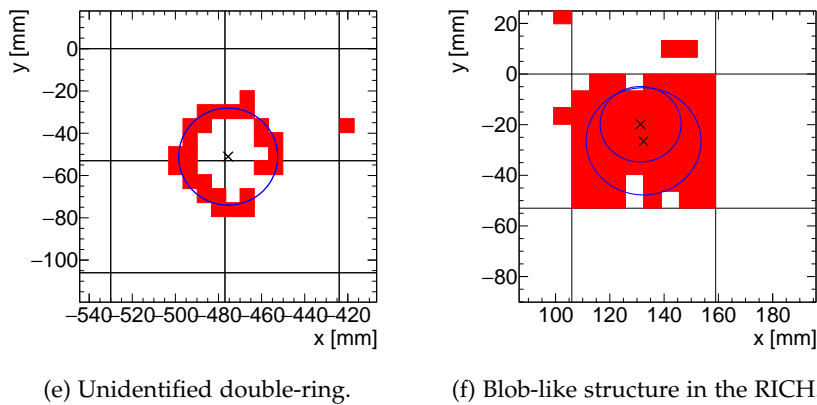


Figure 3.9: Zoom-in views of event displays observed on the HADES RICH MAPMT plane. Single MAPMTs are indicated by black lines. Cals are shown in red, fitted rings in blue and ring centers are indicated by blue crosses. (a) shows a reconstructed isolated ring on the MAPMT plane. In (c) and (d) reconstructed close-by rings are shown with small distance in between. If the rings approach that close, that Cals are located on directly neighbouring pixels, they can not be separated any longer and only one ring is fitted (e). A blob-like structure covering almost a whole MAPMT is observed in (f) and is fitted with two rings by the ring finding algorithm.

In this chapter the analysis concept of this work is presented. Starting from the general baseline of track-finding (sec. 4.1) and the event selection (sec. 4.2), the electron identification and selection within the track sample is explained and discussed (sec. 4.3, 4.4). From the pairing of electrons a dielectron invariant mass spectrum is obtained (sec. 4.7). The background contributions in the electron sample and in the dielectron spectrum (physical and combinatorial) is studied in simulation (sec. 4.8). An efficiency correction is derived and applied (sec. 4.9) and the combinatorial background is derived and subtracted based on the event-mixing technique (sec. 4.10).

4.1 TRACK RECONSTRUCTION IN HADES

The first step in each particle physics data analysis is the conversion of raw data obtained from the readout electronics of all detector components to possible particle tracks that might have caused these signals. In HADES specific terms this means to produce **Data Summary Tape (DST)** files out of **HADES List Data (HLD)** files. This is a for all analysis within HADES common procedure, no matter what the goal of any specific analysis is, and is performed once (updates in the production code will of course result in a rerun). The possibility of having such a common base for all kind of analysis is given by the HADES software, all built over the **Hades sYstem for Data Reduction and Analysis (HYDRA)** framework which itself is based on the open source data analysis framework **ROOT**. In the following, the process of track finding in HADES is summarized:

- Cluster hits in the inner MDC layers (placed in front of the magnetic field) are matched together to form inner segments. The same is done for the outer MDCs (outer segments).
- Outer segments are matched with **META** (RPC+TOF wall) hits, inner segments with **RICH** hits (rings). The ring-to-track matching is based on the angular differences between the inner segment and a virtual particle originating from the target producing a reconstructed ring. The ring in a specific event leading to the lowest value in terms of differences in Θ and Φ to the inner segment is used for matching. As a proper variable the **RICH Matching Quality (RMQ)** is introduced.

$$RMQ = \sqrt{(\Theta_{ring} - \Theta_{track})^2 + ((\Phi_{ring} - \Phi_{track}) \sin \Theta)^2} \quad (4.1)$$

In case the event does not include any ring that matches the conditions $\Theta_{ring} - \Theta_{track} < 8^\circ$ and $\Phi_{ring} - \Phi_{track} < 8^\circ$ no ring information

is assigned to the inner segment. It has to be noted that within this matching process a coordinate transformation from Cartesian x and y position of RICH rings on the MAPMT plane to spherical Φ and Θ for tracks from the target is performed. Due to the extended target this transformation significantly depends on the target segment which has been hit in each event. To account for this effect, a numerical approximation method is applied. For the outer segment to META matching, a similar procedure is performed.

- Inner and outer segments are matched using a Runge-Kutta method that propagates the particles through the magnetic field based on their cluster hits. The quality of matching is controlled by the χ parameter allowing to select only for well matched inner and outer segments that most likely originate from the same particle. The main output of this computation is a momentum vector representing the reconstructed track. Using timing information of the detectors also a velocity is calculated.

The tracks reconstructed during this procedure serve as input for the analysis presented in the next chapters. They are visualized in fig. 4.1 in terms of their main reconstructed properties, momentum and relativistic velocity $\beta = v/c$. As indicated by solid black lines that represent common particles observed by HADES, each pair of momentum and velocity clearly identifies a specific particle ($p = \gamma mv$) by its mass. However, due to momentum and timing resolution, the latter resulting in velocity resolution unambiguous particle identification is difficult. In particular at high momenta where precise timing gets more difficult, a clear separation between particle species based on momentum and velocity becomes challenging, especially for light particles as electrons and pions. In order to still get a clean sample of leptons, necessary for the analysis presented here, the highly performing RICH detector is used.

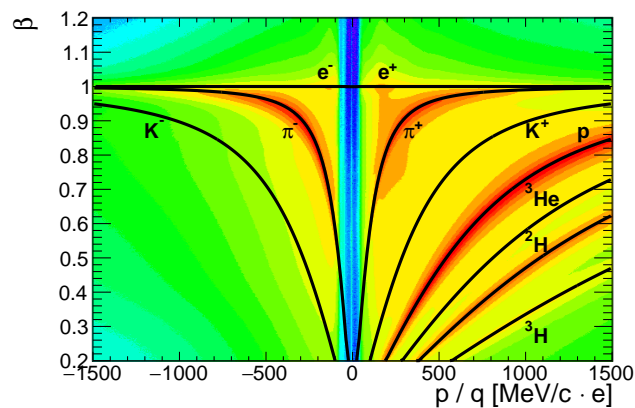


Figure 4.1: β vs. p/q for all reconstructed tracks after the track finding procedure. Theoretical signatures of particles identified in the HADES detector are indicated by solid lines.

4.2 EVENT SELECTION AND CENTRALITY ESTIMATION

During the Ag+Ag beam time in March 2019, in total about 13 billion collisions fulfilling the PT2 trigger conditions (compare chapter 2.6) have been recorded. Not all of them are of equal high quality. Therefore, further event selection criteria are applied. Those are based on binary flags, that have been set for each event during the track reconstruction procedure. In this analysis, the following requirements have been applied:

- There have to be more than 20 hits in the TOF and RPC that are correlated to a hit in the START detector (physical PT₃ trigger condition). Lower multiplicities mainly originate from very peripheral collisions in the target or interactions of the beam nuclei with lighter nuclei such as Carbon, that can be found in the beam pipe and the target holding structure. (kGoodTrigger)
- A converged cluster vertex fit is required. The fitting procedure is based on cluster hits in the inner MDCs and finds the most probable target segment, that has been hit by the beam particle via scanning. Fitted cluster vertices of all events are shown in fig. 4.2 in red. A cluster vertex position of $z > -70 \text{ mm}$ is required. Smaller values indicate interactions with the START detector, the entries at -1 indicate a not converged fit. (kGoodVertexCluster)

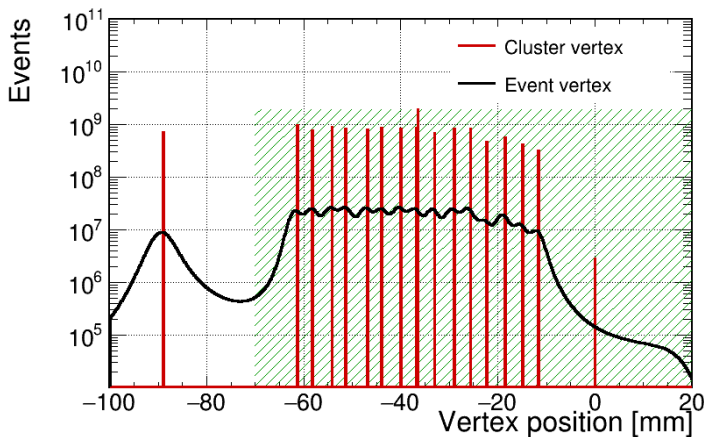


Figure 4.2: Event (black) and cluster vertex (red) distributions before cuts. The cluster vertex is bound to the target segment positions. A position of $Vtx_{cl} = -88 \text{ mm}$ indicates an interaction of beam particles with the Start detector. Values at $Vtx_{cl} = -1 \text{ mm}$ correspond to a not converged cluster fit. Event vertices within the green shaded area ($Vtx_{evt} > -70 \text{ mm}$) and cluster vertices fulfilling $-70 \text{ mm} < Vtx_{cl} < -10 \text{ mm}$ are accepted for the analysis.

- The same requirements holds for the event vertex. It is also calculated from cluster hits in the inner MDCs but not bound to target segments. The event vertex is shown in fig. 4.2 in black. (kGoodCandidateVertex)
- A hit in the START detector is required as it sets the baseline for time-of-flight calculation. (kGoodStart)

As event characteristics such as centrality are mainly determined by the amount of reconstructed tracks, it is necessary to reject events overlapping in time, so called pile-up events. For this purpose, the following flags are included:

- The event is discarded, if another START hit is registered within a $\pm 15 ns$ time window. (kPileUpSTART)
- There should not be any VETO hit inside a $\pm 15 ns$ time window around the START hit. (kGoodVETO)
- Events where a second START hit within $+15 ns$ to $+350 ns$ is found, that has no correlated VETO hit within $\pm 2 ns$ are excluded from the analysis. (kGoodSTARTVETO)

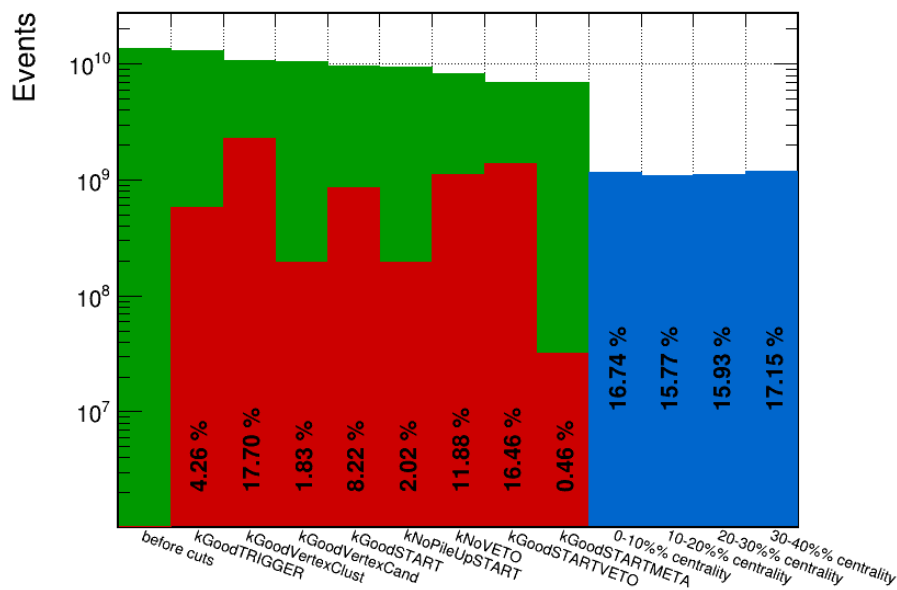


Figure 4.3: Effect of all event selection criteria on the whole event sample and classification in centrality bins. The amount of events accepted after each cut or assigned to the corresponding centrality bin are shown in green. The red area denotes the amount of rejected events by each cut. The numbers correspond to the fraction of events rejected by the current cut based on the current sample. In blue, events assigned to a specific centrality class are shown, starting with the most central 0 – 10%. The values given refer to the event sample that is left after all cuts. Events of lower centrality are not taken into account in this analysis.

Centrality class	0 – 10 %	10 – 20 %	20 – 30 %	30 – 40 %
N_{hit} TOF & RPC	101 - 189	77 - 100	56 - 76	40 - 55
N_{events} [10^9]	1.1609	1.0938	1.1047	1.1896

Table 4.1: Definition of centrality bins by hits in the RPC and TOF detector and corresponding amount of events left for analysis after cuts.

- It is still possible after the previous selection to have a second START hit with VETO correlation for $\Delta t > 15 ns$. These events are rejected if the second START hit is correlated to at least 4 META hits within a time window of $7 \pm 5 ns$. The offset of $7 ns$ corresponds to the time, it takes the fastest particles (speed of light) to travel from the START to the META detector. (kGoodSTARTMETA)

About 53.25 % ($6.9359 \cdot 10^9$ events) of the initial $13.0259 \cdot 10^9$ events are left for analysis after application of the mentioned event selection cuts. An overview on how the single cuts act on the event sample is given in fig. 4.3, indicating also the fraction of events rejected by each cut (red) from the events that passed the previous cuts (green). An important event characteristics is the centrality of the collision (given by the impact parameter) as directly linked to the system size and thus the number of participants.

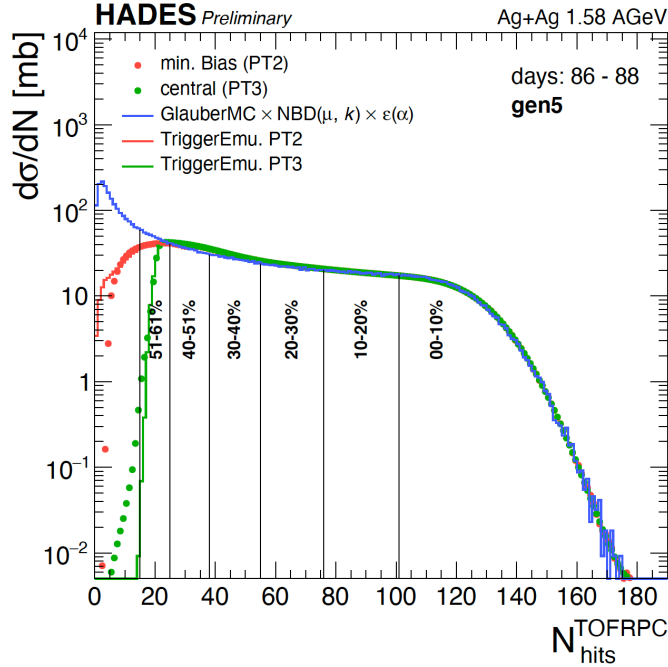


Figure 4.4: Classification of the reconstructed events in centrality classes of 10% based on a Glauber Monte Carlo approach. For explicit numbers of analyzed events in the specific centrality classes see tab. 4.1. Taken from [148].

Based on a Glauber Monte Carlo approach the amount of hits in the META detectors (RPC and TOF) gives an estimation of the centrality and allows for a classification in 10% centrality classes as shown in fig. 4.4. The underlying analysis is carried out in the same way as described for the Au+Au data at $\sqrt{s_{NN}} = 1.23 \text{ GeV}$ in [149]. For the most peripheral 30% a perfect agreement within the model and the data is observed which becomes worse with more peripheral centrality classes, e.g. because of contamination with $Ag + C$ collisions originating from interactions with the beam pipe material. Therefore only the most central 40% events are used in this analysis divided in four bins of 10% centrality each. An overview on the exact definition of the event classes based on the amount of META hits and the corresponding amount of analyzed collisions in each class is provided in table 4.1.

4.3 ELECTRON IDENTIFICATION

A major key to obtain physics results in any analysis is to provide a clean sample of the particles of interest. In this work electrons have to be identified within all reconstructed tracks. Requiring specific conditions on tracks or special features such as reconstructed rings in the RICH detector, the purity of the sample can be increased. However at the same time, the reconstruction efficiency of the desired particle species is lowered, as no observable provides a perfect distinction in particle species. Due to this trade off between purity and efficiency it is impossible to reach a perfectly clean sample.

In this analysis, one has to distinguish between two sources of contamination within the electron track sample chosen for the analysis: At first there are tracks, that have not been produced by electrons but may be misidentified as such. A high separation quality between electrons and the lightest hadrons, pions, is thus aimed to be achieved. Here, the high performing RICH detector becomes crucial. The particle separation by time-of-flight methods becomes difficult for (ultra-) relativistic particles (as is visible in fig. 4.1, where the calculated lines approach each other with increasing momentum). Even using the RICH detector there is some tiny pion contribution left as wrong matching between rings and tracks may appear. Second, physical background - electrons produced via photon conversion - has to be rejected, which is done more efficiently than ever before based on close pair identification enabled by the RICH detector. The electron identification presented in the following is used as baseline for all physics analysis presented in chapter 6.

4.3.1 Pre-selection of tracks

The pre-selection of tracks is performed in the so called *track sorting* procedure and serves two major purposes in this analysis. At first, there are many random combinations made up by hits in various detector components which have to be reduced. Second, soft electron selection criteria are applied.

In HADES terminology, these pre-selection cuts are combined within two flags, namely *kIsUsed* and *kIsLepton*. In detail, the track quality cuts applied read:

- Rejection of fake hits in the MDCs. In the hit reconstruction in the MDCs it is possible to built up hits from fired wires that are unphysical, as the wires have been fired by particles somewhere else and randomly match at some point. A graphical explanation is provided in fig. 4.5. In case an MDC hit consists of shared wires only, it is rejected. If it shares only a fraction of wires with another hit, the hit that shares less wires in total is rejected. For an equal amount of shared wires, the hit with lower χ^2 in the segment fitting procedure is rejected.
- For all detector hits (except the RICH detector) it is required to match best in terms of χ^2 of the Runge-Kutta fitting to the reconstructed track. In case e.g. the corresponding META hit matches better to another track, the current track is rejected. Following from this, each detector hit is only used once for track building. This is essential for the rejection of fake tracks. However, sometimes, as in the case of conversion processes, tracks might be that close, that they can not be resolved by the detector. To track down such electrons, the RICH detector can provide useful information.
- The inner segment fit has to be converged $\chi_{in-seg}^2 > 0$ and the overall fitting has to be reasonably good ($\chi_{track}^2 < 1000$).
- The match-quality between track and META hit (**META-Match-Quality**, MMQ) has to be better than $MMQ < 3\sigma$ referring to the META cluster size.

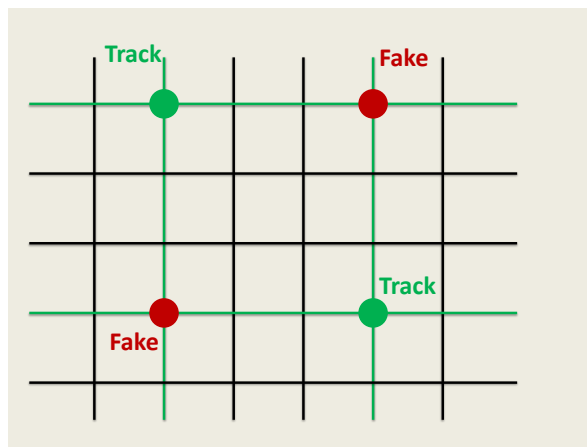


Figure 4.5: Explanation of the origin of fake hits in the MDCs in a simplified model. MDC wires are shown in black, fired wires are colored green. Two tracks (green dots) fire two wires each. In total, the four fired wires have four crossing points which will all be recognized as hits. Fake hits (red dots) can be identified using matching information with other detector components.

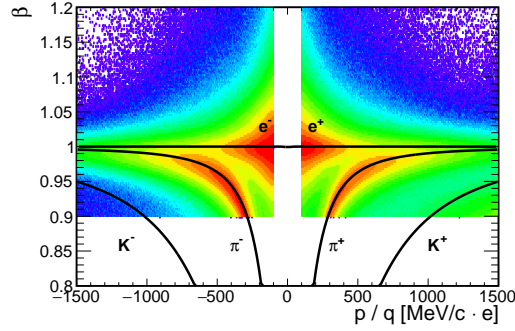
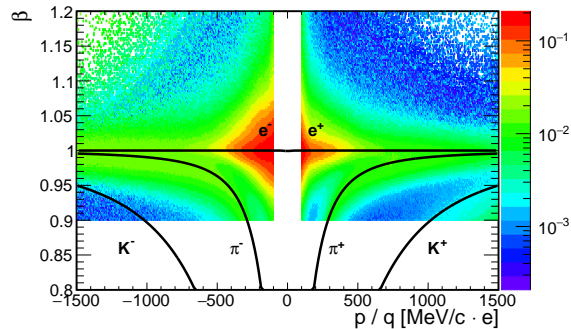
(a) β vs. p/q of tracks after pre-selection.(b) Fraction of tracks that passed the pre-selection relative to fig. 4.1 in terms of β vs. p/q .

Figure 4.6: (a) shows β vs. p/q of tracks that have passed the pre-selection. Due to the cut at $\beta = 0.9$ contributions of hadrons heavier than pions are strongly suppressed. (b) shows the relative amount of particles that passed the pre-selection based on the input shown in fig. 4.1. The pion contribution has been significantly reduced applying track quality and soft lepton identification requirements. Due to random matching of pion tracks to rings, those still account for a significant contribution.

As loose electron identification cuts serve:

- A velocity of $\beta > 0.9$ is required.
- The momentum of all tracks is required to exceed $p > 100 \text{ MeV}$ and to be smaller than $p < 1200 \text{ MeV}$. The lower cut is applied to overcome possible acceptance and efficiency issues at the detection threshold. Momenta that exceed $p = 1200 \text{ MeV}$ are most likely fake tracks as it is almost impossible¹ to reach such high momenta at the given \sqrt{s} . Before this cut is applied, a momentum correction regarding the energy loss of electrons in the MDCs is applied. This correction is derived from simulation and depends on the polar angle Θ , as it scales with the detector material budget. The correction values are in the order of $1 - 2 \text{ MeV}/c$.

¹ The pure cinematic cutoff is much lower, but due to Fermi momentum in nuclei, also higher values than $p = 1200 \text{ MeV}$ are possible but very unlikely.

- The track has to be matched with a RICH hit (ring) and the angular difference between track and ring is required to be $\Delta\Theta < 4^\circ$ and $\Delta\Phi < 4^\circ$.

The impact of both of these flags on the track sample in velocity and momentum is shown in fig. 4.6. Hadronic contribution from particles heavier than pions have been strongly suppressed in the sample applying the cut in β . As a RICH hit is demanded (although with a rather soft matching window) by *kIsLepton*, the amount of pions in the track sample has also been reduced by a factor of 0.01. Unphysical entries in regions of $\beta \gg 1$ and at high momentum have been significantly reduced due to fake track rejection. Track quality requirements reduce the sample of positively charged tracks more significantly than the negatively charged, as due to the huge fraction of protons in the original sample way more random tracks with positive charge had been generated by the track reconstruction algorithm than those with negative charge.

4.3.2 Single track vertex

In addition to the previous cuts on the event vertex (chapter 4.2), also a cut on the single track vertex, defined as the closest point of the track to the beam line, is applied. Tracking quality worsens towards low momenta mainly because multiple scattering in the detector material increases. Scattering in the RICH mirror, i.e. in the front of the first tracking stations might have a significant impact on the reconstructed vertex position. Thus the cut is chosen to be very loose in order to only reject obvious off-vertex tracks, such as secondary particles as electrons originating from conversion. A 'conversion-map' of HADES based on UrQMD simulations is shown in fig. 4.7. This top view of the HADES detector indicates vertices of Monte-Carlo-true electrons in z and x coordinates. Electrons that are produced within the collision or originate from hadronic decays have vertices placed in the target. Entries apart from the target mostly indicate conversion processes in which electrons are produced. Especially conversion processes in the radiator volume of the RICH detector are of relevance here, as these may still produce reasonable RICH information.

By defining the single track vertex as the closest point to the beam line, the agreement in x and y position to the event vertex is good by definition. Fig. 4.8 shows the difference in z between the single track vertex and the corresponding event vertex. The advantage of considering this observable instead of the pure vertex is that there are no contamination effects of the extended target on the distribution. A cut window of $\Delta z_{Vtx} = 0 \pm 50 \text{ mm}$ is applied on the sample which rejects about 1.71% of the tracks.

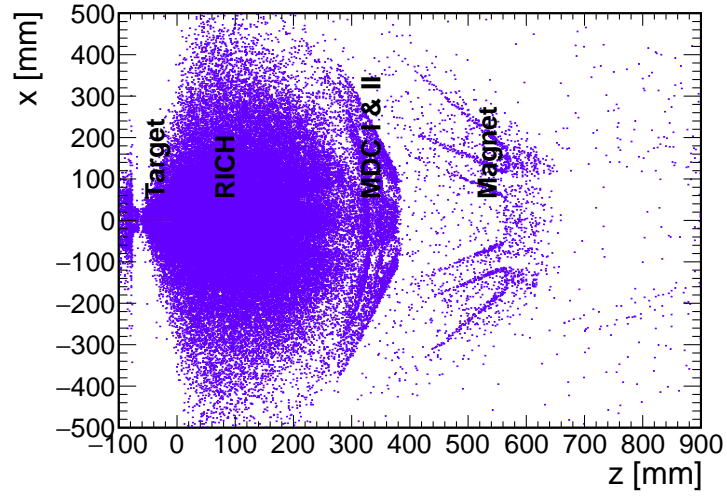


Figure 4.7: Conversion map of HADES from UrQMD simulation in a top view of the HADES detector. Single detector components, such as the RICH detector, MDCs I and II and the magnet can be identified.

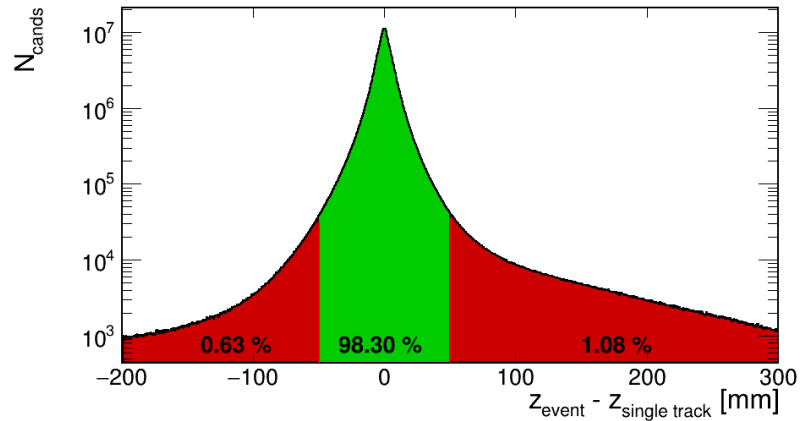


Figure 4.8: The vertex cut is applied on the difference in z between event vertex and the vertex of the reconstructed track. The cut window is set to $\Delta z_{Vtx} = 0 \pm 50 \text{ mm}$. About 1.71% of the tracks are rejected.

4.3.3 RICH detector observables

To fight the remaining hadronic contamination mainly caused by pions, the RICH detector information is used in a more elaborated way than included in the pres-selection criteria. All tracks that are present in the current sample have been matched to a ring identified in the RICH during the track reconstruction procedure in HADES (compare section 4.1). This matching is based on very low requirements and will therefore be tightened and optimized to reject hadrons that are randomly matched with rings because of their agreement in solid angle emission.

4.3.3.1 RICH ring quality requirements

At first the sample of reconstructed rings is checked for those, that are made up from detector noise only and such do not contain any physics information. A RICH ring is characterized by its radius, the amount of Cals attached to it and the position on the detector plane. The according experimental distributions in radius and Cals are shown in chapter 3, fig. 3.8a, 3.8b. To serve as selection criteria, these properties have to be well reproduced in simulation in order not to harm subsequent corrections in efficiency. The comparison between the experimental data presented earlier (compare fig. 3.8) and simulations is shown in fig. 4.9, 4.10. An agreement on a very high level is observed regarding three cases: white electrons², electrons from full UrQMD simulations and experimental data in terms of the overall dependence on the polar angle Θ as well as regarding absolute values.

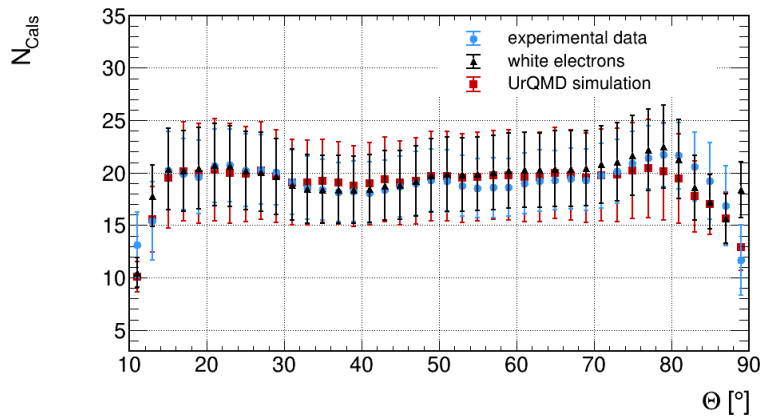


Figure 4.9: $N_{Cals}(\Theta)$ comparison between two types of simulations and experiment. The data points are extracted as shown in fig. 3.8. Experimental data is shown in blue, red data points correspond to full UrQMD simulation and results obtained from embedded single electrons are represented by blue data points.

Fig. 4.11 shows the radius distribution of rings that have been reconstructed in the RICH detector (Θ integrated fig. 3.8b). Cuts are performed

² single electrons embedded in UrQMD or real data

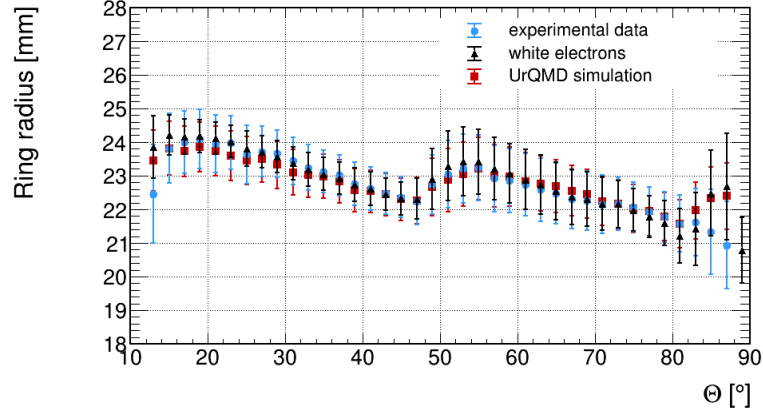


Figure 4.10: $r_{ring}(\Theta)$ comparison between two types of simulations and experiment. The data points are extracted as shown in fig. 3.8. Experimental data is shown in blue, red data points correspond to full UrQMD simulation and results obtained from embedded single electrons are represented by blue data points.

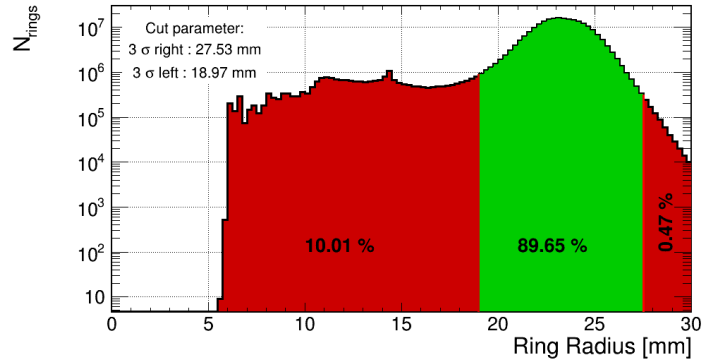


Figure 4.11: Fitted radius distribution of identified rings in the RICH detector. As cut value on the sample, a 3σ window of the fitted Gaussian is applied around the mean value of $\bar{R} = 23.24 \text{ mm}$. About 10.26% of all rings are rejected.

at 3σ values of a fitted Gaussian around the mean value of $\bar{R} = 23.24 \text{ mm}$. In total, 10.26% of the rings are rejected. Fig. 4.12 shows the amount of Cals plotted in dependence of the radius of the ring. The cut on the ring radius extracted in fig. 4.11 is shown in vertical solid black lines. In addition, rings that are made up by less than eight Cals are also rejected (horizontal, solid black line), as their amount is almost independent of the ring radius which indicates them being background only.

The Θ dependence of the ring radius and the amount of reconstructed Cherenkov photons discussed earlier (compare chapter 3.3) is neglected here, as the effects are of minor nature regarding the broad (3σ) selection window in radius. In terms of Cals, no cut is applied on the upper edge of the distribution which includes close-by rings that are needed later in the analysis for

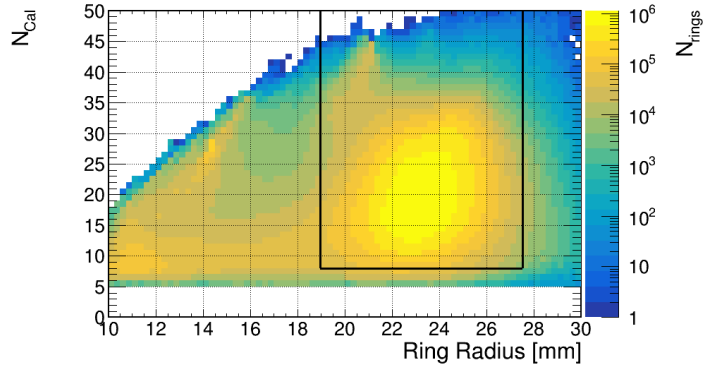
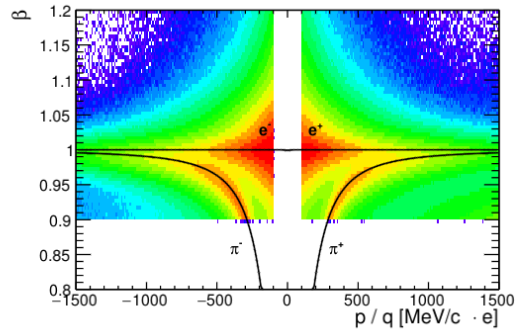
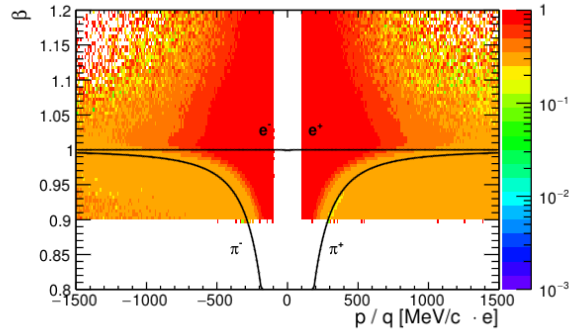


Figure 4.12: The correlation of N_{Cals} and the ring radius is shown. Cuts applied on the ring radius (extracted in Fig. 4.11) are shown in vertical, solid black lines. A cut rejecting rings with less than eight Cals is introduced and shown as a horizontal, solid black line.



(a) β vs. p/q of tracks after RICH ring quality requirements.



(b) Fraction of tracks that passed the RICH ring quality requirements relative to fig. 4.6a in terms of β vs. p/q .

Figure 4.13: β vs. p/q of tracks after RICH ring quality requirements in absolute scale (a) and relative to the previous selection step (b). For details see *text*.

conversion identification and rejection. Applying those ring quality requirements on the sample, the pion contamination present after the pre-selection is drastically reduced as shown in fig. 4.13. Due to the high track density

of pions there is a chance for matches to fake rings which have now been rejected. Nevertheless, pions still account for a significant contribution in the sample.

4.3.3.2 Ring to track matching quality

The *Ring to track Matching Quality* (RMQ) is the most powerful observable the RICH detector provides to reject hadronic contamination in the lepton sample. It allows to effectively reject most of the remaining pions, that have been matched with RICH rings. The RMQ is calculated based on angular differences in the reconstructed polar angle Θ and the azimuth angle Φ as in eq. 4.1. Angular coordinates of the particles are reconstructed via tracking in the MDCs, while those of the rings are calculated assuming a virtual particle originating from the event vertex producing the ring. Tracking of the particles therefore begins after the RICH detector. Thus the particles have to cross material, where multiple scattering effects may take place before the particles are tracked, distracting them from their original trajectory (under which an according ring is reconstructed). Especially in the RICH mirror these scattering effects take place. To counteract the resulting distortion between a particles track and ring coordinates resulting in a worsened RMQ, an analytic correction is derived and applied on the reconstructed angular coordinates of each particle. A schematic explanation of this correction is shown in fig. 4.14. It is based on the assumption, the multiple scattering happens in the mirror of the RICH detector only, as it contains most of the material crossed by particles in front of the MDCs. From the measured particle trajectory in the MDCs (that not necessarily points directly to the event vertex) the crossing point with the RICH mirror is calculated. As non-conversion electrons originate directly from the event vertex (secondary vertices of relevant meson decays are too small to be resolved) a new particle trajectory in the RICH

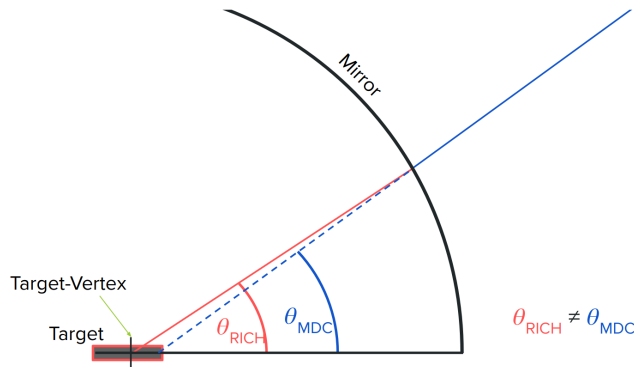


Figure 4.14: Schematic explanation of the scattering correction applied. The angular coordinates of the particles are recalculated assuming multiple scattering only in the RICH mirror based on the reconstructed event vertex. The emission angle $\Theta_{RICH/MDC}$ of the particle does not necessarily correspond to the polar angle Θ in the HADES coordinate system. For details see *text*. Taken from [150].

can be calculated based on the crossing point in the RICH mirror and the event vertex. Subsequently, the angular coordinates (Θ, Φ) of the particles are recalculated.

As displacements in (Θ, Φ) are caused independently of each other and to secure that no bias is added to the analysis applying the segmented target and the scattering correction, differences in the polar and azimuth angles are thus analyzed separately. Distributions of the displacements $d\Phi$ and $d\Theta$ between reconstructed track the matched ring are shown in fig. 4.15 and 4.16, respectively, extracted from simulation with embedded electrons (Monte-Carlo true only) before applying the scattering correction and after doing so. As expected, the distributions are much broader before applying the correction in particular at small momenta, as multiple scattering effects low momentum particles the most. After the correction the width of the distributions is nearly independent on momentum supporting the assumption

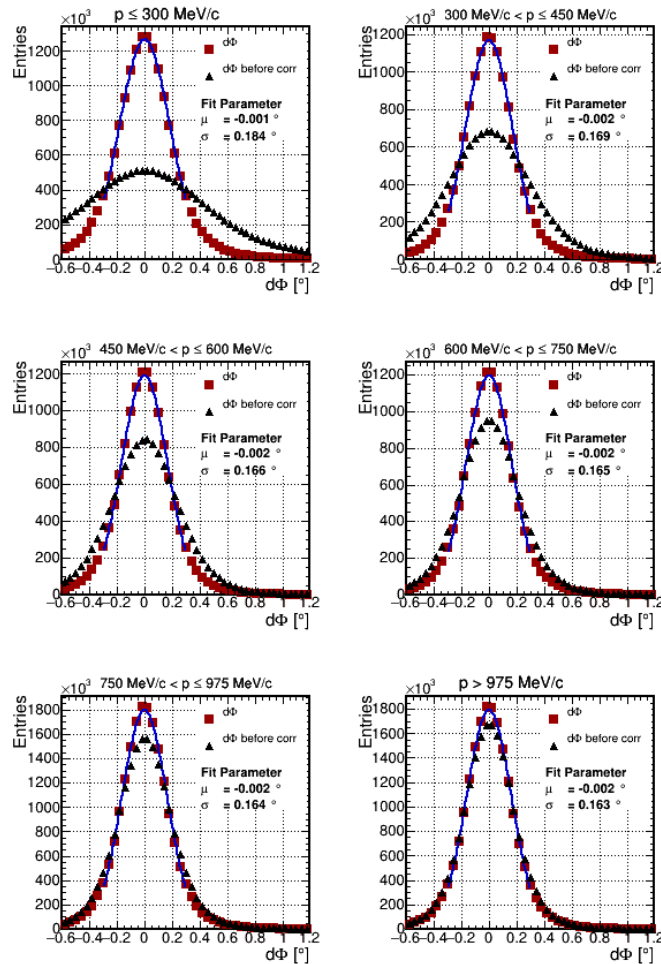


Figure 4.15: Ring to track displacement in the azimuth angle Φ before and after applying the multiple scattering correction in different momentum bins in simulation. Monte-Carlo true data is shown. The given fit parameters correspond to the corrected distribution. For details see *text*.

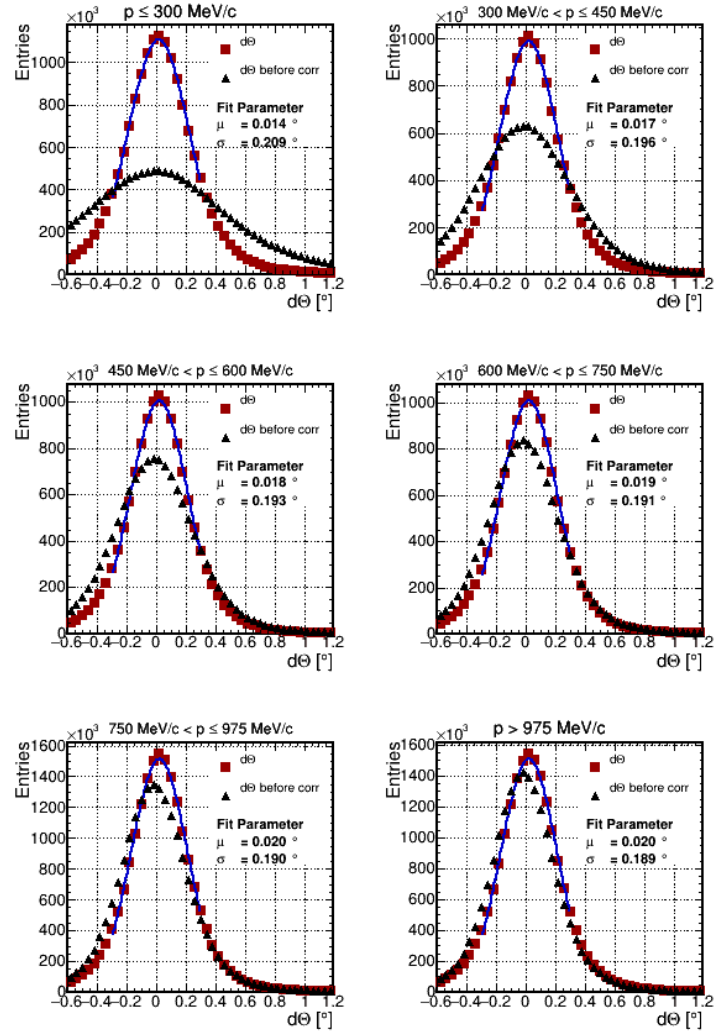


Figure 4.16: Ring to track displacement in the polar angle Θ before and after applying the multiple scattering correction in different momentum bins in simulation. Monte-Carlo true data is shown. The given fit parameters correspond to the corrected distribution. For details see *text*.

that multiple scattering takes place mainly in the RICH mirror. In case of the azimuth displacement, a systematic shift in all distributions is observed after the correction. The shift in positive direction of the angular displacement implies that the reconstructed angular coordinates from the MDCs is systematically larger than the one of the ring. The detailed origin of this shift is unknown so far. However, it can easily be taken into account introducing an offset in the selection window applied on the track sample. The scattering correction has also been applied on pion tracks that can only be randomly matched with a RICH ring to test any systematics. Any improvement on random matchings between rings can tracks was ruled out [151].

In order to extract a proper selection window, the fit parameters obtained in fig. 4.16 and 4.15, are themselves fitted regarding the slight momentum dependence using exponential functions as indicated by the data, see fig. 4.17. A fit can not be performed in case of the momentum dependent shift in $d\Phi$, which is therefore assumed to be constant at $\mu_{d\Phi} = -0.002$. The resulting selection of tracks based on the ring-track matching corresponds to an ellipse in the $d\Phi - d\Theta$ plane. It reads for a selection window width of $n \cdot \sigma_{d\Theta/d\Phi}$

$$\frac{(d\Theta_{track} - \mu_{d\Theta}(p))^2}{(n \cdot \sigma_{d\Theta}(p))^2} + \frac{(d\Phi_{track} - \mu_{d\Phi}(p))^2}{(n \cdot \sigma_{d\Phi}(p))^2} \stackrel{!}{<} 1 \quad (4.2)$$

with the corresponding momentum dependencies extracted in fig. 4.17

$$\sigma_{d\Phi} = 0.1636 + \exp(-2.391 - 0.00717 \cdot p) \quad (4.3)$$

$$\sigma_{d\Theta} = 0.1897 + \exp(-2.709 - 0.00613 \cdot p)$$

$$\mu_{d\Phi} = -0.002$$

$$\mu_{d\Theta} = 0.020 - \exp(-4.271 - 0.00447 \cdot p)$$

The resulting selection window in the ring to track matching in the $d\Phi - d\Theta$ plane is exemplary shown in fig. 4.18 at different momenta using a 3σ selection window. The overall momentum dependence is small and quickly

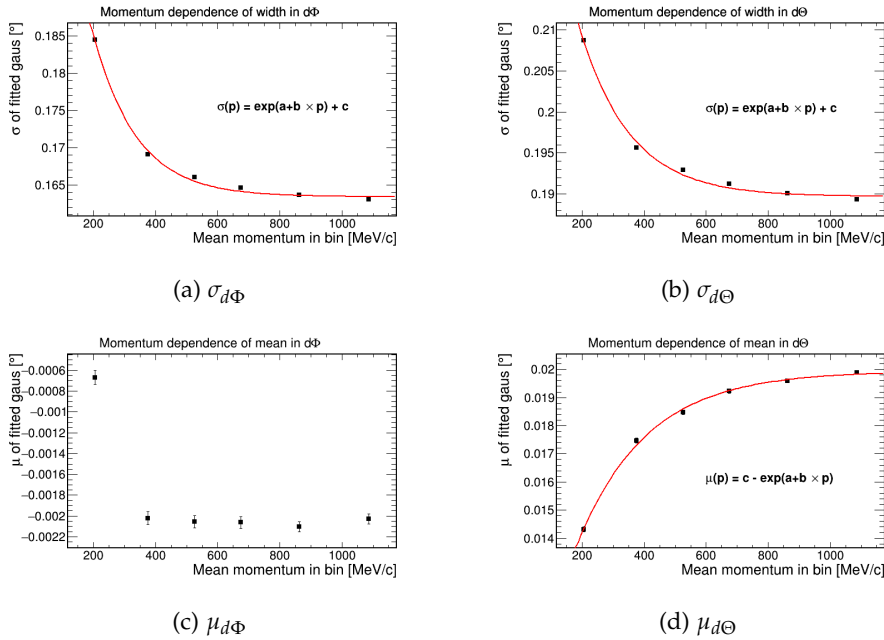


Figure 4.17: Momentum dependence of angular displacements between rings and tracks. The data points are extracted in fig. 4.16, 4.15 and described by converging exponentials. For details see *text*.

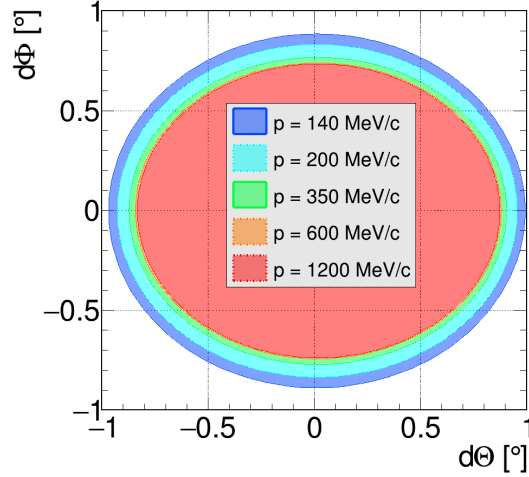


Figure 4.18: Momentum dependent ring to track matching selection window in the $d\Phi - d\Theta$ plane. For details see *text*.

converges with increasing momentum, which again points out, that the correction removes the effects of multiple scattering on a high level. The remaining distortion now originates from the ring reconstruction precision in the RICH and the tracking precision in the MDCs, with the latter being dominant.

Up to now, only simulation data was studied regarding the RMQ. The agreement between simulation and experiment in terms of the ring to track matching has been intensively studied and found to be on a good level. However, deviations originate from a tiny mirror tilt, that is not possible to include in simulation, see e.g. [152]. In order to account for these differences, the same procedure as explained for simulation data is also performed in the experimental data. Using the same cut function, formula (4.2) with $n_{Sim} = n_{Exp}$, in simulation and experimental data but the momentum dependence of the parameters for the corresponding data set, it is ensured to encounter the same electron efficiency. For experimental data, the extracted momentum dependence reads

$$\sigma_{d\Phi,exp} = 0.2671 - 1.60 \cdot 10^{-4} \cdot p + 1.84 \cdot 10^{-7} \cdot p^2 \quad (4.4)$$

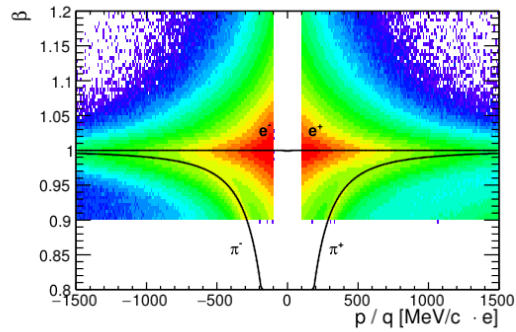
$$\sigma_{d\Theta,exp} = 0.2800 - 1.52 \cdot 10^{-4} \cdot p + 1.77 \cdot 10^{-7} \cdot p^2$$

$$\mu_{d\Phi,exp} = -0.0032 \cdot \exp(-0.00414 \cdot p) + 0.0079$$

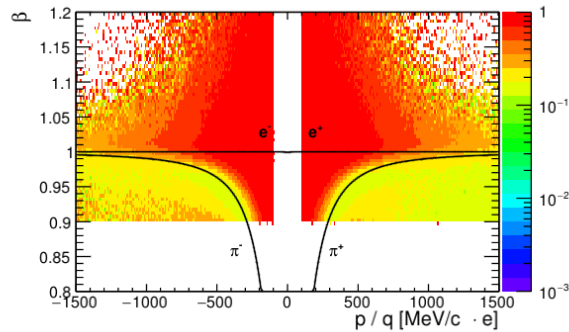
$$\mu_{d\Theta,exp} = 0.0075 - \exp(-4.378 - 0.00296 \cdot p).$$

β vs. p/q spectra of all tracks left after applying the selection criteria in $d\Phi$ and $d\Theta$ are shown in fig. 4.19. Based on the high efficient RICH detector of the HADES, the pion contribution to the sample has almost been fully rejected, thus adding almost another order of magnitude in pion suppression applying tightened ring to track matching requirements to the sample. Only

minor contributions are visible at the pion position. The purity of the sample can only be further improved by rejecting specific regions in the β vs. p/q spectra which equals a mass cut and is discussed in the next chapter.



(a) β vs. p/q of tracks after ring-track matching requirements.



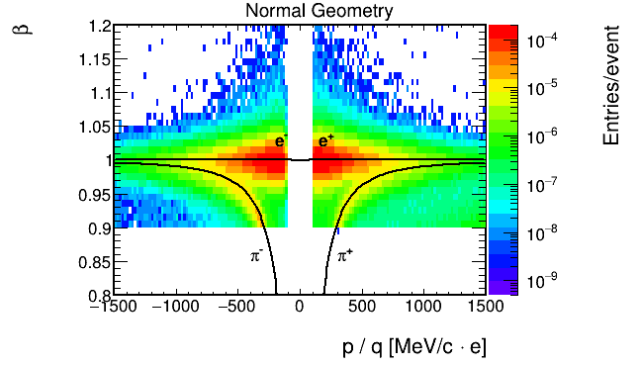
(b) Fraction of tracks that passed the ring-track matching requirements relative to fig. 4.13a in terms of β vs. p/q .

Figure 4.19: β vs. p/q of tracks after the ring-track requirements in absolute scale (a) and relative to the previous selection step (b). For details see *text*.

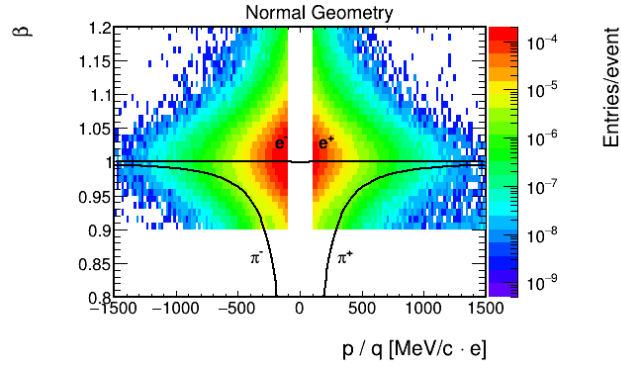
4.3.4 The effective mass

The measurement of a particles velocity (β) and momentum allows the calculation of its mass ($m = p/\beta\gamma c$). As especially a velocity measurement becomes challenging and inaccurate with increasing momentum due to timing precision, it will be denoted as effective mass. The effective mass can be used to further discriminate between different particle species. Different masses are nominally located on hyperbolic trajectories in the β vs. p/q spectrum usually shown. With different timing precision in both META detectors, namely the RPC and TOF wall, a distinction between electrons and remaining pions has to be performed in both systems separately. The corresponding spectra are shown in fig. 4.20 after all previously explained cuts. In the RPC wall the electron signal appears to be much more narrow than in the TOF originating from the better timing precision in the RPC compared to the TOF. On the other hand, the pion contamination is higher in the RPC

wall because of the higher track density at small polar angles resulting in a much larger probability of random matches between rings and tracks.



(a) β vs. p/q of reconstructed tracks in the RPC after ring-track matching requirements.



(b) β vs. p/q of reconstructed tracks in the TOF after ring-track matching requirements.

Figure 4.20: β vs. p/q of reconstructed tracks separated in both META systems, RPC and TOF. For details see *text*.

In order to quantify the remaining pion contamination in the sample, the so-called RICH rotation method, which is well established within HADES, is used to estimate the purity of the track sample. In this procedure, the detected ring coordinates are rotated by 60° against the rest of the detector. Afterwards, the standard ring to track matching is carried out. Therefore, combinations of rings and tracks can be of random nature only. The RICH rotation technique is graphically explained in fig. 4.21.

Applying the same selection criteria on reconstructed tracks on the rotated and the not-rotated sample, the purity P of the lepton sample is defined as a function of momentum p and velocity β by

$$P(p, \beta) = \frac{S(p, \beta)}{S(p, \beta) + BG(p, \beta)} = \frac{N_{no-rot}(p, \beta) - N_{rot}(p, \beta)}{N_{no-rot}(p, \beta)} \quad (4.5)$$

with $N_{no-rot}(p, \beta)$ labeling the amount of tracks reconstructed in the analysis using regular detector geometry (including signal and background) and $N_{rot}(p, \beta)$ in case of the rotated RICH detector (background). However, the

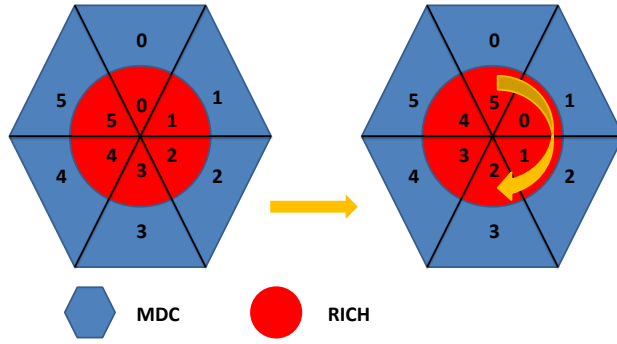
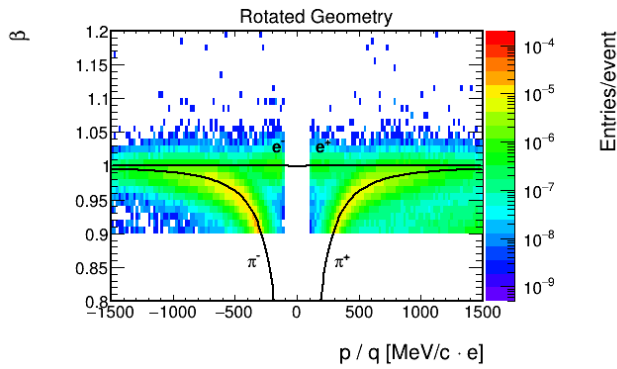
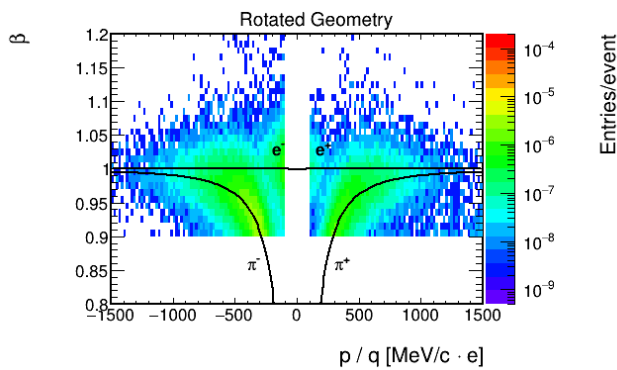


Figure 4.21: RICH rotation technique: The RICH detector is software-wise rotated by $\Delta\Phi = 60^\circ$ (equals one HADES sector) against the other detector components.

background estimation is an upper limit as there is the possibility of rotating



(a) β vs. p/q of reconstructed tracks in the RPC after ring-track matching requirements using a rotated RICH geometry.

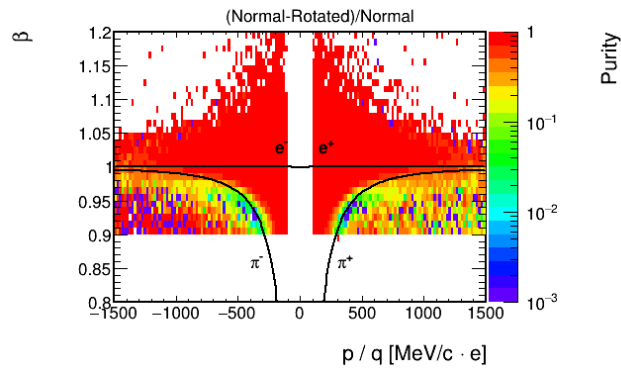


(b) β vs. p/q of reconstructed tracks in the TOF after ring-track matching requirements using a rotated RICH geometry.

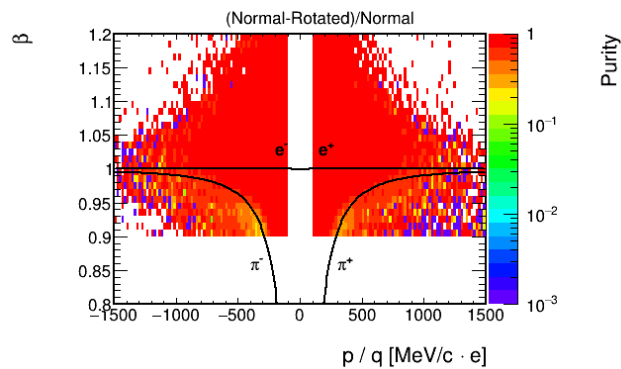
Figure 4.22: β vs. p/q of reconstructed tracks separated in both META systems, RPC and TOF using a rotated RICH geometry. For details see *text*.

true rings such, that they are matched with another true electron. In fig. 4.22 the resulting spectra are separately shown for the RPC and TOF wall using the rotated RICH geometry. The colour code can be directly compared to the previously shown normal geometry spectra in fig. 4.20. In the RPC (4.22a), the pion bands appear in the same significance indicating background only regions here. The same applies to higher effective mass regions. Entries in the electron region are suppressed by two orders of magnitude comparing the normal geometry to the rotated one. The resulting background in this region arises mainly from a random match between true electron tracks and good rings separated by $\Delta\Phi \sim 60^\circ$ in real data. In the TOF system (4.22b) the overall background is smaller due to the lower track multiplicity at high polar angles suppressing random matches of rings and tracks. As a consequence of the lower timing precision of the TOF wall, the pion bands observed show a larger width making it more difficult to discriminate.

Fig. 4.23 shows the purity calculated in accordance to eq. 4.5 in logarithmic scale. In the RPC (fig. 4.23a), the purity is reduced to values of less than $P < 0.01$ approaching the nominal mass of pions at medium momenta. At the nominal electron regions the purity is calculated to values close to $P \sim 1$.



(a) Purity of the track sample in β vs. p/q in the RPC after ring-track matching requirements.

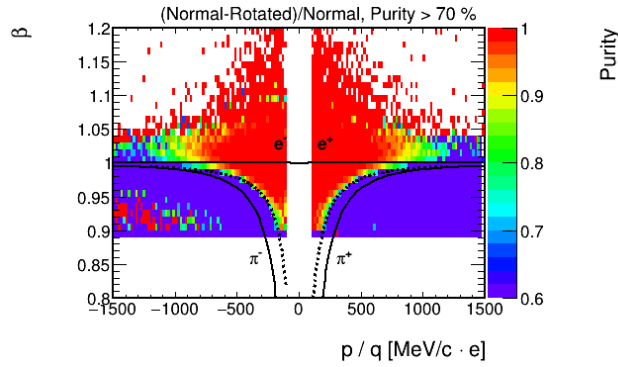


(b) Purity of the track sample in β vs. p/q in the TOF after ring-track matching requirements.

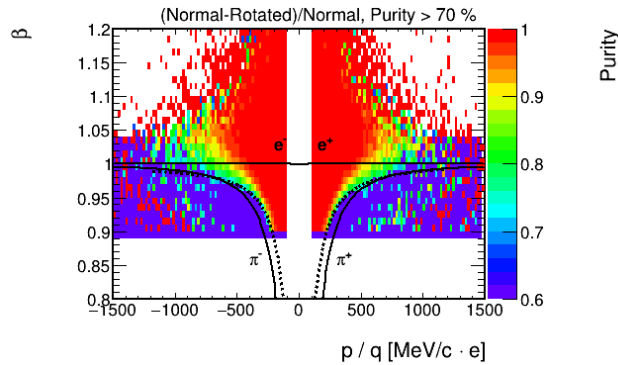
Figure 4.23: Purity of the track sample separated in both META systems, RPC and TOF, estimated using a rotated RICH geometry. Note the logarithmic scale. For details see *text*.

An overall high purity is observed in case of the TOF wall (fig. 4.23b) with only slight drops at the nominal pion bands.

In the following, regions with a purity less than $P < 70\%$ are rejected from the analysis. To extract a steady selection function, the borderline between the high purity region ($P > 70\%$, around the nominal electron regions) and the low purity region ($P < 70\%$) is fitted using a momentum dependent effective mass function $m(p)$ shown in fig. 4.24 as dashed line in linear scale. For a better visualisation, low purity areas are initialized with values of $P = 0.1$. In the RPC (fig. 4.24a), the selection function is located significantly higher in β than in the TOF (fig. 4.24b) caused by the higher pion background. At higher momenta the cut function can not describe the border line any longer. Therefore a more strict momentum cutoff at $p_{max} = 1200 \text{ MeV}/c$ is additionally applied on the track sample. The integrated purity of the track sample that is left for analysis exceeds $P > 99\%$ according to the RICH-rotation-technique, which is in agreement with results from simulation, see chapter 4.8.



(a) $m(p)$ selection function in β vs. p/q in the RPC.



(b) $m(p)$ selection function in β vs. p/q in the TOF.

Figure 4.24: $m(p)$ selection function (dashed line) in β vs. p/q in both META systems, RPC and TOF, based on the estimated purity. Note the linear scale. For details see *text*.

4.4 PHYSICAL BACKGROUND REJECTION USING THE RICH DETECTOR

Electrons produced in conversion processes do not carry information from the fireball created in an heavy-ion collision, but contribute to the pairings of electron and positrons, thus increase the combinatorial background significantly. The upgraded RICH detector enables new methods to efficiently detect and suppress the contribution of conversion electrons in the track sample. The two most successful methods that are used in this analysis are presented in the following.

4.4.1 *Conversion identification based on the opening angle between RICH rings*

As photons do not have mass, the opening angle between both leptons produced in a conversion process physically is zero. In earlier HADES data analysis (compare e.g. [59]), conversion has been identified and rejected based on the opening angle between two reconstructed tracks that have been identified to be electrons. This method of conversion rejection is limited by the close track resolution of the MDCs. With the upgraded RICH detector, close by electrons can be identified with a way higher efficiency than based on the MDCs, for simulation studies see e.g. [153]. Thus, for a reconstructed electron track it is no longer checked for a second close-by electron track, but the RICH detector is checked for a second close-by ring. From the location of the second ring on the PMT plane the emission direction of the causative particle is clearly defined, allowing the calculation of an opening angle between rings. This procedure is illustrated in fig. 4.25, where the second (dashed) track does not necessarily has to be reconstructed by the MDCs in order to identify the tracked electron (solid track) to be produced (most likely) in a conversion process due to the small opening angle α between the matched ring and the second close-by ring. Whenever a second ring in the vicinity of the ring matched to the considered electron track with an opening angle of less than 9° between both rings is found, the track is removed from the sample. It has been shown, that this method of conversion rejection based on the opening angle between RICH rings is three times more efficient, than only relying on fully reconstructed electron tracks [153].

4.4.2 *Conversion identification on the level of calibrated objects (Cals) in the RICH*

Conversion rejection based on reconstructed rings in the RICH detector is limited by the identification of close-by or even overlapping rings. Fig. 4.26 shows the close pair identification efficiency based on reconstructed rings (double-ring efficiency) as a function of the pair opening angle in UrQMD simulation. At a pair opening angle of about 3° the efficiency starts to drop drastically towards lower values. The reason is, that Cals produced by a pair with such a small opening angle form a cluster, where Cals originating from different particles are located on directly neighboured pixels. In such cases, the ring finding algorithm does not recognize the existence of two rings. The

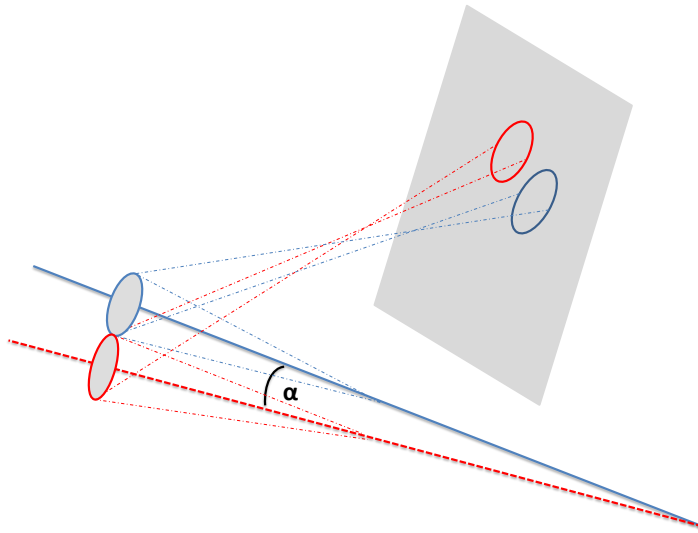


Figure 4.25: Schematic illustration of the opening angle cut applied on the single lepton sample. For each lepton candidate, the opening angle between the matched ring and all other accepted rings (compare ring selection criteria in chapter 4.3.3.1) in the current event is checked. The location of a ring on the PMT plane corresponds to a specific emission direction of an electron. In case the considered ring forms an opening angle $\alpha < 9^\circ$ with some other ring, the lepton candidate is removed from the sample as it was most likely produced in a conversion process. In this procedure of conversion identification it is not necessary to reconstruct the track of the conversion partner, thus it is independent of the MDC resolution for close-by tracks.

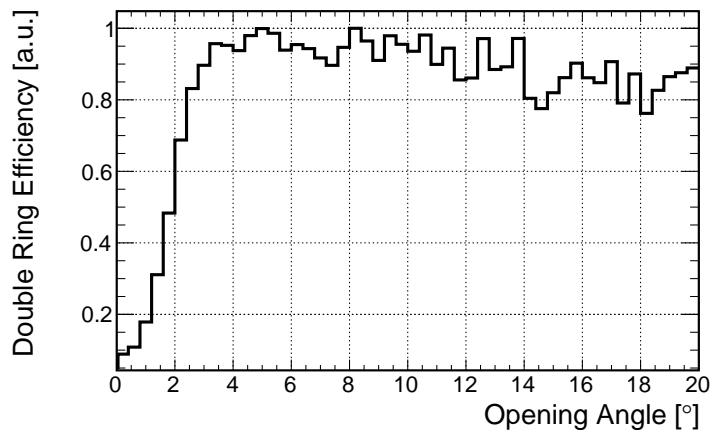


Figure 4.26: Reconstruction efficiency of close-by rings in the RICH detector in dependence on their opening angle in UrQMD simulation. A significant drop for opening angles $\alpha < 3^\circ$ is observed, as rings start to overlap. For details see *text*.

slight drop towards large opening angles is caused by correlated acceptance effects of the pairs³. RICH event displays of close by tracks are shown in chapter 3 in this work (compare 3.9).

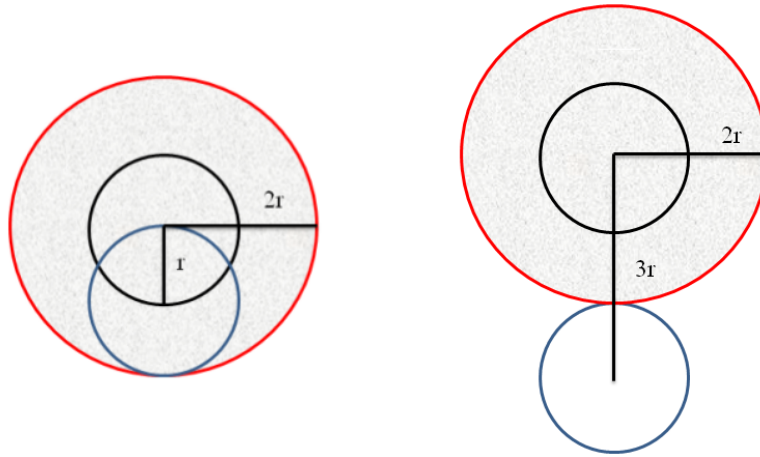
Within this analysis a method of close pair identification and rejection for small opening angles has been developed, that does neither rely on tracking in the MDCs, nor on the ring finding algorithm of the RICH detector. It is based on the number of Cals, the most basic RICH detector information available in analysis. For each reconstructed track left in the sample at this point of the analysis, the amount of Cals is counted in the vicinity of the matched RICH ring. The relevant area on the PMT plane is a circle with the centre being the middle of the ring and an radius that equals two times the ring radius. Even in cases where no second ring has been identified on the RICH PMT plane, a larger amount of Cals will be located in the surrounding of the ring matched to the considered track if the electron originates from a conversion process, where a second electron also emits Cherenkov photons in the direct vicinity. The size of the area where Cals are counted, roughly ⁴ corresponds to a maximum opening angle of 6° between two tracks. Choosing this value carefully is crucial because:

1. The cut is thought to identify double rings for opening angles smaller than 3° (equals one ring radius in distance), because here the ring finding efficiency drops. This angle implies, that Cals have to be counted in an area of twice the ring radius, see fig. 4.27a. even larger area than 3° apart from the ring center, as Cal to ring centre distance of the second ring is about an additional ring radius. To count for all Cals that make up the second ring, one has to search in an area of at least two ring radii (6°). fig. 4.27 (a) provides a graphical insight.
2. In order to not contaminate the distribution in N_{Cals} by Cals that form rings being further apart than 9° the area can not be chosen larger, see fig. 4.27b.
3. Close by tracks matched to two identified rings have been rejected from the sample up to an opening angle of 9° by the previously applied opening angle cut between rings. Here, this cut rejects contamination in the Cal distribution from pairs with opening angles between 3° and 9° where only a fraction of the Cals forming the second ring would have been counted.

The resulting distribution in N_{Cals} from this counting is shown in fig. 4.28. It can be well described by a double Gaussian fit with parameters

$$\mu_1 = (16.197 \pm 0.003) Cals \quad \sigma_1 = (3.620 \pm 0.002) Cals \quad (4.6)$$

- 3 Although the maximum of the distribution is set to one, there are still non-constant, correlated acceptance effects that distort the pure efficiency. For small opening angles (of relevance is the region of about 3°) this effect can be neglected.
- 4 The correlation between pair opening angle and distance between two rings slightly varies with Θ and Φ due to the RICH geometry.



(a) Cal counting for a close-by pair with opening angle of 3° . (b) Cal counting for a close-by pair with opening angle of 9° .

Figure 4.27: Cals are counted in a circle shaped area with $r = 2r_{ring}$ around the ring centre. The area is chosen such, that all Cals of rings separated by less than $\alpha = 3^\circ$ are counted (a). For rings separated by more than $\alpha = 9^\circ$ only Cals of one ring are counted (b).

$$\mu_2 = (26.628 \pm 0.005) \text{ Cals} \quad \sigma_2 = (5.609 \pm 0.007) \text{ Cals}.$$

The straight forward understanding of this distribution is that the first Gaussian corresponds to isolated rings (such as shown in fig. 3.9a) and the second Gaussian represents close-by rings, where one of them has not been

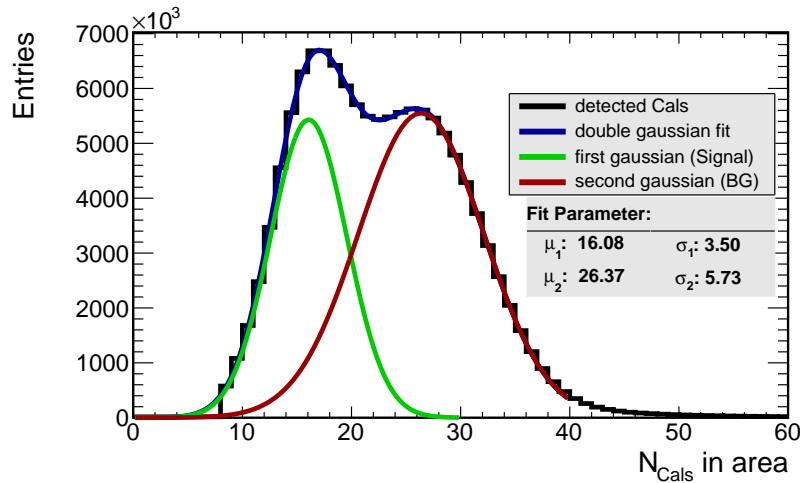


Figure 4.28: Detector integrated distribution of Cals counted inside a $2r_{ring}$ circle around the ring centre (in black). The distribution is described by a double Gaussian fit. The first Gaussian (green) describes ring produced by isolated leptons, whereas the second Gaussian (red) represents close-by rings in the RICH most likely produced by photon conversion pairs.

identified by the ring finding algorithm. This interpretation is underlined regarding the fit parameters: Taking into account that double hits on single PMT pixels are not identified the assumptions for doubling a Gaussian distribution roughly hold ($\mu_2 = 2\mu_1$, $\sigma_2 = \sqrt{2}\sigma_1$). For a detailed discussion see chapter 4.6. The width of the second Gaussian is enlarged due to blob-like

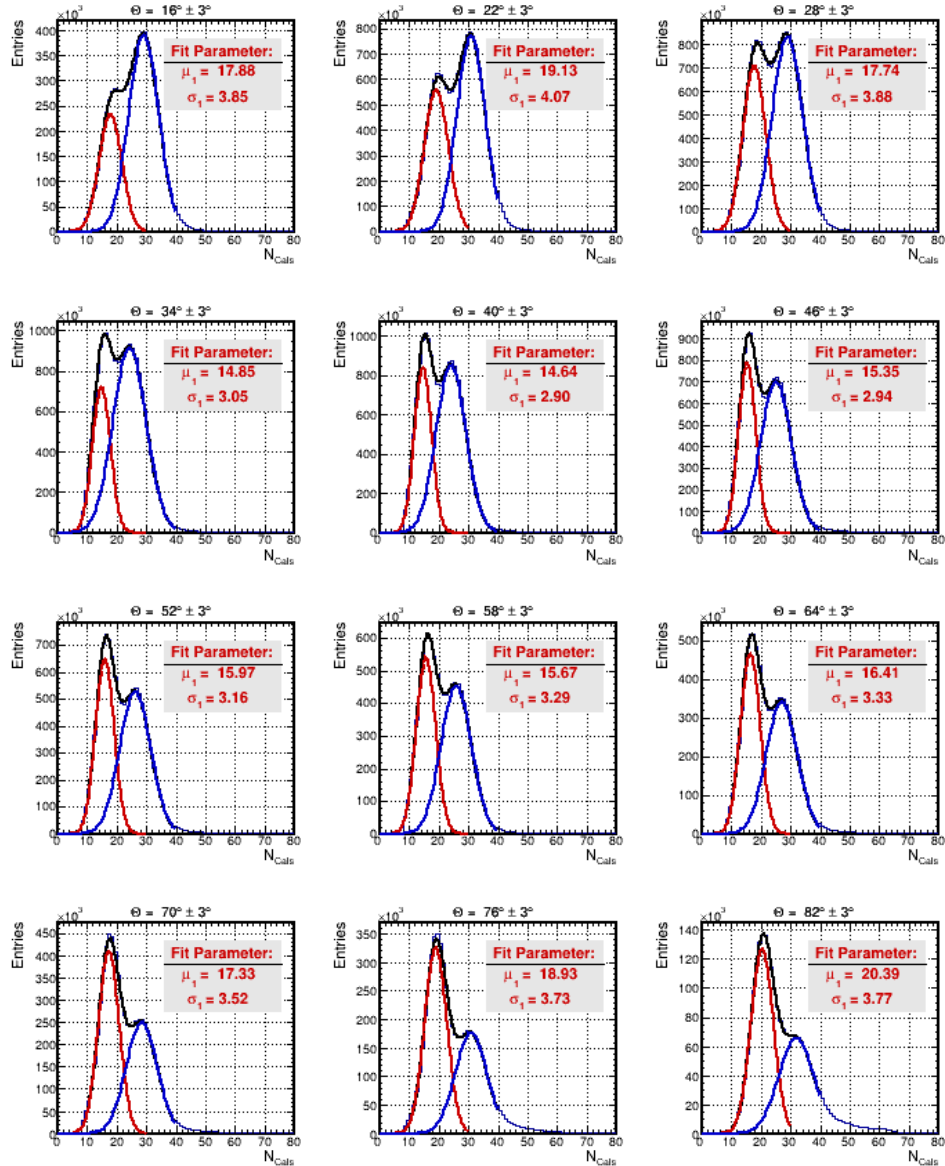


Figure 4.29: The amount of Cals in an area around fitted rings is analysed in Θ bins of $\Delta\Theta = 6^\circ$ widths over the whole RICH acceptance. The double-peak structure is fitted by two Gaussian functions. The first Gaussian (red) corresponds to isolated rings (signal), the second Gaussian represents double-rings (mainly physical background). Fit parameter of the signal peak are given. The mean value varies with Θ in agreement with fig. 3.8a. For high-value Θ bins the signal contribution becomes dominant indicating conversion being mainly located in forward direction.

structures (compare fig. 3.9f) contributing with extremely high numbers of Cals.

As previously discussed in detail (see chapter 3.3) the amount of Cals originating from one particle depends on the azimuth angle Θ due to the RICH geometry and partial WLS coating of the RICH PMT plane. To account for this dependency, the above explained procedure is performed within 6° windows in Θ . The results including Gaussian fit parameters for the first peak are shown in fig. 4.29. The N_{Cals} dependence on Θ is clearly visible in the variation of fit parameters of the first Gaussian for different Θ bins: For small Θ values, isolated rings consist of about 18 Cals (mean value of Gaussian fit) which is consistent with data shown in fig. 3.8a taking into account, that fig. 3.8 still includes a significant double ring contribution. For increasing Θ values N_{Cals} at first suddenly decreases where the WLS coated PMTs are not covered any more, followed by a steady increase due to the RICH geometry.

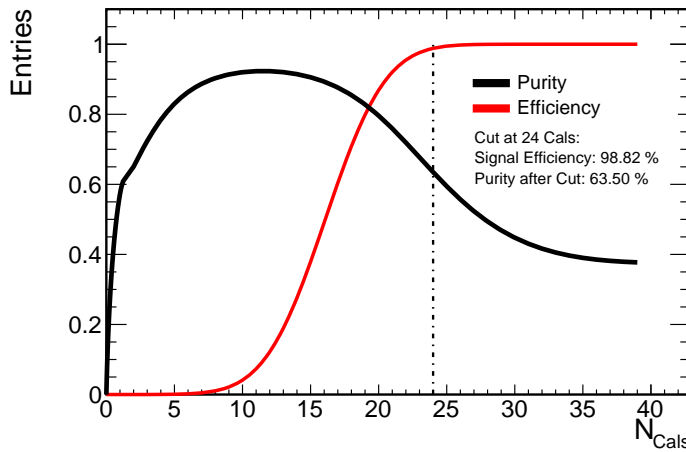


Figure 4.30: Efficiency and purity of the Cal dependent conversion rejection. Values are given for a possible cut at $N_{Cal} = 24$ which is indicated by a dashed vertical line. The calculation is based on integral values of the fitted Gaussians in fig. 4.28.

In the analysis presented in this work, isolated and double rings are separated applying a cut at $N_{Cals}^{max} = \mu + 2\sigma$, whereas μ and σ represent the parameters from the first Gaussian fit. The resulting purity and efficiency of this cut is exemplary shown Θ -integrated in fig. 4.30. The values are calculated by the integrals of the Gaussian fits as given in eq. 4.7. For a possible cut at $N_{Cals} = 24$, the signal efficiency is calculated to $Eff = 98.82\%$ and the purity reaches a value of $P = 63.50\%$ which has to be compared to a purity of $P = 37.83\%$ before applying the cut.

$$Eff = \int_0^{N_{cut}} Fit_{signal} / \int_0^{\infty} Fit_{signal}$$

$$P = \int_0^{N_{cut}} \left(\text{Fit}_{signal} / \text{Fit}_{signal} + \text{Fit}_{BG} \right) \quad (4.7)$$

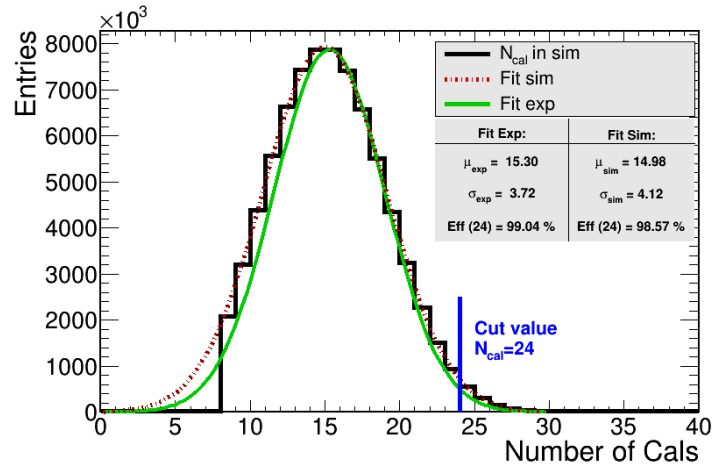
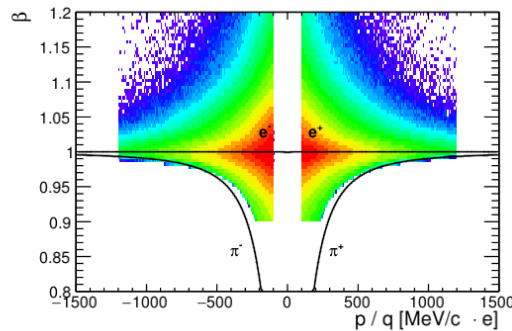
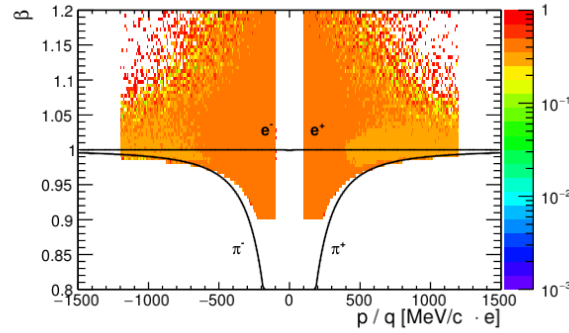


Figure 4.31: Comparison of N_{Cal} of isolated rings in experiment and electron-only simulation. The agreement is on a very high level, especially in the cut relevant region. Efficiency values given for a quantitative comparison are calculated following equation 4.7 at $N_{Cal} = 24$.

In order to apply a Cal based cut on the track sample it is necessary, that it is well described by simulation. Fig. 4.31 shows the amount of Cals that have been counted in a two radius area around a ring in single electron simulations. Each event contains six electrons (positrons), that are distributed homogeneously in p , Θ and Φ and therefore are well separated. The distribution is described by a single Gaussian fit (dashed red). For comparison, the corresponding fit function extracted in experimental data (fig. 4.28) is shown in green. The overall agreement is on a high level proving the hypothesis of the origin of both Gaussian and thus enabling the use of Cals as valid cut parameter in this analysis. For explicit comparison, efficiency values derived for a cut at $N_{Cal} = 24$ are given in fig. 4.28 stating the high-level reproduction of experimental data by simulation.



(a) β vs. $q \cdot p$ of tracks after conversion cuts.



(b) Fraction of tracks that passed the conversion cuts relative to fig. 4.19a in terms of β vs. $q \cdot p$.

Figure 4.32: (a) shows β vs. $q \cdot p$ of tracks that have passed the conversion cuts. (b) shows the relative amount of particles that passed the conversion rejection based on the sample after the ring-track matching requirements shown in fig. 4.19a. An almost constant fraction of rejection is achieved over the whole plane indicating a homogeneous presence of conversion electrons before.

Applying the conversion rejection cuts on the present track sample the resulting effect is shown in fig. 4.32 as a function of β and $q \cdot p$. Conversion electrons are rejected over the full plane in an approximately constant fraction. In total, this cut removes more than 40% of electrons from the sample, that are almost only conversion electrons, thus significantly reducing the combinatorial background without cutting the signal.

4.5 OVERVIEW ON THE EFFECT OF ALL ELECTRON SELECTION CRITERIA

An insight on the impact of all selection criteria is given in fig. 4.33. In green, the total amount of tracks after each cut is shown, normalized to the sample size after the pre-selection. After the electron identification cuts, namely the vertex cut (chapter 4.3.2), the RICH ring cuts (chapter 3.3), the ring-to-track matching cut (chapter 4.3.3.2) and the mass cut (chapter 4.3.4), about 39.8% of the original tracks are left. Thus, the electron identification is based on the RICH detector only, whereas time-of-flight methods are only used to reject low purity kinematic regions. A total fraction of 59.2% of the afterwards remaining electron tracks are marked as conversion and rejected by the opening angle cut and the Cal cut. Afterwards, about 16.2% of the total tracks are left for analysis. The fraction of rejection by each individual cut in relation to the sample left after the previously applied selection step is shown in red. Here, the linear scale on the corresponding y-axis has to be noted.

The effect of all cuts on the track sample applied after the pre-selection is visualized in dependence of $q \cdot p$ and β in fig. 4.34. At small momenta where the discrimination between electrons and pions is naturally easy, about 50%

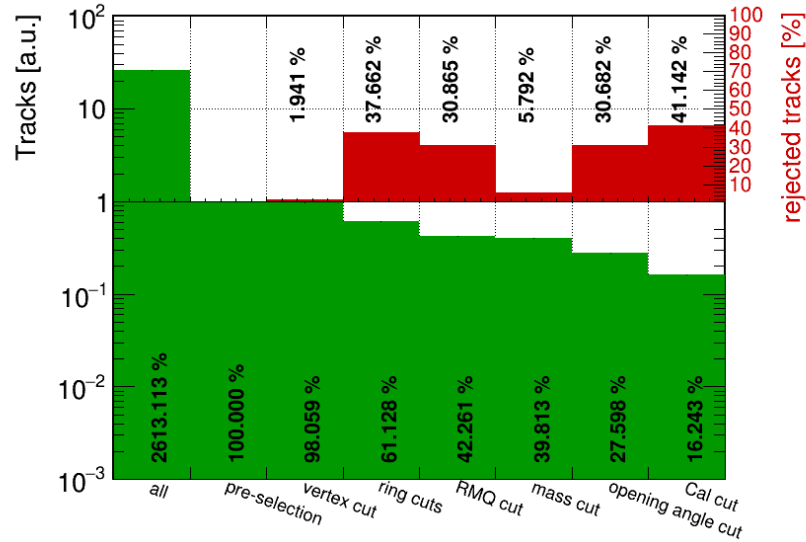


Figure 4.33: The effect of the individual lepton selection criteria on the track sample is shown. Green data denotes the amount of tracks that pass each selection step in relation to the sample after the pre-selection. In red, the amount of tracks rejected by each cut in relation to the sample in the preceding step is shown.

of all tracks pass the quality requirements. Towards high momenta and especially close to the nominal pion pole mass only a small fraction of all reconstructed tracks is accepted for the analysis.

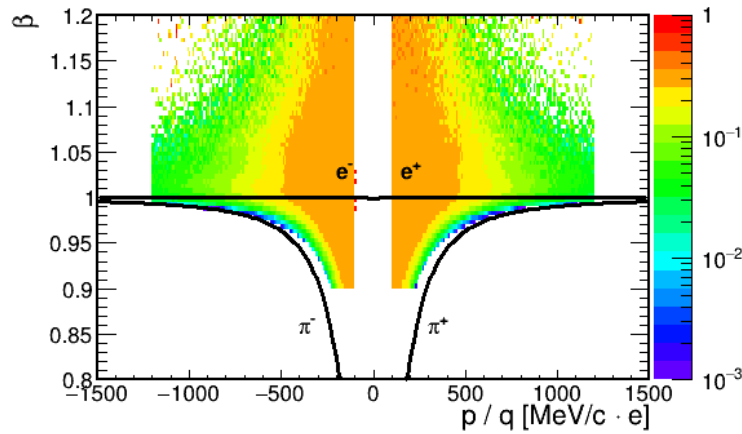


Figure 4.34: Impact of all selection cuts on the track sample as a function of $q \cdot p$ and β relative to the initial sample after the pre-selection.

4.6 POSSIBLE IMPROVEMENTS IN CONVERSION RECOGNITION

In this work, conversion (close by rings) is identified based on the amount of converted Cherenkov photons detected around a fitted ring centre. A promis-

ing upgrade of this method based on the recognition of double hits (2+ Cherenkov photons) on PMT pixels is discussed and tested in this chapter. It might be of relevance in future data analysis especially when it comes to experiments that have to deal with even more conversion background such as the currently constructed CBM experiment [61], [62], [154]. The basic concept is that the signal obtained from a double hit on a PMT pixel should have about twice the strength of a single hit. A direct distinction would be possible if this strength would be measured, however, the only information available in HADES (and the future CBM experiment as well) is the ToT value of the signal which differs slightly only when it comes to single and double hits. Nevertheless it can be pointed out that even based on ToT values only, at least slight gains in conversion recognition can be achieved. The possibility of double photon hits can be easily calculated based on a few assumptions:

- A typical ring has a radius of about 22 mm (compare fig. 4.10), which equals about one third of the side length of a PMT. The area A possibly covered by Cherenkov photons forming the ring with a width of $r_2 - r_1$ therefore calculates to

$$A = \int_{r_1}^{r_2} \int_0^{2\pi} r dr d\phi = \pi (r_2^2 - r_1^2) \quad (4.8)$$

- The position resolution of a Cherenkov photon is assumed to be the size of one pixel and therefore $r_2 - r_1 = 6.25 \text{ mm}$ and $r_2 = 22 + 3.125 \text{ mm}$, $r_1 = 22 - 3.125 \text{ mm}$ resulting in a ring area possibly covered with Cherenkov photons of

$$\pi (r_2^2 - r_1^2) = 864 \text{ mm}^2 \quad (4.9)$$

which has to be compared to the size of a PMT with about $A_{PMT} = 2500 \text{ mm}^2$ (about a third). However it has to be taken into account, that this area is not perfectly covered by complete pixels but due to the assumed position resolution and the differences of ring and pixel geometry by only half-pixels. The ring specific sensitive area in this model is therefore assumed to be $N_{pixel} = 2 \cdot \frac{1}{3} \cdot N_{pixel/PMT} \sim 42$ (about two thirds of the PMTs total pixels) which compares rather well to the studies of event displays such as shown in fig. 3.9.

- On average an isolated ring consists of about $N_{fired_1} = 16$ fired pixels (compare fig. 4.28) and structures of close-by double rings consist of about $N_{fired_2} = 26$ fired pixels.

Using this as input one can calculate the mean amount of double hits $\langle n \rangle$ per ring. Therefore, one at first needs to derive the probability P_n for $n = 1, n = 2, n = 3, \dots$ double hits. As a starting point, the probability for zero double hits P_0 randomly distributing $k = 16$ Cals on $N = 42$ pixels is derived to

$$P_0(N = 42, k = 16) = \frac{42!}{42^{16} \cdot (42 - 16)!} = 0.037 \quad (4.10)$$

For explanation purpose it is now assumed, that the Cals are randomly distributed one after another on all available pixels. In case of exactly one double hit, one has to take into account, that it may appear in each step after the first one (the first Cal that is put can not be a double hit), resulting in an additional factor of $1 + 2 + 3 + \dots + 15 = \sum_{i=0}^{15} i$ (the second Cal has one possibility to produce a double hit, the 16th one has 15). Therefore it reads

$$P_1(N = 42, k = 16) = \frac{42!}{42^{16} \cdot (42 - 15)!} \cdot \sum_{i=1}^{i=15} i = 0.165 \quad (4.11)$$

In an analogue way, one has to take into account, that in case of exactly two double hits, those may appear in any combination of steps (but not in the same) leading to a double summation in the corresponding formula that reads

$$P_2(N = 42, k = 16) = \frac{42!}{42^{16} \cdot (42 - 14)!} \cdot \sum_{i=1}^{i=14} i \sum_{j=1}^{j=i-1} j = 0.246 \quad (4.12)$$

Accordingly the probabilities for higher amount of double hits (or multiple hits, it might also happen that three or more Cherenkov photons hit the same pixel) derive to $P_3(N = 42, k = 16) = 0.223$, $P_4(N = 42, k = 16) = 0.118$, etc. For the mean amount of double hits per ring it follows

$$\langle n \rangle = \sum_{n=1}^{n=15} P_n \cdot n \sim 3 \quad (4.13)$$

In other words it means, that the first Gaussian in fig. 4.28 is shifted by $\Delta Cal_1 = 3$ to lower values due to multiple hits on pixels. A calculation in accordance to the presented one with $k = 26$ reveals a shift of about $\Delta Cal_2 = 9$ for close by double rings. Together, this leads to a relative shift of both signals of 6 Cals, which exactly explains why $\mu_2 = 2 \cdot \mu_1$ does not hold, but $2\mu_1 - \mu_2 = 6$ is observed in fig. 4.28. This observation implies, that a high efficient detection of multiple hits on PMT pixels would further improve the detection of conversion signals in the RICH detector. In experiment, instead of measuring the number of Cherenkov photons hitting one pixel, only the integrated signal strength which is proportional to the ToT is measured. However, the ToT only shows a weak dependence on the number of photons. In order to test whether nevertheless the ToT carries the double hit information, the same analysis as in chapter 4.4.2 is carried out, here adding ToT values instead of counting Cals. The resulting spectrum is shown in fig. 4.35 and described by the known double Gaussian shape. For comparison purpose, the absolute values are divided by a factor of four to fit to the same range as using Cals only. The fitted Cal distributions extracted in fig. 4.28 are shown as reference. The separation between both Gaussians is slightly improved due to the mild double hit influence in the ToT values. With a

stronger correlation of ToT and double hits the separation could be further improved, however the currently used MAPMTs and electronics can not provide more. As ToT values are anyway not included in simulations so far, they are not used in the analysis as the efficiency correction would be biased. Including ToT values in simulation might introduce new systematic effects, which does not justify the possible small gains.

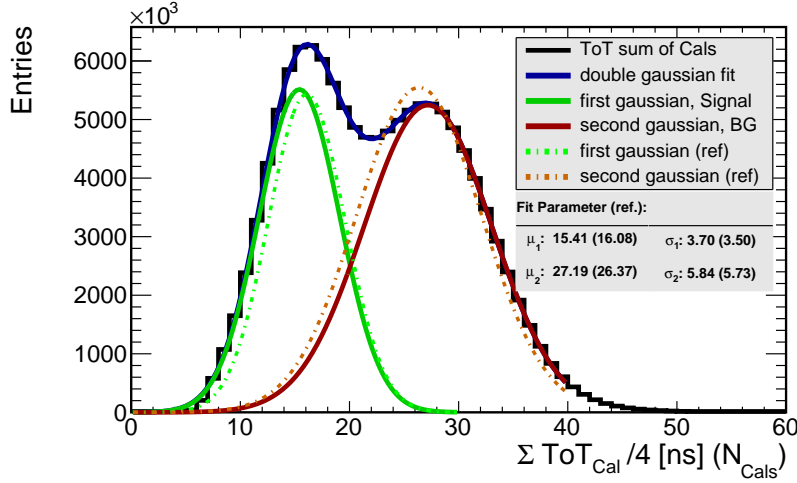


Figure 4.35: The summed ToT values of all Cals inside a $2r$ circle around the center of RICH rings are summed (black data). The spectrum is described by a double Gaussian fit (blue curve). For a comparison with reference data (taken from fig. 4.28, dashed lines), the ToT values are divided by four. See *text* for details.

4.7 ELECTRON-PAIR FORMATION

All selected electrons are combined with positrons to pairs. As one does not know, which electron and positron originate from the same initial source, one has to pair each electron with each positron reconstructed in the same event. This procedure naturally leads to a significant combinatorial background, namely electrons and positrons that do not stem from the same source. Here, the selection effort described in the previous chapters becomes crucial, as the amount of background pairs scales quadratically with the amount of true pairs. Physics observables of the pairs are calculated from the reconstructed Lorentz Vectors of the single particles. The invariant mass is defined by the 4-momenta of the single leptons in the Minkowski-metric and calculated based on their reconstructed momenta and the known mass of electrons to

$$M_{ee} = \sqrt{(P_1 + P_2)^2} = \sqrt{2m_e^2 + 2p_1 p_2 (1 - \cos \alpha)}. \quad (4.14)$$

The centrality integrated invariant mass spectrum of all formed pairs is shown in fig. 4.36. Due to the conversion rejection cuts applied on the track

$M_{ee} [MeV/c^2]$	< 200	200 - 700	700 - 800	> 800
N_{pairs}	$1.305 \cdot 10^6$	$2.631 \cdot 10^5$	858	321
$\langle N_{pairs} \rangle$ /event	$3.17 \cdot 10^{-4}$	$6.396 \cdot 10^{-5}$	$2.086 \cdot 10^{-7}$	$7.803 \cdot 10^{-8}$

Table 4.2: Number of reconstructed e^+e^- pairs in bins of M_{ee} and average amount of reconstructed pairs per event.

sample, the spectrum includes pairs with opening angles $\alpha > 9^\circ$ only. The total amount of reconstructed pairs in specific M_{ee} bins is listed in table 4.2. Pairs are reconstructed up to an invariant mass of $M_{ee} < 1200 MeV/c^2$. For small invariant masses ($M_{ee} < 140 MeV/c^2$) the spectrum is dominated by e^+e^- pairs produced in π^0 -Dalitz decays and followed by a continuous decrease. At around the pole mass of the ω -meson at $m_\omega = 782.66 MeV$, a slight enhancement in the data is seen. However, the enhancement is of broad nature compared to the ω -vacuum width of about $\Gamma_\omega^{vac} = 8.49 MeV/c$. A detailed discussion and analysis focusing on the ω -meson is presented in chapter 6.6. Following an exponential downfall in the intermediate mass region an enhancement in only one bin at the pole mass of the ϕ -meson ($m_\phi = 1019.46 MeV$) is observed. With reconstructed pairs in the order of $N_{pair} \sim 10$ at these high invariant masses an analysis of the ϕ -meson regarding its leptonic decay channel can not be performed. A decomposition of the reconstructed spectrum in all of its hadronic sources is discussed in chapter 6.2.

In order to study the stability of data taking and therefore the reliability of the subsequent efficiency corrections, fig. 4.37 shows the amount of reconstructed pairs in the four invariant mass bins of table 4.2 per collision for each day of data taking together with the fitted mean values. The amount

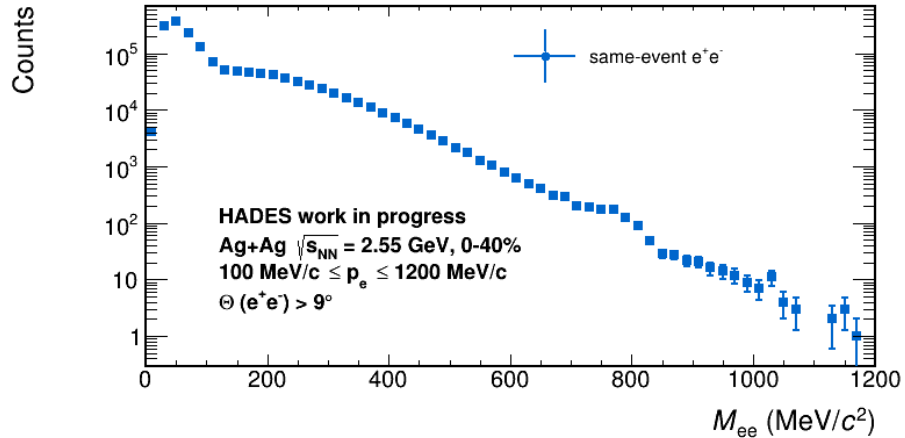


Figure 4.36: Full statistics invariant mass spectrum of same-event e^+e^- pairs after all track selection cuts in bins of $20 MeV/c^2$. The errors are statistical only.

of registered pairs is constant in a good approximation from day 62 on. The largest deviations from the mean value are in the order of 5% which is taken into account in the estimation of systematic errors. The data measured on day 58 is rejected from the analysis as the electron efficiency appears to be an order of magnitude smaller than in the following days. However, the fraction of statistics collected on this day is negligibly small as it was mainly intended to carefully test the detector and accelerator setup. During the days 59-61 no data has been taken.

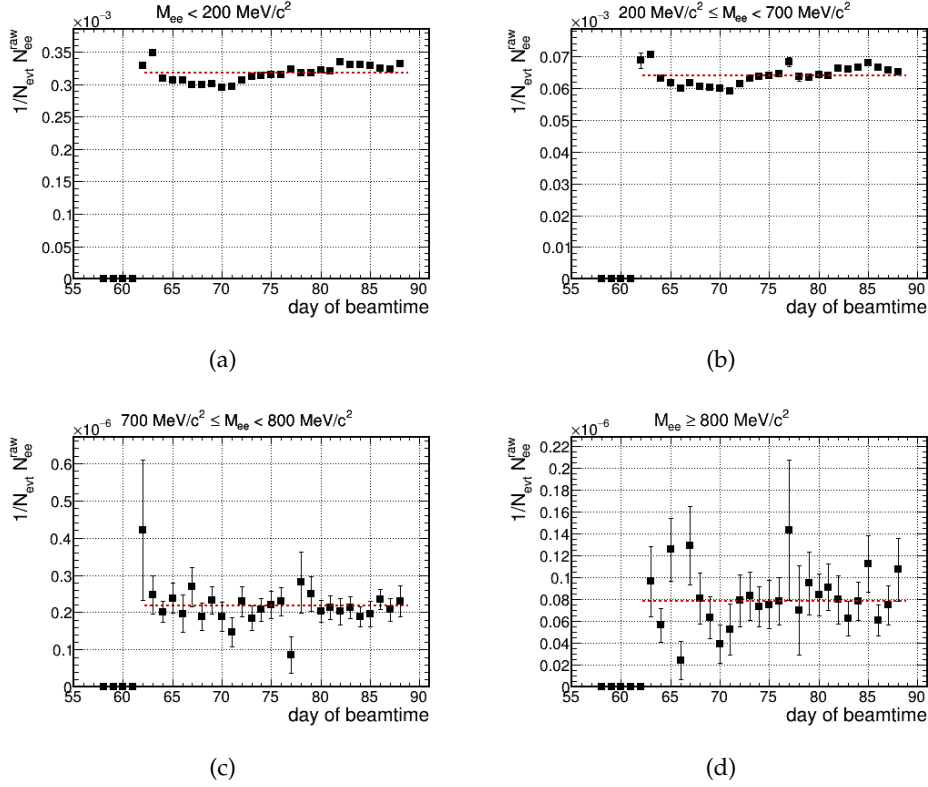


Figure 4.37: Reconstructed dielectron pairs in specific bins of the invariant mass per event and day of data taking. Mean values are indicated by horizontal lines.

Another crucial test of the detector performance is the homogeneity of the reconstructed electrons and dielectron pairs. It is quantitatively estimated in an $\Theta - \Phi$ map of single leptons forming pairs in the previously introduced bins of invariant mass in fig. 4.38. The Φ coverage appears to be rather homogeneous within the detector acceptance (gaps between the MDC sectors are visible equally distanced by $\Delta\Phi = 60^\circ$) thus indicating efficiencies of about the same level in all HADES sectors. Absolute numbers in the specific sectors are listed in table 4.3. Assuming an homogeneous electron production in the azimuth angle Φ , these numbers can directly be compared and translated into a relative efficiency between the different sectors as none of the electron selection criteria depend on Φ . Regarding the azimuth angle Θ more particles are produced and thus reconstructed at small values with

HADES being a fixed target experiment resulting in a forward boost of the whole collision system. At small values of Θ low momentum positrons (and thus low invariant mass pairs) can easily be bent out of acceptance of some sub-detectors leading to a decrease in reconstructed electrons. With higher electron momentum (higher invariant mass bins) the systematics in Θ vanish as the bending effects in the magnetic field are weaker and the large pair opening angles result in a decoupling of the dielectron emission angles and the single lepton angles.

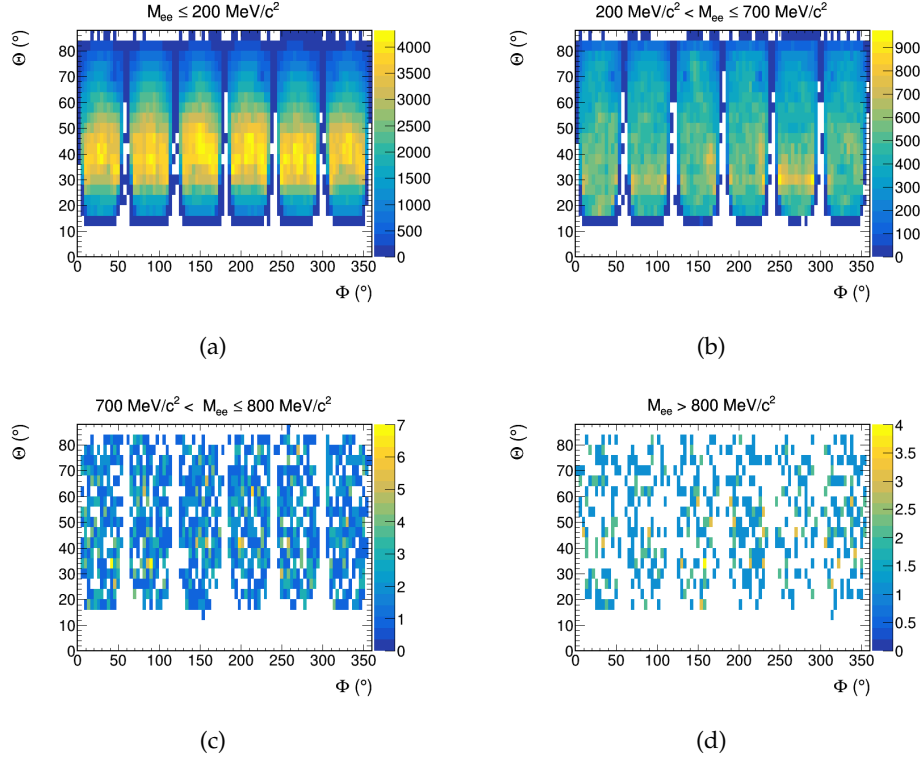


Figure 4.38: $\Theta - \Phi$ map of single leptons forming pairs in four invariant mass bins indicated on top. For sector integrated absolute values see tab. 4.3.

$M_{ee} [MeV/c^2]$	$< 200 [10^3]$	$200 - 700 [10^3]$	$700 - 800$	> 800
Sector 1	427	88.5	303	104
Sector 2	456	89.8	295	100
Sector 3	463	89.4	278	113
Sector 4	456	89.8	294	118
Sector 5	440	88.0	383	83
Sector 6	417	83.4	265	124

Table 4.3: Reconstructed electrons per sector in bins of the pair invariant mass. The numbers correspond to fig. 4.38, integrated in $\Delta\Phi = 60^\circ$ slices.

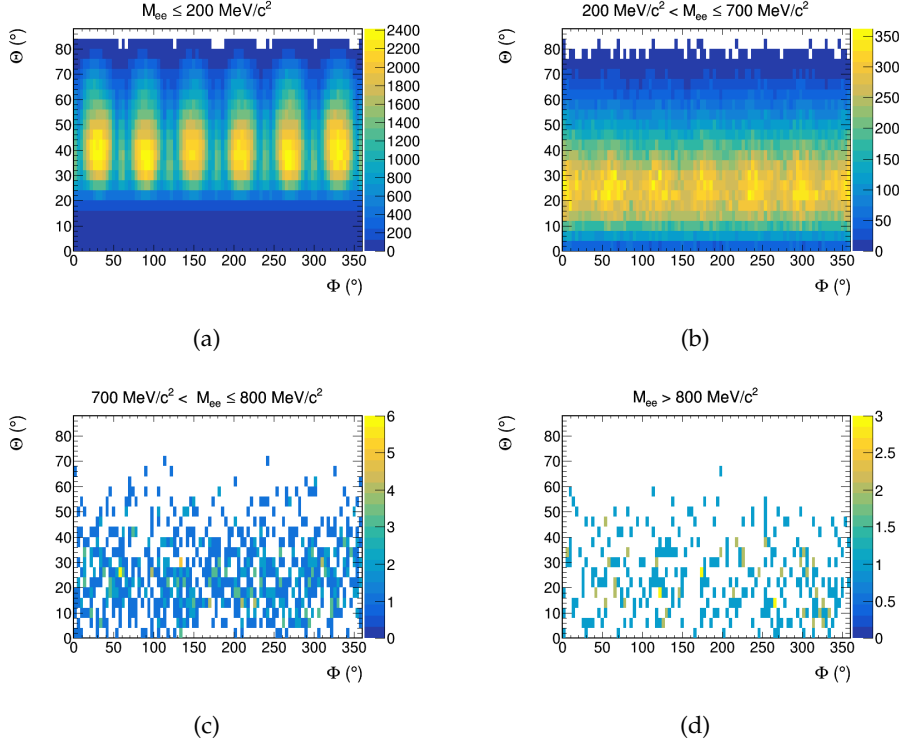


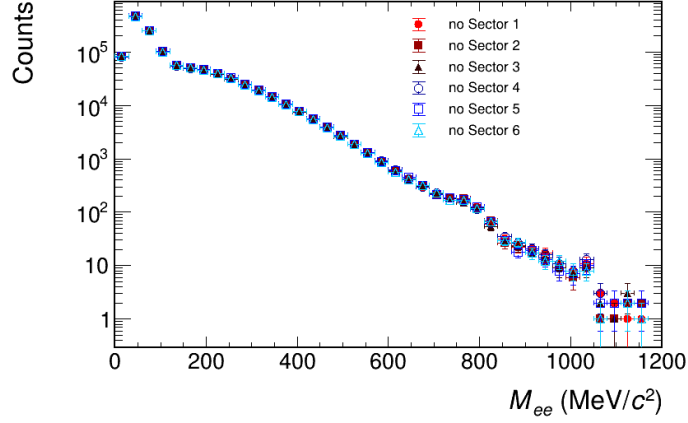
Figure 4.39: $\Theta - \Phi$ map of reconstructed dielectrons in specific invariant mass bins. For sector integrated absolute values see tab. 4.3.

$M_{ee} [MeV/c^2]$	$< 200 [10^3]$	$200 - 700 [10^3]$	$700 - 800$	> 800
Sector 1	228	45.0	142	49
Sector 2	221	43.8	129	50
Sector 3	211	43.1	146	56
Sector 4	213	43.6	146	47
Sector 5	226	44.4	155	57
Sector 6	230	44.6	141	62

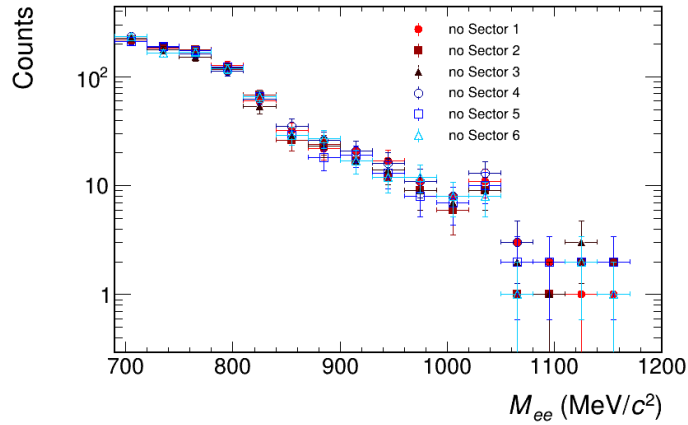
Table 4.4: Reconstructed dielectrons per sector in bins of the pair invariant mass. The numbers correspond to fig. 4.39, integrated in $\Delta\Phi = 60^\circ$ slices.

The $\Theta - \Phi$ coverage of reconstructed pairs is shown in the introduced bins of invariant mass in fig. 4.39, with the according absolute numbers listed sector wise in table 4.4. Small invariant mass pairs are characterized by small opening angles. Therefore the distinct HADES sectors are well visible in the smallest invariant mass bin with peak like structures in the centres. The polar angle Θ is limited by the detector acceptance at small values as the acceptance gap of $\Delta\Theta \sim 30^\circ$ can hardly be overcome by small opening angle pairs. With increasing invariant mass the sector borders smear out and the small polar angle region gets populated. Here, pairs can not be

reconstructed at high polar angles, as one electron would have to be out of acceptance due to the large opening angles of high invariant mass pairs. In the azimuth angle Φ the detector coverage is observed to be homogeneous without any clustering at specific positions.



(a) Full invariant mass range.



(b) Zoom-in into the $M_{ee} > 700 \text{ MeV}/c^2$ region.

Figure 4.40: Dielectron invariant mass spectra excluding in each run a specific HADES sectors from the analysis. Note the changed binning to $\Delta M_{ee} = 30 \text{ MeV}/c^2$ compared to $\Delta M_{ee} = 20 \text{ MeV}/c^2$ used previously in fig. 4.36.

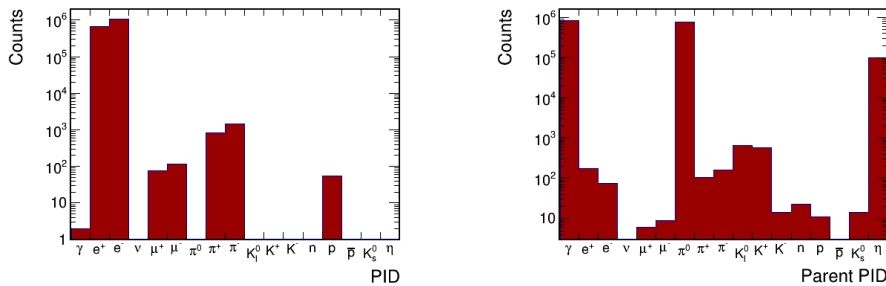
The observation of an overall homogeneously covered detector is quantitatively confirmed in even smaller bins of invariant mass analyzing the data sample while in each step excluding a specific sector in terms of single lepton identification. Fig. 4.40a shows the corresponding invariant mass spectra, that perfectly match each other up to medium invariant masses. Statistical fluctuations naturally lead to slight deviations at high invariant masses. A zoom-in into this region is shown in fig. 4.40b. Especially the high agreement in all cases in the region of the ω -meson pole mass is notable.

4.8 BACKGROUND ESTIMATION USING URQMD SIMULATION

Simulations offer the unique possibility to study the exact composition of the track sample after the electron selection and the resulting invariant mass spectrum. For this purpose, full UrQMD simulations without additionally embedded PLUTO signal are propagated through the HADES geometry utilizing HGeant are used, compare chapter 2.7. The particle ID of reconstructed tracks after all selection steps is shown in 4.41a and clearly dominated by e^\pm . The pion contamination as main background source is suppressed by three orders of magnitude indicating a momentum integrated purity close to $P = 99.9\%$ corresponding well to the results obtained during the track selection applying the RICH-rotation technique, compare sec. 4.3.4. As second largest background source, myons are suppressed by an additional order of magnitude compared to pions, whereas the μ/π ratio roughly corresponds to the fraction of pions decaying before reaching the detector. Protons also account for a minor fraction in the overall very small background.

Fig. 4.41b shows the parent PIDs of the reconstructed electrons. It basically mirrors the sources of the reconstructed electrons, namely photons that undergo conversion, π^0 and η mesons. Besides these prominent electron production sources, also the rare leptonic decays of long-living myons, charged pions and kaons contribute a little. Vector mesons as electron sources of higher invariant mass are not included in UrQMD due to their strongly suppressed branching fraction. Other particle may produce electrons in scattering reactions after the primary collision, e.g. protons.

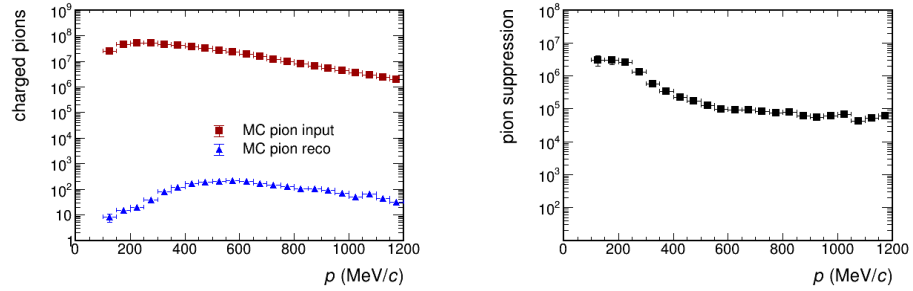
The rejection of pions within the electron selection is further quantified introducing the pion suppression factor (fig. 4.42b), which is calculated as the ratio of initial pions to those present in the track sample after applying the selection criteria (fig. 4.42a). At small momenta the pion suppression factor reaches values up to $\pi_{sup} = 3 \cdot 10^6$ and drops slightly below $\pi_{sup} =$



(a) PID of all reconstructed tracks passing the selection criteria. (b) PID of the parent particles of all reconstructed tracks passing the selection criteria.

Figure 4.41: PID of reconstructed tracks and corresponding parent-PID in UrQMD simulation. Primary particles have a parent-PID of -1 and are not included.

10^5 towards high momenta. The high pion suppression factor is a signature of the high performance of the HADES RICH detector serving as the key part for pion rejection in this analysis (besides soft time-of-flight criteria). It does not only exceed the aimed pion suppression factor of $\pi_{sup} = 100 - 500$ of the planned RICH detector at the CBM experiment by several orders of magnitude, but even surpasses the targeted RICH-TRD combined pion suppression factor in CBM of up to $\pi_{sup} = 10^4$ [155].



(a) Momentum distribution of pions produced and reconstructed after applying the electron selection criteria in UrQMD simulations. (b) Momentum dependent pion suppression factor.

Figure 4.42: Momentum dependent pion suppression in UrQMD simulation applying the lepton selection criteria. It is calculated as the ratio of the reconstructed pion spectrum to the pion input distribution. Errors are of statistical nature.

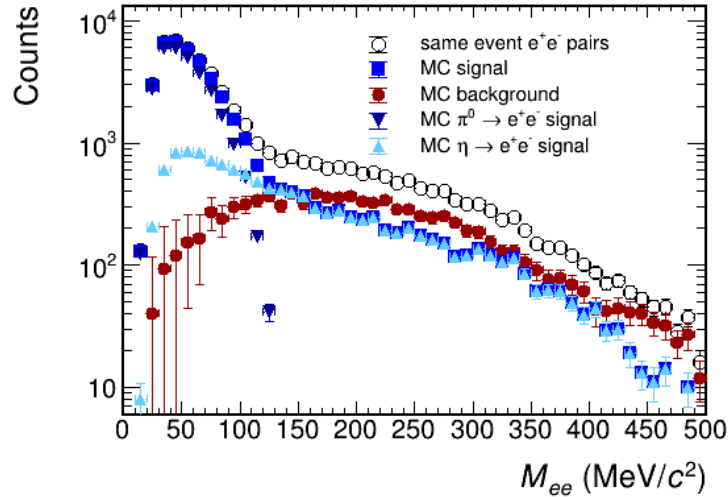


Figure 4.43: e^+e^- invariant mass spectrum in UrQMD simulation. The spectrum is decomposed into signal (and the corresponding sources) and background based on MC-true information.

Fig. 4.43 shows the invariant mass spectrum of electron pairs in UrQMD simulation decomposed into the pure signal and its sources and the back-

ground based on MC-true information. At low invariant masses, the spectrum is dominated by the $\pi^0 \rightarrow \gamma e^+ e^-$ Dalitz decay with only minor background contribution. Beyond the π^0 pole mass, the signal is made up from the $\eta \rightarrow \gamma e^+ e^-$ Dalitz decay only as other sources (having less impact in the low invariant mass regime anyway) are missing in UrQMD. Here, the background slightly exceeds the signal. A decomposition of the background is shown in fig. 4.44. Due to the high pion suppression, pairs that include at least one pion only make up a minor fraction of the background and are mainly located at small invariant masses. At around the ω pole mass only very few of such pairs are registered that are statistically distributed. Reconstructed photons are also a neglectable background source indicating that the opening angle cut is highly effective. On the other hand, pairs including one conversion electron only dominate the background. In such cases, the partner electron could not be detected (e.g. in case of absorption) and therefore the underlying conversion process was not identified. Despite being the dominant background source this contribution has been significantly reduced applying the conversion-rejection-cut based on detected photons in the RICH (see chapter 4.4.2). Possible further improvements have been discussed in chapter 4.6 clearly pointing out the potential of further suppressing combinatorial background from conversion electrons. The remaining background is made up from random combinations of signal electrons which obviously can not be reduced.

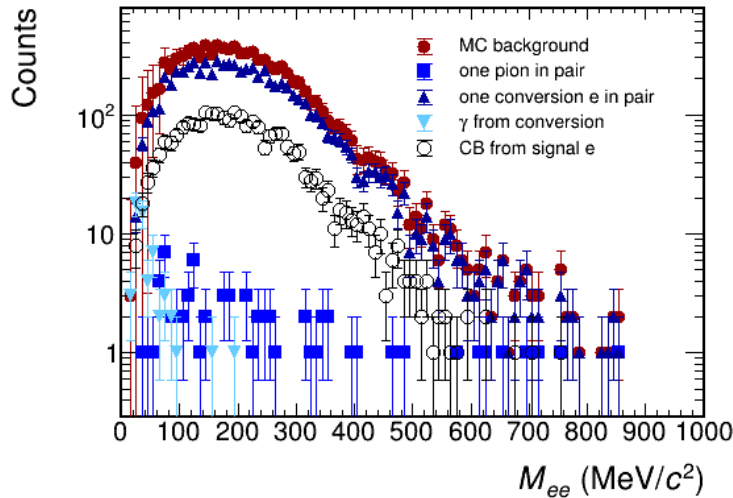


Figure 4.44: Decomposition of the UrQMD MC-true background in its different sources.

4.9 EFFICIENCY AND ACCEPTANCE CORRECTION

Applying selection cuts on the track sample, not only non-electrons are rejected, but also electrons themselves do not fulfill all criteria. This is caused by deviations from the theoretical $\delta(O_{theory} - O_{exp})$ -functions in all measured

observables O towards statistically broadened distributions. The width of these distributions depends on the detector resolution. HADES furthermore does not cover the full 4π hemisphere but is restricted to the forward direction only with an additional gap at small polar angles where the beam pipe is located., resulting in a total polar angle coverage of $16^\circ < \Theta < 83^\circ$.

To obtain physics results it is necessary to correct for these signal losses. Therefore correction matrices on the basis of single electron tracks are calculated. A differentiation between simulation and experiment is necessary, as efficiencies in simulation do not depend on the track density which is the case for real data. Efficiency correction matrices for simulated data are therefore derived from electron tracks embedded in UrQMD simulations whereas embedding into experimental data (day 86 of the beam time) is used for efficiency extraction in real data. The correction matrices are defined as the ratio of reconstructed electron spectra divided by the corresponding input spectra, both within the HADES acceptance which is given by the MDC acceptance where a crossing of at least four of the six chambers in each layer is required. The such derived correction then is applied on the basis of single electrons in the analysis procedure. Different approaches of the efficiency correction are exemplary tested in simulation of the $\eta \rightarrow \gamma e^+ e^-$ decay, compare fig. 4.45, with the goal of reproducing the initial input invariant mass distribution (red data points). For a proper description of the reconstruction efficiency ϵ , the correction has to be derived as

$$\epsilon(p_{in}, \Theta_{in}, \Phi_{in}) = \frac{N_{reco,ee}(p_{in}, \Theta_{in}, \Phi_{in})}{N_{in,ee}(p_{in}, \Theta_{in}, \Phi_{in})} \Big|_{inAcc} \quad (4.15)$$

using the input kinematic properties, not the reconstructed momenta, of the single leptons also in the reconstruction in a differential formulation of

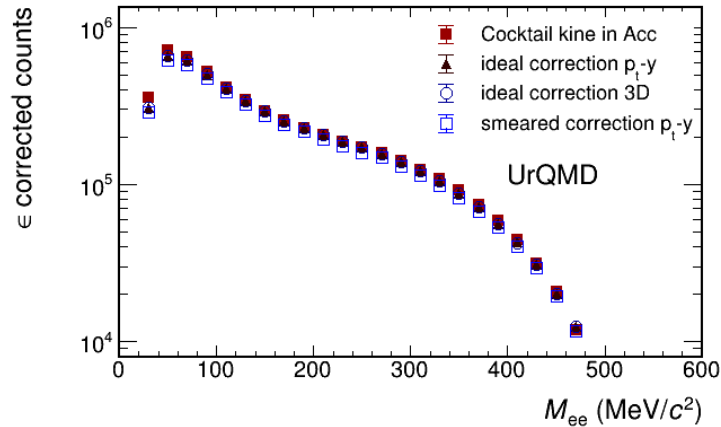


Figure 4.45: Different approaches of efficiency correction are tested in simulation of the $\eta \rightarrow \gamma e^+ e^-$ decay channel. Efficiency corrected spectra are compared to the initial input invariant mass distribution within the HADES acceptance. See text for details.

the efficiency (referred to as *ideal correction* in fig. 4.45). Minor differences especially at small invariant masses are discussed when addressing systematic errors in chapter 4.11. Using the reconstructed kinematic properties (*smeared correction*) in the derivation of the correction matrices leads to a significant under-correction of the data of approximately 10 – 15%. The result shows only a minor dependence on the set of variables used for the correction procedure, here performed for the ideal correction method in phase space (p_t, y) and 3-dimensional momentum space (p, Θ, Φ) . The usage of corrections in two different sets of variables allows for an estimation of the systematical error introduced to the analysis applying the efficiency correction.

The calculated efficiency matrices are shown in fig. 4.46 (electrons) and fig. 4.47 (positrons) for electrons embedded into UrQMD simulations. Instead of the used three dimensional matrices in p, Θ, Φ , two dimensional projections in p, Θ and p, Φ are shown in (a) and (b) of both figures for a better visualisation. Subfigure (c) shows the electron (positron) efficiency as a function of p_t, y . From this representation of the efficiency, the HADES acceptance in this analysis can be read of. For electrons it ranges from $16^\circ \leq \Theta \leq 83^\circ$ in the polar angle Θ and includes the full single lepton momentum range of $100 \text{ MeV}/c \leq p_e \leq 1200 \text{ MeV}/c$. At high polar angles and small momenta the efficiency significantly drops as the magnetic field begins to bend electrons outside the acceptance. However, this effect can be corrected for as long as the efficiency does not reach zero. The same applies for the azimuth angle Φ . Choosing a sufficiently large binning, acceptance gaps in between of the six HADES sectors can be overcome assuming a homogeneous particle production in Φ .

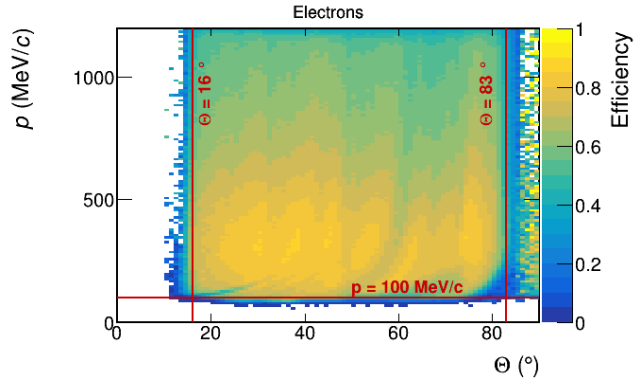
For positrons an acceptance gap is observed at low momenta and small polar angles. This gap originates from the bending of positrons in the beam pipe region of $\Theta < 16^\circ$ where they can not be detected. The borderline to the acceptance gap is fitted by an exponential and excluded from the analysis, thus requiring for positrons the additional condition of

$$p > e^{-0.135 \cdot \Theta + 8.3} + 100 \text{ MeV}/c \quad (4.16)$$

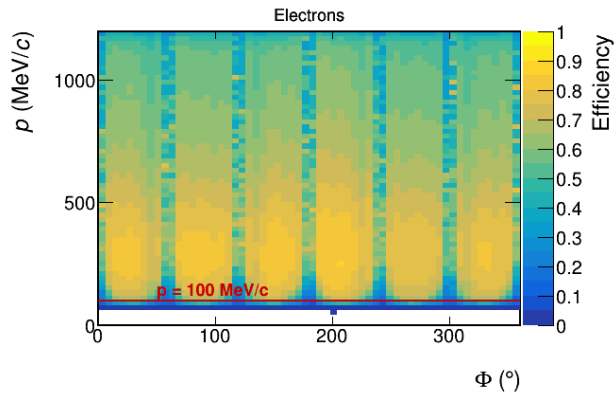
with fitted parameters in the exponential and a convergence towards $p_0 = 100 \text{ MeV}/c$ in the limit of $\Theta \rightarrow \infty$. In the p_t, y coordinates this acceptance gap is also visible (here at large rapidity and small transverse momenta) where the same separation function f is introduced reading in the transformed variables

$$p_t > \sin(2 \arctan(e^y)) \cdot (e^{-0.135 \cdot 2 \arctan(e^y) + 8.3} + 100) \text{ MeV}/c. \quad (4.17)$$

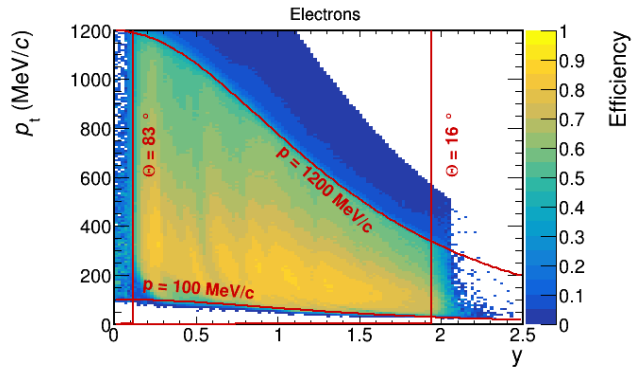
The electron efficiency extracted for the correction of real data, obtained from embedding electron tracks into experimental data is shown in different centrality classes and thus track densities in fig. 4.48 as a function of track momentum. A momentum independent drop in efficiency is observed with



(a)

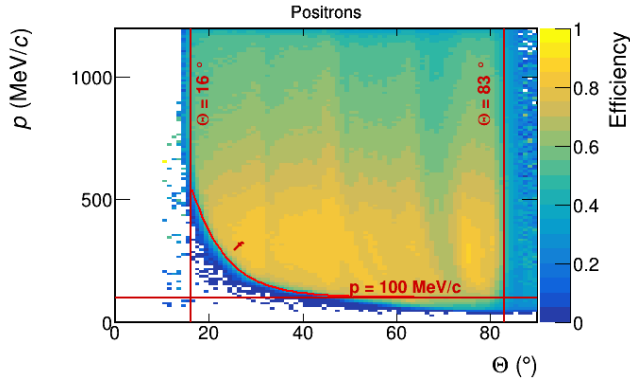


(b)

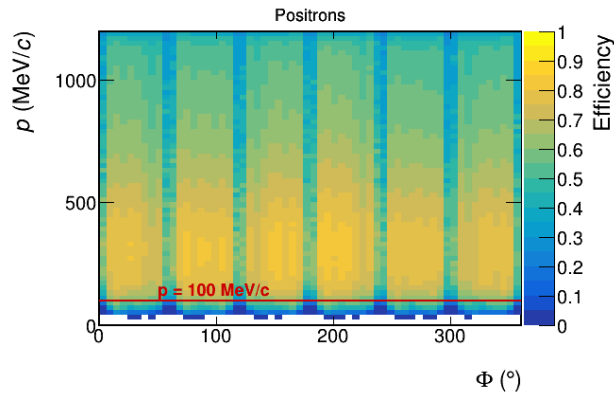


(c)

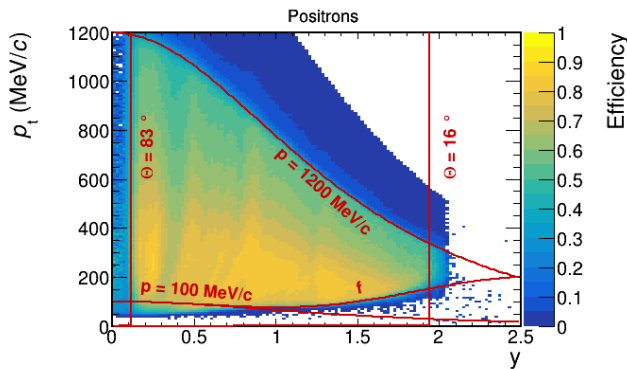
Figure 4.46: Electron efficiency extracted from electron simulation embedded into UrQMD simulations in p, Θ (a), p, Φ (b) and p_t, y (c). This analysis is restricted to single lepton momenta $100 \text{ MeV}/c \leq p_e \leq 1200 \text{ MeV}/c$ as indicated in the figures. The HADES acceptance for electrons can be read from the figures to be within $16^{\circ} \leq \Theta \leq 83^{\circ}$ shown by red lines. Assuming an homogeneous particle production in Φ , acceptance gaps between the HADES sectors can be corrected for choosing a sufficiently large binning in the azimuthal angle.



(a)



(b)



(c)

Figure 4.47: Positron efficiency extracted from positron simulations embedded into UrQMD simulations in p, Θ (a), p, Φ (b) and p_t, y (c). This analysis is restricted to single lepton momenta $100 \text{ MeV}/c \leq p_e \leq 1200 \text{ MeV}/c$ as indicated in the figures. An acceptance gap at small polar angles and momenta is fitted (curve f) and excluded from the analysis. See text for details.

increasing track density (centrality). The mean value of all centrality classes compares well to the electron efficiency extracted from embedding electrons into UrQMD simulation. However, in the more central collisions the dielec-

tron yield is higher compared to more peripheral collisions. Therefore the dominant impact of the lowered efficiency in the most central collisions leads to an overall lowered efficiency embedding electrons into real data compared to embedding into UrQMD simulation. The efficiency correction on real data is performed in the same set of coordinates as for simulation data.

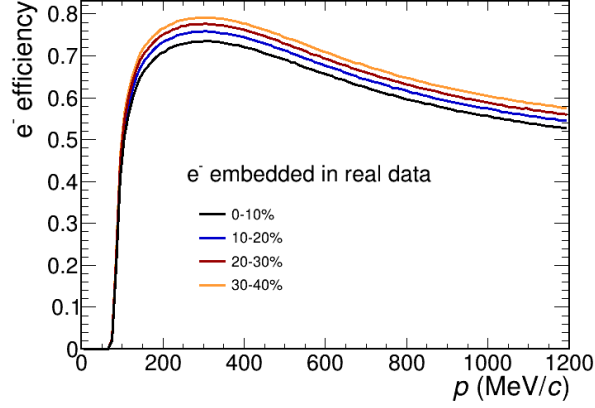


Figure 4.48: Centrality dependence of the electron efficiency as a function of momentum extracted from electron tracks embedded into real data.

Summarizing, the acceptance of this analysis is defined based on single leptons. Those dielectrons with e^+, e^- both fulfilling $16^\circ \leq \Theta \leq 83^\circ$, $100 \text{ MeV}/c \leq p_e \leq 1200 \text{ MeV}/c$ and in case of positrons additionally eq. 4.16 are used for the further analysis including the derived efficiency correction.

Even within the HADES acceptance not all particles can possibly be reconstructed due to minor acceptance gaps, e.g. in between the six sectors or at the borders of single detector cells. However, an acceptance correction within this region is well possible without introducing any model dependence as a sufficiently large binning in the correction matrices allows for an interpolation from neighboured detector regions. It is then defined as

$$a(p_{in}, \Theta_{in}, \Phi_{in}) = \frac{N_{in,ee}(p_{in}, \Theta_{in}, \Phi_{in})|_{inAcc}}{N_{in,ee}(p_{in}, \Theta_{in}, \Phi_{in})|_{initial}} \quad (4.18)$$

with the product of the efficiency and acceptance

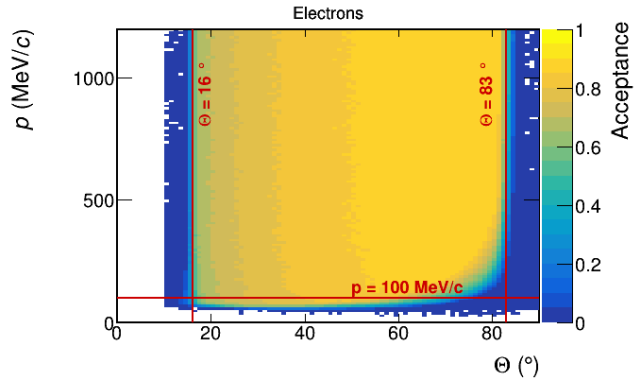
$$a(p_{in}, \Theta_{in}, \Phi_{in}) \times \epsilon(p_{in}, \Theta_{in}, \Phi_{in}) = \frac{N_{reco,ee}(p_{in}, \Theta_{in}, \Phi_{in})|_{inAcc}}{N_{in,ee}(p_{in}, \Theta_{in}, \Phi_{in})|_{initial}} \quad (4.19)$$

being obviously independent of the exact definition of efficiency (e.g. whether possible hits in four or five of the six MDC chambers are required or even the requirement of hits in other detectors) and only determined by the detector geometry and the choice of cut values on the track sample. The acceptance

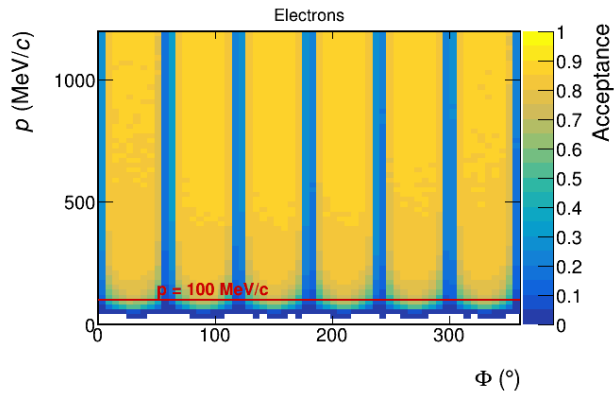
correction matrices for the kinematic region of this analysis are shown in fig. 4.49 for electrons and fig. 4.50 for positrons, each in the previously introduced sets of variables. Only minor differences for electrons and positrons are visible besides the acceptance gap in the case of positrons at small momenta and polar angles. In general, the acceptance increases with higher polar angles, as the by area fraction of the dead areas in between of the sectors shrinks. Despite momenta of $p_e > 1200 \text{ MeV}/c$ have a high acceptance, their efficiency is drastically reduced as a high level pion rejection becomes impossible and they are therefore rejected from the analysis.

The reconstructed dielectron spectrum first introduced in fig. 4.36 (0 – 40 % in centrality) is shown in fig. 4.51a applying the efficiency correction in both sets of kinematic variables (electrons for efficiency correction derivation are embedded into real data). Both spectra overlay almost perfectly stating that the efficiency correction applied is highly stable and consistent. An inset shows the relative difference normalized to the correction in p_t, y . It is well below $\Delta \text{Corr}_e < 0.5\%$ within the full range of invariant mass. The statistical errors of both spectra are obviously strongly correlated, such that no errors of the relative difference are shown. Anyway, the statistical errors are much larger than the systematic error found to be introduced in the efficiency correction. Applying also the acceptance correction based on single leptons⁵ yields the dielectron spectra shown in fig. 4.51b. Still, the agreement in both sets of kinematic variables is on an extremely high level with differences $\Delta \text{Corr}_{e,a} < 1\%$. In fig. 4.51c a comparison of the dielectron spectrum after each step of correction is shown. The corresponding inset shows the ratio of the efficiency corrected spectrum to raw data, and the ratio of efficiency and acceptance corrected data to efficiency corrected data only, thus the efficiency and acceptance as a function of invariant mass. At small invariant masses the efficiency (inverse correction factor) is almost constant with $\epsilon \sim 0.56$ and starts to lower towards high invariant masses reaching a value of $\epsilon \sim 0.4 M_{ee} = 950 \text{ MeV}/c^2$. These high invariant mass pairs are characterized by high single electron momenta. With increasing single particle momentum, the electron selection criteria have been tightened in the track selection process to ensure a high pion suppression thus leading to a lowered efficiency. The acceptance shows no significant dependence on the invariant mass with a constant value of $a \sim 0.63$.

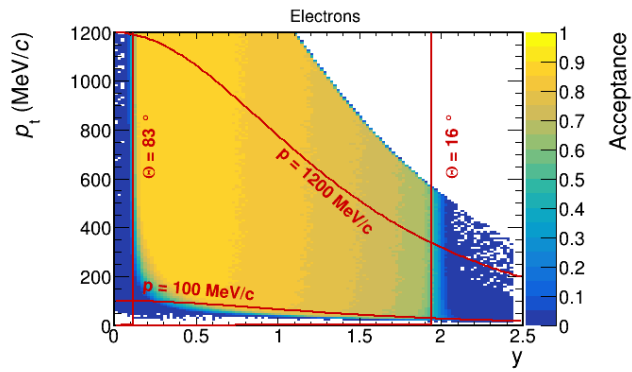
⁵ single leptons emitted in $16^\circ < \Theta < 83^\circ$ with $100 \text{ MeV}/c < p_e < 1.2 \text{ GeV}/c$ and fulfilling the additional cut function for positrons are corrected only



(a)

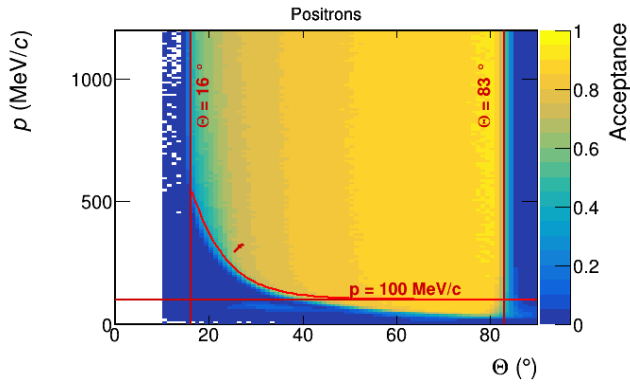


(b)

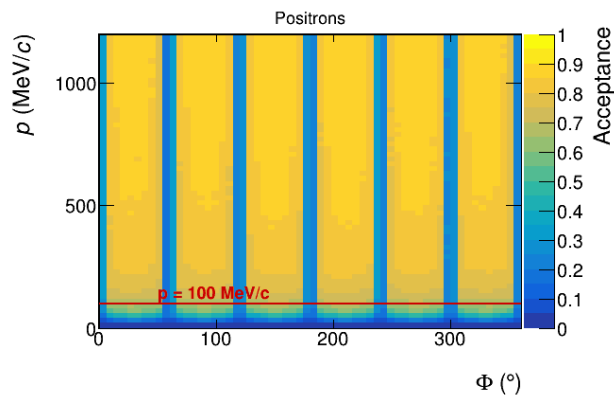


(c)

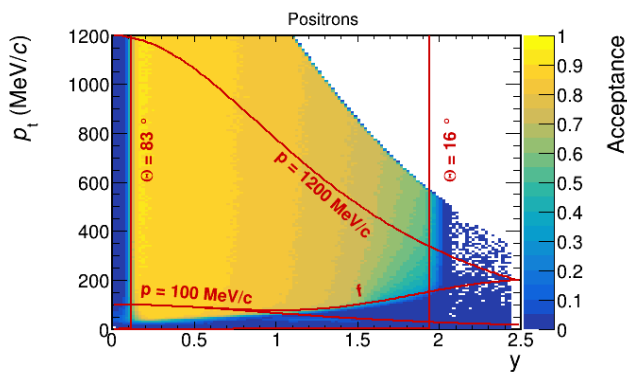
Figure 4.49: Electron acceptance extracted from electron simulation embedded into real data in p, Θ (a), p, Φ (b) and p_t, y (c). The kinematic regions the analysis is restricted to are indicated by red lines.



(a)

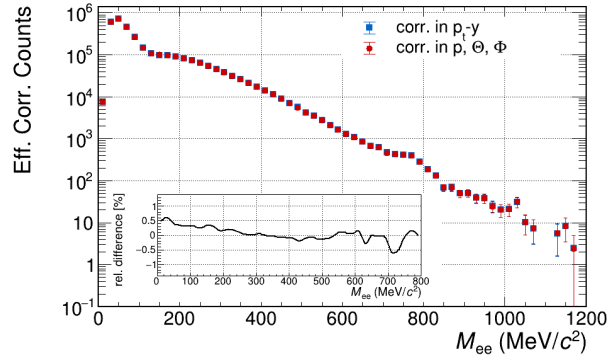


(b)

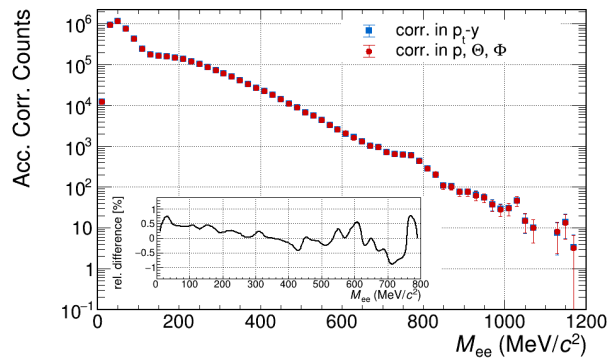


(c)

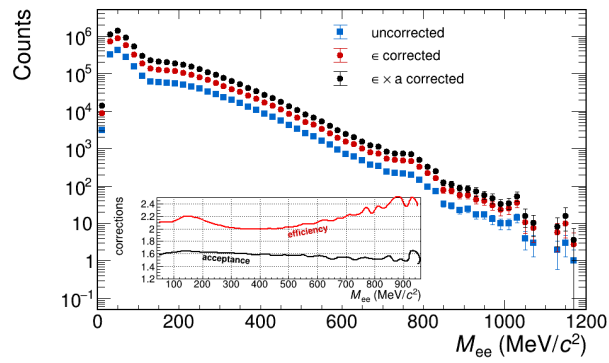
Figure 4.50: Positron acceptance extracted from positron simulation embedded into real data in p, Θ (a), p, Φ (b) and p_t, y (c). Red lines indicate the kinematic region this analysis is restricted to.



(a)



(b)



(c)

Figure 4.51: Comparison of dielectron spectra corrected for efficiency and acceptance in different sets of kinematic variables, p_t , y and p , Θ , Φ . In (a) only the efficiency correction is applied, (b) additionally includes the acceptance correction and (c) compares the spectra in different correction steps. Relative differences are shown in insets in (a) and (b). The inset in (c) shows the efficiency and acceptance correction factors calculated as the ratio of efficiency corrected data to uncorrected data and efficiency and acceptance corrected data to efficiency corrected data, respectively. All errors are statistically only.

A comparison of the corrected reconstructed dielectron spectrum and the input distribution in UrQMD with additionally embedded $\eta \rightarrow \gamma e^+ e^-$ signal reveals a remaining under-correction of the data especially at small invariant masses of up to $\Delta = 15\%$, compare fig. 4.52. This under-correction is a matter of efficiency only (compare eq. 4.15 for the definition used here). The underlying reason is correlations between close-by electrons, especially for low momenta and small opening angles, as present at small invariant masses. These correlations are not present by design in the simulation used to derive the efficiency correction, as one electron per sector is used. To account for this effect, an additional pair correction has to be applied on the dielectron spectrum. As it consists of various sources and the deviations between the corrected, reconstructed spectrum and the input are observed to slightly differ depending on the input, a correction is only applied on the π^0 -meson region up to $M_{ee} < 120 \text{ MeV}/c^2$ where the largest discrepancies are observed. Deviations at higher invariant masses are included in the systematic error which is discussed in sec. 4.11.

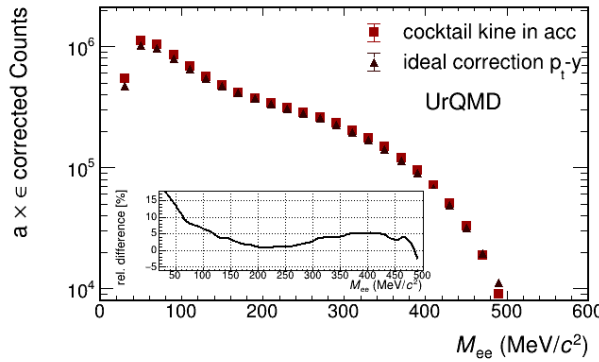


Figure 4.52: Comparison of the efficiency and acceptance corrected reconstructed dielectron spectrum with the input data in UrQMD simulation with additionally embedded $\eta \rightarrow \gamma e^+ e^-$ decays. The inset shows the relative difference of both spectra. Errors are statistical only. See text for details.

In the low invariant mass region the $\pi^0 \rightarrow \gamma e^+ e^-$ is the by far dominant dielectron source, thus corresponding simulations are used to extract the pair correction factor, compare fig. 4.53, in the same way as shown for the $\eta \rightarrow \gamma e^+ e^-$ channel. In a comparison with the inset in fig. 4.52 please note that the shown range differs. The drop at $M_{ee} = 120 \text{ MeV}/c^2$ even reaching to negative values at higher invariant masses is caused as in pure π^0 -Dalitz simulations statistics dies out here and is therefore not representative for the experimental dielectron spectrum.

With this efficiency and acceptance corrected data sample within the kinematically accessible regions of HADES (single leptons emitted in $16^\circ < \Theta < 83^\circ$ with $100 \text{ MeV}/c < p_e < 1.2 \text{ GeV}/c$ and fulfilling the additional cut function for positrons), any further acceptance correction to the full 4π space e.g.

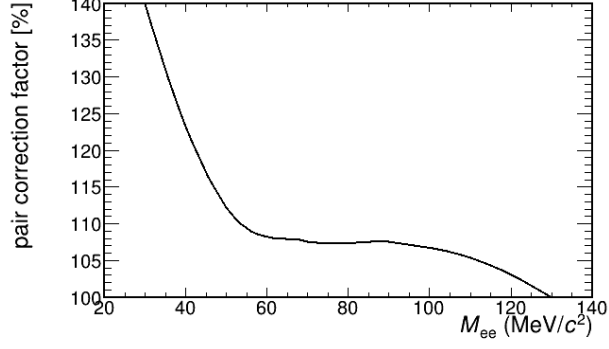


Figure 4.53: Additional efficiency correction factor derived from $\pi^0 \rightarrow \gamma e^+ e^-$ simulation to account for electron correlation effects not included in the white electron simulation.

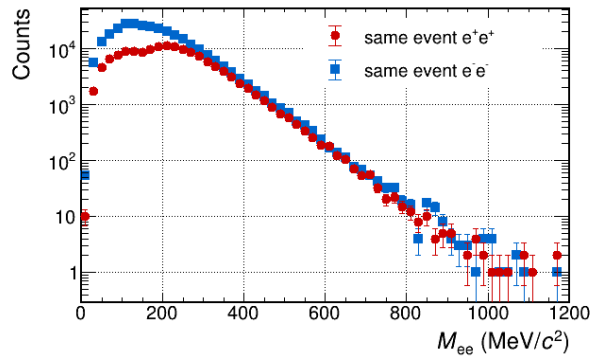
in bins of invariant mass is now straight forward and can easily be extracted within any specific model to compare with.

4.10 COMBINATORIAL BACKGROUND ESTIMATION

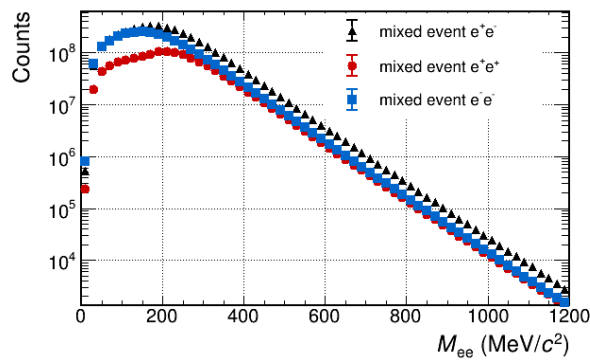
The sample of reconstructed unlike-sign (referring to the charge of the single electrons) dielectron pairs does not only include physical pairs, but also random combinations of electrons and positrons that do not originate from the same mother particle. This fraction of combinatorial background can be estimated based on the formation of like-sign pairs ($e^- e^-$, $e^+ e^+$) as first published in [98]. A detailed derivation can be found in appendix A. The geometric mean of these pairs has to be corrected with the so called *k-factor* to account for efficiency and acceptance differences in the detection of electrons and positrons. The result of this lengthy calculation reads

$$\langle BG_{+-} \rangle = \frac{\langle fg_{+-} \rangle}{2\sqrt{\langle fg_{++} \rangle \langle fg_{--} \rangle}} 2\sqrt{\langle FG_{++} \rangle \langle FG_{--} \rangle} = k 2\sqrt{\langle FG_{++} \rangle \langle FG_{--} \rangle}. \quad (4.20)$$

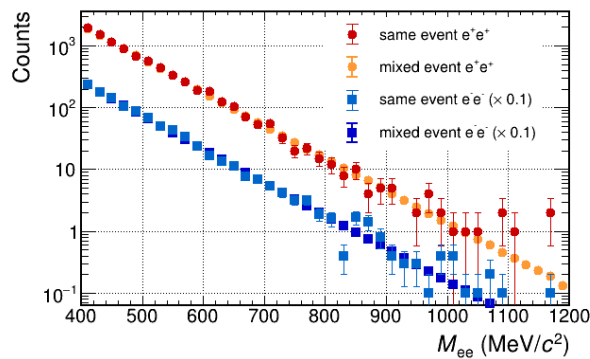
The *k-factor* is derived from the *event-mixing technique*, in which electrons and positrons from different events of the same centrality are combined to pairs creating a sample of background only also in the unlike-sign case. Pair spectra calculated via this method are denoted by small letters in equation 4.20. The like-sign same-event spectra $\langle FG_{++} \rangle$, $\langle FG_{--} \rangle$ and the mixed-event spectra $\langle fg_{++} \rangle$, $\langle fg_{--} \rangle$, $\langle fg_{+-} \rangle$ are shown in fig. 4.54a and fig. 4.54b, respectively. In the same-event like-sign spectra a bump at around the pion pole mass can be observed originating from possible correlations of like-sign electrons due to the two-photon decay of the π^0 with subsequent double conversion $\pi^0 \rightarrow \gamma\gamma \rightarrow e^+ e^- e^+ e^-$. As a 'drawback' of the high efficient conversion rejection based on the RICH detector without the requirement of two reconstructed tracks, the statistics in the same-event like-sign spec-



(a)



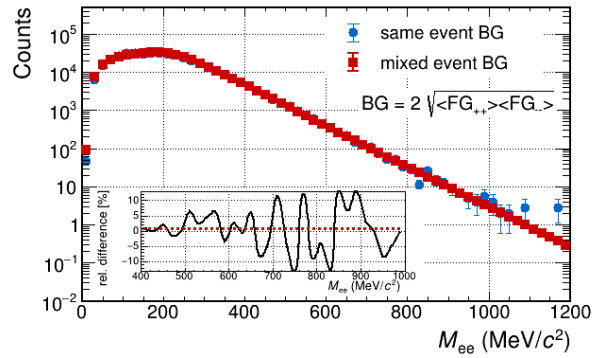
(b)



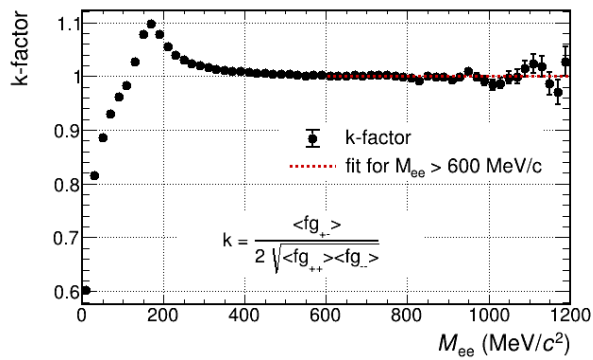
(c)

Figure 4.54: (a) shows the same event like-sign dielectron spectra. In (b) dielectron spectra obtained from the mixed event technique are shown. The slope of same-event and mixed-event like-sign spectra is compared in (c). Note the downscaling of the e^-e^- spectra in (c) for a better visualization.

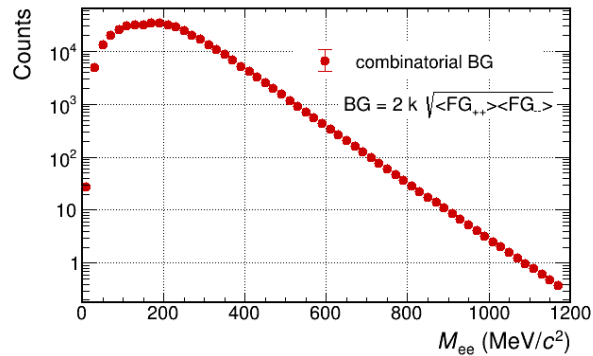
tra appears to be insufficient for a high precision background estimation. The mixed event spectra benefit from almost unlimited statistics and therefore vanishing statistical errors. Besides the π^0 pole mass region, no correlation in like-sign pairs is present and thus the slope of the same-event



(a)



(b)



(c)

Figure 4.55: (a) shows a comparison of the combinatorial BG (without weighting with the k-factor) extracted from same-event and mixed-event like-sign spectra. The inset shows the corresponding relative difference with a fitted mean value in good agreement to zero in the invariant mass region $M_{ee} > 400 \text{ MeV}/c^2$. The k-factor is shown in (b) where the high invariant mass region is fitted by a constant yielding $k_{M_{ee} > 600 \text{ MeV}/c^2} = 1.0010 \pm 0.0004$. The resulting combinatorial background is shown in (c).

and mixed-event like sign spectra agrees as shown in fig. 4.54c for invariant masses $M_{ee} > 400 \text{ MeV}/c^2$. The normalization of the mixed event spectra is provided in the region of $400 \text{ MeV}/c^2 < M_{ee} < 700 \text{ MeV}/c^2$. It is therefore possible, to use the mixed-event spectra in this medium and high invariant mass regime instead of the same-event spectra which provides the huge advantage of negligible statistical errors. Eq. 4.20 is thus modified for $M_{ee} > 400 \text{ MeV}/c^2$ to

$$\langle BG_{+-} \rangle = k2\sqrt{\langle fg_{++} \rangle \langle fg_{--} \rangle}. \quad (4.21)$$

A comparison of the combinatorial background spectra (without the k-factor) obtained from same-event and mixed event like-sign spectra is shown in fig. 4.55a. Both spectra agree on a high level despite statistical fluctuations in the same-event case that increase towards high invariant masses. To exclude any systematic effects, the relative difference is shown in an inset and fitted with a constant yielding $\Delta BG = (0.04 \pm 0.14)\%$. The shape of the differences furthermore clearly reveals the statistical nature of the differences. Fig. 4.55b shows the k-factor extracted from mixed-event spectra calculated according to eq. 4.20. It is characterized by a strong rise followed by a peak at around the π^0 pole mass and converges towards $k = 1$ already at medium invariant masses. As even in the mixed-event spectra statistical fluctuations start to appear at $M_{ee} \gtrsim 800 \text{ MeV}/c^2$, the region of $M_{ee} > 600 \text{ MeV}/c^2$ is fitted by a constant yielding $k_{M_{ee} > 600 \text{ MeV}/c^2} = 1.0010 \pm 0.0004$. To reduce statistical fluctuations in the resulting dielectron signal spectrum this value is used instead of the calculated one for high invariant masses $M_{ee} \geq 600 \text{ MeV}/c^2$. Fig. 4.55c shows the resulting combinatorial background as it is used for the analysis of the 0 – 40% centrality data. The dielectron signal is then defined as the difference of the reconstructed same-event like-sign spectrum and the estimated combinatorial background.

4.11 ESTIMATION OF SYSTEMATIC ERRORS

For systematic errors, three possible sources are discussed:

1. The impact of the choice of single track selection criteria on the dielectron spectrum is accessed repeating the analysis with modified selection criteria. With a change in selection criteria also the combinatorial background and the efficiency changes. Therefore any systematic effect can only be studied regarding the signal spectrum, after efficiency and acceptance correction and subtraction of the combinatorial background. In order not to introduce any possible bias from pion contamination in the electron sample and thus in the comparison, the selection windows can not be opened too far. The changes are applied as listed in tab. 4.5 with the resulting dielectron signal spectra (combinatorial BG subtracted) shown in fig. 4.56a. The data is corrected for efficiency but not for acceptance, as the acceptance correction is the same for

both spectra. The relative difference between both spectra, shown in the inset of fig. 4.56a, clearly states a minor impact of the choice of cut values on the spectrum. Besides statistical fluctuations at high invariant masses the corresponding systematic error can be stated to be $\Delta S_{\text{cut}}/S < 3\%$ over the full invariant mass range.

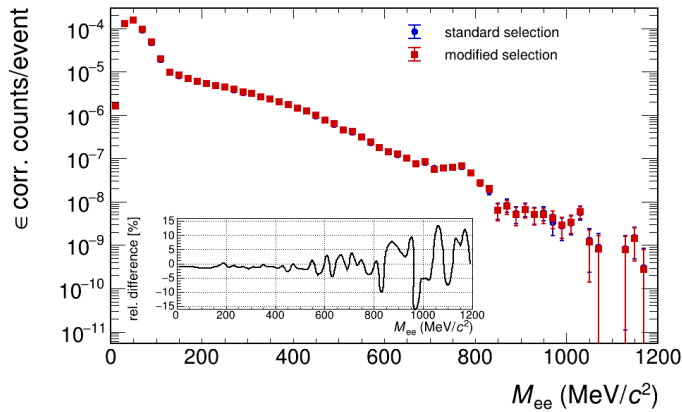
2. The efficiency and acceptance correction has been performed in two sets of variables, p_t, y and p, Θ, Φ , thus the comparison allows for an estimation on the systematic error caused by the choice of variables. In accordance to fig. 4.51b this error is well below one percent and can thus be neglected compared to the overall systematic error introduced by the chosen concept of efficiency and acceptance correction. This is estimated in UrQMD simulation in a comparison of the efficiency and acceptance corrected reconstructed dielectron spectrum with the input distribution, as shown in fig. 4.52. In the π^0 -meson mass region below $M_{ee} < 120 \text{ MeV}/c^2$ a correction has been applied. The remaining differences are taken as systematic error, which therefore is estimated to $\Delta S_{\text{corr}}/S < 5\%$ for the whole invariant mass region.
3. Systematic uncertainties in the estimation of the combinatorial background. The usage of mixed-event like-sign spectra in the calculation of the geometrical mean within the background estimation has been found to not contribute in any significant way to the systematic error, compare chapter 4.10. To study the accuracy of the overall procedure, the background estimation is carried out in UrQMD simulations, analysed in the same way as the experimental data, and compared to the actual number of background pairs in the dielectron sample. The resulting spectra are shown in fig. 4.56b. Despite using a sample of 100 million collisions, the statistics practically dies out for $M_{ee} > 800 \text{ MeV}/c^2$ which is mainly caused by the missing high momentum electrons from vector meson virtual photon decays as these are not included in UrQMD. In statistically significant regions, the dif-

cut observable	analysis value	varied value
effective mass (chapter 4.3.4)	momentum dependent cut function	$m_{eff} \leq$ $100 \text{ MeV}/c^2$
RICH ring radius (chapter 4.3.3.1)	3σ deviation	2σ deviation
RMQ (chapter 4.3.3.2)	momentum dependent 4.5σ width	momentum dependent 3.5σ width

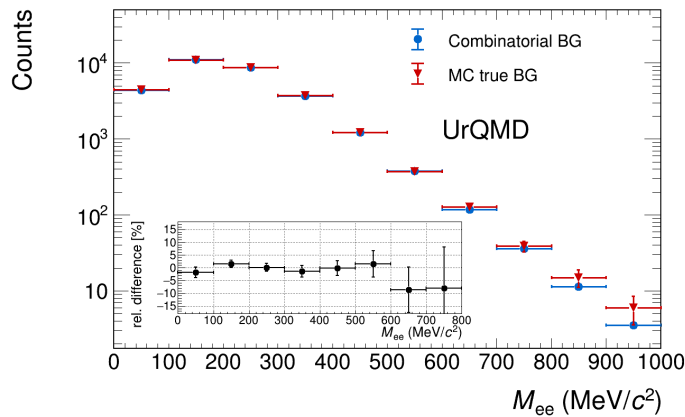
Table 4.5: Variation in the cut parameter for track selection to test the efficiency correction and extract corresponding systematic uncertainties.

ferences are well below $\Delta < 2\%$ which is therefore used as an upper limit on the systematic error in the background estimation. As the combinatorial background contributes in an additive way to the dielectron signal, the error reads $\Delta S_{BG}/S < 0.02 \cdot BG/S$.

The contribution of all systematic error sources as well as their sum and variance are shown in fig. 4.57 relative to the total dielectron signal. The assumed 5% error on the efficiency and acceptance correction is the dominant source for the whole invariant mass region. The contribution of the combinatorial background, estimated to 2% of the BG/S ratio has a significant impact only at small invariant masses (in the order of 5%), where the huge



(a)



(b)

Figure 4.56: Systematic error calculation of the lepton selection criteria and the combinatorial background estimation. A comparison of the efficiency corrected dielectron signal spectra using different cut values is shown in (a). (b) shows the comparison of the calculated combinatorial background to the Monte-Carlo (MC) true background in UrQMD simulation. The insets show relative differences in the comparisons. Errors are statistical only.

amount of electrons produced in Dalitz decays of the π^0 strongly increases the combinatorics in the pair formation procedure. Again, here the upgraded RICH detector being capable of highly efficient identification of conversion electrons pays off, especially comparing the systematic error stemming from the combinatorial background to earlier analysis in $Au + Au$ [156] reaching values up to $\Delta S_{BG}/S|_{Au+Au} \sim 40\%$. The total systematic error is calculated as the sum of the different sources. Another possibility to estimate the systematic error is the quadratic sum $\Delta/S = \sqrt{\sum_i \Delta X_i}$ of the different error sources X_i . As an underestimation of the systematic error has to be avoided, the latter one is not used, but the sum instead, which is significantly higher. The total error thus peaks at invariant masses of $M_{ee} \sim 200 \text{ MeV}/c^2$ reaching values of $\Delta S/S_{sys} \approx 13\%$. For higher invariant masses the systematic error decreases and is smaller than 10% for $M_{ee} > 400 \text{ MeV}/c^2$.

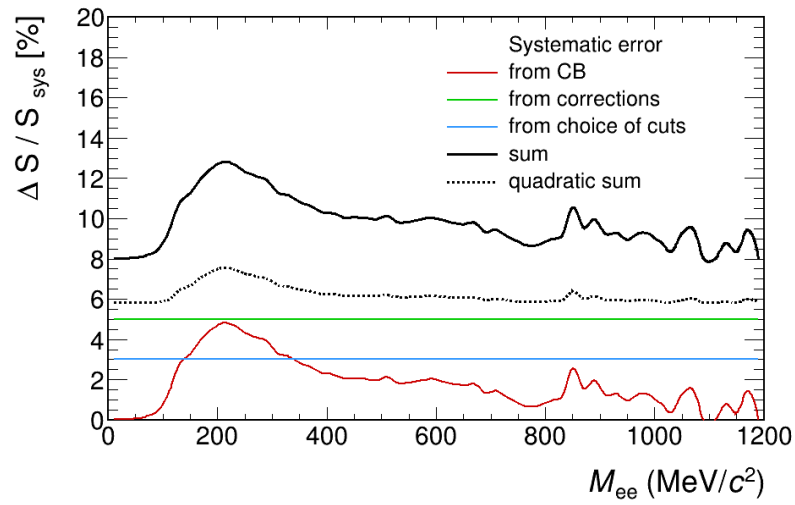


Figure 4.57: Relative systematic error of the dielectron signal spectrum and the contributing sources. The sum of all individual systematic error sources is used as total systematic error.

ESTIMATION OF HADRON MULTIPLICITIES

In order to decompose the measured dielectron spectrum in its different contributions it is necessary to have a precise knowledge about the hadron production multiplicities contributing to the dielectron yield. These multiplicities are used for the scaling of simulated dielectron spectra of the relevant hadron decays. In this chapter, the multiplicities of the η (chapter 5.1) and the π^0 (chapter 5.2) contributing with their Dalitz decays ($\eta \rightarrow \gamma e^+ e^-$) to the dielectron yield are estimated. Furthermore, the multiplicity of the ω can be approximated directly from its $\omega \rightarrow e^+ e^-$ decay (chapter 5.4).

5.1 η MULTIPLICITY ESTIMATION

The decay of the η meson is dominated by three-pion channels with $f_{3\pi}^\eta \approx 0.556$ ($\eta \rightarrow 3\pi^0/\pi^+\pi^-\pi^0$). A reconstruction via this channel is impossible regarding the statistics of charged pions and the requirement of previously reconstructing a π^0 . As pseudoscalar meson, the η can also decay into two photons ($\eta \rightarrow \gamma\gamma$, $f_{2\gamma}^\eta \approx 0.394$). It is also capable of a leptonic Dalitz decay ($\eta \rightarrow \gamma\gamma^*$) with a branching fraction of $f_{\gamma\gamma^*}^\eta \approx 0.0069$. Both decays can be reconstructed via a detector signature of four electrons requiring all photons to convert. Although the branching fraction in the Dalitz decay is much smaller than in the two photon channel, it significantly contributes to the analysis with only one conversion process being required. Electrons are selected in the following way:

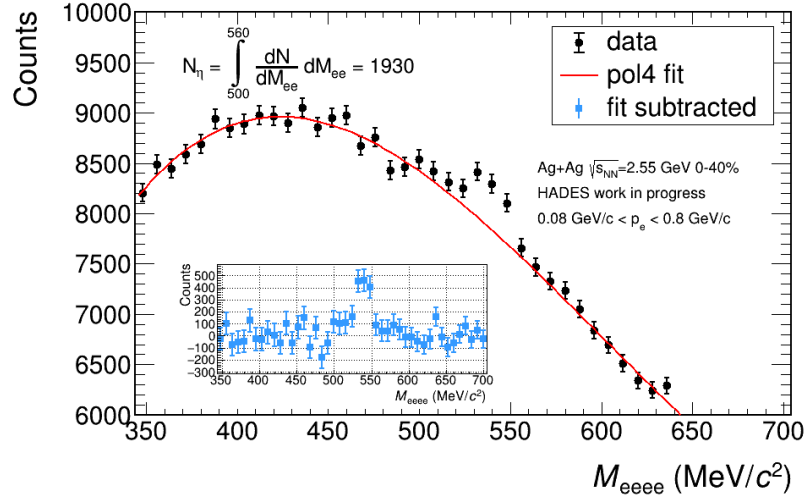
- The pre-selection of electrons is almost identically as described in chapter 4.3.1. In the track reconstruction procedure, the sharing of hits in the inner MDC layer is allowed, as conversion pairs are characterized by small opening angles that often can not be separated in front of the magnetic field with the given tracking precision. Furthermore, as higher momentum cutoff $p_{max} = 800 \text{ MeV}/c$ is used.
- Hadron contamination is reduced based on an effective mass cut only as described in chapter 4.3.4.
- There is **no** requirement on any matching to a RICH ring, as this would require a photon conversion before the radiator volume (in the target or beam pipe material). With the conversion probability being already very small (given by the HADES design with low material budget), this requirement would badly harm the statistics. The same applies to selection criteria to enhance (previously suppress) conversion as these also involve the RICH detector.

In each reconstructed set of $2e^+2e^-$ four photons can be formed, however, they yield the same meson invariant mass. Therefore it is not required to

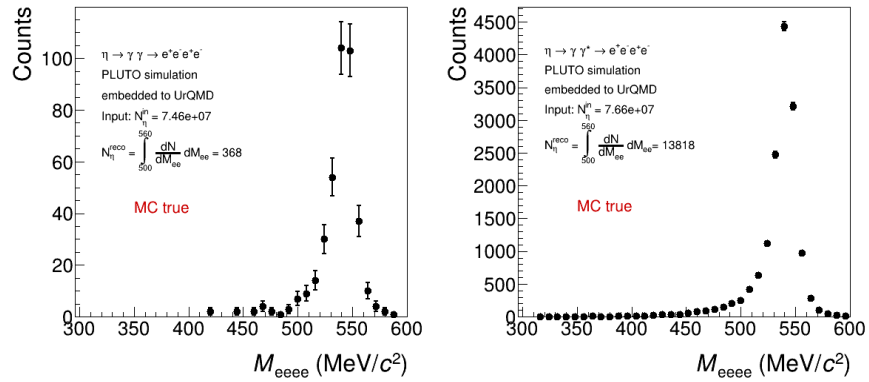
identify the correct electron pairing to photons. Nevertheless, opening angle restrictions on pairs of electrons are used to significantly reduce the background contributions. Opening angles of $\alpha_{ee} < 10^\circ$ are required for one of the two possible sets of photons.

The experimentally reconstructed invariant mass spectrum is presented in fig. 5.1a showing a clear enhancement at the nominal invariant mass of the η meson. The continuous background is fitted by a fourth order polynomial in the side-band regions $350 \text{ MeV}/c^2 < M_{eeee} < 500 \text{ MeV}/c^2$ and $560 \text{ MeV}/c^2 < M_{eeee} < 700 \text{ MeV}/c^2$, with the inset showing the data after subtraction of the fitted background. The amount of reconstructed η mesons is given by the integral in the invariant mass region of $500 \text{ MeV}/c^2 < M_{eeee} < 560 \text{ MeV}/c^2$ yielding $N_\eta^{reco} = 1930$.

To correct for efficiency and acceptance losses, PLUTO simulation of the relevant decay channels are performed and the resulting particles (either $\gamma\gamma$



(a) real data



(b) simulation

Figure 5.1: Reconstruction of the η in the $\eta \rightarrow e^+e^-e^+e^-$ channel in real data (a) and PLUTO simulations embedded to UrQMD (b).

or $\gamma e^+ e^-$) are embedded into UrQMD Ag+Ag events (see also chapter 2.7). A temperature of $T^\eta = 93 \text{ MeV}$ is used producing a thermal distribution of η mesons in PLUTO. These simulations are analyzed in the exactly same way as the experimental data, in particular including a centrality selection as the single track reconstruction efficiency depends on the overall track density. Fig. 5.1b shows the resulting reconstructed invariant mass spectra of the PLUTO input (Mont-Carlo true). The huge difference in the amount of reconstructed signal mesons results from the small conversion probability of photons which is given by the ratio $p_{conv} = N_\eta^{reco, \gamma\gamma} / N_\eta^{reco, \gamma\gamma^*} = 2.66\%$. The efficiency and acceptance correction factor is derived for both channels to

$$\begin{aligned} \epsilon \times a^{\gamma\gamma} &= \frac{N_{\gamma\gamma}^{reco}}{N_{\gamma\gamma}^{in}} = \frac{368}{7.46 \cdot 10^7} = 4.9 \cdot 10^{-6}, \\ \epsilon \times a^{\gamma\gamma^*} &= \frac{N_{\gamma\gamma^*}^{reco}}{N_{\gamma\gamma^*}^{in}} = \frac{13517}{7.66 \cdot 10^7} = 1.8 \cdot 10^{-4}. \end{aligned} \quad (5.1)$$

The η multiplicity is then given by weighting both channels with the corresponding branching ratios,

$$\eta_{mult}^{up}|_{0-40\%} = \frac{N_{exp}^\eta}{N_{evt} \cdot (BR_{\gamma\gamma} \cdot \epsilon \times a^{\gamma\gamma} + BR_{\gamma\gamma^*} \cdot \epsilon \times a^{\gamma\gamma^*})} \quad (5.2)$$

Changing the fit range for the estimation of the background contribution in the experimental data, the amount of N_η^{reco} can be varied between $N_\eta^{reco} \sim 1400$ to 1930 , yielding an η multiplicity of $\eta_{mult}^{low}|_{0-40\%} = 0.091$ to 0.127 . As result of this analysis the mean value is taken with the difference used as systematic error. The statistical error is calculated via error propagation from the statistical error in the experimental spectrum ($err_{stat} = \sqrt{N_{eeee}} = 271$) and the statistical errors in the simulation spectra in the corresponding range of M_{eeee} . The result then reads

$$\eta_{mult}|_{0-40\%} = 0.109 \pm 0.018|_{sys} \pm 0.015|_{stat} \quad (5.3)$$

A signal of the η meson can also be reconstructed in the 10% sub-centrality classes, with the invariant mass spectra shown in fig. B.1 - B.4 in appendix B. In a simple estimation, neglecting changes in the single track efficiency based on the overall track density, multiplicities can be calculated in the sub-centrality classes assuming the same efficiency and acceptance correction factors as in the integrated case, following eq. (5.3). The such obtained results are summarized in tab. 5.1 together with calculated values starting from the centrality integrated analysis assuming a linear scaling with $\langle A_{part} \rangle$. The errors are calculated as in the centrality integrated analysis. In case of the $\langle A_{part} \rangle$ scaling, they are lineally scaled up. The trend of a rising η production cross section with the system size is confirmed. However, the

Centrality class	0 – 40 %	0 – 10 %	10 – 20 %	20 – 30 %	30 – 40 %
$\langle A_{part} \rangle$	101.3	160.9	114.5	81.1	56.5
η_{mult} analysis	0.107 $\pm 0.027 _{sys}$ $\pm 0.015 _{stat}$	0.253 $\pm 0.040 _{sys}$ $\pm 0.070 _{stat}$	0.096 $\pm 0.033 _{sys}$ $\pm 0.034 _{stat}$	0.064 $\pm 0.020 _{sys}$ $\pm 0.021 _{stat}$	0.016 $\pm 0.011 _{sys}$ $\pm 0.023 _{stat}$
η_{mult} linear $\langle A_{part} \rangle$ scaling	0.107 $\pm 0.027 _{sys}$ $\pm 0.015 _{stat}$	0.170 $\pm 0.044 _{sys}$ $\pm 0.024 _{stat}$	0.121 $\pm 0.027 _{sys}$ $\pm 0.015 _{stat}$	0.086 $\pm 0.020 _{sys}$ $\pm 0.011 _{stat}$	0.060 $\pm 0.014 _{sys}$ $\pm 0.008 _{stat}$

Table 5.1: η multiplicity in different centrality classes. Experimental results in each class are compared to a linear scaling approach based on the centrality integrated analysis.

exact correlation remains unclear from the experimental data due to large errors, both statistically and systematically.

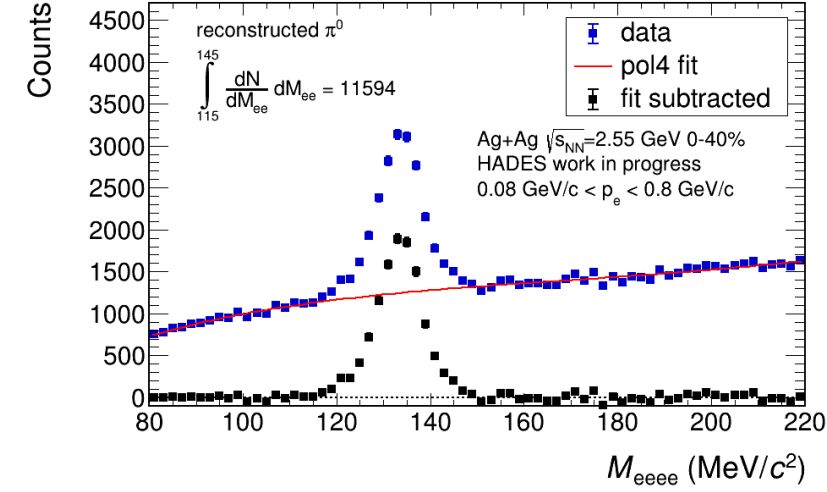
The systematic error can be reduced using the event mixing technique for background estimation, which indeed yields promising results, compare chapter 5.3. The precision of the derived η multiplicity would also be improved using embedded η mesons into real data for efficiency and acceptance correction in order to include the centrality dependence of the single electron efficiency. Having sufficient simulation at hand to perform an analysis in bins of $p_t - y$ with a subsequent extrapolation to uncovered phase space regions would also enhance the accuracy of the estimated η multiplicity. Possibilities of doing so while using reasonable disc space are currently under investigation. The η multiplicity used as input for the dielectron analysis is discussed in sec. 5.5 in a comparison to previously measured TAPS data and model predictions.

5.2 π^0 MULTIPLICITY ESTIMATION

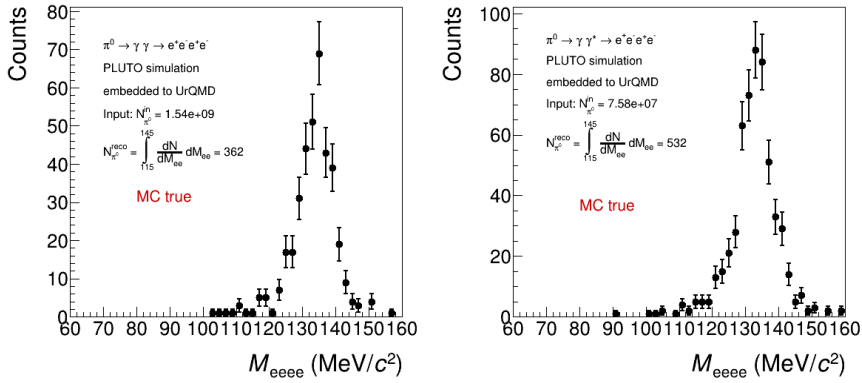
The π^0 is reconstructed in the same way as the η , in a decay pattern of $\pi^0 \rightarrow e^+e^-e^+e^-$. With the π^0 being the lightest meson, it is not capable of hadronic decay channels, thus the branching fraction in the relevant decay channels are enhanced compared to the η . They are valued $f_{2\gamma}^{\pi^0} \approx 0.988$ and $f_{\gamma\gamma^*}^{\pi^0} \approx 0.012$. Although having a much smaller branching fraction, the Dalitz-decay contributes significantly as only one photon is required to convert.

The electron selection is identical as in case of the η , described in the previous section, 5.1, with the result shown in fig. 5.2a. The background is fitted in the side-band regions $80 \text{ MeV}/c^2 < M_{eeee} < 115 \text{ MeV}/c^2$ and $145 \text{ MeV}/c^2 < M_{eeee} < 200 \text{ MeV}/c^2$ by a fourth order polynomial. The remaining excess in the invariant mass region $115 \text{ MeV}/c^2 < M_{eeee} < 145 \text{ MeV}/c^2$ amounts to $N_{\pi^0}^{reco} = 11208$.

For efficiency and acceptance correction PLUTO simulations are performed



(a) real data



(b) simulation

Figure 5.2: Reconstruction of the π^0 in the $\pi^0 \rightarrow e^+e^-e^+e^-$ channel in real data (a) and PLUTO simulations embedded to UrQMD (b).

in both relevant decay channels, that are embedded in UrQMD Ag+Ag collisions (see also chapter 2.7). To properly model the energy distribution, two temperatures are needed in case of the π^0 , representing different production processes. $T_1 = 49 \text{ MeV}$ accounts for the production via decays of Δ resonances, whereas $T_2 = 93 \text{ MeV}$ represents the direct production. The total yield of π^0 is dominated by the first, taken into account by weighting factors of $w_{T_1} = 0.98$ and accordingly $w_{T_2} = 0.02$. Thus the simulated π^0 mesons have a rather small energy leading to a strongly reduced efficiency and acceptance compared to the η . In order to still collect enough statistics, not only embedded π^0 are analyzed, but also those included in the underlying UrQMD events. The efficiency and acceptance correction factors then amount to

$$\epsilon \times a^{\gamma\gamma^*} = \frac{N_{\gamma\gamma^*}^{reco}}{N_{\gamma\gamma^*}^{in}} = \frac{532}{7.58 \cdot 10^7} = 7.0 \cdot 10^{-6},$$

$$\epsilon \times a^{\gamma\gamma} = \frac{N_{\gamma\gamma}^{reco}}{N_{\gamma\gamma}^{in}} = \frac{362}{1.54 \cdot 10^9} = 2.35 \cdot 10^{-7}. \quad (5.4)$$

The π^0 multiplicity is derived by weighting both channels with the corresponding branching ratios to

$$\pi_{mult}^0|_{0-40\%} = \frac{N_{exp}^{\pi^0}}{N_{evt} \cdot (BR_{\gamma\gamma} \cdot \epsilon \times a^{\gamma\gamma} + BR_{\gamma\gamma^*} \cdot \epsilon \times a^{\gamma\gamma^*})} = 7.37 \pm 0.43|_{sys} \pm 0.11|_{stat}, \quad (5.5)$$

with $N_{exp}^{\pi^0} = N_{\pi^0}^{reco} = 11208$.

The systematic error is estimated enlarging the fit range within the background estimation to $60 \text{ MeV}/c^2 < M_{eeee} < 115 \text{ MeV}/c^2$ and $145 \text{ MeV}/c^2 < M_{eeee} < 240 \text{ MeV}/c^2$. A possible systematic error from differences in the spatial distributions of the π^0 in experiment and PLUTO simulations is not included. As the same PLUTO simulation are also used to form the hadronic dielectron cocktail, these effects cancel out within this work.

The resulting experimental invariant mass spectra in 10% sub-centrality classes are provided in fig. B.5 - B.8, see App. B. In the approximation of the single track efficiency not depending on the centrality of the collision the π^0 multiplicity can be estimated using eq. 5.4, 5.5. The results are shown in tab. 5.2 together with a linear $\langle A_{part} \rangle$ scaling approximation based on

Centrality class	0 – 40 %	0 – 10 %	10 – 20 %	20 – 30 %	30 – 40 %
$\langle A_{part} \rangle$	101.3	160.9	114.5	81.1	56.5
π_{mult}^0 analysis	7.37 $\pm 0.43 _{sys}$ $\pm 0.11 _{stat}$	13.63 $\pm 0.25 _{sys}$ $\pm 0.37 _{stat}$	7.68 $\pm 0.58 _{sys}$ $\pm 0.25 _{stat}$	5.93 $\pm 0.05 _{sys}$ $\pm 0.18 _{stat}$	4.39 $\pm 0.04 _{sys}$ $\pm 0.13 _{stat}$
π_{mult}^0 linear $\langle A_{part} \rangle$ scaling	7.37 $\pm 0.43 _{sys}$ $\pm 0.11 _{stat}$	11.71 $\pm 0.71 _{sys}$ $\pm 0.18 _{stat}$	8.33 $\pm 0.43 _{sys}$ $\pm 0.11 _{stat}$	5.90 $\pm 0.32 _{sys}$ $\pm 0.08 _{stat}$	4.11 $\pm 0.22 _{sys}$ $\pm 0.06 _{stat}$
π_{mult}^0 from π^\pm	-	11.85 $\pm 1.1 _{sys}$	8.35 $\pm 0.8 _{sys}$	6.05 $\pm 0.7 _{sys}$	-

Table 5.2: π^0 multiplicity in different centrality classes. Experimental results in each class are compared to a linear scaling approach based on the centrality integrated analysis and results of a charged pion analysis [157].

the centrality integrated result. Within errors both approaches agree, however, the results from the centrality dependent analysis tend to be higher in the central collisions. A significant difference here would indicate, that a linear scaling of the π^0 production with A_{part} does not hold. However, besides the systematic error given based on the background estimation, these differences may also be caused by the efficiency correction based on simulation. As shown in section 4.9 there are differences in the electron efficiency based on the track density in the detector and therefore on the centrality. To include this effect in the efficiency study of the π^0 and also the η , embedding into experimental data is necessary. Different approaches of doing so with reasonable consumption of disk space are currently under investigation.

Furthermore, the results can be compared to values obtained from a charged pion analysis, assuming $\pi_{mult}^0 = 0.5 \cdot (\pi_{mult}^+ + \pi_{mult}^-)$ [157]. Values are available in the 0 – 30% most central collisions and compare very well to the results obtained within the linear scaling approximation but also from the analysis. This promising agreement supports the assumption, that differences in the centrality dependent analysis and the linear scaling approximation arise from the named systematic errors in the analysis in centrality bins. Therefore for the further analysis, the values obtained within the linear scaling approximation are used. A comparison to previous TAPS measurements is performed in sec. 5.5.

5.3 RECENT IMPROVEMENTS WITH FOUR LEPTON EVENT-MIXING

In order to reduce the systematic error introduced to the analysis by fitting the side-bands of the signal region with a fourth order polynomial, the event-mixing technique can also be used to describe the background. The difference to the background estimation via event-mixing in this four lepton analysis to the dielectron event-mixing presented in chapter 4.10 is, that complicated correlations between single electrons might appear. E.g. one photon might be correctly reconstructed but paired with two uncorrelated electrons (such a contribution is labeled as $2e + 1e + 1e$ in the following). From simulations it turns out, that the background is dominated by $2e + 2e$ contributions with a significant addition of a $3e + 1e$ contribution [158]. Fig. 5.3 clearly demonstrates that a reasonable description of the background is not possible based on the $2e + 2e$ contribution only. The $2e + 2e$ case corresponds to two correctly reconstructed photons, that themselves are uncorrelated. In case of the $3e + 1e$ contribution, both photons from either an η or π^0 decay have converted, but only three of the four electrons have been correctly identified and are paired with an uncorrelated track. In order to account for these different background sources, two different event mixers are used, both based on single tracks. In the first scenario two pairs of selected tracks are used from different events and paired. In the second scenario, three tracks from one event are paired with one track from another event. The resulting invariant mass spectra of both event-mixing setups are shown in fig. 5.4. The $3e + 1e$ contribution appears to be broader compared to the $2e + 2e$ contribu-

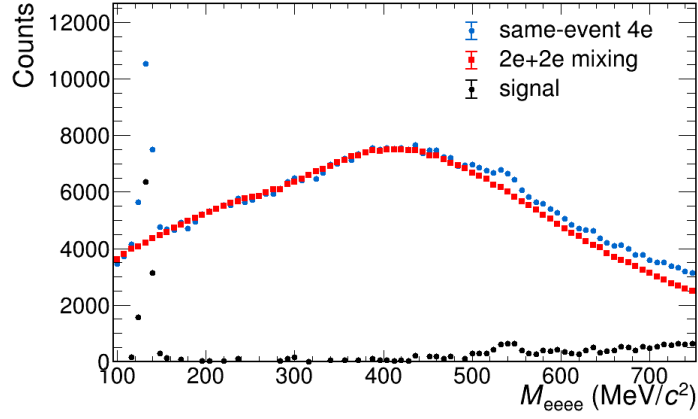


Figure 5.3: Background in the $4e$ invariant mass spectrum calculated from $2e+2e$ event-mixing only. Large discrepancies are observed at invariant masses beyond the η signal. The data shown correspond to an electron selection as in chapter 5.3 and 5.5.

tion and shifted to higher invariant masses. Both mixed-event distributions are normalized to the same-event spectrum in the invariant mass region of $200 < M_{ee}(\text{MeV}/c^2)^{-1} < 400$. The relative weighting of both mixed-event spectra is then obtained requiring a vanishing signal at invariant masses beyond the η invariant mass,

$$\int_{580}^{740} \langle FG_{+--+} \rangle - BG = 0, \quad (5.6)$$

with

$$BG = c \langle fg_{2e+2e} \rangle + (1 - c) \langle fg_{3e+1e} \rangle = 0. \quad (5.7)$$

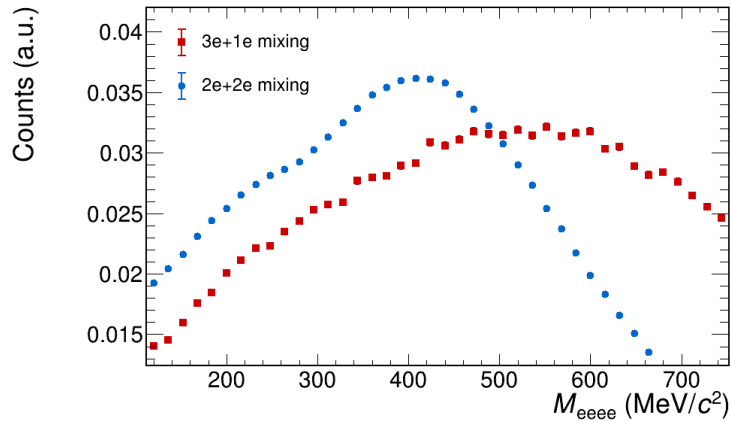


Figure 5.4: The $2e + 2e$ and $3e + 1e$ contributions to the four particle event mixing. The shape and also the peak position strongly differ.

$\langle FG_{+--+} \rangle$ denotes the four electron same-event invariant mass spectrum and $\langle fg_{2e+2e} \rangle$, $\langle fg_{3e+1e} \rangle$ denote the $2e + 2e$ and $3e + 1e$ mixed-event spectra, respectively, after normalization to the side-band $200 \text{ MeV}/c^2 < M_{ee} < 400 \text{ MeV}/c^2$. The relative weighting factor c strongly depends on the track selection criteria. In an example of tightened selection criteria compared to chapter 5.1 and 5.2 (the photon opening angle is required to be $\alpha < 4^\circ$), it is found $c = 0.982$ is required. The corresponding data is shown in fig. 5.5. An overall excellent description of the background is achieved with the π^0 and η signal clearly showing up. The signal counts are extracted by an integral in the corresponding invariant mass region, yielding $N_\eta^{\text{reco}} = 1304$ and $N_{\pi^0}^{\text{reco}} = 10427$. The signal shape is well described by a Gaussian in both cases. The fitted mean values are slightly smaller ($\sim 1.5\%$) than the PDG listed masses of the particles ($m(\pi^0)^{\text{PDG}} = 134.98 \text{ MeV}/c^2$, $m(\eta)^{\text{PDG}} = 547.86 \text{ MeV}/c^2$) indicating energy loss in the HADES detector. A similar shift in invariant mass is also observed regarding the ω , compare chapter 5.4.

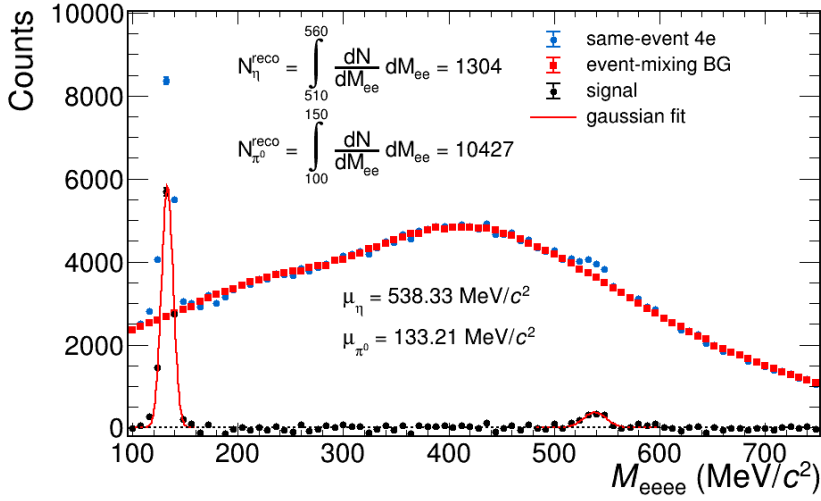
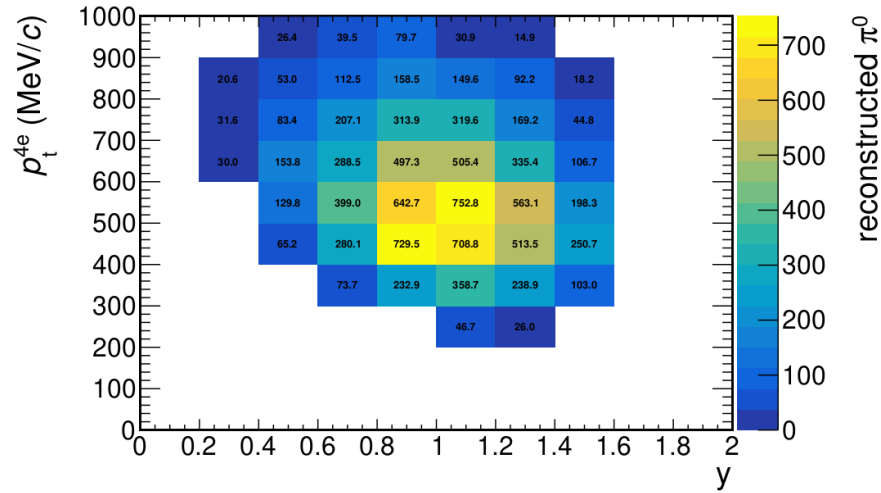


Figure 5.5: Four electron invariant mass spectrum with BG calculated from event-mixing. In a comparison to fig. 5.1a and 5.2a, the amount of reconstructed π^0 and η is smaller as the track selection is tightened. For details see *text*.

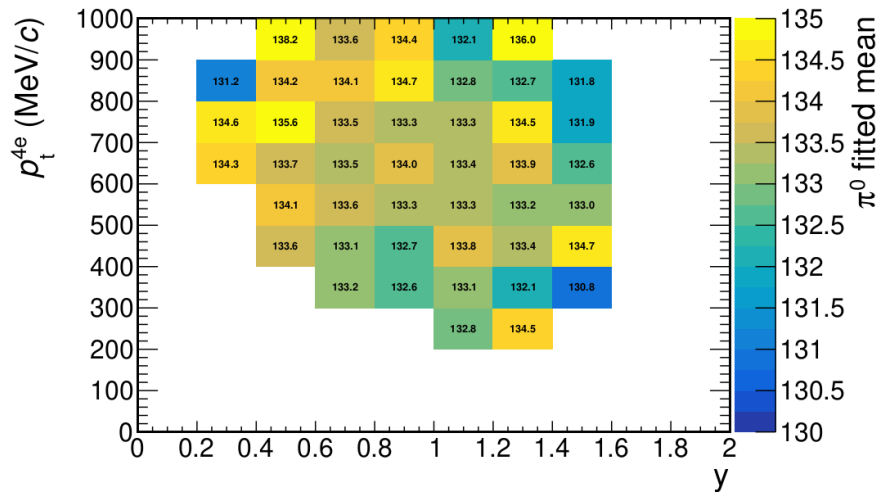
The precise description of the background using the event-mixing technique for background description instead of fitting the background is crucial especially in case of the η , where the signal-to-background ratio is $S/B \sim 0.1$ is observed and thus uncertainties in the BG have a large impact on the resulting signal. Performing an efficiency and acceptance correction as in chapter 5.3 and 5.5 yield the same multiplicities ($\pm 2\%$). However in case of the η the systematic error from the background estimation could be reduced from $\sim 30\%$ to $\sim 5\%$ resulting from a comparison of Monte-Carlo true BG in simulation to the calculated BG from event-mixing.

In order to further improve the precision of the analysis, an analysis in bins of $p_t - y$ is aimed at. Regarding the limited statistics for the η , only 3 – 4

bins in either p_t or y are possible, the corresponding spectra splitting the sample in four bins of rapidity are included in Appendix B, fig. B.9 - B.12. For the π^0 the statistics is significantly higher, thus a reconstruction in bins of $p_t - y$ is well possible. The resulting invariant mass spectra, the calculated background and the corresponding signal is shown exemplary in four bins in Appendix B, fig. B.13 - B.16. It is clearly shown, that the event-mixing technique describes the background reasonably well in all bins. A full $p_t - y$ map of the amount of reconstructed π^0 is provided in fig. 5.6a. The bulk of reconstructed π^0 is reconstructed at $y > y_0$ in the medium p_t region. However, the high S/B ratio ~ 3 in case of the π^0 and the precise understanding of the background allow for a signal extraction even at high p_t far away from



(a)



(b)

Figure 5.6: Reconstructed π^0 in bins of $p_t - y$ (a) and the fitted mean value of the signal (b). The corresponding invariant mass spectra are provided exemplary in four bins in Appendix B, fig. B.13 - B.16.

y_0 . The corresponding fitted mean value of the π^0 signal is shown in fig. 5.6b. No systematic dependence in y and p_t of the observed shift in invariant mass compared to the PDG listed values is observed.

Having a $p_t - y$ map of reconstructed π^0 (and four bins in y for the η) at hand, the analysis of the experimental data is completed. In order to extract a more precise multiplicity as done in chapter 5.1 and 5.2, high statistics simulation are needed to extract efficiency and acceptance correction factors in each experimental bin. Therefore, different simulation setups are currently investigated [159].

5.4 ω MULTIPLICITY ESTIMATION

The decay channels of the ω meson mainly involve pions, e.g. $\omega \rightarrow \pi^+ \pi^- \pi^0$ ($f_{3\pi}^\omega = 0.892$) and $\omega \rightarrow \pi^0 \gamma$ ($f_{\pi^0 \gamma}^\omega = 0.084$). A signal reconstruction in these channels is impossible regarding the low efficiency and acceptance in the π^0 reconstruction, the small fraction of π^0 originating from ω meson decays and the huge combinatorial background in charged pions. As vector meson, the ω is also capable of a pure leptonic decay, $\omega \rightarrow e^+ e^-$. However, the branching ratio is extremely small ($f_{e^+ e^-}^\omega = 7.36 \cdot 10^{-5}$) reflecting the strength of the electromagnetic coupling in relation to the strong coupling. Thus, a signal of $N_\omega^{reco} < 200$ only is expected in this channel assuming a reconstruction efficiency of $\epsilon_{\omega \rightarrow e^+ e^-} = 0.5$ according to simulations (the beam time proposal [160]).

Electron (-pair) reconstruction is mainly performed as in the dielectron analysis, described in chapter 4. Slight changes are applied in order to increase the S/B ratio, which here mainly implies the $\omega \rightarrow e^+ e^- / \rho \rightarrow e^+ e^-$ ratio. The combinatorial background is on a low level in this region of invariant mass (see sec. 6.1) and eventual physical background is proven to be neglectable (sec. 4.8). These changes are

- the lower momentum cutoff is raised from $p_{min} = 100 \text{ MeV}/c$ to $p'_{min} = 300 \text{ MeV}/c$
- the opening angle of reconstructed pairs is required to be $\alpha(e^+ e^-) > 45^\circ$
- in a second version of cuts, referred to as *soft cuts*, the upper momentum cutoff is raised from $p_{max} = 1200 \text{ MeV}/c$ to $p'_{max} = 2000 \text{ MeV}/c$ and the analysis is restricted to pair opening angles $\alpha(e^+ e^-) > 50^\circ$

The invariant mass spectra obtained within this analysis are shown in fig. 5.7 (hard cuts), 5.8 (soft cuts), on the left hand side. As the event mixing technique can not distinguish between true electron pairs from an ω - or ρ -meson decay, background estimation has to be performed fitting the side-bands of the signal region. Therefore, a fourth order polynomial is fitted in the invariant mass regions of $450 \text{ MeV}/c^2 < M_{ee} < 740 \text{ MeV}/c^2$ and $800 \text{ MeV}/c^2 < M_{ee} < 900 \text{ MeV}/c^2$. The signal is then obtained as integral of the excess in the invariant mass range $740 \text{ MeV}/c^2 < M_{ee} < 800 \text{ MeV}/c^2$.

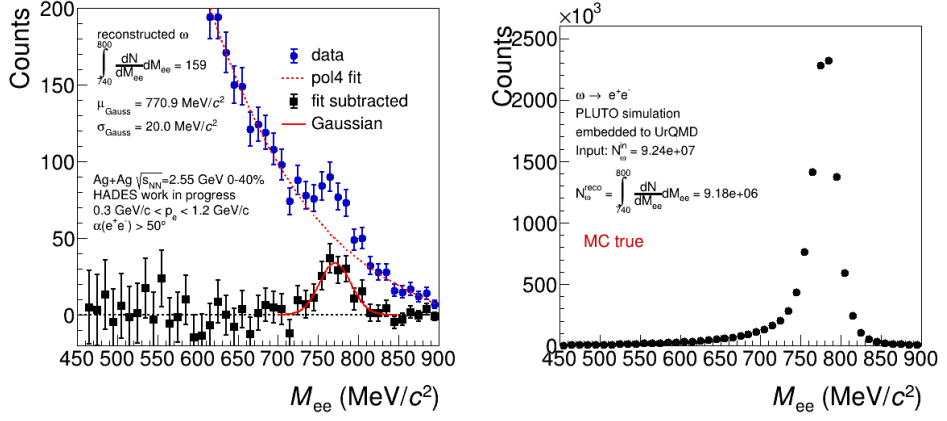


Figure 5.7: ω -meson analysis with hard cuts. Left: Electron pair invariant mass spectrum with fitted BG and extracted signal. Right: Monte-Carlo true signal from PLUTO simulations for efficiency and acceptance correction.

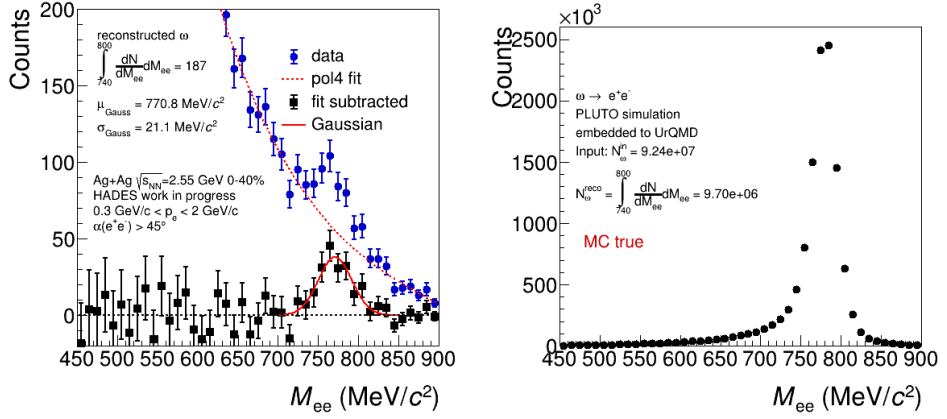


Figure 5.8: ω -meson analysis with soft cuts. Left: Electron pair invariant mass spectrum with fitted BG and extracted signal. Right: Monte-Carlo true signal from PLUTO simulation for efficiency and acceptance correction.

A Gaussian fit reveals a peak position of $\mu \sim 770.9 \text{ MeV}/c^2$ in both data sets corresponding to a shift with respect to the listed PDG value $m(\omega)_{PDG} = 782.6 \text{ MeV}/c^2$ of about 1.5% as also observed for the π^0 and the η , compare chapter 5.1 and 5.2. This shift is thought to originate from energy loss in the detector and is also observed in hadronic decay channels, e.g. the K_s^0 [161] and currently under investigation. For efficiency and acceptance correction a thermal distribution of ω -mesons with $T = 100 \text{ MeV}$ is simulated using PLUTO. One ω per event is embedded in Ag+Ag UrQMD simulations, whereas each ω is forced to decay into e^+e^- . The ratio of Monte-Carlo true reconstructed ω to the amount of initial ones directly gives access to efficiency and acceptance

$$\epsilon \times a^\omega|_{hard} = \frac{N_\omega^{reco}}{N_\omega^{in}} = \frac{9.18 \cdot 10^6}{9.24 \cdot 10^7} = 0.099.$$

$$\epsilon \times a^\omega|_{soft} = \frac{N_\omega^{reco}}{N_\omega^{in}} = \frac{9.70 \cdot 10^6}{9.24 \cdot 10^7} = 0.105. \quad (5.8)$$

As multiplicity one therefore derives

$$\omega_{mult}|_{0-40\%} = \frac{N_{exp}^\omega}{N_{evt} \cdot BR_{e^+e^-} \cdot \epsilon \times a^\omega} = (4.53 \pm 0.50|_{sys} \pm 0.63|_{stat}) \cdot 10^{-3} \quad (5.9)$$

as a mean value of the hard- ($N_{exp}^\omega = 159$) and soft-cut data ($N_{exp}^\omega = 187$). The systematic error is evaluated by a change in the fit range of the continuous background and regarding the different results in both cut sets. As the limited statistics does not allow for an analysis in centrality classes, according multiplicities are obtained based on a linear scaling with $\langle A_{part} \rangle$, for explicit values see tab. 5.3.

Centrality class	0 – 40 %	0 – 10 %	10 – 20 %	20 – 30 %	30 – 40 %
$\langle A_{part} \rangle$	101.3	160.9	114.5	81.1	56.5
ω_{mult}	(4.53	(7.20	(5.12	(3.63	(2.53
linear	$\pm 0.50 _{sys}$	$\pm 0.82 _{sys}$	$\pm 0.50 _{sys}$	$\pm 0.37 _{sys}$	$\pm 0.26 _{sys}$
$\langle A_{part} \rangle$	$\pm 0.63 _{stat}$	$\pm 1.04 _{stat}$	$\pm 0.64 _{stat}$	$\pm 0.47 _{stat}$	$\pm 0.33 _{stat}$
scaling	10^{-3}	10^{-3}	10^{-3}	10^{-3}	10^{-3}

Table 5.3: ω multiplicity in different centrality classes based on a linear scaling with $\langle A_{part} \rangle$.

5.5 COMPARISON TO TAPS MEASUREMENTS

The TAPS experiment has measured the production of π^0 and η mesons in C+C and Ca+Ca collisions at beam energies between $E_{beam} = 1 - 2 \text{ AGeV}$ [162] [163]. The corresponding data normalized to the system size is shown in fig. 5.9 as a function of beam energy together with polynomial fits. The HADES data extracted in the previous sections is added with red data points. At first, we note that for both mesons, the HADES data lay below the TAPS extrapolation. In case of the π^0 the differences are small. The difference of the Ag+Ag data to Ca+Ca (which is closer in system size) is in the same order as the TAPS difference between Ca+Ca and C+C. It can therefore be concluded that in case of the π^0 the work-in-progress HADES measurement is consistent with the TAPS systematics. In case of the η both TAPS measurements predict a similar multiplicity of about $N_\eta^{4\pi}/A_{part}(1.58 \text{ AGeV}) \approx 0.2$,

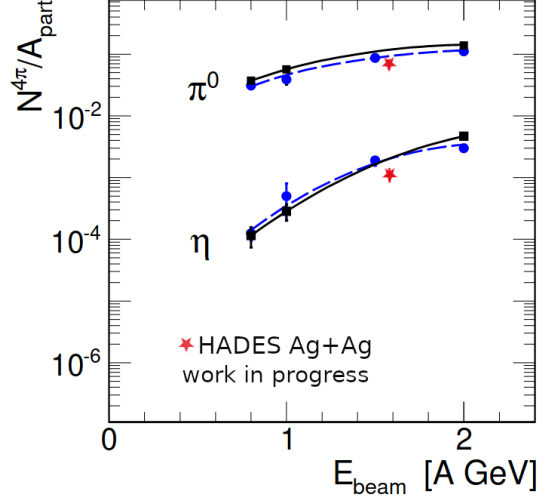


Figure 5.9: Comparison of the extracted π^0 and η multiplicity with TAPS measurements in C+C (black data points) and Ca+Ca (blue) collisions [162] [163]. Taken from [110] and modified.

which is almost a factor of two higher than the work-in progress HADES data. This deviation may partially arise from a possible system size dependence on the η production that remains unclear from the TAPS data. On the other hand there are still systematic uncertainties in the HADES analysis, that need to be reduced. Using event-mixing for the background estimation was proven to work, compare chapter 5.3. For efficiency and acceptance correction in bins of $p_t - y$ with subsequent extrapolation to uncovered phase space region simulation are currently developed including embedding into real data.

For the dielectron analysis performed in this work, the extracted π^0 multiplicity of $mult_{\pi^0} = 7.37$ is used for the 0 – 40% centrality data. In case of the η the multiplicity predicted by the transport model GiBUU of $mult_{\eta} = 0.14 \pm 0.42$ is used which corresponds to the mean value of the TAPS prediction and the HADES work-in-progress result. For the sub-centrality classes a linear A_{part} extrapolation based on these values is performed. For the interpretation of the results obtained from the dielectron analysis it is of key importance to gain a more precise knowledge on the η multiplicity.

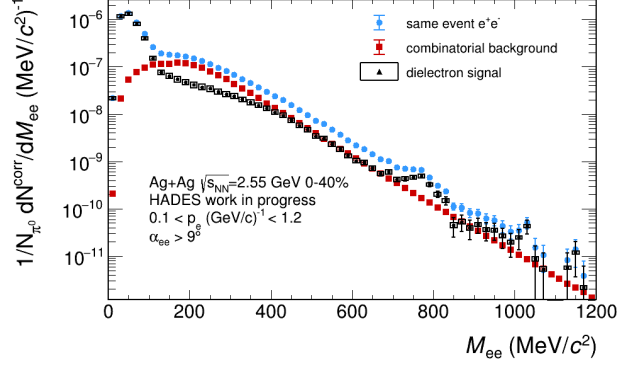
EXPERIMENTAL RESULTS

In this chapter the obtained dielectron signal is presented, discussed and analyzed in various aspects. To disentangle the different contributions to the dielectron signal, the dielectron signal spectrum is decomposed into the contributing sources performing hadronic cocktail simulation based on PLUTO and simulating the initial NN contributions using the transport model GiBUU. From the revealed in-medium contribution, the excess yield and mean temperature of the medium is extracted, which is compared to data previously measured by HADES. The analysis is furthermore performed in dependence on the system size, thus in different centrality classes. The (transverse) pair momentum dependence of the dielectron yield is studied.

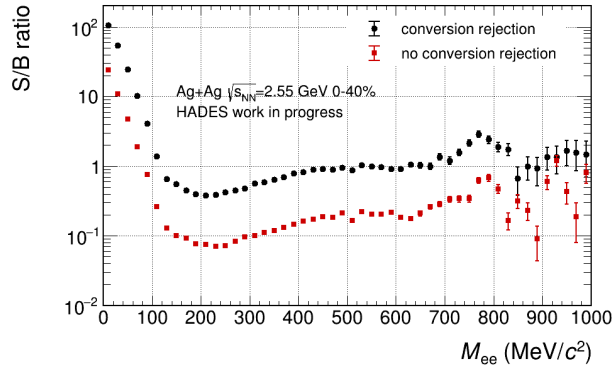
6.1 THE DIELECTRON SIGNAL

The centrality integrated (0 – 40%) dielectron invariant mass signal spectrum is shown in fig. 6.1a along with the reconstructed same-event e^+e^- pair spectrum and the calculated combinatorial background (chapter 4.10). The spectrum is efficiency, but not acceptance corrected (chapter 4.9) and the extracted pair efficiency correction factor is applied for invariant masses $M_{ee} < 120 \text{ MeV}/c^2$. An acceptance correction within the nominal HADES acceptance, where the shown data is restricted to ($0.1 \text{ GeV}/c < p_e < 1.2 \text{ GeV}/c$, $16^\circ < \Theta < 83^\circ$ and an additional acceptance gap for positrons), can be easily applied, as shown in chapter 4.9. Further extrapolation to the 4π yield can be subsequently applied model dependent. For conversion suppression purpose only pairs with opening angles $\alpha > 9^\circ$ are included. At small invariant masses ($M_{ee} < 100 \text{ MeV}/c^2$), the signal spectrum shows a strong peak originating from Dalitz decays of π^0 -mesons. Towards higher invariant masses the spectrum shows a kink at $M_{ee} \sim 400 \text{ MeV}/c^2$, where the $\eta \rightarrow e^+e^-\gamma$ contribution begins to die out. At even higher invariant masses, a second peak shows up which can be identified with a signature of the $\omega \rightarrow e^+e^-$ decay. In the pole mass region of the ϕ -meson ($m_\phi \sim 1020 \text{ MeV}/c^2$) the statistics of the data sample dies out, however exactly at the ϕ pole mass a statistically significant enhancement is observed although in one bin only. The amount of pairs after applying the corrections and subtracting the combinatorial background is summarized in tab. 6.1 in absolute values.

Fig. 6.1b shows the corresponding signal-to-background ratio including a comparison to the resulting values without using the conversion suppression based on the RICH detector. The improvement in terms of signal-to-background is about a factor of eight over the whole invariant mass range. The ratio peaks at $S/B > 100$ for small invariant masses followed by a steep decrease below $S/B = 1$ reaching its minimum at around $M_{ee} =$



(a)



(b)

Figure 6.1: Centrality integrated, efficiency corrected dielectron spectrum and the corresponding signal-to-background ratio. For the same-event and BG data only statistical errors are shown, whereas the systematic error calculated for the signal according to chapter 4.11 is shown as additional boxes.

$200 \text{ MeV}/c^2$. For invariant masses above $M_{ee} > 500 \text{ MeV}/c^2$ it is larger than unity and even reaches up to about $S/B > 3$ at the ω -meson pole mass.

Fig. 6.2 shows the anticipated S/B ratio obtained from simulation as published in the beam-time proposal. No conversion rejection based on the number of Cals in the RICH was anticipated here. A comparison to the achieved one (fig. 6.1b) reveals a gain of almost one order of magnitude in the data towards the simulations, which again proves the high performance of the HADES RICH detector. The simulations have been performed at the initially aimed at beam energy of $E_{kin}^{sim} = 1.65 \text{ AGeV}$ which had to be lowered to a value of $E_{kin}^{exp} = 1.58 \text{ AGeV}$ due to low accelerator performance.

$M_{ee} [\text{MeV}/c^2]$	< 200	200 - 700	700 - 800	> 800
N_{pairs}	$2.187 \cdot 10^6$	$1.860 \cdot 10^5$	1465	469

Table 6.1: Dielectron signal pairs in specific invariant mass bins.

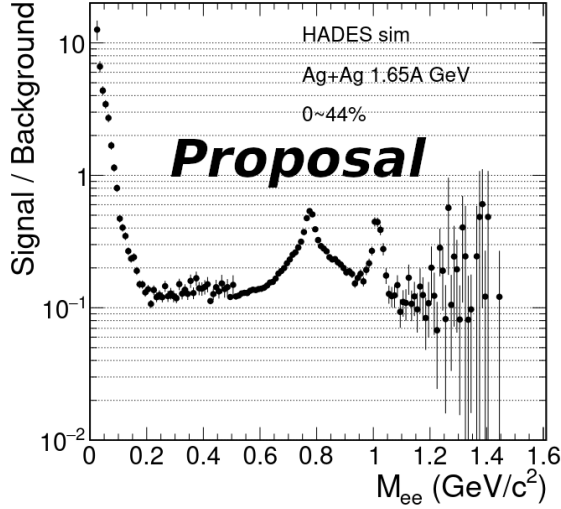


Figure 6.2: Simulated signal-to-background ratio as published in the beam-time proposal for the Ag+Ag data run. Taken from [160].

6.2 HADRONIC COCKTAIL SIMULATION

The dielectron signal spectrum shown in chapter 6.1 consists of different contributions. Namely, the total yield is build by dielectrons produced in initial NN collisions, e.g. bremsstrahlung, in-medium radiation and the decay of hadronic resonances after the fireball has expanded and cooled down. The main point of interest is the in-medium contribution. In order to reveal this contribution, the others have to be subtracted from the total signal. In this section, simulations are performed to study the hadronic cocktail component. For the initial NN contributions see chapter 6.3.

Relevant contributions arise from the pseudoscalar mesons π^0 and η being capable of Dalitz decays $\pi^0/\eta \rightarrow \gamma e^+ e^-$ and the vector mesons ω and ϕ . Besides the direct virtual photon decay of the vector mesons, in case of the ω

channel	hadron multiplicity	branching fraction	temperature
$\pi^0 \rightarrow e^+ e^- \gamma$	7.37	$1.17 \cdot 10^{-2}$	$T_1 = 49 \text{ MeV}$, $T_2 = 93 \text{ MeV}$
$\eta \rightarrow e^+ e^- \gamma$	0.14 ± 0.42	$6.90 \cdot 10^{-3}$	93 MeV
$\omega \rightarrow e^+ e^- \pi^0$	$4.53 \cdot 10^{-3}$	$7.70 \cdot 10^{-4}$	100 MeV
$\omega \rightarrow e^+ e^-$	$4.53 \cdot 10^{-3}$	$7.36 \cdot 10^{-5}$	100 MeV
$\phi \rightarrow e^+ e^-$	$1.53 \cdot 10^{-5}$	$2.97 \cdot 10^{-4}$	110 MeV

Table 6.2: Hadronic cocktail components at freeze-out together with according multiplicity, branching fraction and effective temperature used for PLUTO simulation.

also the Dalitz decay $\omega \rightarrow \pi^0 e^+ e^-$ is considered. As input the freeze-out multiplicities of these hadrons are required. These are extracted and discussed in chapter 5 for the π^0 , η and ω -mesons. As the statistics is not high enough in the $\phi \rightarrow e^+ e^-$ channel for a clear signal extraction, results from the HADES $\phi \rightarrow K^+ K^-$ analysis are used [164]. A compilation of the different channels, the according hadron multiplicities and the according branching fractions is also shown in tab. 6.2. The ρ meson is also capable of a leptonic decay channel ($\rho \rightarrow e^+ e^-$) and known to strongly contribute to the total dielectron yield (compare chapter 8). Nevertheless, it is not considered in the hadronic cocktail as it is that short-living, that it decays in the fireball, thus accounting to the in-medium radiation.

Using the Monte Carlo based simulation package PLUTO as event generator, thermal distributions of the relevant channels are produced, see sec. 2.7. In case of the π^0 two temperatures are used to reflect different production channels, compare also sec. 5.5. The input temperatures to the *PFireball* class originate from inverse slope fits of the spectra of charged pions, and the ϕ itself (in the $K^+ K^-$ channel) [157] [164]. The temperature of the η which can not be directly measured can be extrapolated from charged Kaons having a similar mass [164]. This relation between particle mass and effective temperature [165] can also be used to extrapolate a value for the ω . In general the effective temperature rises with the particle masses due to flow effects. The used temperature values are listed in tab. 6.2.

The generated events are embedded into full Ag+Ag UrQMD simulations (sec. 2.7), one per collision. The data is propagated through HGeant to simulate the interaction with the detector material. Afterwards, tracks are re-

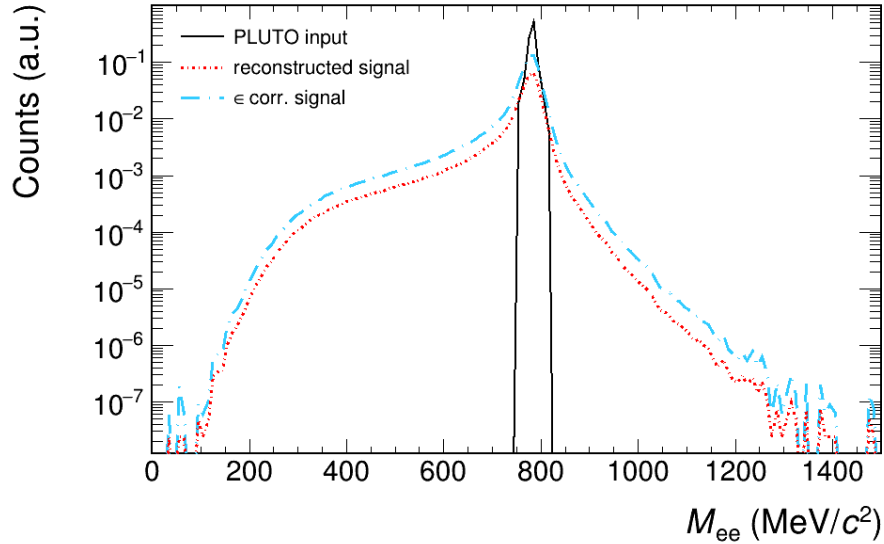


Figure 6.3: Invariant mass distribution of the $\omega \rightarrow e^+ e^-$ channel from the PLUTO input, after passing the electrons through HGeant and after additionally performing the efficiency correction.

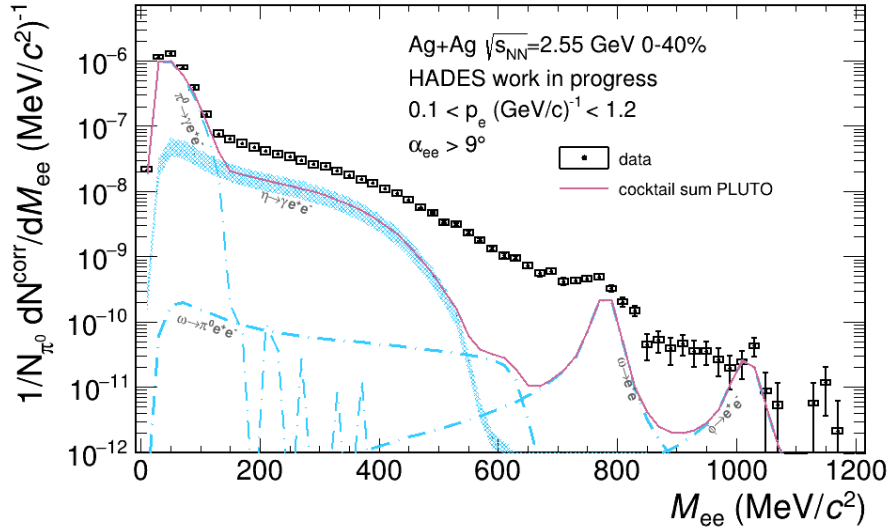


Figure 6.4: Hadronic cocktail simulation in 0 – 40% centrality.

constructed in the same way as in experimental data yielding the same acceptance and momentum smearing. For efficiency correction of simulated data, white electrons also embedded into simulated data are used taking into account differences in the efficiency in simulation and real data, compare sec. 4.9. Experimental data is corrected based on electrons embedded into real data. An overview on the effect of passing the simulated signal through HGeant and performing the efficiency correction is given in fig. 6.3 using the $\omega \rightarrow e^+e^-$ channel as example. The signal is broadened due to multiple scattering of the single electrons in the detector material and the momentum resolution of the detector. Towards small invariant masses a tail of the spectrum is observed, which originates from energy of the single electrons.

The resulting invariant mass spectra are shown together with the experimental data in fig. 6.4. According to the systematic uncertainty in the η multiplicity the corresponding contribution is represented by a broad band. For the whole invariant mass range the data shows a clear excess above the freeze out contribution of hadrons. This excess consists of radiation produced in the initial NN collisions and dielectrons radiated by the fireball itself. The initial NN contributions are studied in the next section.

The dielectron signal and hadronic cocktail simulations for the different 10% sub-centrality classes are shown in Appendix D, fig. D.1 - D.4. Also the simulated NN contributions extracted in the following chapter are already included.

6.3 NN REFERENCE

Besides the hadronic cocktail contributions (see sec. 6.2) also the contribution from initial NN collisions has to be taken into account to reveal the in-medium contribution to the total measured dielectron yield. In March 2022 HADES has measured p+p collisions at the same energy in order to experimentally extract this contribution. However, the analysis is of course still pending. Therefore the *Giessen BUU project*, GiBUU model, is used to simulate these contributions. It is an hadronic transport model providing numerical simulations of nuclear reactions [166] [167]. It provides a unified transport framework and underlying theory for a broad energy range from elementary to heavy ion collisions. Being an hadronic model, the basic degrees of freedom are baryons and mesons, where in total 61 baryons and 31 mesons are included with parameters according to the PDG compilation. The central piece of the GiBUU is the *Boltzmann-Uehling-Uhlenbeck* (BUU) equation, which is solved for each particle species yielding the spectral particle phase-space distributions $F(x, p)$ [168]. The GiBUU version used in this work is the 2021 patch 1 release from 11th of Mai 2021. The jobcards used to perform the simulation have been set up in collaboration with Alexei Lariouov and are attached in Apendix C. The event type of the collision is set to *HiPion A (12)*, which is commonly used for elementary reaction. The statistics of the run is specified by the number of ensembles, the amount of runs with the same energy and the number of projectiles per ensemble. In case of p+n collisions, the default production cross section for the η meson is scaled down by almost a factor two, in order to reproduce experimental results from the DLS experiment [169]. All the other settings, those that are reset in the jobcard and also those that are not explicitly mentioned (thus they stay as default values in the GiBUU 2021 release) are the same as in [170]. The obtained invariant mass spectra are shown in fig. 6.5 for both collision types.

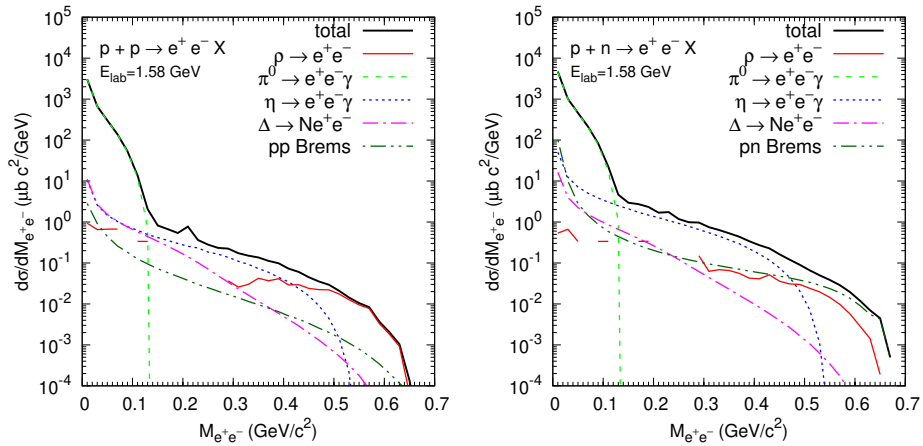


Figure 6.5: Invariant mass spectra for pp (left) and pn (right) collisions simulated with GiBUU.

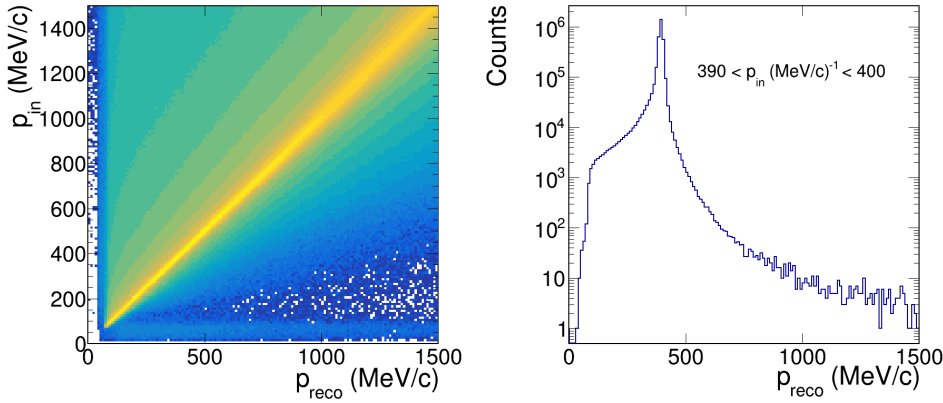


Figure 6.6: Momentum smearing applied to GiBUU simulation, extracted from single electron simulation embedded in real data. Left: The initial electron momentum vs. the reconstructed momentum. The distributions peaks at $p_{in} = p_{reco}$ with a Gaussian broadening caused by the detector resolution. The width varies with the momentum. Additionally, a tail towards lower momenta is observed, corresponding to energy loss. Right: Projection for input momenta $390 \text{ MeV}/c < p_{in} < 400 \text{ MeV}/c$.

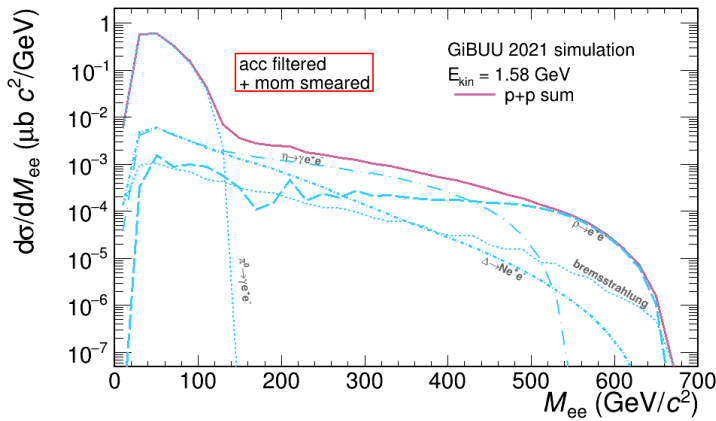


Figure 6.7: Acceptance filtered and momentum smeared dielectron spectrum in p+p GiBUU simulation.

In elementary reactions no Fermi-Motion is present that may enhance the available energy, thus no formation of ω or even ϕ mesons is possible. As the 2019 HADES setup is not implemented in GiBUU, no acceptance filtering can be performed in GiBUU directly. However, GiBUU also provides the possibility of an output of the four-momentum properties of all single electrons produced. Based on this information, an acceptance filtering can be applied which is set up using white electron simulation. Acceptance is defined - as commonly in HADES - by a particle crossing the active detector material of at least four of the six layers in each of the four MDCs. Additionally, the lower and higher momentum cutoff included in the HADES data as

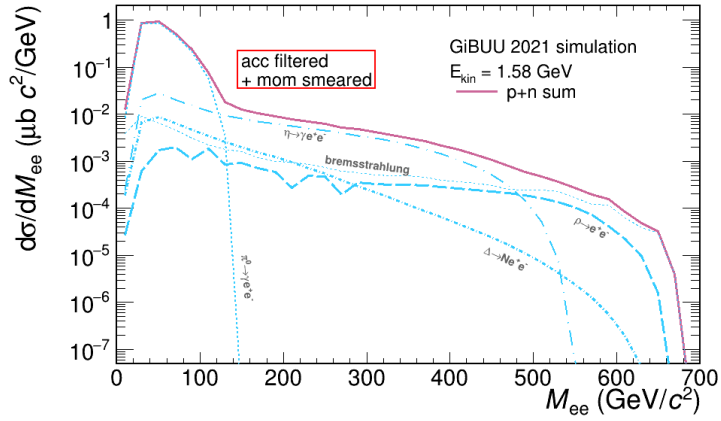


Figure 6.8: Acceptance filtered and momentum smeared dielectron spectrum in p+n GiBUU simulation.

well as the pair opening angle restriction to values $\alpha_{ee} > 9^\circ$ is applied. Furthermore the experimental momentum resolution is included to the GiBUU data: The GiBUU momenta of single leptons are smeared statistically based on the resolution $\Delta p/p$ observed in electron simulations embedded in real data, compare fig. 6.6. The obtained spectra after acceptance filtering and momentum smearing are shown in fig. 6.7, 6.8. Furthermore, the GiBUU spectra have to be normalized to the total cross section in the elementary reactions being available at the GiBUU database [167], namely $\sigma_{pp} = 55 \text{ mb}$

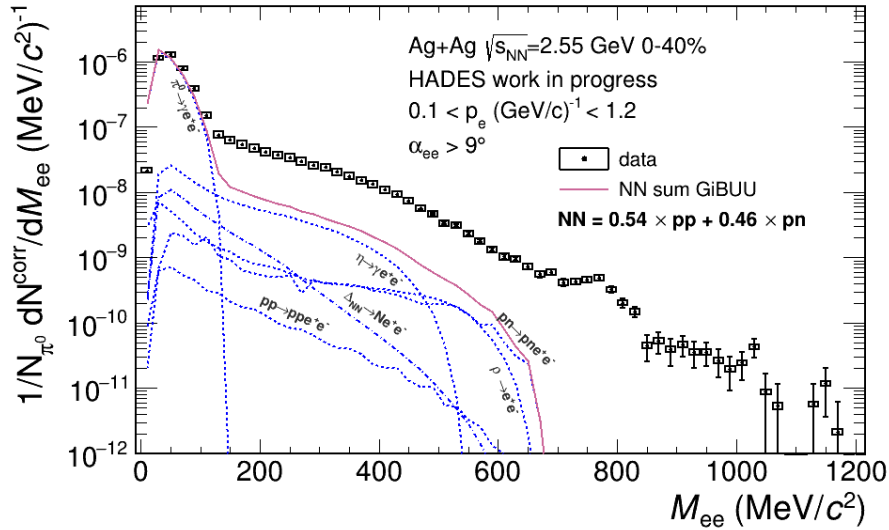


Figure 6.9: NN reference calculated according to eq. (6.1) based on GiBUU p+p and p+n simulation. The contributing channels are individually shown by dashed blue lines.

and $\sigma_{pn} = 41 \text{ mb}$, that are used as simulation input. To account for the correct ratio of pp to pn collisions, the NN is reference is built using

$$\frac{dN_{ref}^{NN}}{dM_{ee}} = \langle A_{part} \rangle \left(0.54 \frac{dN^{pp}}{dM_{ee}} + 0.46 \frac{dN^{pn}}{dM_{ee}} \right) \quad (6.1)$$

with the prefactors reflecting the isospin composition of the collision system [59]. The resulting NN reference is shown in fig. 6.9 together with the Ag+Ag data. The contributions arising from the π^0 and η are already included in the hadronic cocktail and are therefore not considered again. The short-lived ρ meson decays in the medium in A+A collisions and therefore accounts to the in-medium contribution. As additional channels therefore p+n and p+p bremsstrahlung as well as the $\Delta \rightarrow Ne^+e^-$ channel is taken into account. The Ag+Ag dielectron signal spectrum together with these initial NN channels and the hadronic cocktail is shown in fig. 6.10. The additional NN channels only have a minor impact on the total yield. Over the whole invariant mass range the data shows a clear enhancement compared to the sum of the hadronic freeze out contribution and the initial NN contributions. This excess radiation is emitted directly from the fireball and is therefore called in-medium radiation. It is studied in detail in the following sections.

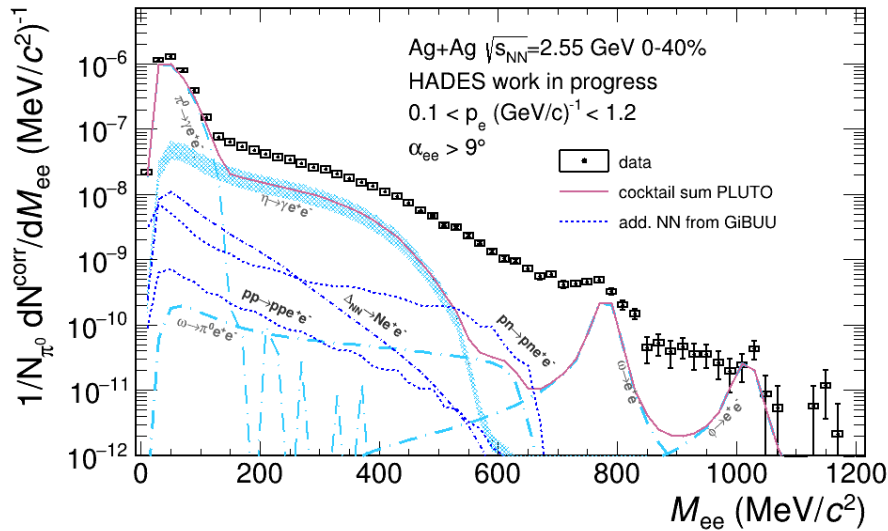


Figure 6.10: Hadronic cocktail and relevant NN channels from GiBUU simulation. See *text* for details.

6.4 ESTIMATION OF THE MEDIUM TEMPERATURE

The emission rate of dileptons from a thermal source per volume and time d^4x in a four-momentum bin d^4q is given by

$$\frac{dN_{ll}}{d^4x d^4q} = -\frac{\alpha_{em}^2}{M^2 \pi^3} f^B(q_0; T) \text{Im}\Pi_{EM}(M, q; \mu_B, T). \quad (6.2)$$

with $\text{Im}\Pi_{EM}(M, q; \mu_B, T)$ being the in-medium spectral function of the electromagnetic current. As $\text{Im}\Pi_{EM}/M^2$ is constant for $M_{ee} > 200 \text{ MeV}/c^2$, the spectrum is dominated by f^B and can therefore be fitted with $dN/dM_{ee} \propto (M_{ee})^{3/2} \exp(-M_{ee}/kT)$ (black-body spectral distribution) [59].

The in-medium contribution of the dielectron spectrum is obtained subtracting the hadronic cocktail and initial NN contributions, see fig. 6.10. The resulting in-medium contribution is restricted to the HADES acceptance, which might bias the slope of the spectrum. Therefore an acceptance correction is performed. It is based on $\rho \rightarrow e^+e^-$ PLUTO simulation as this channel dominates the in-medium contribution. The correction factor $1/a$ is obtained as the ratio of input dielectrons normalized to the amount of reconstructed dielectrons and shown in fig. 6.11 as a function of invariant mass. It is almost constant at high invariant masses with $1/a \approx 3.5$, but strongly rises towards small invariant masses. This rise is caused by the momentum cutoff at $p_e = 100 \text{ MeV}/c^2$, the pair opening angle restriction $\alpha_{aa} < 9^\circ$ and the acceptance gap for positrons at small polar angles resulting in a significant drop in acceptance towards low invariant masses. The $\rho \rightarrow e^+e^-$ is simulated only down to the mass of the two pion threshold. For smaller invariant masses down to $M_{ee} = 200 \text{ MeV}/c^2$ the acceptance correction is extrapolated from a fit to the data in the region $280 \text{ MeV}/c^2 < M_{ee} < 500 \text{ MeV}/c^2$. Please

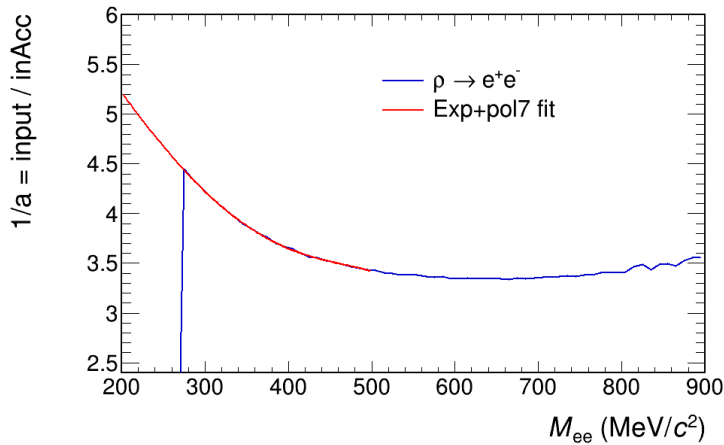


Figure 6.11: Acceptance correction obtained from PLUTO $\rho \rightarrow e^+e^-$ simulation. For small invariant masses an extrapolation is used based on a fit in the invariant mass region $280 \text{ MeV}/c^2 < M_{ee} < 500 \text{ MeV}/c^2$.

note, that the derived acceptance correction is applied to the dielectron excess spectrum for which all freeze-out contributions and the simulated NN reference have been subtracted. Thus no correction accounting for different kinematic properties of dielectrons originating from other channels than the $\rho \rightarrow e^+e^-$ are necessary.

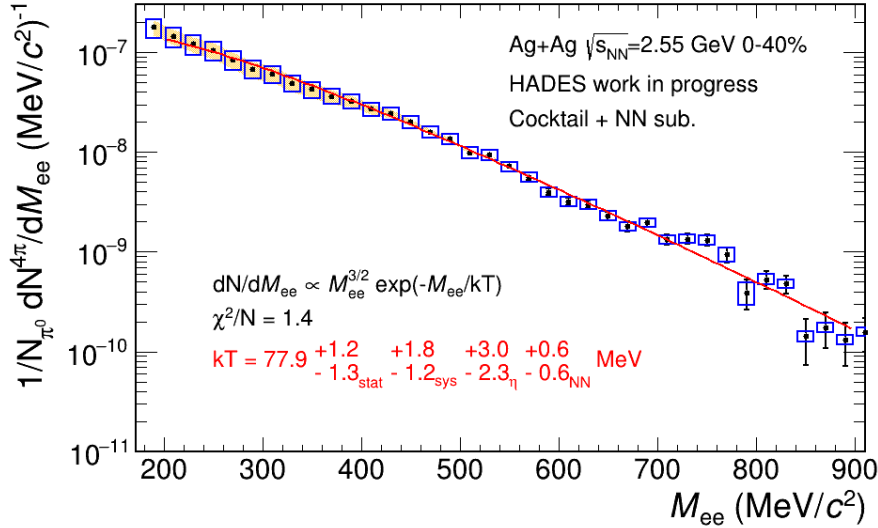


Figure 6.12: Temperatur estimation in 0 – 40% centrality. The invariant mass spectrum is fitted in the range $200 \text{ MeV}/c^2 < M_{ee} < 900 \text{ MeV}/c^2$ with a thermal function. The yellow shaded area corresponds to systematic uncertainties arising from the η multiplicity.

The acceptance corrected dielectron excess spectrum is shown in fig. 6.12 for the 0 – 40% centrality class. A thermal fit in the invariant mass range $200 \text{ MeV}/c^2 < M_{ee} < 900 \text{ MeV}/c^2$ reveals a temperature of $kT = 77.9^{+3.7}_{-2.9} \text{ MeV}$. The errors combine statistical and systematic uncertainties, which are dominated by the uncertainty in the η multiplicity shown as a yellow band around the data points. This temperature has to be interpreted as weighted average temperature of the medium, as dielectrons are emitted during all stages of the fireball evolution. It compares well with the temperature of $kT^{Au+Au} = 71.8 \pm 2.1 \text{ MeV}$ measured in Au+Au collisions by HADES at slightly lower beam energy of $E_{kin} = 1.23 \text{ AGeV}$ [59].

The high statistics of the data allow also to study the medium temperature as a function of centrality. Corresponding results to fig. 6.12 in the 10% subcentrality classes are shown in the Appendix B, sec. D.2. For the two most peripheral bins, the fit range is restricted to $200 \text{ MeV}/c^2 < M_{ee} < 700 \text{ MeV}/c^2$ due to limited statistics in the high invariant mass region. The obtained inverse slope of the fit function is show as a function of the participant number in fig. 6.13. The data points all align at similar values, indicating that the temperature is independent from the system size at least up to the 40% most central collisions. This observation also holds for the most peripheral data

point, where a contamination by Ag+C collisions is known (see e.g. fig. 4.4). This has a stronger impact on the excess yield, compare sec. 6.5.

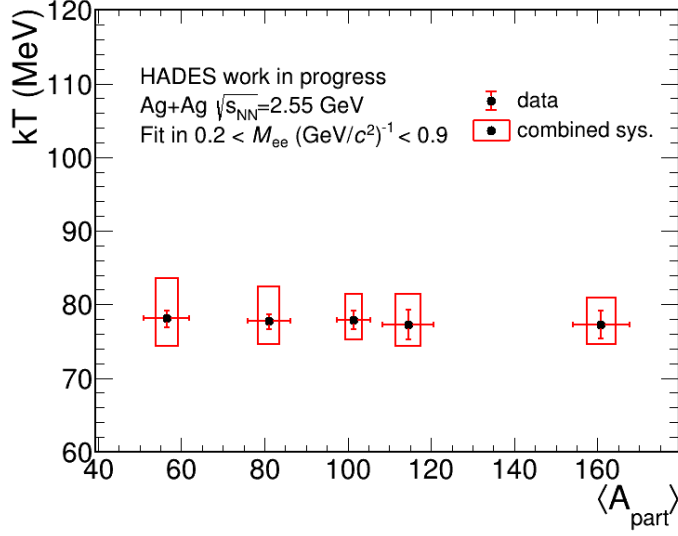


Figure 6.13: Dependence of the medium temperature on the centrality of the collision (four 10% centrality bins between 0% and 40% and the integrated 0 – 40% centrality bin).

6.5 THE DIELECTRON EXCESS

As dielectron excess radiation, the additional yield in A+A collisions with respect to elementary reaction is labeled. In elementary reactions, the total dielectron yield consists of bremsstrahlung and the decay of produced hadrons/hadronic resonances only. The dielectron excess therefore corresponds to the additional in-medium component observed in A+A collisions. One possibility of quantification of the excess yield is to define the dielectron excess ratio R_{AA} as the ratio of the dielectron yield in A+A and elementary collisions. A normalization to the same amount of primary interactions is provided by scaling the dielectron yield to the π^0 production multiplicity.

$$R_{AA} = \frac{N_{\pi^0}^{NN} dN^{AA}/dM}{N_{\pi^0}^{AA} dN^{NN}/dM} \quad (6.3)$$

At the Ag+Ag energy of $\sqrt{s_{NN}} = 2.55 \text{ GeV}$ currently no NN reference is available. Therefore, data taken at a slightly lower energy of $\sqrt{s_{NN}} = 2.42 \text{ GeV}$ is used [171]. The difference in energy has major impact on the η production as the $N(1535)$ resonance (branching fraction in $N\eta$ of 30 – 55% [6]) can not be formed at the NN, but at the Ag+Ag energy. Therefore the $\eta \rightarrow \gamma e^+ e^-$ contribution has to be subtracted from both data sets, the Ag+Ag data and the NN reference before calculating R_{AA} . The different spectra are

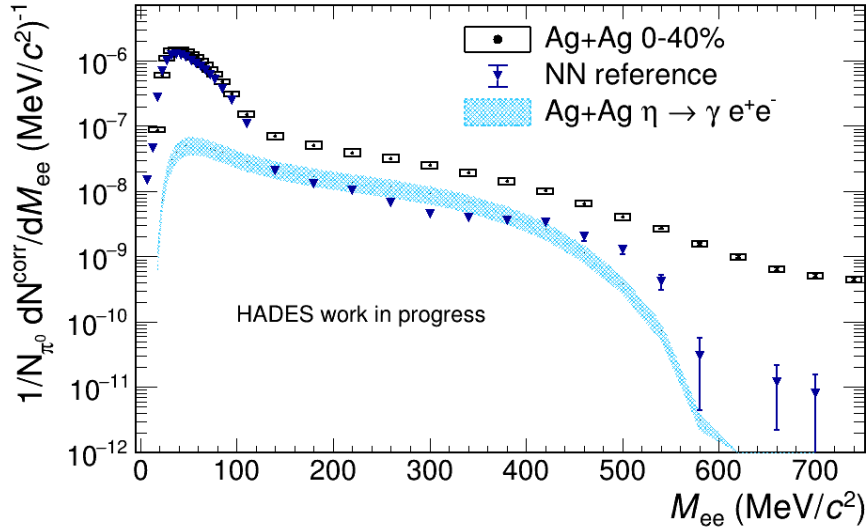


Figure 6.14: NN reference measured at $\sqrt{s} = 2.42 \text{ GeV}$ together with the $\eta \rightarrow \gamma e^+ e^-$ PLUTO cocktail component for $\sqrt{s_{NN}} = 2.55 \text{ GeV}$ and the dielectron signal in Ag+Ag collisions at $\sqrt{s_{NN}} = 2.55 \text{ GeV}$. The η component at $\sqrt{s} = 2.42 \text{ GeV}$ is already subtracted from the NN reference.

shown in fig. 6.14 with the systematic uncertainties in the η contribution ($\Delta mult_\eta / mult_\eta = 0.3$) at $\sqrt{s_{NN}} = 2.55 \text{ GeV}$ represented by a band.

Due to different magnetic field settings in the data taking of the Ag+Ag data and the NN reference at $\sqrt{s_{NN}} = 2.42 \text{ GeV}$, slight acceptance differences

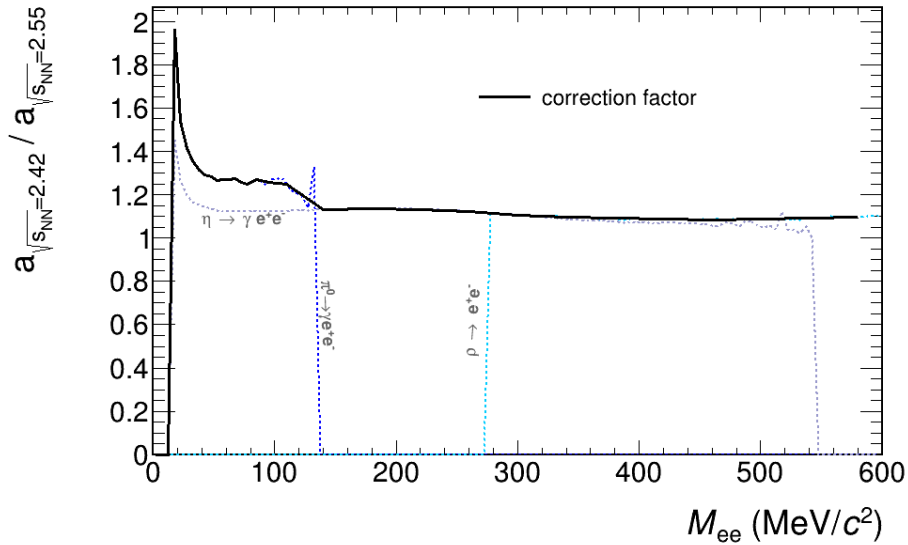


Figure 6.15: Relative acceptance correction for $\sqrt{s_{NN}} = 2.55 \text{ GeV}$ data wrt. $\sqrt{s_{NN}} = 2.42 \text{ GeV}$ arising from the different magnetic field strength used in the data takings.

arise. These are most prominent in the low invariant mass region, where low momentum electrons dominate the sample. This effect is taken into account correcting the Ag+Ag data with the relative acceptance of both data sets. The acceptance in both data sets is extracted passing PLUTO generated thermal distributions of the dominant hadronic contributions through HGeant. The acceptance ratio for the $\pi^0/\eta \rightarrow \gamma e^+ e^-$ and $\rho \rightarrow e^+ e^-$ contributions is shown in fig. 6.15. For invariant masses $M_{ee} < 140 \text{ MeV}/c^2$ the correction factor is extracted from the π^0 -Dalitz simulation. Afterwards the ρ contribution becomes dominant which perfectly agrees with the η -Dalitz simulation in the overlapping region. Differences in the η and π^0 acceptances in the low energy regime originate from different masses and thus differences in the decay electron momenta and their opening angles.

Applying this correction on the Ag+Ag data, the resulting dielectron excess ratio is shown in fig. 6.16 in black data points. At small invariant masses it only slightly exceeds unity as here the π^0 contribution is dominant and the excess is only a minor contribution to the total yield. Beyond the π^0 the R_{AA} significantly rises reaching a mean value of $\langle R_{AA}^{Ag+Ag} \rangle = 3.05$ in the range $130 \text{ MeV}/c^2 < M_{ee} < 520 \text{ MeV}/c^2$. The yellow band reflects systematic uncertainties arising from the η multiplicity shown as brackets for individual data points.

Corresponding data is also available for Au+Au collisions measured at $\sqrt{s_{NN}} = 2.42 \text{ GeV}$ and Ar+KCl collisions at $\sqrt{s_{NN}} = 3.18 \text{ GeV}$. In both data sets the same trend with a slight excess over unity at small invariant masses followed by a sudden increase beyond the π^0 mass is observed. However, the abso-

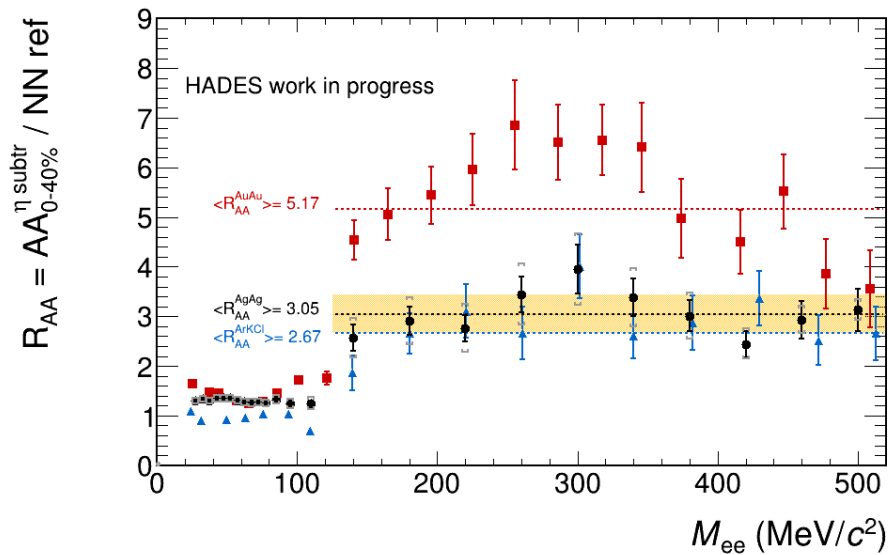


Figure 6.16: The dielectron excess ratio R_{AA} . The yellow shaded area corresponds to the systematic error dominated by the η multiplicity. Data from Au+Au ($\sqrt{s_{NN}} = 2.42 \text{ GeV}$, red) and Ar+KCl ($\sqrt{s_{NN}} = 3.18 \text{ GeV}$, blue) are also shown. The mean excess for $M_{ee} > 130 \text{ MeV}/c^2$ is fitted by a constant.

System	Ar+KCl	Ag+Ag	Au+Au
$\sqrt{s_{NN}}$ [GeV]	3.18	2.55	2.42
$\langle A_{part} \rangle$	38.5	101.3	173
$\langle R_{AA} \rangle$ ($M_{ee} > 130 \text{ MeV}/c^2$)	2.67	3.05	5.17

Table 6.3: The dielectron excess ratio R_{AA} measured in different systems at different energies.

lute values strongly differ indicating a rise of the R_{AA} with the system size, see tab. 6.3 for a compilation of energy, system size and R_{AA} in the different systems. In order to further classify the dependence of the R_{AA} on the system size, a reduction of the systematic error in the Ag+Ag data, namely a precise knowledge of the η production multiplicity is needed. Besides the reduction of systematic errors in the corresponding analysis, also an experimental NN reference at $\sqrt{s_{NN}} = 2.55 \text{ GeV}$ will reduce the systematic error from extrapolating between energies.

The system size dependence of the dielectron excess yield can also be studied calculating the R_{AA} for the different 10% centrality classes as shown in fig. 6.17 (compare Appendix D, fig. D.1 - D.4 for the dielectron signal spectra). Assuming the η multiplicity to scale linearly with the number of participating nucleons, the systematic uncertainty in the η multiplicity itself does not influence the relative position of the excess ratios. These align or-

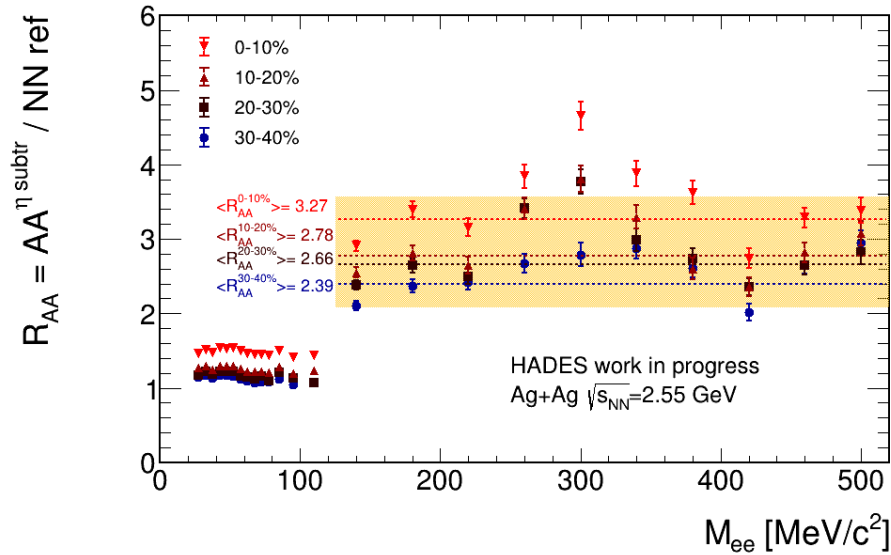


Figure 6.17: Centrality dependence of the dielectron excess yield. Systematic errors are not shown individually as they do not influence the relative position of the data points assuming $\eta_{mult} \propto A_{part}$. The yellow band indicates the overall systematic error originating from the uncertainty in the η multiplicity resulting in $\Delta R_{AA}^{sys,\eta} = 0.3$.

Centrality	0 – 10%	10 – 20%	20 – 30%	30 – 40%
$\langle R_{AA} \rangle$	3.27	2.78	2.66	2.39
$\langle A_{part} \rangle$	160.9	114.5	81.1	56.5

Table 6.4: The R_{AA} measured in different centralities for Ag+Ag collisions at $\sqrt{s_{NN}} = 2.55 \text{ GeV}$.

dered by the system size with average values fitted for $M_{ee} > 125 \text{ MeV}/c^2$ of $\langle R_{AA}^{0-10\%} \rangle = 3.27$ down to $\langle R_{AA}^{30-40\%} \rangle = 2.39$. A compilation of the R_{AA} values and the number of participants in the according centrality classes is given in tab. 6.4. The increase in R_{AA} is observed to scale with $\propto A_{part}^\alpha$, $\alpha \sim 0.5$. The excess yield scaling with the system size can be understood by a longer lifetime of a larger fireball. However, the most peripheral centrality data appears not to fit in this picture. However, in peripheral collisions a contamination by Ag+C collisions is present (see also fig. 4.4 and the corresponding text), which should affect the excess ratio significantly towards lower values.

The system size dependence of the excess yield can also be directly visualized by the integral of the spectrum, which is of course also connected to the life-time of the medium. To reveal this integrated excess yield, the hadronic cocktail contributions (see fig. 6.4) and initial contributions (fig. 6.10), namely the bremsstrahlung components and initial Δ -resonance formation with sub-

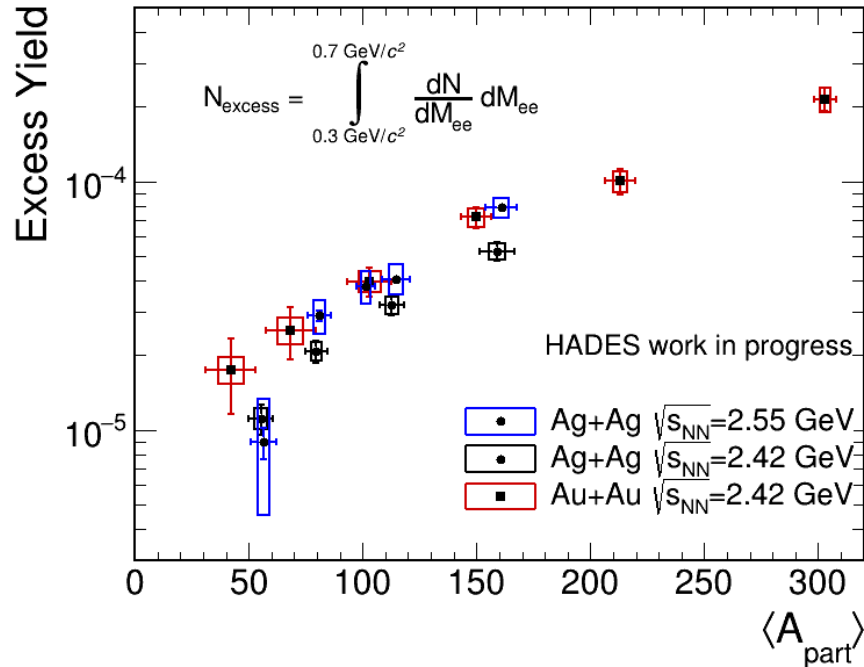


Figure 6.18: Centrality dependence of the integrated dielectron excess yield. Ag+Ag and Au+Au data measured at $\sqrt{s_{NN}} = 2.42$ are shown for comparison.

sequent electromagnetic decay have to be subtracted. The excess yield is measured in the invariant mass region $300 \text{ MeV}/c^2 < M_{ee} < 700 \text{ MeV}/c^2$ having the advantage, that this region is dominated by the excess and mainly consists of the in-medium $\rho \rightarrow e^+e^-$ contribution. The impact of systematic uncertainties in the hadron multiplicities (and the NN contributions) is therefore minimized. The results are shown in fig. 6.18 together with data measured in Ag+Ag and Au+Au collisions at $\sqrt{s_{NN}} = 2.42$. The rise of the excess with the number of participants is much more pronounced in this representation compared to the R_{AA} representation as no normalization to the system size, i.e. the π^0 multiplicity is performed. The data points roughly fall together with the Au+Au data except the most peripheral data point, which most likely is connected to Ag+C contamination in the 30 – 40% centrality class. The significantly lower Ag+Ag data points measured at $\sqrt{s_{NN}} = 2.42$ are currently under investigation [172]. One possible interpretation of the data would be linked to a temperature dependence of the excess yield. Thus the excess yield increases with system size but also with temperature.

6.6 (TRANSVERSE) MOMENTUM-DIFFERENTIAL ANALYSIS

With mean life times of $\tau_\omega = 7.5 \cdot 10^{-23} \text{ s}$ and $\tau_\phi = 1.5 \cdot 10^{-22} \text{ s}$ of the vector mesons ω and ϕ their decay length is in the order of a few tenth of fermi (e.g. $s_\omega = (p/m) \cdot 22.5 \text{ fm}$). This value is in the same order as the estimated fireball lifetime of about $\tau_{fb} \sim 25 \text{ fm}$ [174], thus indicating that a fraction of the produced vector mesons decays in the fireball, whereas a significant part also decays outside the medium. The latter one can be enhanced selecting for high pair momenta in the reconstructed dielectron sample. Such an analysis has previously been performed with HADES in $p + Nb$ collisions at $\sqrt{s_{NN}} = 3.18 \text{ GeV}$ and is compared to $p + p$ reference data in fig. 6.19

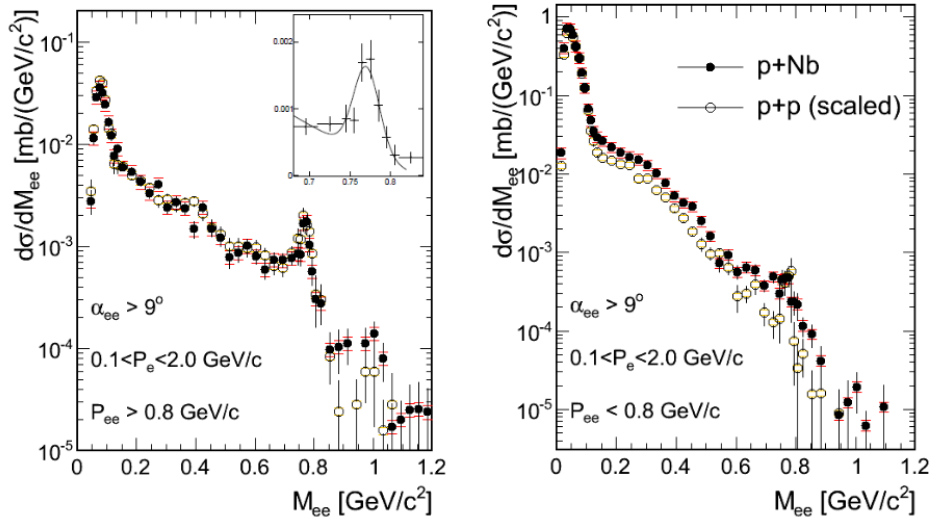


Figure 6.19: Dielectron spectra in $p + Nb$ collisions at $\sqrt{s_{NN}} = 3.18 \text{ GeV}$ and comparison to $p + p$ data measured by HADES. Taken from [173].

[173]. The dielectron sample has been split into pair momenta exceeding $p_{ee} > 800 \text{ MeV}/c$ and those below. In the high momentum data, the $p + Nb$ agrees well with the $p+p$ reference data both showing a clear signal peak of the ω meson which is slightly shifted to lower values of invariant mass ($\mu \approx 770 \text{ MeV}/c^2$, see the inset in fig. 6.19). This effect is shown to correspond to energy loss of the electrons in the detector material only. The fitted width is in the order of $\sigma = 13 - 19 \text{ MeV}/c^2$ giving no hint to any broadening in nuclear matter. The low momentum data on the other hand show a significant enhancement in $p + Nb$ below the ω pole mass paired with an almost completely vanished peak structure. The interpretation is, that the observed excess originates from ρ -like channels as it is the dominating contribution to medium radiation, whereas the ω disappearance is linked to in-medium absorption.

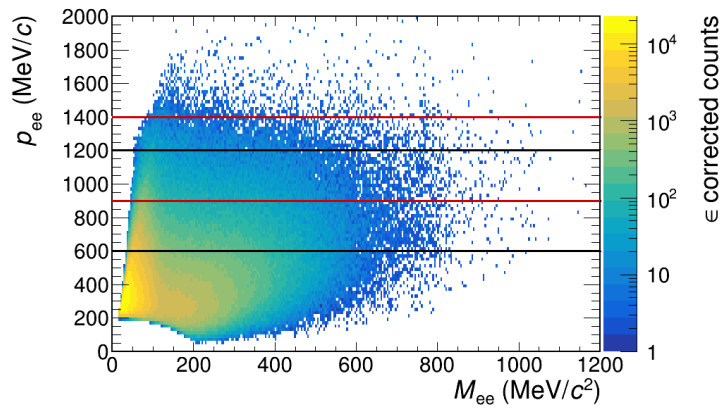
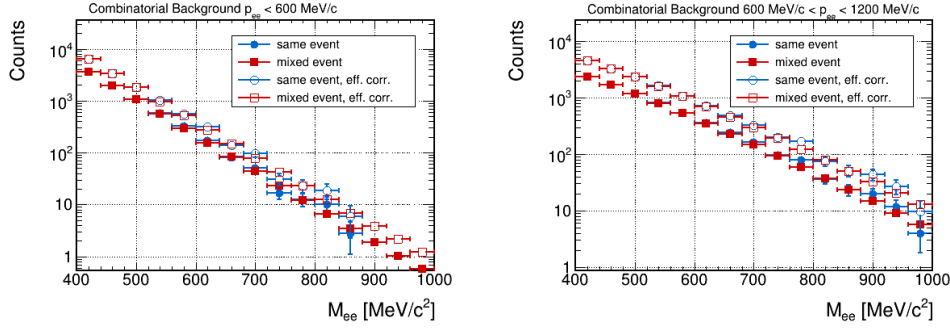
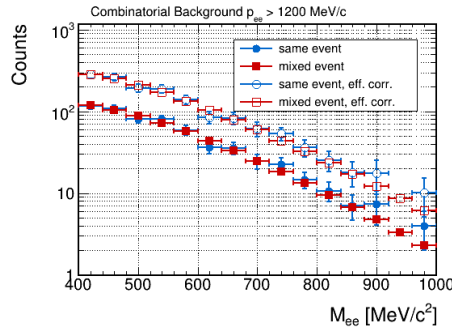


Figure 6.20: Two dimensional efficiency corrected same-event dielectron spectrum in pair momentum p_{ee} vs. invariant mass M_{ee} . The bins in pair momentum are indicated by black (3 bins) and additional in red (5 bins) horizontal lines.

The HADES $Ag + Ag$ data sample provides sufficient statistics in the ω mass region to also perform a momentum differential analysis. The reconstructed same-event dielectron spectrum is shown in fig. 6.20. The analysis is carried out identically as described in section 4, including the efficiency correction. The combinatorial background is estimated from the geometrical mean of same-event like-sign pairs weighted with the k -factor according to eq. 4.20. As the statistics is further reduced introducing the momentum binning, it becomes even more crucial to use mixed-event spectra for the background estimation at high invariant masses. The comparison between same-event and mixed-event background is shown in fig. 6.21 in the case of three bins in pair momentum, namely $p_{ee} \leq 600 \text{ MeV}/c$ referred to as low momentum bin in the following, the intermediate momentum bin in the range $600 \text{ MeV}/c < p_{ee} \leq 1200 \text{ MeV}/c$ and an high momentum bin with $p_{ee} > 1200 \text{ MeV}/c$. For normalization of the mixed event spectra the invariant mass region of $400 \text{ MeV}/c^2 < M_{ee} < 700 \text{ MeV}/c^2$ is used. In all three bins of pair momentum the agreement is on a high level and small devia-



(a) Low pair momenta $p_{ee} \leq 600 \text{ MeV}/c$. (b) Medium pair momenta $600 \text{ MeV}/c < p_{ee} \leq 1200 \text{ MeV}/c$.

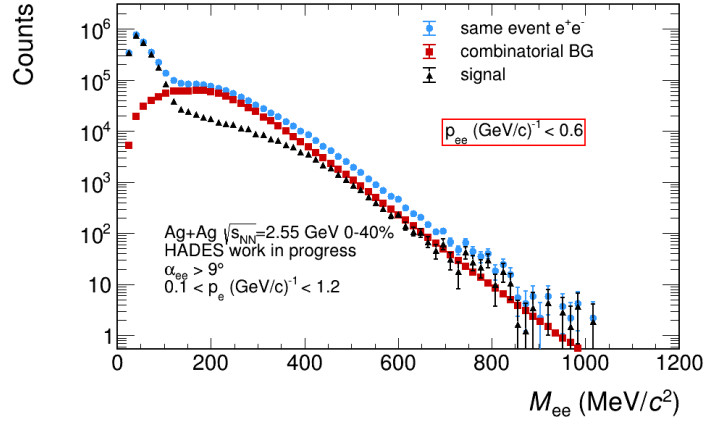
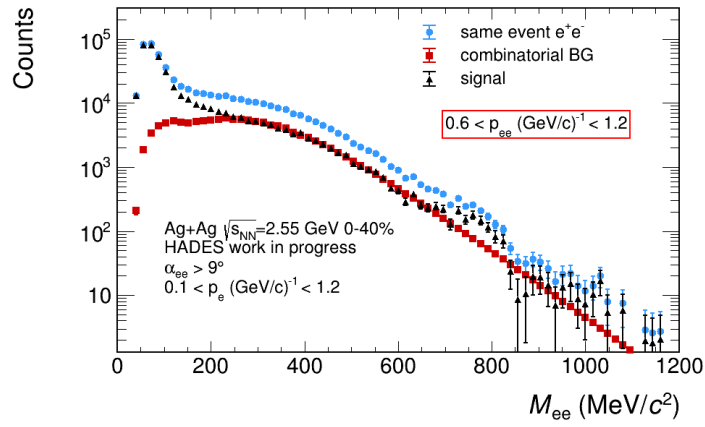
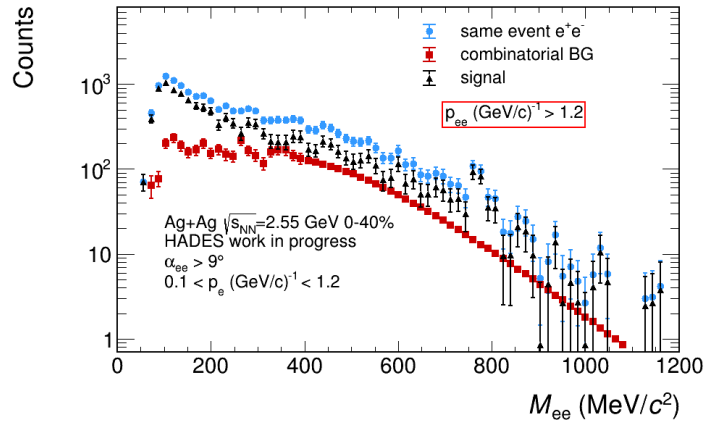


(c) High pair momenta $p_{ee} > 1200 \text{ MeV}/c$.

Figure 6.21: Comparison of the calculated combinatorial background distributions from same-event and mixed-event like-sign dielectron spectra. Open markers denote efficiency corrected data, while filled markers represent raw data.

tions clearly originate from the lack of statistics in the same-event spectra. For $M_{ee} > 400 \text{ MeV}/c^2$ the combinatorial background is therefore calculated from the mixed-event spectra. Furthermore, the effect of the efficiency correction is also shown in the comparison of the spectra, fig. 6.21. Being based on single lepton efficiencies extracted from simulated electrons/positrons into real data, it appears as an almost constant factor scaling up the reconstructed spectra.

The resulting dielectron spectra in bins of the pair momentum are shown in fig. 6.22, the amount of reconstructed pairs before and after the efficiency correction listed in tab. 6.5. The small pair momentum bin contains the major part of the π^0 -Dalitz yield, which vanishes almost completely for high pair momenta. This reduction is also seen in fig. 6.19, whereas the yield at high masses increases. Statistics decreases towards higher momenta as do the combinatorics (but much stronger due to the quadratic correlation), resulting in $S/B \gtrsim 1$ in the medium momentum bin over the full invariant mass range and $S/B \gg 1$ with $S/B|_{M_{ee}=m_\omega} \approx 8$ in the high momentum bin. Strong differences in the line-shape of the dielectron spectra are visible in the $\rho - \omega$ mass region. Whereas a broad excess above the continuum is observed

(a) Low pair momenta $p_{ee} \leq 600 \text{ MeV}/c$.(b) Medium pair momenta $600 \text{ MeV}/c < p_{ee} \leq 1200 \text{ MeV}/c$.(c) High pair momenta $p_{ee} > 1200 \text{ MeV}/c$.Figure 6.22: Efficiency corrected **same-event**, **combinatorial background** and **signal** spectra in three bins of pair momentum.

$p_{ee} [MeV/c]$		N_{pair} in $M_{ee} [MeV/c^2]$ bins			
		< 200	200 - 600	600 - 800	> 800
$p_{ee} \leq 600$	uncorr.	$1.042 \cdot 10^6$	$6.564 \cdot 10^4$	434	26
	ϵ corr.	$2.342 \cdot 10^6$	$1.431 \cdot 10^5$	941	56
$600 < p_{ee} \leq 1200$	uncorr.	$1.488 \cdot 10^5$	$3.770 \cdot 10^4$	1230	136
	ϵ corr.	$3.271 \cdot 10^5$	$8.782 \cdot 10^4$	3075	338
$p_{ee} > 1200$	uncorr.	$2.111 \cdot 10^3$	$1.936 \cdot 10^3$	261	56
	ϵ corr.	$6.261 \cdot 10^3$	$5.727 \cdot 10^3$	850	157

Table 6.5: Reconstructed and efficiency corrected number of pairs in bins of momentum and invariant mass.

in the small and medium momentum bins, a peak structure is visible in the high momentum data. With respect to this change in line-shape, the signal spectra are also compared in three (five) bins of pair momentum in fig. 6.23

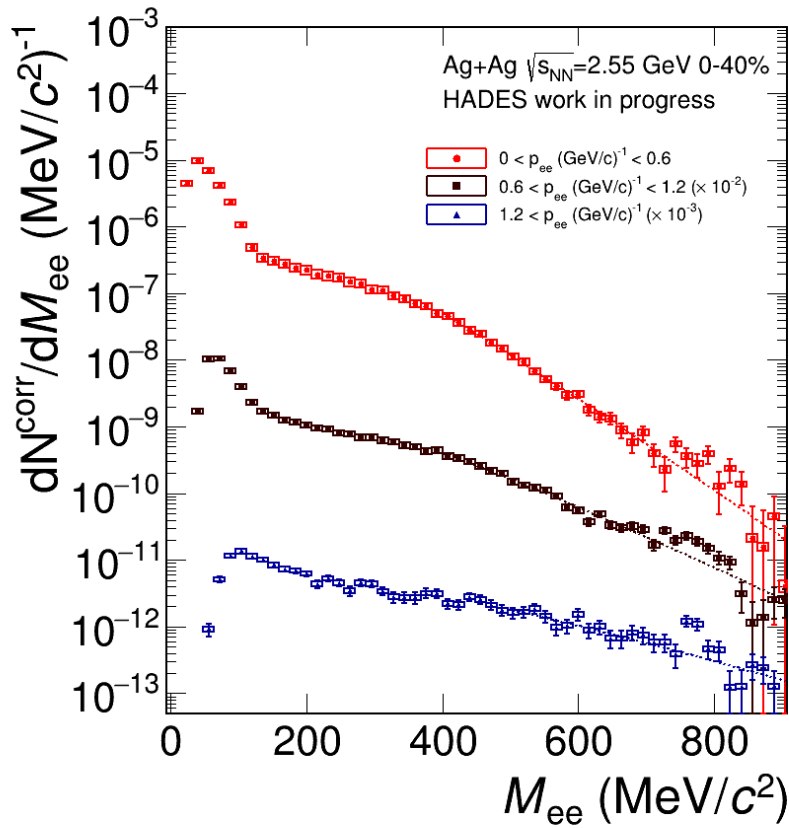


Figure 6.23: Dielectron signal spectra in three bins of pair momentum. Thermal fits to the continuum for $500 MeV/c^2 < M_{ee} < 700 MeV/c^2$ are shown as dashed lines.

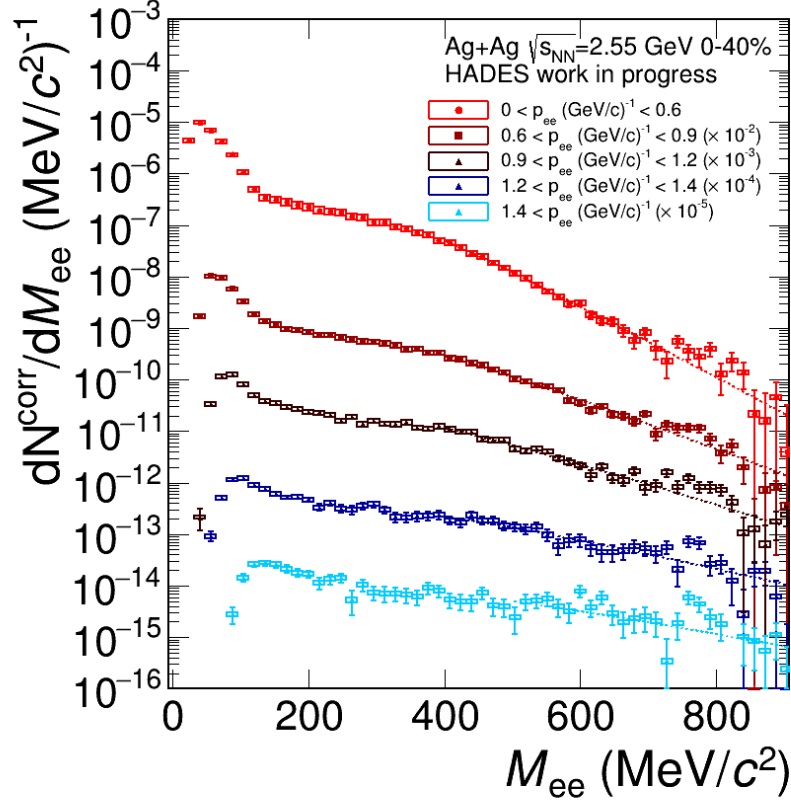


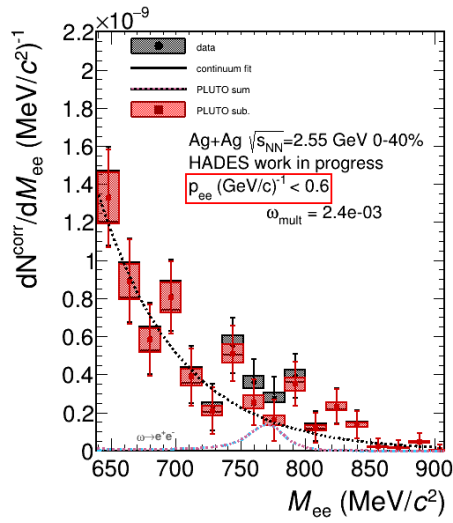
Figure 6.24: Dielectron signal spectra in five bins of pair momentum. Thermal fits to the continuum for $500 \text{ MeV}/c^2 < M_{ee} < 700 \text{ MeV}/c^2$ are shown as dashed lines.

(6.24) including a thermal fit to the continuum in the region $500 \text{ MeV}/c^2 < M_{ee} < 700 \text{ MeV}/c^2$ pointing out the excess in the $\rho - \omega$ mass region. There are two different scenarios how to understand the observed differences. Both of them rely on the assumption that the peak structure observed in the high momentum data corresponds to the $\omega \rightarrow e^+e^-$ signal.

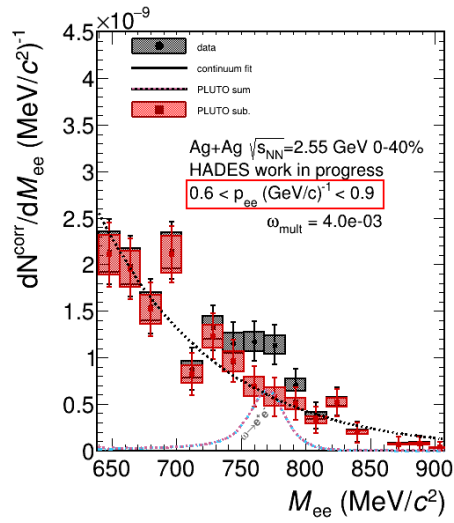
- The $\omega \rightarrow e^+e^-$ peak is hidden under some broad excess originating from the $\rho \rightarrow e^+e^-$ contribution in the low momentum data. In this case, a change in the line-shape of the $\rho \rightarrow e^+e^-$ contribution with momentum is the consequence.
- Relating the excess to the $\omega \rightarrow e^+e^-$ signal only in all momentum bins implies a broadening of the ω with momentum and thus a broadening in the medium, as low momentum data is dominated by in-medium decays whereas high momentum ω -mesons more likely can escape from the medium before decaying.

To conclude on one of the scenarios, i.e. in order to perform a line-shape analysis of the $\omega \rightarrow e^+e^-$ signal, the knowledge of the ρ line-shape is es-

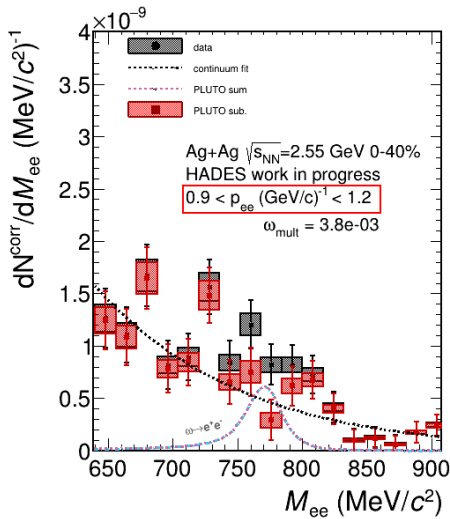
sential, which requires input from theory. According calculations will be performed in near future. However, for the moment being, an analysis of the momentum dependent ω production can be performed assuming the scenario of an unmodified $\omega \rightarrow e^+e^-$ signal. Therefore, a thermal momentum distribution of the ω meson is simulated using the PLUTO event generator with $T_{eff} = 100 \text{ MeV}/k$. The ω multiplicity is then fitted in each momentum bin, to describe the excess in the best possible manner, see fig. 6.25 for an analysis in five bins of pair momentum. In the lower momentum bins the broad excess can obviously not be removed completely by a comparably small peak structure. Due to the obvious uncertainties in the extraction of the ω yield, the obtained multiplicities can only serve as an upper limit. The resulting ω multiplicity is shown in fig. 6.26 as



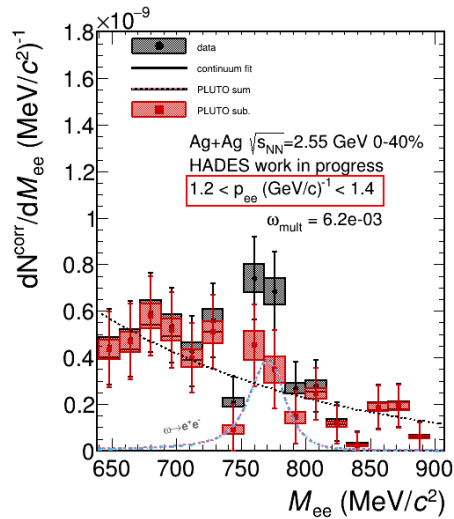
(a)



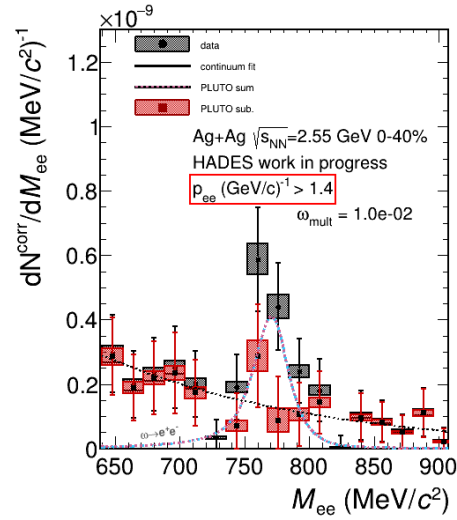
(b)



(c)



(d)



(e)

Figure 6.25: Momentum dependent dielectron signal in five bins of invariant mass (black data points). The excess observed in the $\rho - \omega$ mass region is removed in each bin based on a simulated thermal distribution of the $\omega \rightarrow e^+e^-$ signal without medium modifications fitting the ω multiplicity to the spectra. Note the linear scaling.

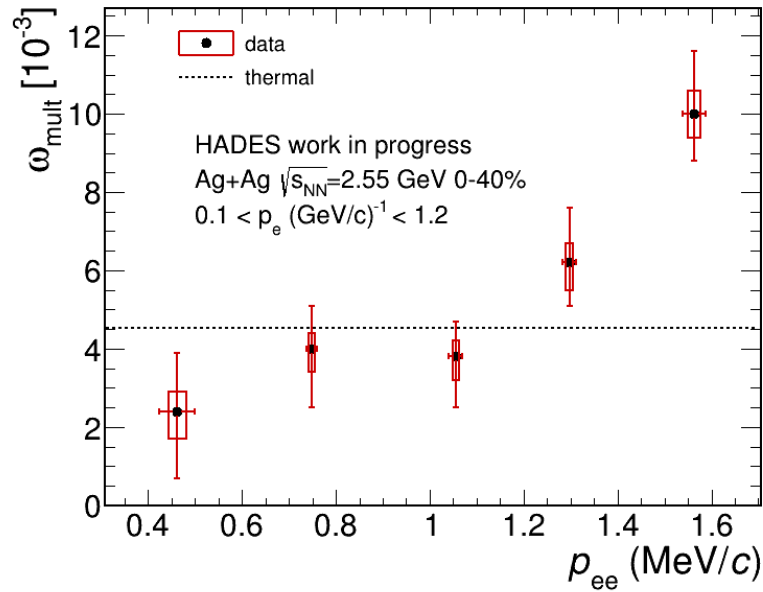


Figure 6.26: ω multiplicity as a function of pair momentum. The data points are extracted using a PLUTO based $\omega \rightarrow e^+e^-$ simulation to describe the observed excess in the $\rho - \omega$ mass region in each pair momentum bin.

a function of the mean pair momentum in the range of $700 \text{ MeV}/c^2 < M_{ee} < 800 \text{ MeV}/c^2$ in each of the bins. The errors, statistical and systematic

are extrapolated from the corresponding errors in the invariant mass distributions. The systematic error therefore does not include the 'scenario uncertainty'. Instead of a flat distribution at a multiplicity of $\omega_{mult} = 4.53 \cdot 10^{-3}$ as seen in the integrated spectra (compare chapter 5.9 and e.g. fig. 6.4) which would have been expected in case of a thermal production of the ω -mesons, a strong rise of the multiplicity with the pair momentum is seen. It can be concluded, that in case of an unmodified $\omega \rightarrow e^+e^-$ signal over the whole range of pair momenta, the ω -meson production is by far not of thermal nature. An in-medium absorption scenario as it has been observed in the $p + Nb$ data would be a reasonable explanation for the missing ω yield at small pair momenta, as well as a broadening of the ω signal itself.

The modification of the line-shape of the dielectron spectrum observed as a function of pair momentum can be even further pronounced switching into the coordinate system of the fireball: As HADES is a fixed target experiment, the fireball itself has a certain momentum in direction of the beam-line. In order to select for dielectrons that are produced in- or outside the fireball the

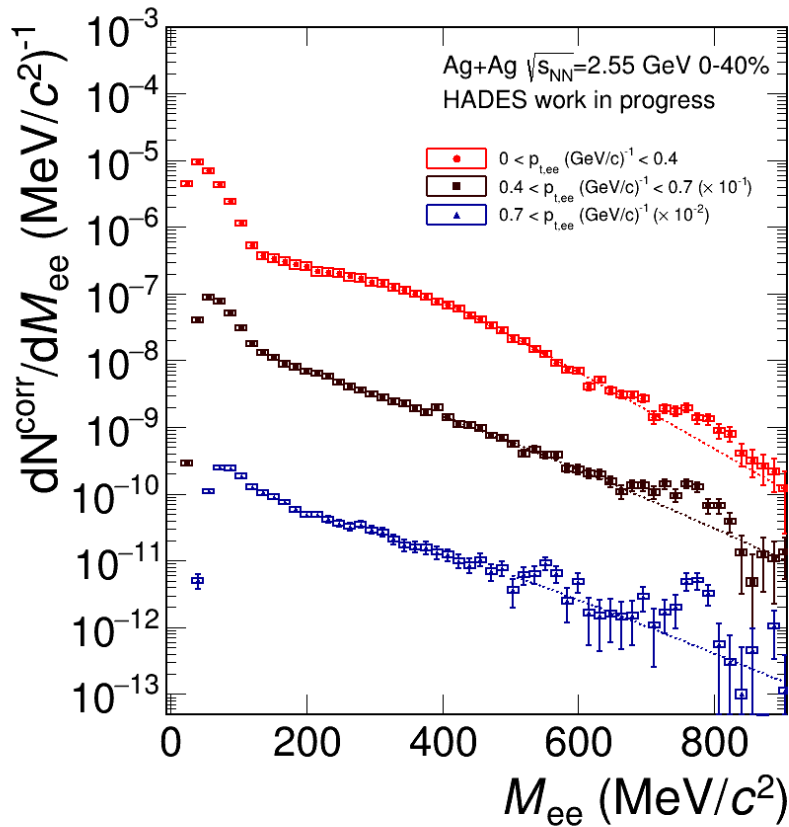
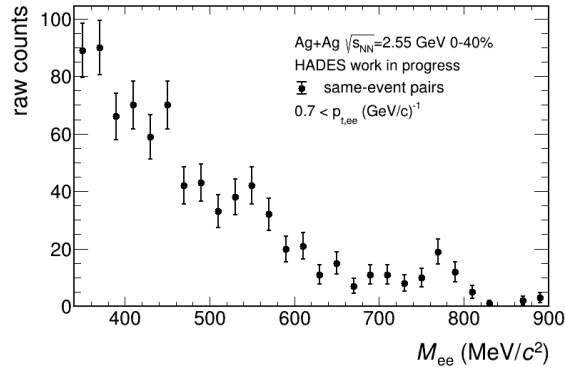


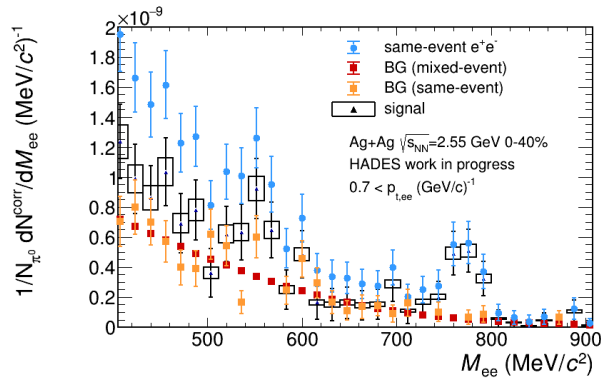
Figure 6.27: Dielectron signal spectra in three bins of transverse pair momentum. Thermal fits to the continuum for $500 \text{ MeV}/c^2 < M_{ee} < 700 \text{ MeV}/c^2$ are shown as dashed lines.

transverse pair momentum p_t is a better choice as it is not biased by the fireball momentum. The dielectron spectrum decomposed into three bins of pair p_t is shown in fig. 6.27. Comparing to the momentum differential analysis (compare fig. 6.23), the observations are the same. For low p_t a substantial broad enhancement in the $\rho - \omega$ mass region is seen, which transform into a narrow peak structure towards higher p_t . However, the deviations from the thermal continuum (fitted by a dashed line) are much stronger than in the momentum differential case. An analysis identical to the momentum dependent one is carried out confirming also quantitatively the obtained results. The corresponding plots are shown in Appendix D, fig. D.9 - D.11.

Interestingly, in the highest p_t bin, a second peak structure shows up at invariant masses around $550 \text{ MeV}/c^2$. The width compares rather well to the one observed in the peak structure at $\sim 770 \text{ MeV}/c^2$ indicating another narrow resonance. In this invariant mass region no such resonance has ever been measured before. This peak is already present in the uncorrected same-event data (no background subtracted), see fig. 6.28a. Applying the efficiency



(a) Uncorrected same-event e^+e^- pairs for $p_{t,ee} > 0.7 \text{ GeV}/c$.



(b) Efficiency corrected same-event pairs, the same-event and mixed-event BG and the resulting signal using the mixed-event background for $p_{t,ee} > 0.7 \text{ GeV}/c$.

Figure 6.28: Detailed studies of the observed peak structure at $M_{ee} \sim 550 \text{ MeV}/c^2$ in the high p_t data. Note the linear scale.

correction (fig. 6.28b) leads to an up-scaling of the data but no changes in the observed peak structure. The same- and mixed-event BG spectra agree on a high level with differences originating from statistical fluctuations in the same-event data. Subtracting the mixed-event background from the same-event data yields the signal spectrum for $p_{t,ee} > 0.7 \text{ GeV}/c$ also shown in fig. 6.27. Thus it can be excluded, that the observed peak structure is an artifact from the analysis, but is a real signal that has to be understood.

A comparison with GiBUU calculations points out the possibility of the observed peak structure being caused by the strongly helicity suppressed $\eta \rightarrow e^+e^-$ decay channel [175] [176]. In the used GiBUU 2021 release this decay channel is included with the upper limit as listed in the PDG 2018 data, $(2.3 \cdot 10^{-6})$ [6], yielding a similar enhancement in the dielectron spectrum in the observed invariant mass region. According to GiBUU calculations, this signal has no visible yield in the low (transverse) momentum data as well as in elementary reactions because here the $\rho \rightarrow e^+e^-$ contribution dominates the dielectron yield. Only in A+A collisions where the ρ spec-

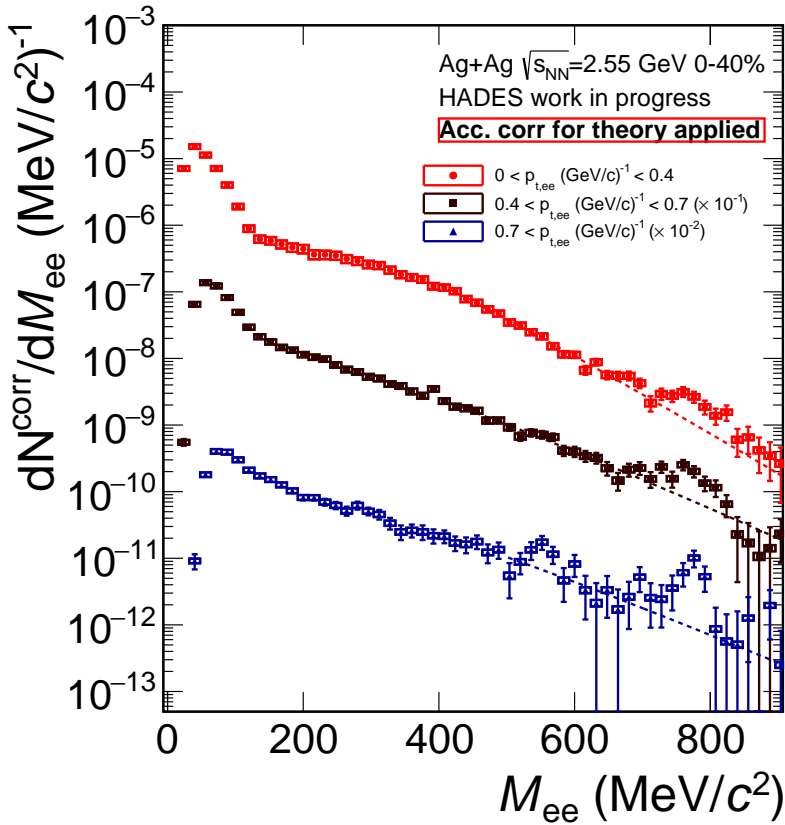


Figure 6.29: Dielectron signal spectra in three bins of transverse pair momentum. Thermal fits to the continuum for $500 \text{ MeV}/c^2 < M_{ee} < 700 \text{ MeV}/c^2$ are shown as dashed lines. The data is efficiency and acceptance corrected within the geometric acceptance of HADES.

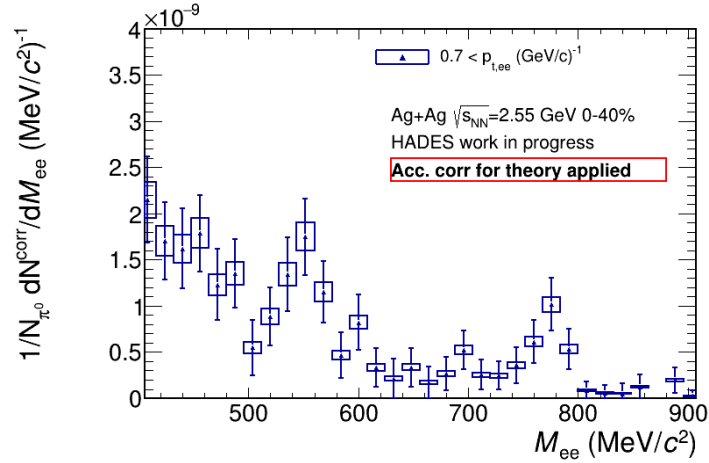


Figure 6.30: High pair p_t invariant mass spectrum corrected for acceptance within the geometric HADES acceptance.

tral function is medium modified and has a strongly reduced yield at high p_t this peak structure shows up. For a future quantitative comparison, the experimental data is acceptance correction within the nominal geometric acceptance of HADES in fig. 6.29, see chapter 4.9 for details on this correction. The high p_t data bin is also shown in linear scale in fig. 6.30, where both peak structures at $M_{ee} \sim 550$ and $M_{ee} \sim 750$ clearly show up in about the same strength. The comparison to the $\omega \rightarrow e^+e^-$ signal allows for a rough estimation of the branching fraction of the $\eta \rightarrow e^+e^-$ assuming that the first peak indeed can be identified therewith: The freeze out multiplicities of $\eta_{mult} = 0.14$ (compare chapter 5.3) and $\omega_{mult} = 4.53 \cdot 10^{-3}$ (compare chapter 5.9) have been estimated earlier in this work. Assuming similar extrapolation factors to the full phase space for the η and the ω , $BR(\eta \rightarrow e^+e^-)/BR(\omega \rightarrow e^+e^-) = \eta_{mult}/\omega_{mult}$ holds. With $BR(\omega \rightarrow e^+e^-) = 7.36 \cdot 10^{-5}$ one derives $BR(\eta \rightarrow e^+e^-) = 2.4 \cdot 10^{-6}$ which corresponds to the upper limit listed in the PDG data [6]. This value is of course a very rough estimate only and thus has to be taken with care. However it points out, that the possible explanation of the observed peak structure caused by the $\eta \rightarrow e^+e^-$ decay as proposed by GiBUU does not stand in contradiction to previous measurements. The correct understanding, interpretation and further investigation of this peak structure is of huge relevance especially as this would be the first measurement of this decay channel ever.

SUMMARY

In this work the analysis of Ag+Ag collisions at $\sqrt{s_{NN}} = 2.55 \text{ GeV}$ measured with the **H**igh **A**cceptance **D**i**E**lectron **S**pectrometer (HADES) with respect to dielectron production has been presented. The combination of the achieved electron efficiency (~ 0.7) paired with a high pion suppression factor ($\sim 10^5$) and new methods of conversion electron recognition sets new standards and yields dielectron spectra of unprecedented quality. For the first time ever, signal-to-background values around unity are achieved for the whole invariant mass region reaching up to the ϕ -meson mass.

In order to decompose the measured dielectron spectrum into its different components, hadronic cocktail simulations are performed based on PLUTO. The freeze-out multiplicities of the input hadrons are therefore estimated previously. For the π^0 a multiplicity of $\pi_{mult}^0 = 7.37 \pm 0.43|_{sys} \pm 0.11|_{stat}$ has been extracted being in agreement with charged pion measurements and TAPS extrapolations. The measured η multiplicity of $\eta_{mult} = 0.109 \pm 0.018|_{sys} \pm 0.015|_{stat}$ is significantly smaller than predicted by TAPS. A future efficiency and acceptance correction with a high statistics simulation sample will yield more precise results. Furthermore, the dielectron spectrum shows a clear signal of the $\omega \rightarrow e^+e^-$ decay, which allows for a multiplicity extraction.

Lacking a measured NN reference at the energy of the Ag+Ag data, elementary reactions are simulated using the transport model GiBUU. Subtracting the relevant NN channels and the hadronic cocktail from the dielectron signal spectrum the in-medium contribution is isolated. A thermal fit allows for the estimation of a mean medium temperature of $kT = (77.9 + 3.7 - 2.9) \text{ MeV}$ being in agreement with previous HADES measurements in Au+Au collisions, although at slightly lower energy.

The observed in-medium contribution is quantified by the dielectron excess ratio R_{AA} aligning in accordance to the system size in between of the HADES Au+Au and Ar+KCl data.

A (transverse) pair momentum dependent analysis of the dielectron yield reveals modifications in the $\rho - \omega$ invariant mass region. Whereas a broad enhancement above the thermal continuum is observed in the low (transverse) momentum data, a peak structure is visible for high (transverse) momenta. A possible modification, i.e. broadening, of the ω spectral function in the medium needs theoretical input for the ρ line-shape for confirmation. In the high transverse momentum data a second peak shows up at around $M_{ee} \sim 550 \text{ MeV}$ that is also seen in GiBUU simulations and therein identified as $\eta \rightarrow e^+e^-$ contribution.

Part II

ONE-LOOP SELF-CONSISTENT SPECTRAL
FUNCTIONS WITH THE FRG

DILEPTONS IN THEORY

In the second part of this work, the calculation of spectral functions with the Functional Renormalization Group (FRG) including one-loop self-energies in a self-consistent way will be presented, which has already been published in [177]. This first chapter is intended to give a general overview on how and why to address spectral functions in theory. The general method and the basic underlying concepts of this work are presented in the second chapter while results are shown in the third.

The central object in the calculation of thermal electromagnetic (em) emission rates of a strongly interacting medium is the current-current correlation function $\Pi_{em}^{\mu\nu}$. It is defined as

$$\Pi_{em}^{\mu\nu}(q_0, q) = -i \int d^4x e^{iq \cdot x} \Theta(x^0) \langle\langle [j^\mu(x), j^\nu(0)] \rangle\rangle, \quad (8.1)$$

with the photon energy q_0 , three-momentum q and where the latter part represents the thermal expectation value of the retarded em current operator where the dependence on T and μ_B arises from. From the imaginary part, the em spectral function, one can directly access thermal photon and dilepton rates [178] via

$$q_0 \frac{dN_\gamma}{d^4x d^3q} = -\frac{\alpha_{em}}{\pi^2} f^B(q \cdot u; T) \text{Im} \Pi_{EM}(q_0 = q; \mu_B, T), \quad (8.2)$$

$$q_0 \frac{dN_{ll}}{d^4x d^4q} = -\frac{\alpha_{em}^2}{M^2 \pi^3} L(M^2) f^B(q \cdot u; T) \text{Im} \Pi_{EM}(M, q; \mu_B, T). \quad (8.3)$$

Here, the Jüttner function f^B [179] represents a Boltzmann distribution extended to include special relativity. As dileptons do carry an invariant mass $M^2 = q_0^2 - q^2$, in contrast to real photons, the dilepton rate additionally depends on a corresponding phase space factor $L(M^2)/M^2$.

In the vacuum, $\text{Im} \Pi_{EM}^{vac}$ is very well known from e^+e^- annihilation experiments, where it can be measured as a direct consequence of the time-reversal invariance of electromagnetic and strong interactions. It is obtained via the so-called R-ratio (which is more famous for the proof of the existence of color in QCD, $N_c = 3$) defined as

$$R = \frac{\sigma_{tot}(e^+e^- \rightarrow \text{hadrons})}{\sigma_{tot}(e^+e^- \rightarrow \mu^+\mu^-)} = N_c \sum_q \frac{e_q^2}{e^2} \propto \frac{\text{Im} \Pi_{EM}^{vac}}{M^2} \quad (8.4)$$

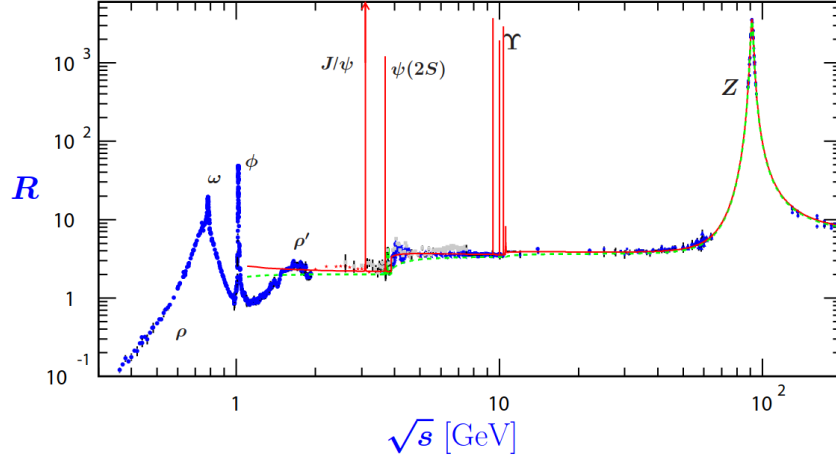


Figure 8.1: Compilation of measured data for $\sigma_{tot}(e^+e^- \rightarrow hadrons)$ normalized to $\sigma_{tot}(e^+e^- \rightarrow \mu^+\mu^-)$. Taken from [182].

and shown in fig. 8.1. It is observed, that in the low-mass regime $\text{Im}\Pi_{EM}^{vac}$ is dominated by the contributions of the light vector mesons ρ, ω, ϕ giving rise to the **Vector-Meson-Dominance (VMD)** model, introduced first in [180], where a mixing between vector mesons and virtual photons is assumed. Within the VMD e.g. the dimuon data measured with NA60 can be well described, see [181]. Π_{EM}^{vac} can therefore be written for $M \lesssim 1.1 \text{ GeV}$ as

$$\text{Im}\Pi_{EM}^{vac}(M) = \sum_{V=\rho,\omega,\phi} \left(\frac{m_V^2}{g_V} \right)^2 \text{Im}D_V^{vac}(M). \quad (8.5)$$

$\text{Im}\Pi_{EM}$ is mainly determined by the ρ -meson (relative strength of 10:1:2 for $\rho : \omega : \phi$ [174]), which therefore moved into the centre of attention. With increasing masses ($M > 1.5 \text{ GeV}$) a perturbative regime is reached (short interaction distances), where the em spectral function in the vacuum can be calculated to

$$\Pi_{EM}^{vac}(M) = -\frac{M^2}{12\pi} \left(1 + \frac{\alpha_s(M)}{\pi} \pm \mathcal{O} \left(\left(\frac{\alpha_s(M)}{\pi} \right)^3 \right) \right) N_C \sum_{q=u,d,s} e_q^2, \quad (8.6)$$

which undergoes restrictions close to the charm and bottom threshold, where additional non-perturbative effects arise. Concluding, dielectron measurements would agree with the spectral shape of $e^+e^- \rightarrow hadrons$ folded with some temperature evolution of the system if there were no medium effects. This applies to regions far away from resonances. In the low-mass regime on the other hand, medium modifications of the resonance spectrum leave their fingerprint and can therefore be studied. E.g., chiral sum rules show a connection between the quark condensate explicitly breaking chiral symmetry (compare chapter 1) and the spectral functions of vector and axial-vector mesons [183]. A possible chiral restoration would manifest in the de-generation of the spectral functions of chiral partners, with the ρ and the a_1

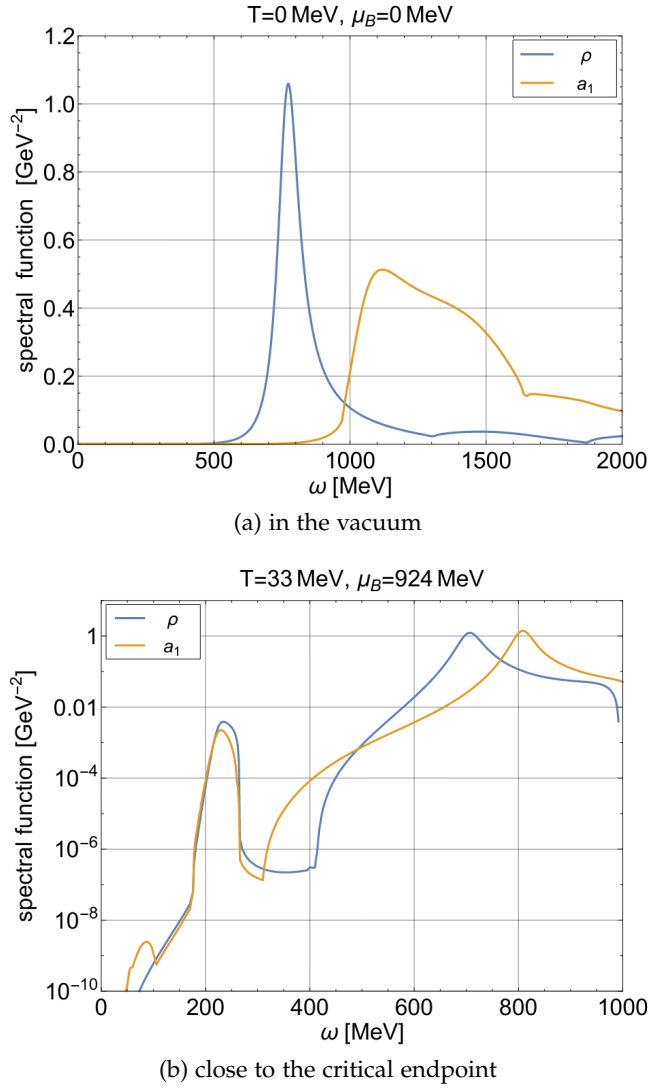


Figure 8.2: Spectral functions of the ρ and a_1 at different values of T, μ_B . Note the linear scale in the upper and the logarithmic scale in the lower figure. For details see text. Taken from [184].

being the most prominent example in the present content. Exemplary, results of a calculation of their spectral functions in a baryon-meson, more specific parity-doublet, model within the **F**unctional **R**enormalization **G**roup (FRG) are shown in fig. 8.2 for different regions in the model dependent phase diagram [184]. The upper figure shows the spectral functions of the ρ and a_1 in the vacuum. In this energy range, the ρ is a pure two-pion resonance ($\rho \rightarrow \pi\pi$ is the only possible decay channel) with its PDG pole mass of $m_\rho = 775 \text{ MeV}/c^2$ and a width of about $\Gamma_\rho \sim 100 \text{ MeV}/c^2$, being comparable to the experimental value of $\Gamma_\rho^{PDG} \sim 150 \text{ MeV}/c^2$. The a_1 spectral function is a very broad peak in the region of $\omega \approx 1000 - 1600 \text{ MeV}$ due to a superimposition of the processes $a_1 \rightarrow \rho\pi$ and $a_1 \rightarrow \sigma\pi$. Close to the critical endpoint (lower panel of fig. 8.2), both spectral functions approach each other with only minor changes in the ρ spectral function (note the change from linear

to logarithmic scale), but significant medium modification occurring to the a_1 . Here, a strong shift in mass towards lower values and also a broadening is seen. This behaviour indicates the emerging restoration of chiral symmetry, possibly leading to a complete degeneracy of both spectral functions at higher densities. The, compared to the vacuum case, additional structure at around $\omega \approx 240 \text{ MeV}$ arises from processes of baryon resonance formation ($\rho/a_1 + N_1 \rightarrow N_2$) possible at such energies, which is a prediction of the parity-doublet model.

Summarizing, reliable calculations of spectral functions are the key observable in theory to access dilepton production and thus understand and interpret experimental measurements.

CONCEPTUAL BASELINE

9.1 INTRODUCTION TO THE FUNCTIONAL RENORMALIZATION GROUP

The **Functional Renormalization Group (FRG)** is a non-perturbative continuum framework mostly used to study quantum field theories usually formulated in Euclidean space-time, see e.g. [185], [186], [187]. It aims at an understanding of the macroscopic physics in terms of the basic microscopic interactions. Therefore one starts with an ansatz for the classical action $S[\phi]$ at some high energy or momentum scale, the ultraviolet (UV) cutoff. The central object in FRG then is the scale dependent effective action $\Gamma[\phi]$, then called *average* effective action, providing the connection between the UV and the infrared (IR) regimes. Lowering the RG energy scale k from the UV to the IR, more and more quantum fluctuations are included, integrating out momentum shell by momentum shell as described by Wilson's coarse-graining procedure [188], [189].

The effective action is the generating function of the one-particle-irreducible (1PI) correlation functions in a theory, which are such diagrams, that can not be disconnected by cutting a single internal line. It is obtained from the generating functional $Z[J]$ of the full Green functions for the source field $J(x)$, which writes as

$$Z[J] = \int \mathcal{D}\varphi \exp\left(-S[\varphi] + \int d^4x J(x) \varphi(x)\right) \quad (9.1)$$

in the Euclidean path integral formalism with some generic field $\varphi(x)$. The connected n -point Green functions are derived from the generating functional for the connected Green functions

$$W[J] = \log Z[J]. \quad (9.2)$$

The effective action is defined as a Legendre transformation of $W[J]$ w.r.t. the expectation value of the field $\varphi(x)$ in presence of the source $J(x)$, $\varphi(x) = \langle \varphi(x) \rangle$,

$$\Gamma[\phi] = \sup_J \left(\int d^4x J(x) \phi(x) - W[J] \right). \quad (9.3)$$

There are different ways of addressing $\Gamma[\phi]$, such as a direct computation or via a vertex expansion leading to the Dyson-Schwinger equations

[190], [191]. This work relies on the computation of $\Gamma[\phi]$ based on RG concepts [192], where a solution via Wilsons idea of integrating out momentum shell by momentum shell is performed. Therefore a regulator function R_k is introduced suppressing momenta below the RG energy scale k . The scale-dependent analogues to the generating functionals $W[J]$ and $\Gamma[\phi]$ then read

$$W_k[J] = \log \int \mathcal{D}\phi \exp \left(-S[\phi] - \Delta S_k[\phi] + \int d^4x J(x) \phi(x) \right), \quad (9.4)$$

$$\Gamma_k[\phi] = \sup_J \left(\int d^4x J(x) \phi(x) - W_k[J] \right) - \Delta S_k[\phi] \quad (9.5)$$

with the regulator insertion

$$\Delta S_k[\phi] = \frac{1}{2} \int \frac{d^4q}{(2\pi)^4} \phi(-q) R_k(q) \phi(q). \quad (9.6)$$

It is quadratic in the field ϕ and therefore acts as a mass terms. The regulator function R_k itself has to satisfy two conditions, which are

- (i) in case $k \gg q$, $R_k(q)$ has to behave as $\sim k^2$ to ensure IR regularization [193]
- (ii) for $q \gg k$ the regulator has to vanish in order to ensure $Z_{k \rightarrow 0}[J] \rightarrow Z[J]$ and $\Gamma_{k \rightarrow 0} \rightarrow \Gamma$.

Γ_k interpolates from the classical action $S[\phi]$ at the UV cutoff Λ to the effective action $\Gamma[\phi]$. At intermediate scales, the effective average action depends on the choice of the regulator. The scale dependence of Γ_k is given by an exact flow equation called *Wetterich equation* [192] [194] which splits into a bosonic and a fermionic part. In the quark-meson model which this work is based on, it reads

$$\begin{aligned} \partial_k \Gamma_k[\phi, \psi, \bar{\psi}] = & \frac{1}{2} \text{Tr} \left\{ \partial_k R_k^B \left(\Gamma_k^{(2,0,0)}[\phi, \psi, \bar{\psi}] + R_k^B \right)^{-1} \right\} \\ & - \text{Tr} \left\{ \partial_k R_k^F \left(\Gamma_k^{(0,1,1)}[\phi, \psi, \bar{\psi}] + R_k^F \right)^{-1} \right\}. \end{aligned} \quad (9.7)$$

A detailed derivation is available in e.g. [195].

9.2 FLOW EQUATION FOR THE AVERAGE EFFECTIVE ACTION IN THE $O(4)$ MODEL

The quark-meson model is a low-energy effective chiral model of QCD. In two flavors, its degrees of freedom are given by those of two quarks and the three pions and the sigma meson. In this work we neglect any quark

contribution, leading to the $O(4)$ model. The Euclidean Lagrangian is therein given by

$$\mathcal{L}_{O(4)}^E = \frac{1}{2} (\partial_\mu \sigma)^2 + \frac{1}{2} (\partial_\mu \vec{\pi})^2 + U(\sigma, \vec{\pi}) \quad (9.8)$$

where the blue term represents the kinetic part and the effective mesonic potential is shown in green. The potential is of the form

$$U(\sigma, \vec{\pi}) = U(\phi^2) - c\sigma \quad (9.9)$$

and consists of a chirally invariant part $U(\phi^2)$ and an explicit breaking term $c\sigma$.

In general, the two-point functions $\Gamma_k^{(2)}$ in eq. (9.7) have themselves to be obtained from their according flow equations as given by the Wetterich equation. Therefore, they will depend on three- and four-point functions leading to an infinite stack of flow equations which has to be truncated at some point. This can be achieved choosing a suitable ansatz for the functional form of the effective action. At first, such an ansatz and the subsequent derivation of a flow equation will be carried out for the standard Local-Potential-Approximation (LPA) procedure to calculate pion and sigma spectral functions as it has been first proposed in [196]. In this work it is used for reference purpose.

9.2.1 Analytically continued LPA flows

Based on the Lagrangian in eq. (9.8), an ansatz for the average effective action can be derived within the local potential approximation ($Z_k(\phi) = 1$, $Y_k(\phi) = 0$ in an derivative expansion). It reads

$$\Gamma_k[\phi] = \int d^4x \left(U_k(\phi^2) - c\sigma + \frac{1}{2} (\partial_\mu \phi)^2 \right). \quad (9.10)$$

The second functional derivative of this ansatz now can be straight forward calculated to be

$$\frac{\delta \Gamma_k[\phi]}{\delta \phi_i(q)} = q^2 \phi_i(-q) + 2U'_k(\phi^2) \phi(-q), \quad (9.11)$$

$$\frac{\delta^2 \Gamma_k[\phi]}{\delta \phi_j(q') \delta \phi_i(q)} = (q^2 \delta_{ij} + 2U'_k(\phi^2) \delta_{ij} + 4U''_k(\phi^2) \phi_i(-q) \phi_j(-q')) (2\pi)^4 \delta^{(4)}(q+q'). \quad (9.12)$$

Inserting the expectation value $\phi_0 = (\sigma_0, 0, 0, 0)$ it reads

$$\frac{\delta^2 \Gamma_k[\phi]}{\delta \phi_j(q') \delta \phi_i(q)} = \Gamma_{k, \phi_i \phi_j}^{(2)} = \delta_{ij} (2\pi)^4 \delta^{(4)}(q+q') (q^2 + m_{\phi_i}^2) \quad (9.13)$$

with the euclidean/curvature masses $(\Gamma_k^{(2)}(0) = (m_k^c)^2, \rho = \phi^2)$

$$m_{\sigma,k}^c = \sqrt{2U_k'(\rho) + 4U_k''(\rho)\sigma^2}, \quad (9.14)$$

$$m_{\pi,k}^c = \sqrt{2U_k'(\rho)}. \quad (9.15)$$

To obtain a flow equation for the average effective action, eq. (9.13) is inserted into the Wetterich equation, eq. (9.7). In the version of the quark-meson model used in this work (no quarks), the Wetterich equation simplifies to

$$\partial_k \Gamma_k[\phi] = \frac{1}{2} \text{Tr} \left\{ \partial_k R_k^B \left(\Gamma_k^{(2)}[\phi] + R_k^B \right)^{-1} \right\} \quad (9.16)$$

as only the bosonic part remains.

We note, that with the effective potential carrying the only scale dependence, the Wetterich equation transforms into a flow equation of the effective potential ($\partial_k \Gamma_k = \partial_k U_k$). It then reads

$$\partial_k U_k = \frac{1}{2} \int \frac{d^4 q}{(2\pi)^4} \frac{\partial_k R_k^B}{\Gamma_{\sigma\sigma}^{(2)} + R_k^B} + \frac{3}{2} \int \frac{d^4 q}{(2\pi)^4} \frac{\partial_k R_k^B}{\Gamma_{\pi\pi}^{(2)} + R_k^B}, \quad (9.17)$$

where the first term represents the σ contribution and the second one the three pions. As bosonic regulator function $R_k^B = (k^2 - \bar{q}^2)\Theta(k^2 - \bar{q}^2)$ [197] has been chosen which clearly satisfies the previously mentioned conditions. This three dimensional regulator only acts on the momenta and does not regulate the energy components. The consequence is a breaking of the Euclidean $O(4)$ symmetry, which however is found to be of minor nature only [196]. The huge advantage in this choice of the regulator is a tremendous simplification of the analytic continuation procedure.

Flow equations for the two-point function are derived from the Wetterich equation taking two functional field derivatives to

$$\begin{aligned} \partial_k \Gamma_{\sigma,k}^{(2)}(p) &= 3(\Gamma_{\sigma\pi,k}^{(3)})^2 J_{\pi,k}(p) + (\Gamma_{\sigma,k}^{(3)})^2 J_{\sigma,k}(p) - \frac{3}{2}(\Gamma_{\sigma\pi,k}^{(4)})^2 I_{\pi,k}^{(2)} - \frac{1}{2}(\Gamma_{\sigma,k}^{(4)})^2 I_{\sigma,k}^{(2)} \\ \partial_k \Gamma_{\pi,k}^{(2)}(p) &= (\Gamma_{\sigma\pi,k}^{(3)})^2 J_{\pi\sigma,k}(p) + (\Gamma_{\sigma\pi,k}^{(3)})^2 J_{\sigma\pi,k}(p) - \frac{3}{2}(\Gamma_{\pi,k}^{(4)})^2 I_{\pi,k}^{(2)} - \frac{1}{2}(\Gamma_{\sigma\pi,k}^{(4)})^2 I_{\sigma,k}^{(2)}. \end{aligned} \quad (9.18)$$

Explicit expressions for the four-point vertex functions and the loop functions are available e.g. in [195]. The three-point vertex functions will also be used in the self-consistent one-loop calculation presented in the following and are given by

$$\begin{aligned} \Gamma_{\sigma,k}^{(3)} &= 12\sigma U_k''(\rho) + 8\sigma^3 U_k'''(\rho), \\ \Gamma_{\sigma\pi,k}^{(3)} &= 4\sigma U_k''(\rho). \end{aligned} \quad (9.19)$$

where $g_{\sigma,k}$ and $g_{\sigma\pi,k}$ are the scale-dependent three-point σ and σ - π coupling constants. $m_{\sigma,k}^p$ and $m_{\pi,k}^p$ denote the scale-dependent pole masses, that now differ from the curvature masses. The renormalization of the self-energies is performed by zero-momentum subtraction, thus $\Pi_R(p) = \Pi(p) - \Pi(0)$, which would be UV divergent otherwise. Therefore the relation between the zero-momentum two-point function and the effective potential and curvature mass, $\Gamma_k^{(2),\text{IL}}(0) = (m_k^c)^2$ remains unchanged by construction compared to the LPA case.

The scale-dependent coupling constants $g_{\sigma,k}$ and $g_{\sigma\pi,k}$ are derived from U_k the same as in the LPA case, eq. (9.19). The derivatives of the potential are evaluated at the scale-dependent minimum $\rho_{0,k}$, which itself is derived from eq. (9.17) as in the LPA case, but with the modified two-point function including the self-energies, eq. (9.21). As regulator function, the four-dimensional Litim regulator [197] is used,

$$R_k(p) = (k^2 - p^2)\Theta(k^2 - p^2). \quad (9.24)$$

We define the particles pole masses as the zero crossings of the real parts of the corresponding two-point functions, $\text{Re}\Gamma^2(m_p) = 0$. These are then given by the solutions of

$$\begin{aligned} (m_{\sigma,k}^p)^2 &= (m_{\sigma,k}^c)^2 - \text{Re}\Pi_{\sigma,k}(p) \Big|_{-p^2=(m_{\sigma,k}^p)^2}, \\ (m_{\pi,k}^p)^2 &= (m_{\pi,k}^c)^2 - \text{Re}\Pi_{\pi,k}(p) \Big|_{-p^2=(m_{\pi,k}^p)^2}. \end{aligned} \quad (9.25)$$

Both equations have to be solved simultaneously at each scale k , as the self-energies themselves depend on both pole masses each. They yield the scale-dependence of the mass parameters in a self-consistent manner that further determines the resonance positions and decay thresholds. After solving this self consistent system of equations for the two-point functions and the effective potential and calculating the couplings and pole masses, one can immediately obtain the spectral functions via analytical continuation of the two-point functions. At zero temperature analytic continuation is performed replacing the Euclidean momentum p_0 by a real frequency ω like

$$p_0 \rightarrow -i(\omega + i\varepsilon), \quad (9.26)$$

in the limit $\varepsilon \rightarrow 0^+$. The spectral function are defined as the imaginary parts of the retarded propagators $D_k^R = -D_k(-i(\omega + i\varepsilon))$ and thus can be calculated from the corresponding two-point function with retarded self-energies

$$\rho_k(\omega) = -\frac{1}{\pi} \text{Im} D_k^R(\omega) = \frac{1}{\pi} \frac{\text{Im} \Gamma_k^{(2),R}(\omega)}{\left(\text{Re} \Gamma_k^{(2),R}(\omega)\right)^2 + \left(\text{Im} \Gamma_k^{(2),R}(\omega)\right)^2}. \quad (9.27)$$

9.2.3 Numerical Implementation

The effective potential is chosen to be of the form

$$U(\rho) = b_1\rho + b_2\rho^2 - c\sigma \quad (9.28)$$

for the LPA and the SC1L setup. The values for b_1, b_2 and c are tuned such, that the IR values of the pion decay constant and the obtained pole masses agree with the PDG listed masses. The pion decay constant can be identified with the IR minimum of the effective potential, $\sigma_{0,IR}$. However, in the SC1L setup this value has to be corrected due to non-vanishing wave-function renormalization factors as discussed later. As UV cutoff $\Lambda = 500 \text{ MeV}$ has been used along an IR scale of $k_{IR} = 40 \text{ MeV}$. Results at scales $k < k_{IR}$ are obtained via extrapolation. All parameters are summarized in tab. 9.1.

	b_1 [Λ^2]	b_2	c [Λ^3]	f_π [MeV]	m_π^p [MeV]	m_σ^p [MeV]
LPA	-0.32456	3.923	0.014	93.0	135	352
SC1L	-0.22524	3.372	0.014	93.0	135	324

Table 9.1: Numerical values for the parameters of the effective potential in the UV for the LPA setup and the self-consistent one-loop setup (SC1L) and the resulting values for the pion coupling constant and the pole masses in the IR.

In order to solve the flow equation for the effective potential, eq. (9.17), the numerical so-called grid-method is used. It is based on a discretization of the field variable ρ into equidistant grid points [198]. The flow equation is reduced to a set of ordinary coupled differential equations, that can be solved applying standard techniques, where the required first and second order derivatives are obtained using the method of finite differences. To check for numerical stability, the number of grid points was varied within $N \in [100, 300]$ in a ρ -field range of $\rho \in [0, 140^2] \text{ MeV}/c^2$ and another numerical technique, the Kurganov-Tadmor finite volume technique [199] has been implemented all yielding the same results.

Having the scale dependent effective potential at hand, all other observables can be analytically calculated in the SC1L setup. In the LPA case, the solution for the effective potential is used as input to the flow equations for the two-point functions, which are then solved using the grid method. In both cases spectral functions are obtained according to eq. (9.27).

RESULTS

In this chapter the results obtained from the LPA and the SC1L setups presented in the previous chapter are shown. At first the pole and curvature masses, the couplings and the effective potential with its minimum are discussed, for both setups each. Second, also the extracted two-point functions and the resulting spectral functions will be presented. All results have already been published in [177].

10.1 MASSES, COUPLINGS AND THE EFFECTIVE POTENTIAL

Due to the non-trivial momentum dependence in the SC1L propagators, the wave function renormalization factors Z_σ and Z_π do not vanish in the SC1L setup as they do in the LPA case. They are given by the second partial derivative of the two-point function in momentum,

$$Z_{\pi,k} = \left. \frac{\partial \Gamma_{\pi,k}^{(2)}(p^2)}{\partial p^2} \right|_{p=0}, \quad Z_{\sigma,k} = \left. \frac{\partial \Gamma_{\sigma,k}^{(2)}(p^2)}{\partial p^2} \right|_{p=0}. \quad (10.1)$$

The obtained wave function renormalization factors are shown as a function of the energy scale k in fig. 10.1. In case of the pion, Z_π is close to one and almost scale independent with $Z_{\pi,k=\Lambda} = 1.07$ at the UV scale $\Lambda = 500 \text{ MeV}$ and $Z_{\pi,k=0} = 1.06$ in the IR. The sigma wave function renormalization factor is much larger with $Z_{\sigma,k=\Lambda} = 1.80$ and $Z_{\sigma,k=0} = 1.58$ and heavily depends on the scale k .

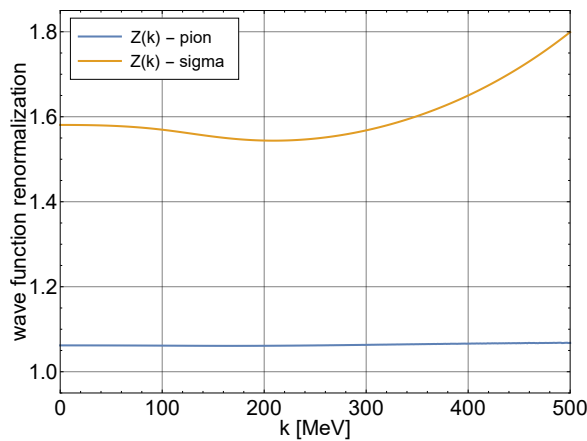


Figure 10.1: The wave function renormalization factors $Z_{\pi,k}$ and $Z_{\sigma,k}$ as a function of the RG scale k for the self-consistent one-loop setup. Taken from [177].

The effective potential $U_k(\rho)$ is shown in fig. 10.2 for the LPA and the SC1L setup in the IR and the UV each. The minimum is located at large σ -values reflecting spontaneous symmetry breaking. This is a natural consequence as the bosonic fluctuations getting included lowering the energy scale k tend to restore chiral symmetry. Differences in the UV potential in both setups arise from the choice of parameters that are optimized such, that the IR values of the pion decay constant (the minimum of the potential) and the pole masses agree. Therefore also the shape of the potential agrees in the IR. As the additional one-loop expressions in the SC1L setup tend to suppress the bosonic fluctuations and such the symmetry restoration, the degree of chiral symmetry breaking is lower in the SC1L case in the UV identified with the minimum located at smaller σ values.

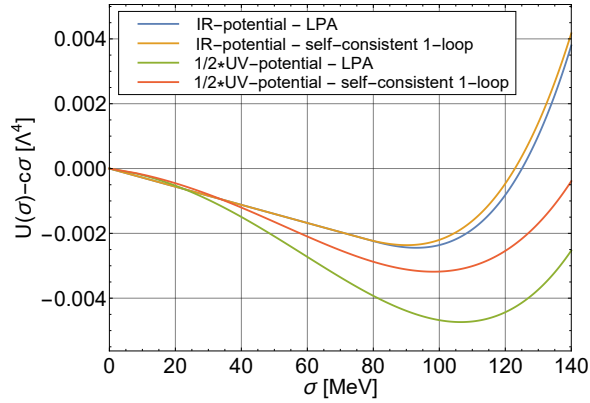


Figure 10.2: The effective potential $U_k(\rho)$ obtained from the LPA flow as well as the SC1L flow are shown in the UV and in the IR, both normalized to zero at $\sigma = 0$, and with the UV potentials divided by a factor of 2 for better comparison. Taken from [177].

Having the wave function renormalization factors at hand, the minimum of the effective potential $\sigma_{0,k}$ identified with the pion decay constant f_π can be compared for the LPA and SC1L setup, see fig. 10.3. It therefore has to be weighted with $\sqrt{Z_{\pi,k}}$ in the SC1L case ($\bar{\sigma}_{0,k} = \sigma_{0,k} \cdot \sqrt{Z_{\pi,k}}$). As already observed from the effective potential in the IR and UV (fig. 10.2) the minimum is shifted towards lower values, lowering the scale with the same arguments holding.

The three-point vertex functions corresponding to the scale-dependent couplings $g_{\sigma,k}$ and $g_{\sigma\pi,k}$ are shown in fig. 10.4 vs. the energy scale k in the LPA and SC1L setup normalized to the UV cutoff. The couplings are obtained from the derivatives of the effective potential (see eq. (9.19)) and such mirror its slope and curvature. Therefore the values in the SC1L setup are generally smaller compared to the LPA setup. In case of $g_{\sigma,k}$ both approach each other lowering the energy scale and almost agree in the IR, see tab. 10.1 for explicit values. The $\pi\pi\sigma$ vertex-coupling $g_{\sigma\pi,k}$ is about three to four times the value of $g_{\sigma,k}$ and significantly larger in the LPA case over the whole energy scale.

In fig. 10.5 the Euclidean curvature masses as calculated from the effective potential (see eq. (9.14), (9.15)) and the pole masses are shown for the LPA

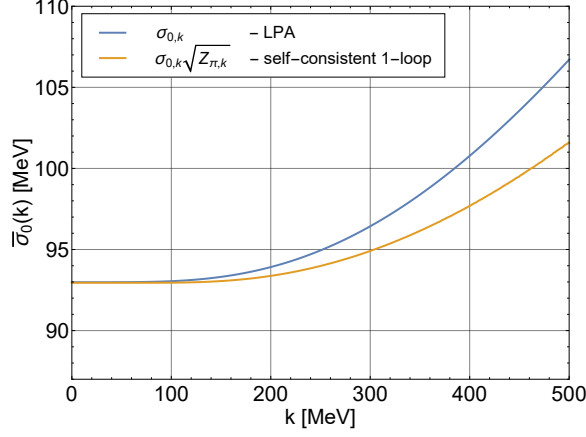


Figure 10.3: The scale-dependent minimum of the effective potential for the LPA setup, $\sigma_{0,k}$ and the renormalized minimum obtained for the self-consistent one-loop setup $\bar{\sigma}_{0,k}$. Taken from [177].

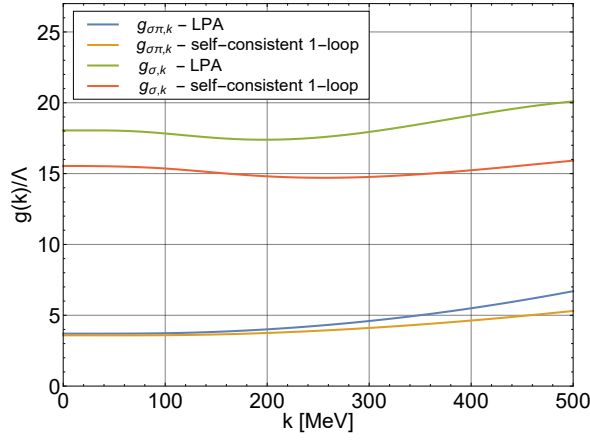


Figure 10.4: Flow of the three-point coupling constants $g_{\sigma\pi,k}$ and $g_{\sigma\sigma,k}$ for the LPA and the self-consistent one-loop setup. Taken from [177].

setup, which agree in the UV by construction. The pole masses are calculated from the zero crossings of corresponding two-point functions. In case of the pion, the pole and curvature masses agree over the whole energy range and reach values of $m_{\pi}^{p,IR} = 135 \text{ MeV}/c^2$ and $m_{\pi}^{c,IR} = 137 \text{ MeV}/c^2$, respectively, where the parameter set of the effective potential has been tuned such, that the pole mass corresponds to its experimental value. For the sigma, the pole mass drops faster than the curvature mass. At about $k = 110 \text{ MeV}$, a sudden increase in the pole mass of the sigma is observed. This is caused by the decay channel $\sigma \rightarrow \pi\pi$ moving there (decay threshold is $E = \sqrt{k^2 + (2m_{\pi}^{c,k})^2}$). Therefore the σ is no longer stable and thus its spectral function suddenly changes from a δ -function to a broad resonance increasing the pole mass.

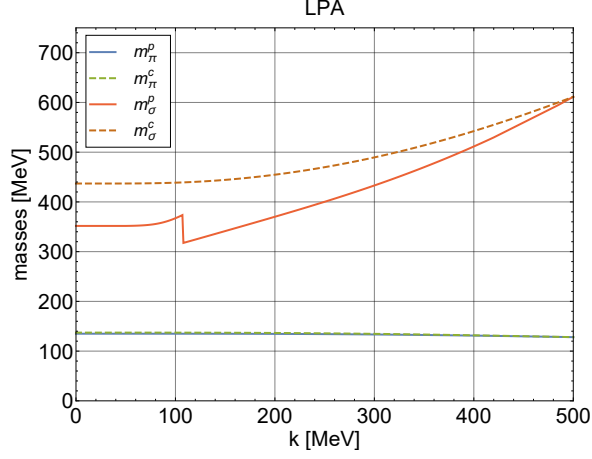


Figure 10.5: The Euclidean curvature masses in comparison to the real-time pole masses of the sigma and pion calculated with the LPA setup. Taken from [177].

The obtained masses in case of the SC₁L setup are shown in their scale dependence in fig. 10.6. Here, the renormalized curvature masses are defined as

$$\bar{m}_{\pi,k}^c \equiv m_{\pi,k}^c / \sqrt{Z_{\pi,k}}, \quad \bar{m}_{\sigma,k}^c \equiv m_{\sigma,k}^c / \sqrt{Z_{\sigma,k}} \quad (10.2)$$

with the wave function renormalization factors as previously introduced, see eq. (10.1). As in the LPA setup, the pion masses do not show any major scale dependence. The behavior of the sigma masses overall also agrees with the LPA case, however the pole and curvature mass disagree already in the UV due to the additional one-loop structure in the propagator. For a compilation of numerical values in the IR see tab. (10.1).

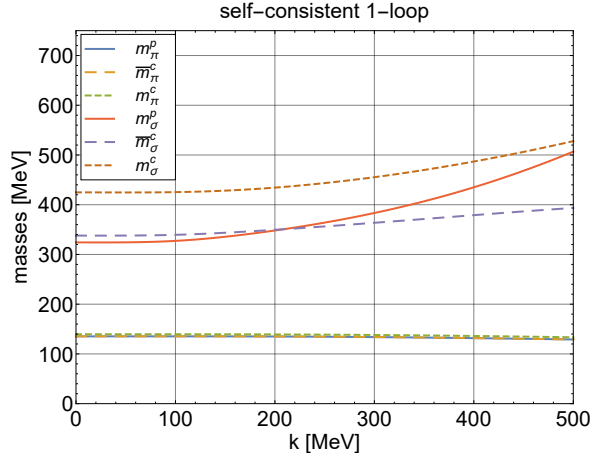


Figure 10.6: The Euclidean curvature masses with and without the wave function renormalization factor in comparison to the real-time pole masses. Taken from [177].

	g_σ [Λ]	$g_{\sigma\pi}$ [Λ]	m_π^c [MeV]	\bar{m}_π^c [MeV]	m_π^p [MeV]	m_σ^c [MeV]	\bar{m}_σ^c [MeV]	m_σ^p [MeV]
LPA	18.0	3.70	137	-	135	437	-	352
SC1L	15.5	3.58	140	135	135	425	338	324

Table 10.1: Numerical values for the coupling constants, the curvature masses, the renormalized curvature masses, and the pole masses as obtained with the LPA and the self-consistent one-loop (SC1L) setup in the IR.

10.2 TWO-POINT FUNCTIONS AND SPECTRAL FUNCTIONS

The real and imaginary parts of the two-point functions reveal the decay thresholds of the sigma and pion. These are determined by the curvature masses in the LPA setup and the pole masses in the SC1L case, corresponding to the zero-crossings of the real parts of the two-point functions. In fig. 10.7 and 10.8 the real and imaginary parts are shown in the IR. In case of the pion both setups agree very well. The only possible threshold is one off-shell pion decaying into an on-shell pion and sigma ($\pi^* \rightarrow \pi\sigma$) given by the according masses and therefore shifted comparing the LPA to the SC1L setup by about $\Delta\omega \approx 110 \text{ MeV}$. For the sigma, the LPA and SC1L calculations agree for small energies, but strongly differ at higher ones. The decay threshold of one off-shell sigma decaying into two on-shell pions ($\sigma^* \rightarrow \pi\pi$) is located at the almost identical energy due to the pion masses being very similar. The SC1L setup clearly shows a second threshold referring to an off-shell sigma decaying into two on-shell ones ($\sigma^* \rightarrow \sigma\sigma$), which is not visible in the LPA one. Additionally, in the LPA setup, the real and imaginary part of the sigma two-point function shows a divergence at $\omega \approx 950 \text{ MeV}$. These differences are generally explained by the cutoff sensitivity of the LPA setup at higher energies, where it thus becomes less reliable.

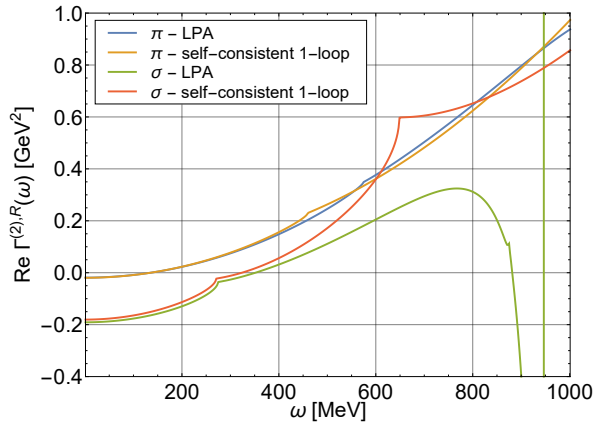


Figure 10.7: The real part of the pion and sigma two-point functions vs. the external energy ω in the IR as obtained from the LPA setup as well as from the self-consistent one-loop setup. Taken from [177].

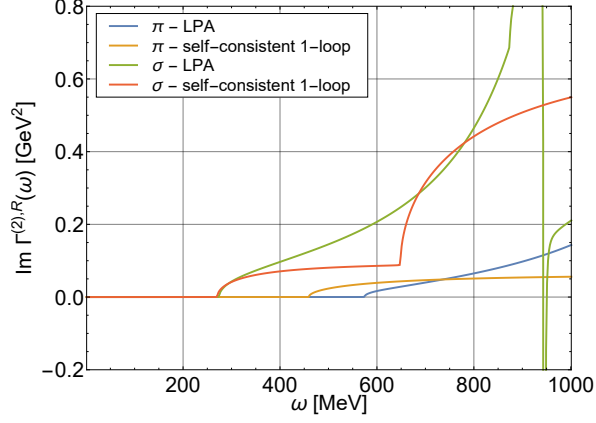


Figure 10.8: The imaginary part of the pion and sigma two-point functions vs. the external energy ω in the IR as obtained from the LPA setup as well as from the self-consistent one-loop setup. Taken from [177].

In the following the spectral functions of the sigma and pion obtained in both setups will be discussed. They are calculated according to eq. (9.27) and shown in fig. 10.9 ($\epsilon = 0.1 \text{ MeV}$) and fig. 10.10 ($\epsilon = 0 \text{ MeV}$). The pion spectral function shows a narrow peak ($\epsilon = 0.1 \text{ MeV}$) at its pole mass, which transforms into a δ -function in the limit $\epsilon \rightarrow 0$. The decay threshold into a pion and a sigma meson is visible as also in the two-point functions previously presented. At values below this threshold, the pion spectral function totally vanishes for $\epsilon \rightarrow 0$. Also the sigma spectral function mimics the behaviour of the two point functions. In the SC1L setup two thresholds are visible at $\omega = 2m_\pi^p$ ($\sigma^* \rightarrow \pi\pi$) and $\omega = 2m_\sigma^p$ ($\sigma^* \rightarrow \sigma\sigma$), whereas in the LPA calculation only the first threshold is visible but a pole at $\omega \approx 950 \text{ MeV}$ which is an artifact of the LPA UV values.

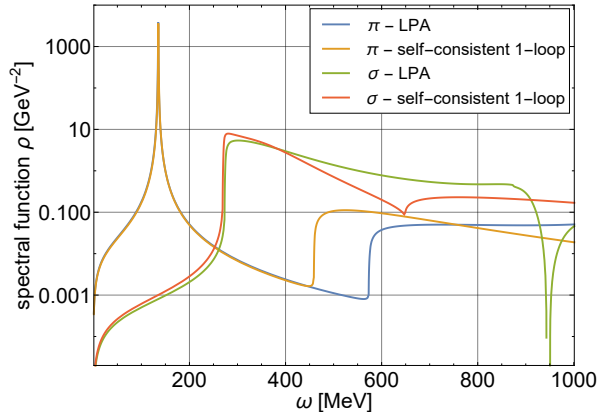


Figure 10.9: The pion and sigma spectral functions vs. the external energy ω in the IR as obtained from the LPA setup and from the self-consistent one-loop setup for $\epsilon = 0.1 \text{ MeV}$. Taken from [177].

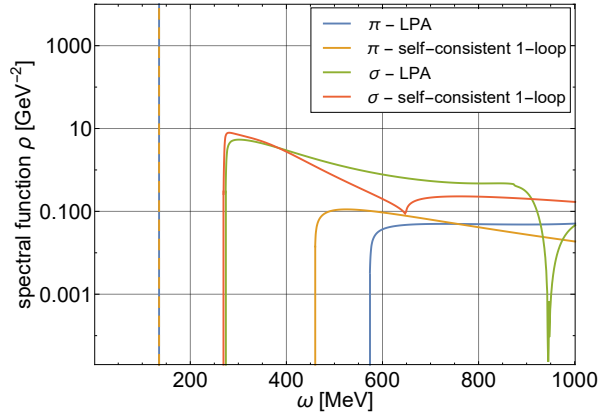


Figure 10.10: The pion and sigma spectral functions vs. the external energy ω in the IR as obtained from the LPA setup and from the self-consistent one-loop setup for $\varepsilon = 0 \text{ MeV}$. Taken from [177].

10.3 SUMMARY AND DISCUSSION

In this work the calculation of spectral functions within a self-consistent way using parametrizations of self energies as direct input to the ansatz for the average effective action has been presented. The results were compared to an established LPA calculation. The most remarkable result within the presented method is the efficiency of the calculation. As only couplings and pole masses carry a scale dependence and have to be calculated, this scheme is comparably economic. Furthermore the implementation is straight forward and the explicit analytic structures provide a clear understanding.

However, the SC1L setup as presented is limited to one-loop processes only and thus can not resolve higher order contributions such as vertex corrections and processes involving more particles. Including such processes in an analytic form into the current setup is possible, but at the cost of its simplicity. Nevertheless it is possible to test the effect of these structural limitations as done in [177] feeding back the momentum dependence of the two-point functions in the flow for the effective potential and the two-point functions themselves. The results however, do not differ much from the SC1L setup, with the only important improvement being a smearing of the unphysically sharp threshold for $\pi^* \rightarrow \sigma\pi$. Regarding a possible phenomenological application, where other processes are involved, this would anyway be less significant as these would provide smearing. Overall the comparison justifies the use of the numerically much more economic SC1L setup which provides very robust results.

Summarizing, the SC1L approach is very well suited to serve as a starting point for more realistic calculations of e.g. spectral functions in a strongly interacting warm and dense medium. It is therefore planned to extend this setup to finite temperatures and densities in a next step.

DERIVATION OF COMBINATORIAL BACKGROUND FORMULAS

The probability to detect n_d of N produced lepton pairs follows a binomial distribution and is therefore given by

$$\omega_d(n_d) = B(n_d, N, \epsilon_d) \quad (\text{A.1})$$

with the detection probability of a single pair ϵ_d . There are three different ways of not detecting a lepton pair: Either only the e^- (the total amount of these pairs is in the following denoted with n_-), the e^+ (n_+) or none of both (n_0) is found. The according multinomial distribution with the normalization conditions $N - n_d = n_0 + n_+ + n_-$ and $\sum_i \epsilon_i = 1$ reads

$$w_{\bar{d}}(n_0, n_-, n_+) = M(n_0, n_+, n_-, N - n_d, \epsilon_0, \epsilon_+, \epsilon_-) \quad (\text{A.2})$$

The detection probability distribution of a single e^-/e^+ for a given N and n_d can be expressed as a sum of such multinomial distributions $w_{\bar{d}}(n_0, n_-, n_+)$

$$\begin{aligned} \omega_{n_+} &= \sum_{n_-=0}^{N-n_d} M(n_0, n_+, n_-, N - n_d, \epsilon_0, \epsilon_+, \epsilon_-) \\ \omega_{n_-} &= \sum_{n_+=0}^{N-n_d} M(n_0, n_+, n_-, N - n_d, \epsilon_0, \epsilon_+, \epsilon_-) \end{aligned} \quad (\text{A.3})$$

The number of reconstructed unlike-sign pairs (**not** only true pairs n_d) is given by a summation over all possible values of n_d

$$\langle N_{+-} \rangle = \sum_{n_d} \langle n_{+-} \rangle B(n_d, N, \epsilon_d) \quad (\text{A.4})$$

with

$$\begin{aligned} \langle n_{+-} \rangle &= n_d^2 + n_d \sum_{n_+=1}^{N-n_d} n_+ \omega(n_+) + n_d \sum_{n_-=1}^{N-n_d} n_- \omega(n_-) \\ &\quad + \sum_{n_+=1}^{N-n_d} \sum_{n_-=1}^{N-n_d} n_+ n_- \omega(n_+, n_-) \end{aligned} \quad (\text{A.5})$$

denoting the amount of reconstructed unlike-sign pairs for a given value of N and n_d .

Inserting the definition of expectation values

$$\sum_{n_{\pm}=1}^{N-n_d} n_{\pm} \omega(n_{\pm}) = E(n_{\pm}) = \epsilon_{\pm}(N - n_d) \quad (\text{A.6})$$

it follows

$$\langle N_{+-} \rangle = \sum_{n_d} [n_d^2 + n_d \epsilon_+ (N - n_d) + n_d \epsilon_- (N - n_d) + \langle n_+ n_- \rangle] B(n_d, N, \epsilon_d) \quad (\text{A.7})$$

with the expectation value of the product of single reconstructed electrons and positrons $\langle n_+ n_- \rangle$. As n_+ and n_- depend on each other, the expectation value of their product is calculated using the displacement law to

$$\begin{aligned} \langle n_+ n_- \rangle &= \langle n_+ \rangle \langle n_- \rangle + \text{cov}(n_+ n_-) \\ &= \epsilon_+ \epsilon_- (N - n_d)^2 + \langle (n_+ - \langle n_+ \rangle)(n_- - \langle n_- \rangle) \rangle \\ &= \dots = \epsilon_+ \epsilon_- (N - n_d)^2 - \epsilon_+ \epsilon_- (N - n_d). \end{aligned} \quad (\text{A.8})$$

After rewriting it follows

$$\langle N_{+-} \rangle = \sum_{n_d} [(n_d + (\epsilon_+ (N - n_d)))(n_d + (\epsilon_- (N - n_d))) - \epsilon_+ \epsilon_- (N - n_d)] B(n_d, N, \epsilon_d) \quad (\text{A.9})$$

Now, the summation can be carried out which leads to

$$\begin{aligned} \langle N_{+-} \rangle &= (1 - \epsilon_+ - \epsilon_- + \epsilon_+ \epsilon_-) \langle n_d^2 \rangle \\ &\quad + (\epsilon_+ N + \epsilon_- N - 2\epsilon_+ \epsilon_- N + \epsilon_+ \epsilon_-) \langle n_d \rangle + \epsilon_+ \epsilon_- N^2 - \epsilon_+ \epsilon_- N \end{aligned} \quad (\text{A.10})$$

With $\langle n_d \rangle = \epsilon_d N$ and $\text{cov}(n_d, n_d) = \text{var}(n_d) = \epsilon_d N(1 - \epsilon_d)$ it simplifies to

$$\langle N_{+-} \rangle = [\epsilon_d + \epsilon_+(1 - \epsilon_d)][\epsilon_d + \epsilon_-(1 - \epsilon_+)](N^2 - N) + \epsilon_d N \quad (\text{A.11})$$

Averaging over N leads to the unlike-sign foreground consisting of unlike-sign combinatorial background and true pairs:

$$\begin{aligned}
 \langle FG_{+-} \rangle &= \sum_N \langle N_{+-} \rangle P(N) \\
 &= [\epsilon_d + \epsilon_+(1 - \epsilon_d)][\epsilon_d + \epsilon_-(1 - \epsilon_+)](\langle N^2 \rangle - \langle N \rangle) + \epsilon_d \langle N \rangle \\
 &= BG_{+-} + S \quad (\text{A.12})
 \end{aligned}$$

Now, the amount of like-sign pairs is calculated. The steps are analogue to the previous calculation and are therefore shortened. The definition of like-sign pairs is given by

$$\begin{aligned}
 \langle N_{\pm\pm} \rangle &= \sum_{n_d} \langle n_{\pm\pm} \rangle B(n_d, N, \epsilon_d) \\
 &= \sum_{n_d} \frac{1}{2} [n_d^2 - n_d + \langle n_{\pm}^2 \rangle + \langle n_{\pm} \rangle (2n_d - 1)] B(n_d, N, \epsilon_d) \quad (\text{A.13})
 \end{aligned}$$

Inserting $[n_{\pm}] = \epsilon_{\pm}(N - n_d)$ and $[n_{\pm}^2] = \epsilon_{\pm}^2(N - n_d)^2 - \epsilon_{\pm}(N - n_d)(1 - \epsilon_{\pm})$ (exactly the same calculation steps as previously in the unlike-sign case) and averaging over n_d leads to

$$\langle N_{\pm\pm} \rangle = \frac{1}{2} (N^2 - N) [\epsilon_d + \epsilon_{\pm}(1 - \epsilon_d)]^2 \quad (\text{A.14})$$

Averaging over N yields the like-sign foreground which is background only per definition and reads:

$$\begin{aligned}
 \langle FG_{\pm\pm} \rangle &= \sum_N \langle N_{\pm\pm} \rangle P(N) \\
 &= \frac{1}{2} (\langle N^2 \rangle - \langle N \rangle) [\epsilon_d + \epsilon_{\pm}(1 - \epsilon_d)]^2 = \langle BG_{\pm\pm} \rangle \quad (\text{A.15})
 \end{aligned}$$

A comparison to equation A.12 leads to the connection

$$\langle BG_{+-} \rangle = \frac{[\epsilon_{+-} + \epsilon_+(1 - \epsilon_{+-})][\epsilon_{+-} + \epsilon_-(1 - \epsilon_{+-})]}{[\epsilon_{++} + \epsilon_+(1 - \epsilon_{++})][\epsilon_{--} + \epsilon_-(1 - \epsilon_{--})]} 2\sqrt{\langle FG_{++} \rangle \langle FG_{--} \rangle} \quad (\text{A.16})$$

The quotient of efficiency values could be calculated using simulation. However this would dramatically pronounce possible shortcomings in simulation. These issues can be overcome generating a data sample without signal, where one has direct access to $\langle BG_{+-} \rangle = \langle FG_{+-} \rangle$. This is achieved applying the *event mixing technique*. In this case, equation A.16 rewrites to

$$\langle fg_{+-} \rangle = \frac{[\epsilon_{+-} + \epsilon_+(1 - \epsilon_{+-})][\epsilon_{+-} + \epsilon_-(1 - \epsilon_{+-})]}{[\epsilon_{++} + \epsilon_+(1 - \epsilon_{++})][\epsilon_{--} + \epsilon_-(1 - \epsilon_{--})]} 2\sqrt{\langle fg_{++} \rangle \langle fg_{--} \rangle} \quad (\text{A.17})$$

where small letters denote the use of event mixing to obtain the corresponding data. Inserting into equation A.16 the final result reads

$$\langle BG_{+-} \rangle = \frac{\langle fg_{+-} \rangle}{2\sqrt{\langle fg_{++} \rangle \langle fg_{--} \rangle}} 2\sqrt{\langle FG_{++} \rangle \langle FG_{--} \rangle} = k 2\sqrt{\langle FG_{++} \rangle \langle FG_{--} \rangle} \quad (\text{A.18})$$

introducing the *k-factor* that, generally spoken, corrects for different efficiencies of electrons and positrons.

ADDITIONAL FIGURES TO CHAPTER 5

B.1 π^0 AND η RECONSTRUCTION IN CENTRALITY CLASSES

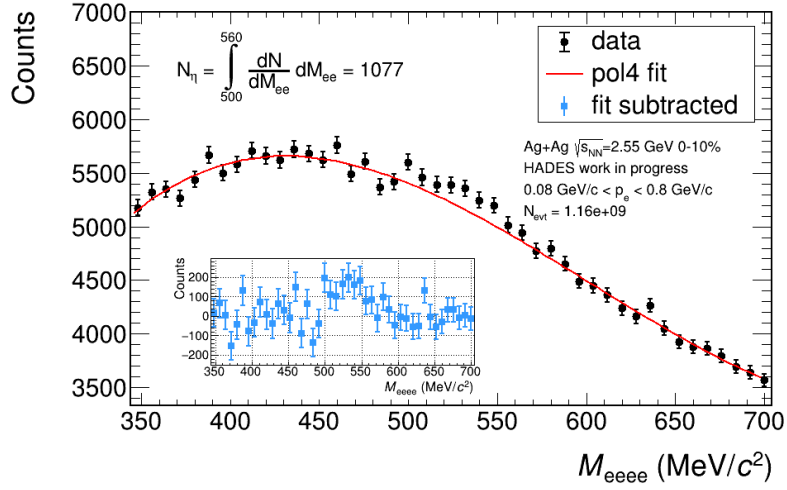


Figure B.1: Four electron invariant mass spectrum and η signal after background subtraction in the 0 – 10% centrality data.

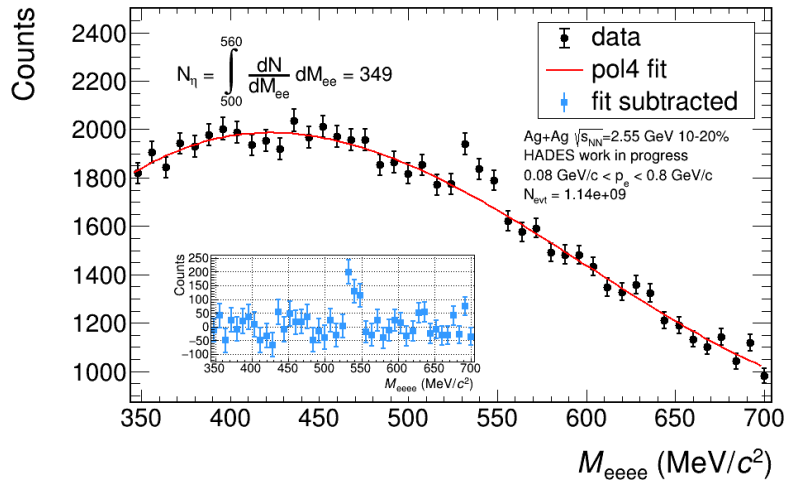


Figure B.2: Four electron invariant mass spectrum and η signal after background subtraction in the 10 – 20% centrality data.

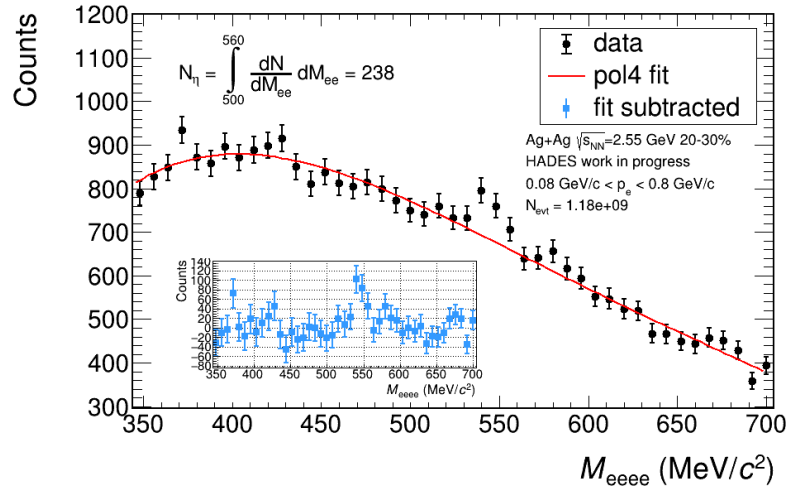


Figure B.3: Four electron invariant mass spectrum and η signal after background subtraction in the 20 – 30% centrality data.

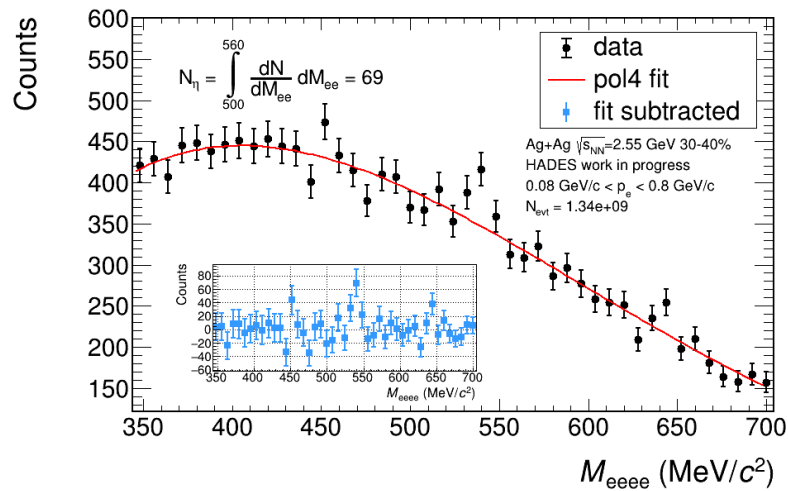


Figure B.4: Four electron invariant mass spectrum and η signal after background subtraction in the 30 – 40% centrality data.

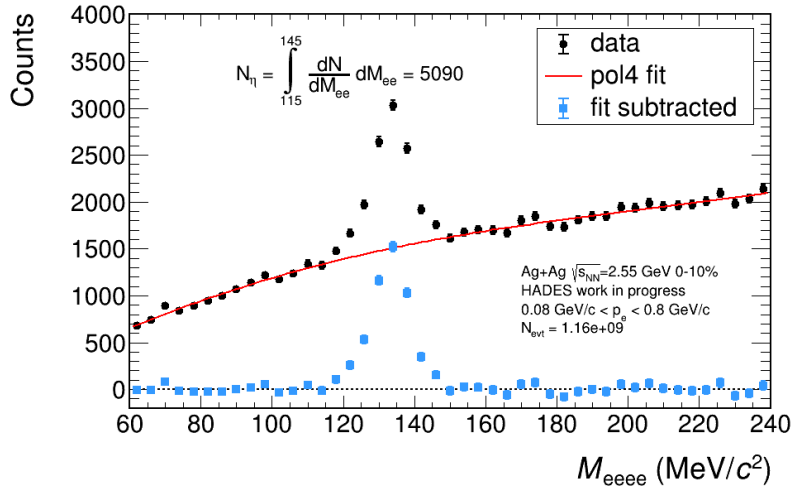


Figure B.5: Four electron invariant mass spectrum and π^0 signal after background subtraction in the 0 – 10% centrality data.

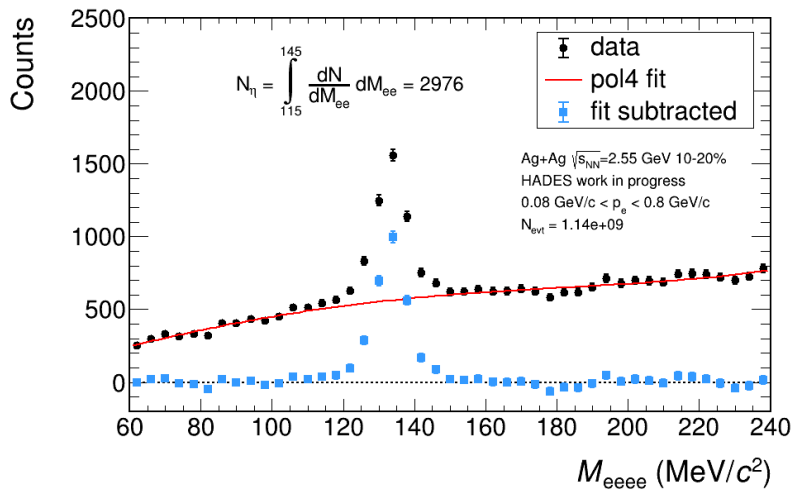


Figure B.6: Four electron invariant mass spectrum and π^0 signal after background subtraction in the 10 – 20% centrality data.

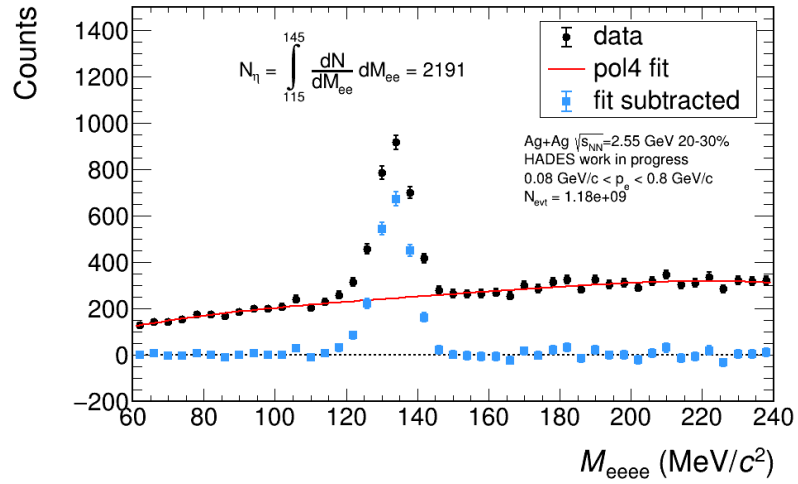


Figure B.7: Four electron invariant mass spectrum and π^0 signal after background subtraction in the 20 – 30% centrality data.

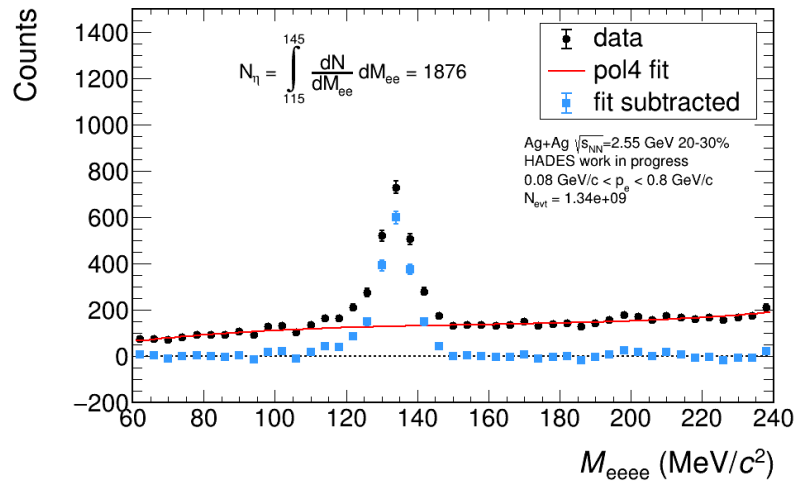


Figure B.8: Four electron invariant mass spectrum and π^0 signal after background subtraction in the 30 – 40% centrality data.

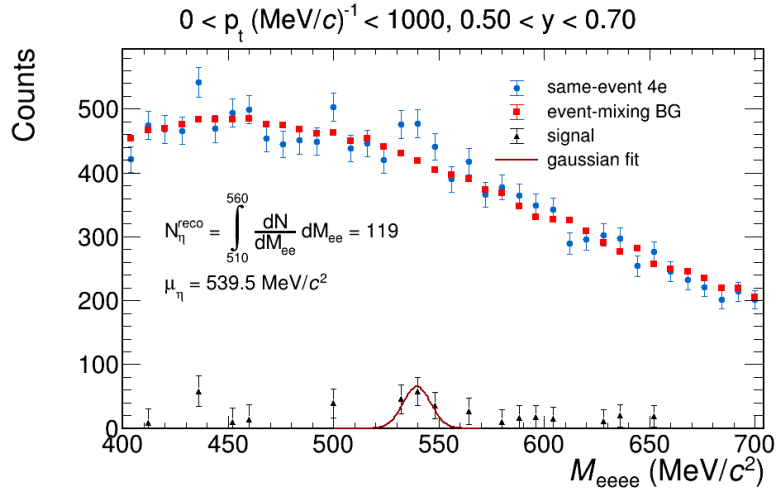
B.2 π^0 AND η RECONSTRUCTION IN BINS OF $p_t - y$


Figure B.9: Four electron invariant mass spectrum for $0.5 < y < 0.7$ in the η mass region. The background is calculated from event-mixing.

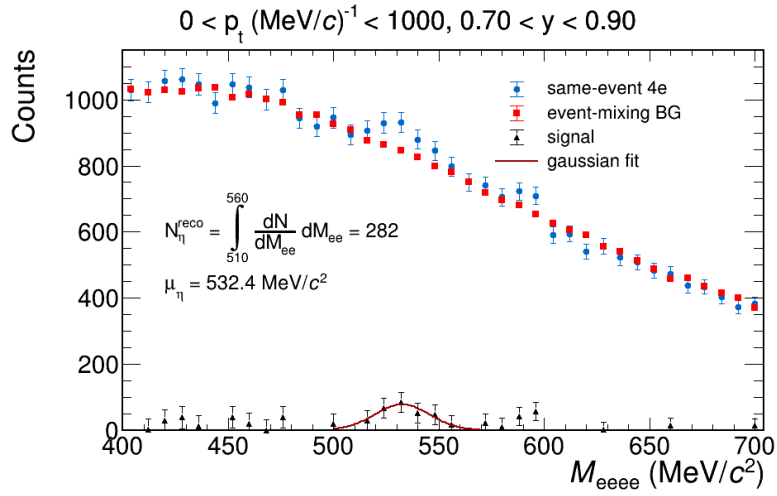


Figure B.10: Four electron invariant mass spectrum for $0.7 < y < 0.9$ in the η mass region. The background is calculated from event-mixing.

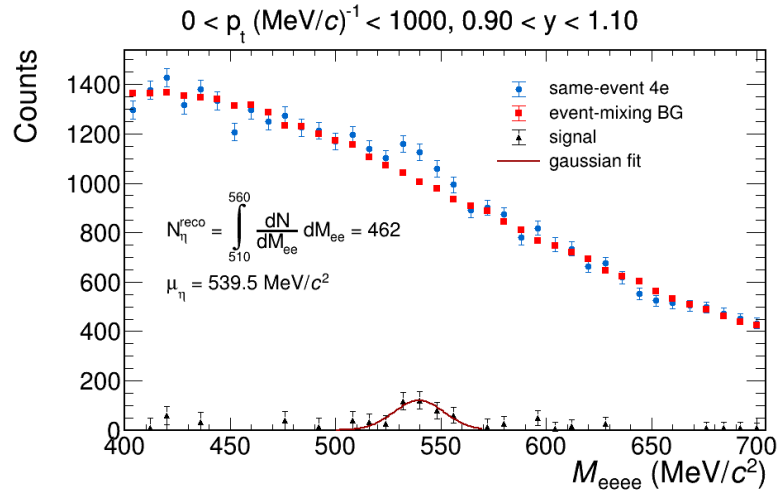


Figure B.11: Four electron invariant mass spectrum for $0.9 < y < 1.1$ in the η mass region. The background is calculated from event-mixing.

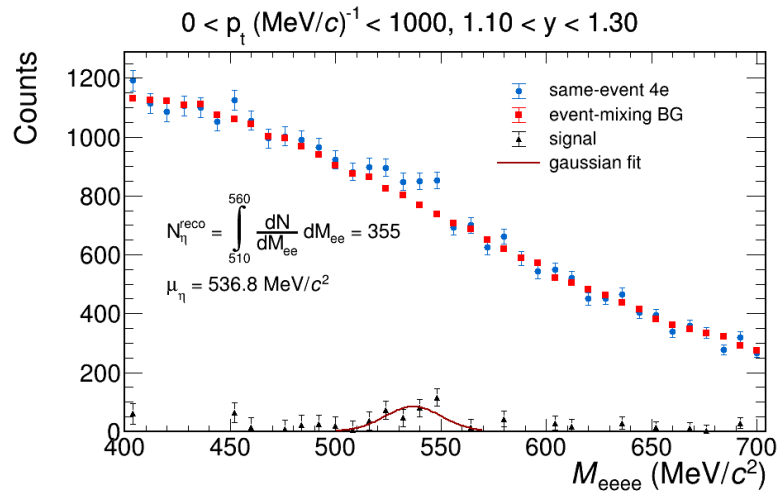


Figure B.12: Four electron invariant mass spectrum for $1.1 < y < 1.3$ in the η mass region. The background is calculated from event-mixing.

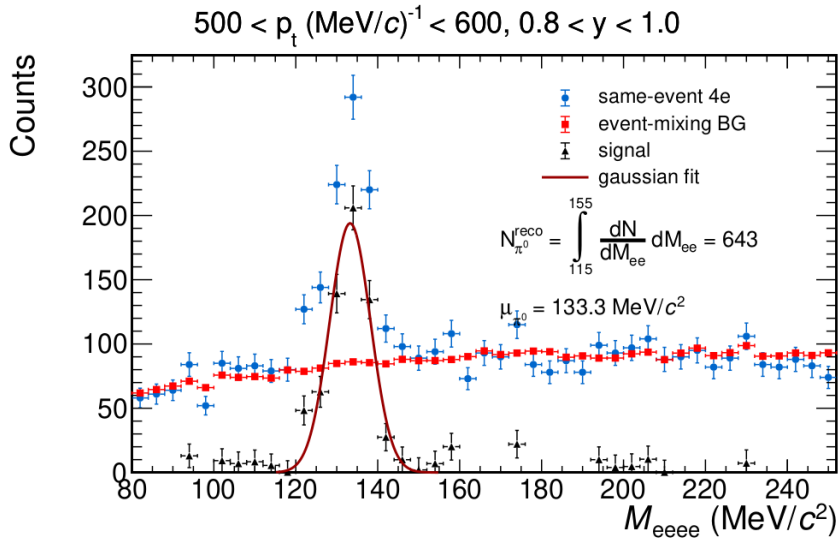


Figure B.13: Four electron invariant mass spectrum for $500 < p_t \text{ (MeV/c)}^{-1} < 600$ and $0.8 < y < 1.0$ in the π^0 mass region. The background is calculated from event-mixing.

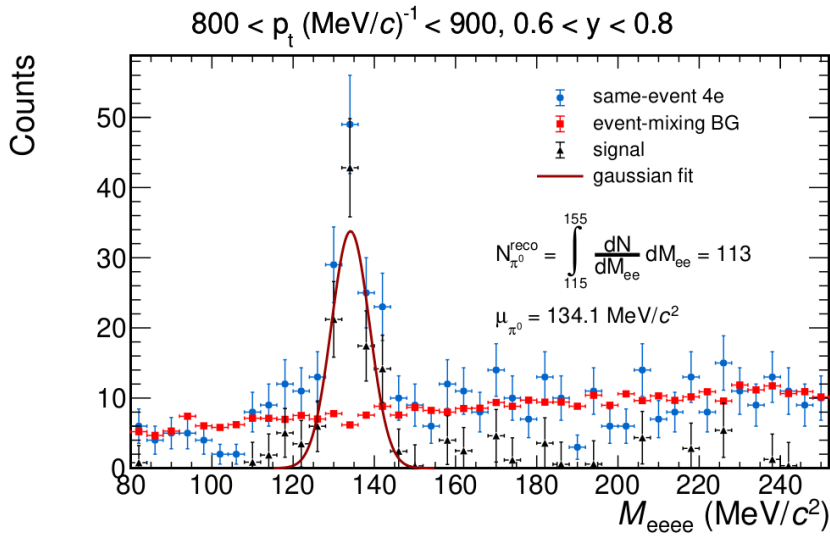


Figure B.14: Four electron invariant mass spectrum for $800 < p_t \text{ (MeV/c)}^{-1} < 900$ and $0.6 < y < 0.8$ in the π^0 mass region. The background is calculated from event-mixing.

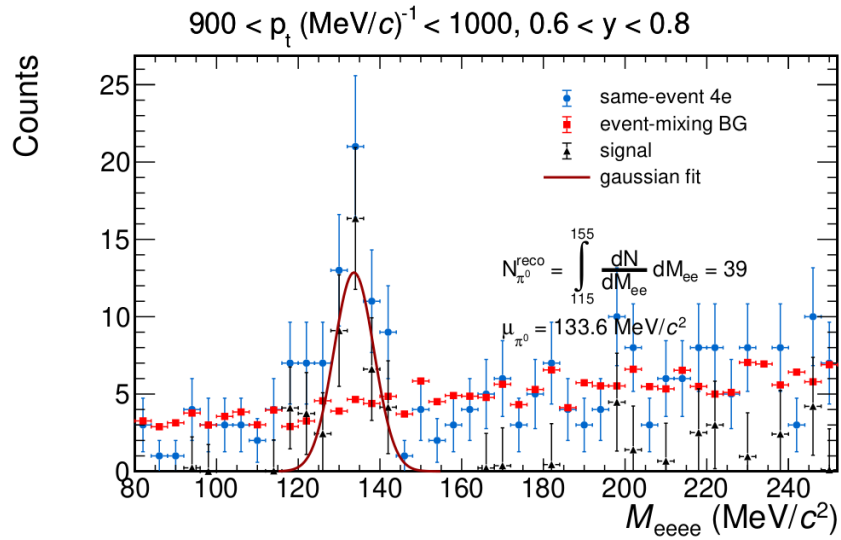


Figure B.15: Four electron invariant mass spectrum for $900 < p_t \text{ (MeV/c)}^{-1} < 1000$ and $0.6 < y < 0.8$ in the π^0 mass region. The background is calculated from event-mixing.

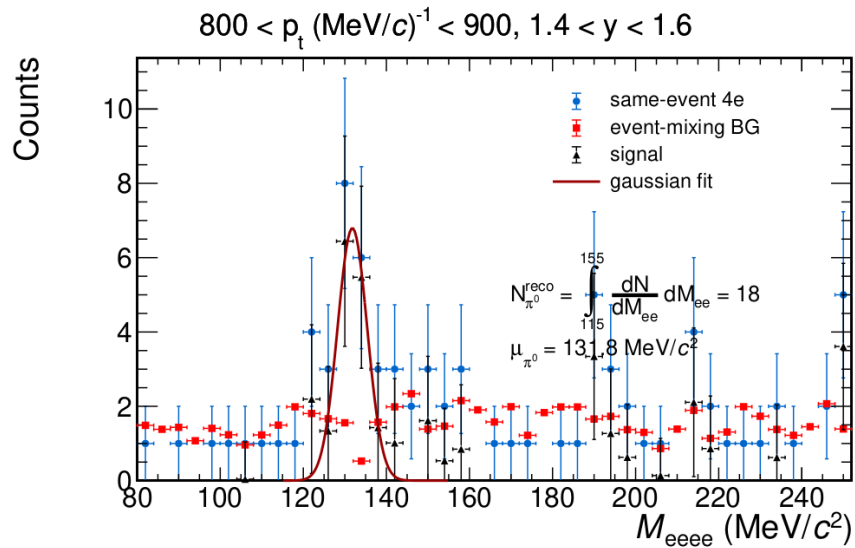


Figure B.16: Four electron invariant mass spectrum for $800 < p_t \text{ (MeV/c)}^{-1} < 900$ and $1.4 < y < 1.6$ in the π^0 mass region. The background is calculated from event-mixing.



GIBUU JOBCARDS FOR NN REFERENCE SIMULATION

C.1 JOBCARD FOR P+N COLLISIONS

```
!-----*- fortran -*-----
! jobcard for p+n Dielectron production.
!-----

! file: ./inputOutput/input.f90
&input
  eventtype      = 12          ! 12 = HiPion A
  numEnsembles   = 4000        ! number of ensembles
  numTimeSteps   = 0          ! number of time steps
  delta_T        = 0.2         ! time step size [fm]
  num_runs_SameEnergy = 200    ! number of runs
  length_perturbative = 250
  freezeRealParticles = T
  path_To_Input  = '~/GIBUU/buinput'
/

&initDatabase
  rho_dilep = T
/

! file ./code/collisions/twoBodyReactions/baryonBaryon/barBar_barBar.f90
&barBar_barBar
  etafac= 3.5 ! default is 6.5
/

! file: ./analysis/DileptonAnalysis.f90
&DileptonAnalysis
  Enable = .true.
  particle_source = T
  binsz = 0.02
  WriteEvents = 1
  filter = 0          ! 1=KEK, 2=HADES(simple), 3=HADES(full,
                      pair), 4=HADES(full,single), 6 = DLS
  massBinning(1:2) = 0.150, 0.500
  brems = 3          ! 1 = SPA, 2 = OBE, 3 = OBE+FF
/

! file: ./init/initHiPion.f90
&HiPionNucleus
  projectileID      = 1          ! ID of projectile
  projectileCharge  = 1          ! charge of projectile
```

```

ekin_lab      = 1.58          ! kinetic energy of projectile
  in lab frame
distance      = -1.          ! distance in z-direction at
  init
nTestParticles = 50          ! number of projectiles per
  ensemble
impact_parameter = -1.      ! impact parameter [fm], <0:
  distributed over disk
doPerturbativeInit = T
minimumMomentum = 0.0
NucCharge = 0              !for p collisions with n from
  deuteron
/

! file: ./density/nucleus.f90
&target
  target_Z= 0, target_A= 1 ! neutron only
/

&insertion
  minimumEnergy = 0.0
/

&HiPion_Analysis
  Enable      = T
  DoOutChannels = T
/

! file code/collisions/twoBodyReactions/master_2Body.f90
&master_2Body
  baryonBaryonScattering=.true.
  baryonMesonScattering=.true.
  mesonMesonScattering=.true.
  HiEnergyThresholdBarBar=4.0
  HiEnergyThresholdBarBarDelta=0.0
/

! file code/potential/baryonPotential.f90
&baryonPotential
  EQS_Type=0 ! 1=soft mom-dep, 2=hard mom-dep, 3=soft non-mom-dep
  , 4=hard non-mom-dep, 5=medium mom-dep
/

! file: ./density/pauliBlocking.f90
&initPauli
  pauliSwitch      = 0 ! 0: no Pauli blocking, 1: dynamic, 2:
  analytic
/

&baryonBaryon
  NNpi_BG = 3      ! (1=Teis, 2=Buss, 3=Weil)
/

```

```
&angular_distribution
    NN_NR_noniso = T
/

&decayChannels
    rhoDelta_is_sigmaDelta = T
/

! file: ./collisions/twoBodyReactions/HiEnergy/DoCollTools.f90
&pythia
    PARP(91) = 0.44      ! width intrinsic kT
/
```

C.2 JOBCARD FOR P+P COLLISIONS

```

!-----*- fortran -*-----
! jobcard for p+p Dielectron production.
!-----

! file: ./inputOutput/input.f90
&input
  eventtype      = 12          ! 12 = HiPion A
  numEnsembles   = 4000        ! number of ensembles
  numTimeSteps   = 0          ! number of time steps
  delta_T        = 0.2         ! time step size [fm]
  num_runs_SameEnergy = 200    ! number of runs
  length_perturbative = 250
  freezeRealParticles = T
  path_To_Input  = '~/GIBUU/buuinput'
/

&initDatabase
  rho_dilep = T
/

! file: ./analysis/DileptonAnalysis.f90
&DileptonAnalysis
  Enable = .true.
  particle_source = T
  binsz = 0.02
  WriteEvents = 1
  filter = 0          ! 1=KEK, 2=HADES(simple), 3=HADES(full,
                      pair), 4=HADES(full,single), 6 = DLS
  massBinning(1:2) = 0.150, 0.500
  brems = 3          ! 1 = SPA, 2 = OBE, 3 = OBE+FF
/

! file: ./init/initHiPion.f90
&HiPionNucleus
  projectileID      = 1          ! ID of projectile
  projectileCharge  = 1          ! charge of projectile
  ekin_lab          = 1.58       ! kinetic energy of projectile
                                in lab frame
  distance          = -1.        ! distance in z-direction at
                                init
  nTestParticles    = 50         ! number of projectiles per
                                ensemble
  impact_parameter  = -1.        ! impact parameter [fm], <0:
                                distributed over disk
  doPerturbativeInit = T
  minimumMomentum  = 0.0
  NucCharge         = 1          !for p collisions with n from
                                deuteron
/

```

```

! file: ./density/nucleus.f90
&target
    target_Z= 1, target_A= 1 ! proton
/

&insertion
    minimumEnergy = 0.0
/

&HiPion_Analysis
    Enable          = T
    DoOutChannels = T
/

! file code/collisions/twoBodyReactions/master_2Body.f90
&master_2Body
    baryonBaryonScattering=.true.
    baryonMesonScattering=.true.
    mesonMesonScattering=.true.
    HiEnergyThresholdBarBar=4.0
    HiEnergyThresholdBarBarDelta=0.0
/

! file code/potential/baryonPotential.f90
&baryonPotential
    EQS_Type=0 ! 1=soft mom-dep, 2=hard mom-dep, 3=soft non-mom-dep
               , 4=hard non-mom-dep, 5=medium mom-dep
/

! file: ./density/pauliBlocking.f90
&initPauli
    pauliSwitch      = 0 ! 0: no Pauli blocking, 1: dynamic, 2:
                       analytic
/

&baryonBaryon
    NNpi_BG = 3      ! (1=Teis, 2=Buss, 3=Weil)
/

&angular_distribution
    NN_NR_noniso = T
/

&decayChannels
    rhoDelta_is_sigmaDelta = T
/

! file: ./collisions/twoBodyReactions/HiEnergy/DoCollTools.f90
&pythia
    PARP(91) = 0.44      ! width intrinsic kT
/

```


ADDITIONAL FIGURES TO CHAPTER 6

D.1 HADRONIC COCKTAIL AND NN CONTRIBUTION SIMULATION

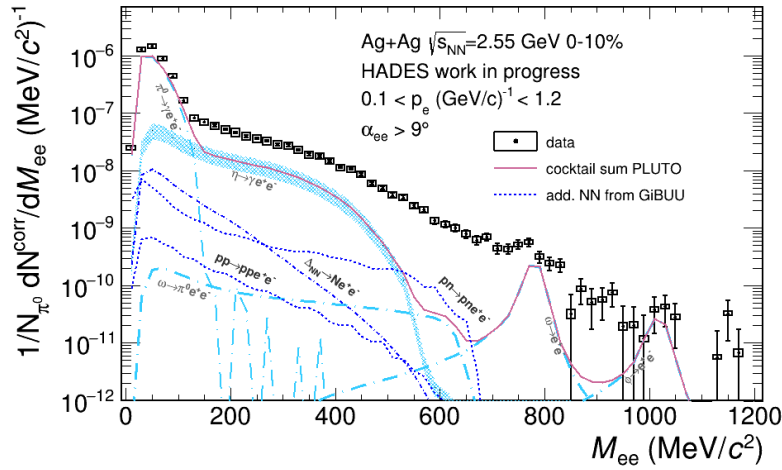


Figure D.1: Hadronic cocktail and relevant NN channels from GiBUU simulation in 0 – 10% centrality.

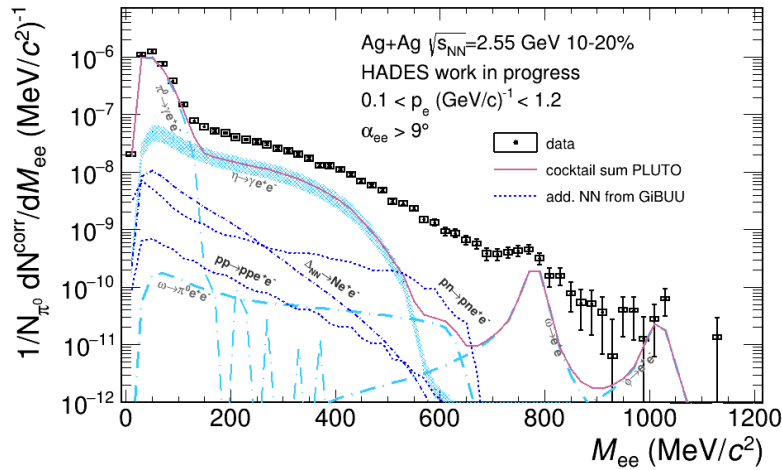


Figure D.2: Hadronic cocktail and relevant NN channels from GiBUU simulation in 10 – 20% centrality.

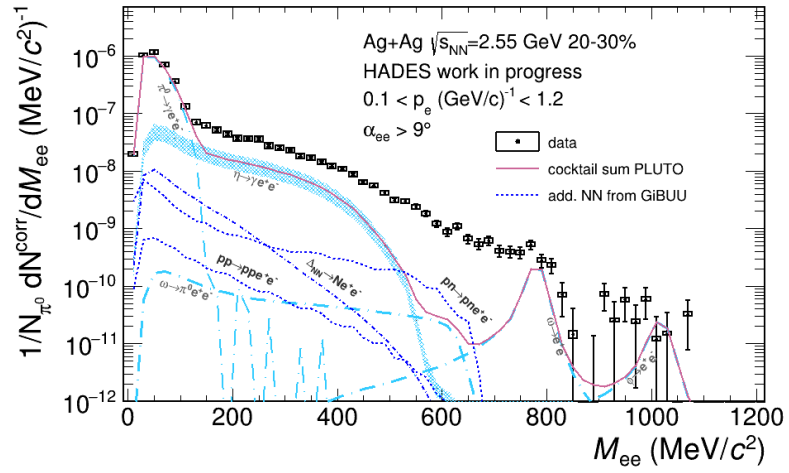


Figure D.3: Hadronic cocktail and relevant NN channels from GiBUU simulation in 20 – 30% centrality.

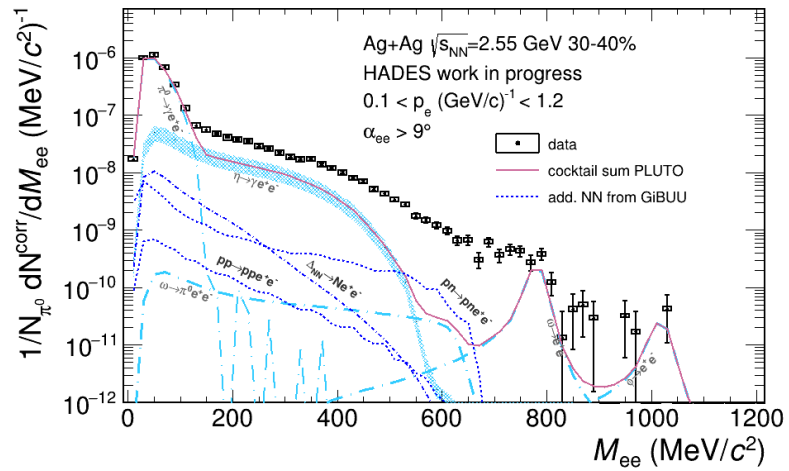


Figure D.4: Hadronic cocktail and relevant NN channels from GiBUU simulation in 30 – 40% centrality.

D.2 MEDIUM TEMPERATURE ESTIMATION

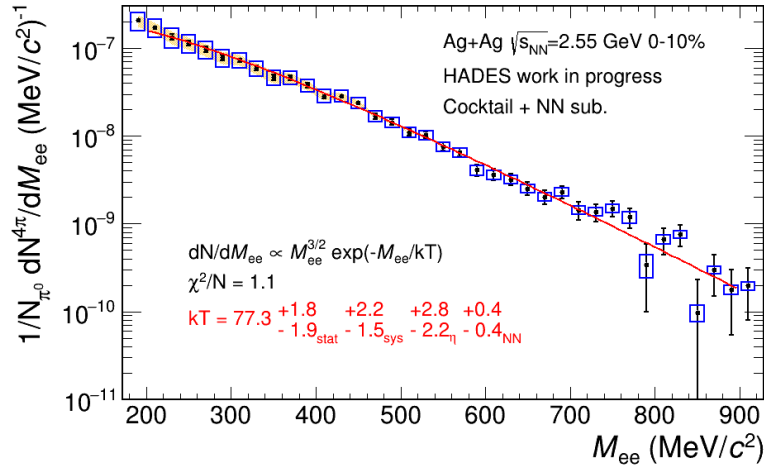


Figure D.5: Temperatur estimation in 0 – 10% centrality using a thermal fit $200 \text{ MeV}/c^2 < M_{ee} < 900 \text{ MeV}/c^2$.

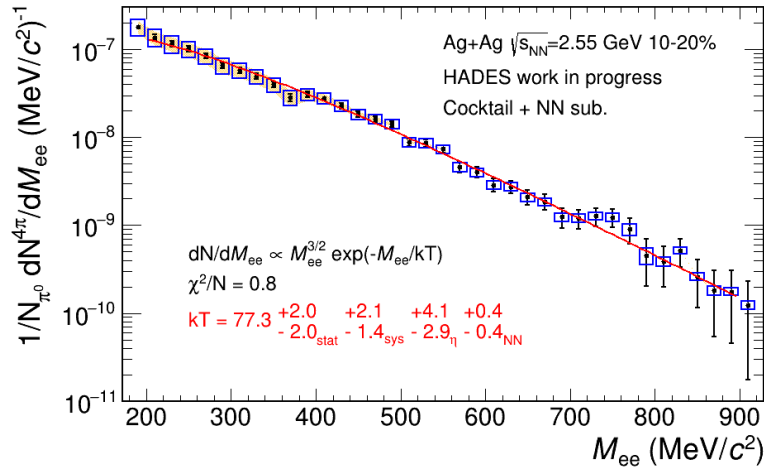


Figure D.6: Temperatur estimation in 10 – 20% centrality using a thermal fit $200 \text{ MeV}/c^2 < M_{ee} < 900 \text{ MeV}/c^2$.

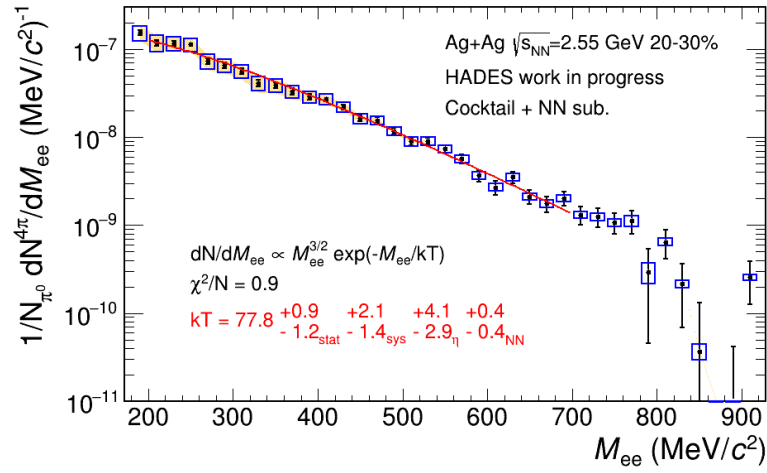


Figure D.7: Temperatur estimation in 20 – 30% centrality using a thermal fit $200 \text{ MeV}/c^2 < M_{ee} < 700 \text{ MeV}/c^2$.

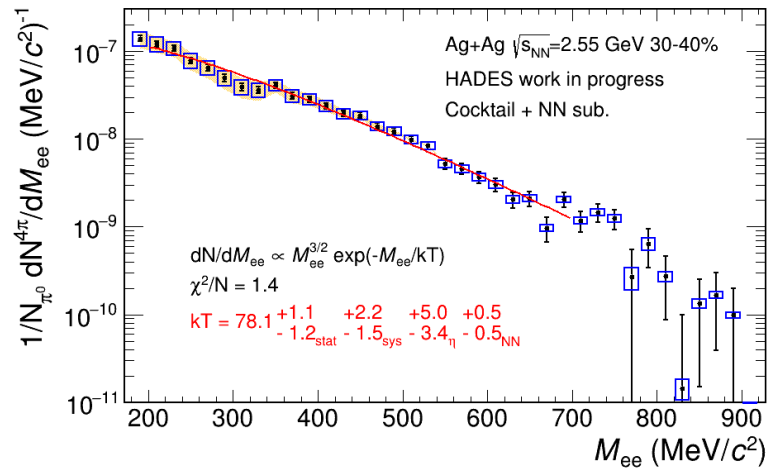


Figure D.8: Temperatur estimation in 30 – 40% centrality using a thermal fit $200 \text{ MeV}/c^2 < M_{ee} < 700 \text{ MeV}/c^2$.

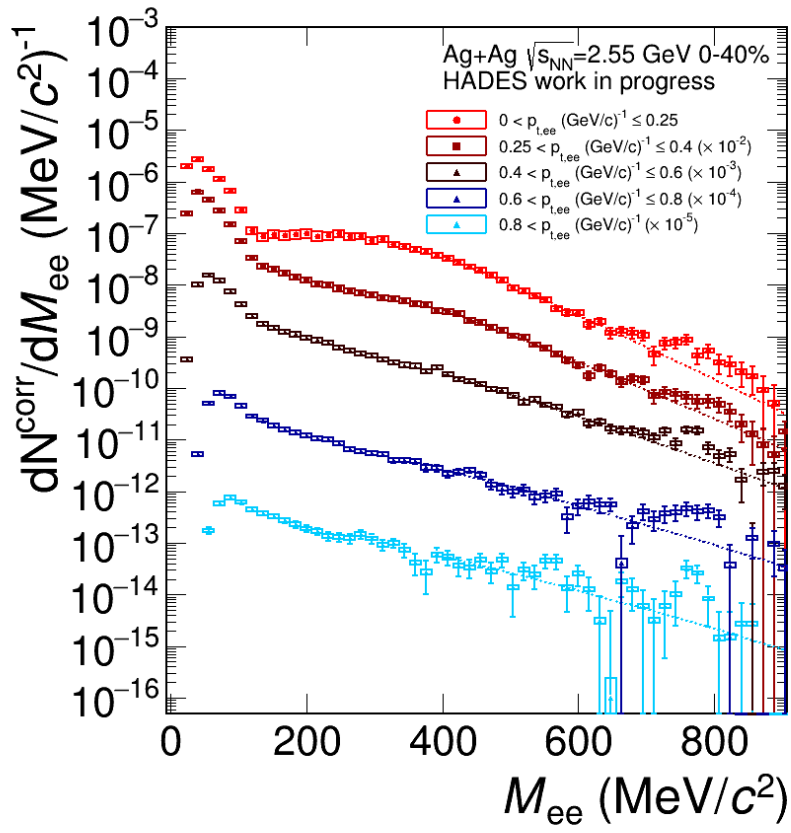
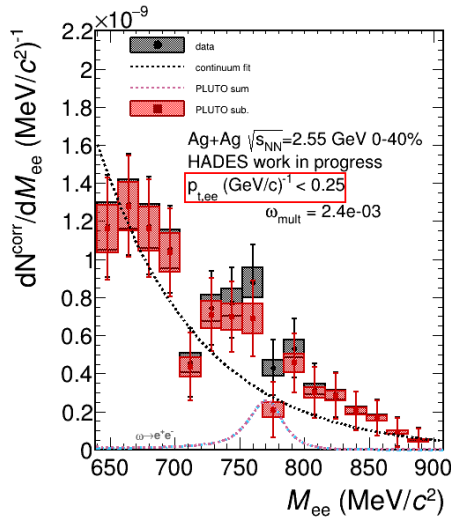
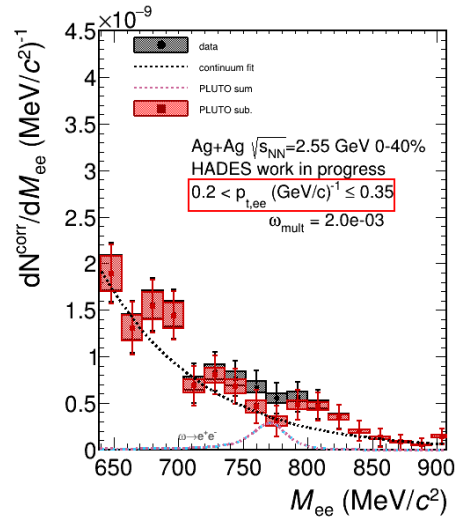
D.3 TRANSVERSE MOMENTUM DEPENDENT ω MULTIPLICITY ANALYSIS

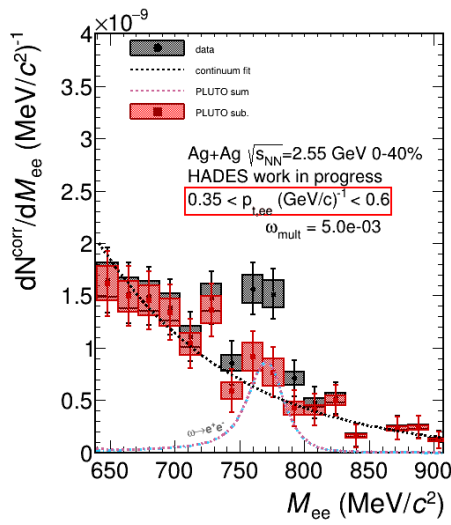
Figure D.9: Dielectron signal spectra in five bins of pair momentum. Thermal fits to the continuum for $500 \text{ MeV}/c^2 < M_{ee} < 700 \text{ MeV}/c^2$ are shown as dashed lines.



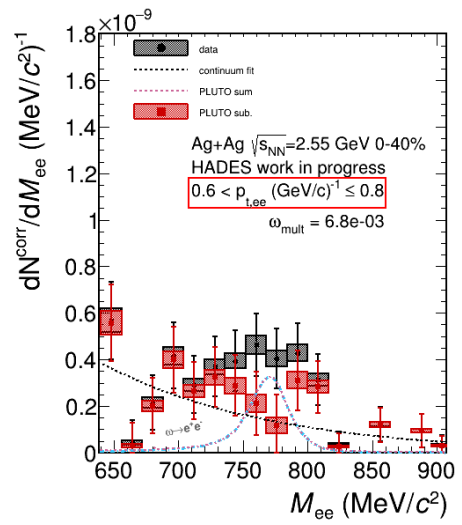
(a)



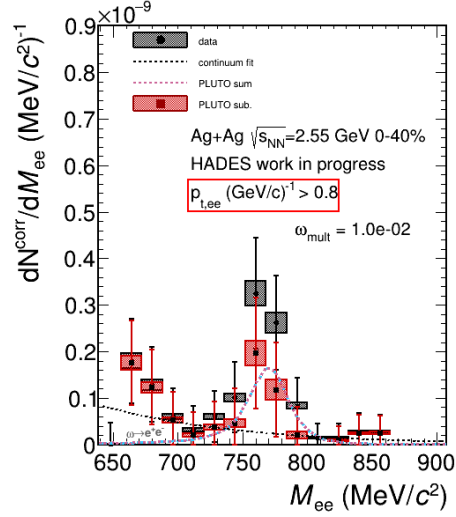
(b)



(c)



(d)



(e)

Figure D.10: Transverse momentum dependent dielectron signal in five bins of invariant mass (black data points). The excess observed in the $\rho - \omega$ mass region is removed in each bin based on a simulated thermal distribution of the $\omega \rightarrow e^+e^-$ signal without medium modifications tuning the ω multiplicity accordingly. Note the linear scaling.

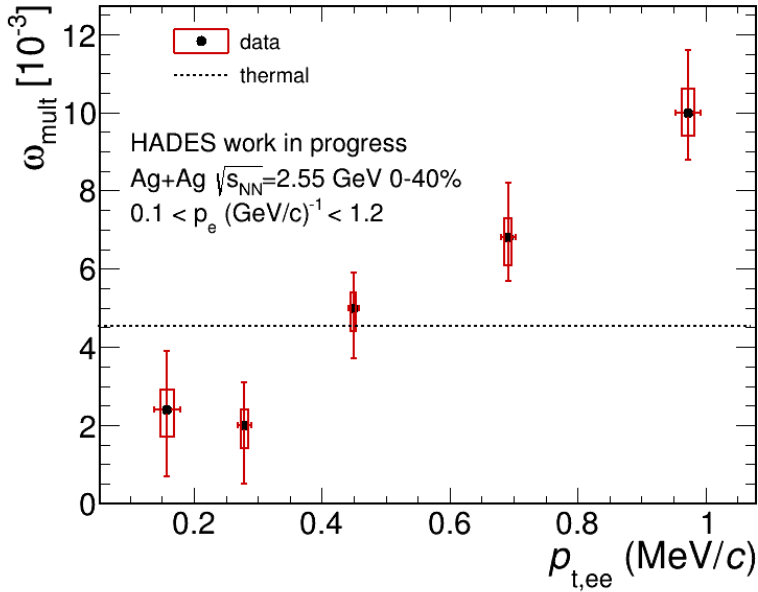


Figure D.11: ω multiplicity as a function of transverse pair momentum. The data points are extracted using a PLUTO based $\omega \rightarrow e^+e^-$ simulation to describe the observed excess in the $\rho - \omega$ mass region in each pair momentum bin.

D.4 ACCEPTANCE CORRECTED SPECTRA FOR THEORY COMPARISON

The shown spectra are acceptance corrected for single electrons and positrons that fulfill $100 \text{ MeV}/c < p_e < 1200 \text{ MeV}/c$, $16^\circ < \Theta_e < 83^\circ$ and $p_{e^+} > e^{-0.135 \cdot \Theta + 8.3} + 100 \text{ MeV}/c$ corresponding to the geometric HADES acceptance with the magnetic field setting used in the Ag+Ag data taking.

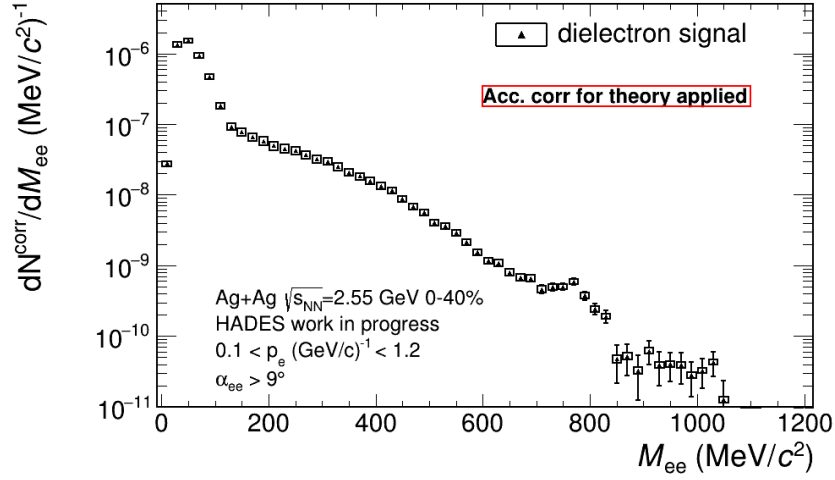


Figure D.12: Dielectron signal in Ag+Ag collisions at $\sqrt{s_{NN}} = 2.55 \text{ GeV}$. The data is corrected for efficiency and acceptance losses within the geometric acceptance of HADES.

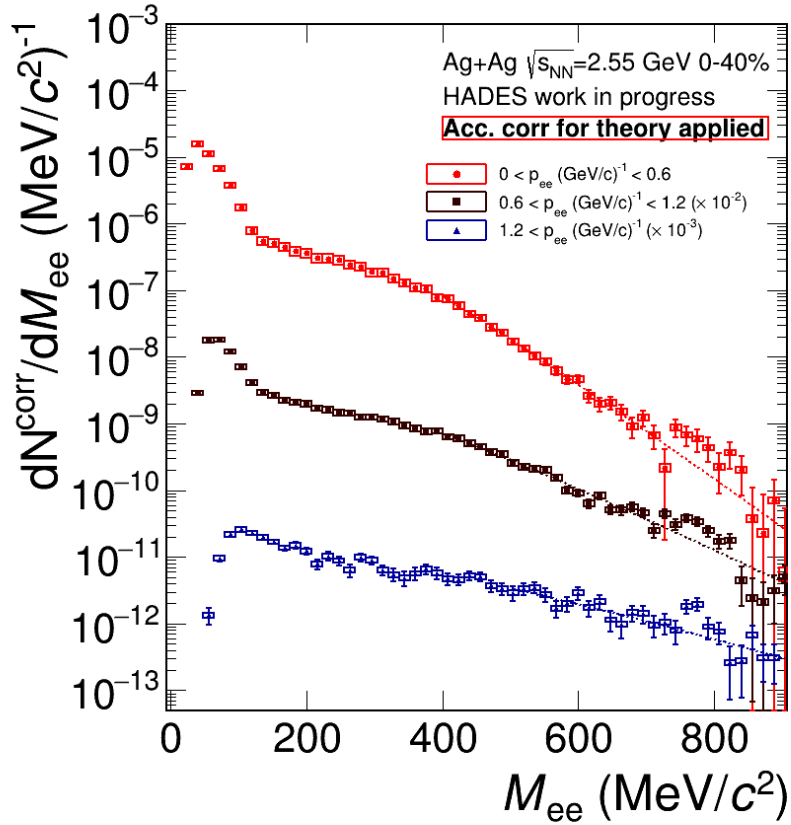


Figure D.13: Dielectron signal in Ag+Ag collisions at $\sqrt{s_{NN}} = 2.55$ GeV in three bins of pair momentum. The data is corrected for efficiency and acceptance losses within the geometric acceptance of HADES.

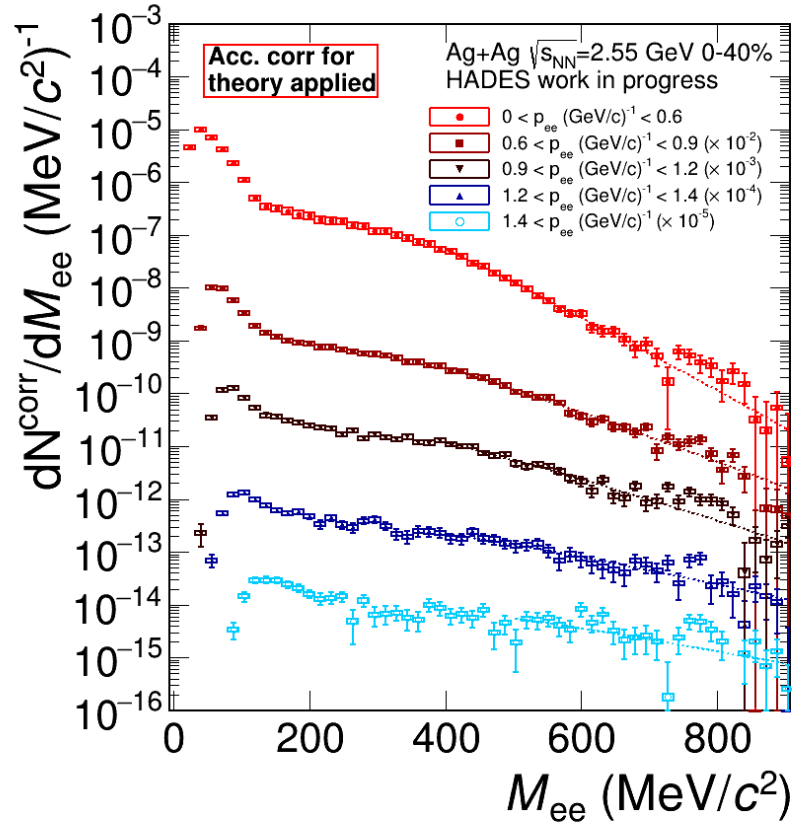


Figure D.14: Dielectron signal in Ag+Ag collisions at $\sqrt{s_{NN}} = 2.55$ GeV in five bins of pair momentum. The data is corrected for efficiency and acceptance losses within the geometric acceptance of HADES

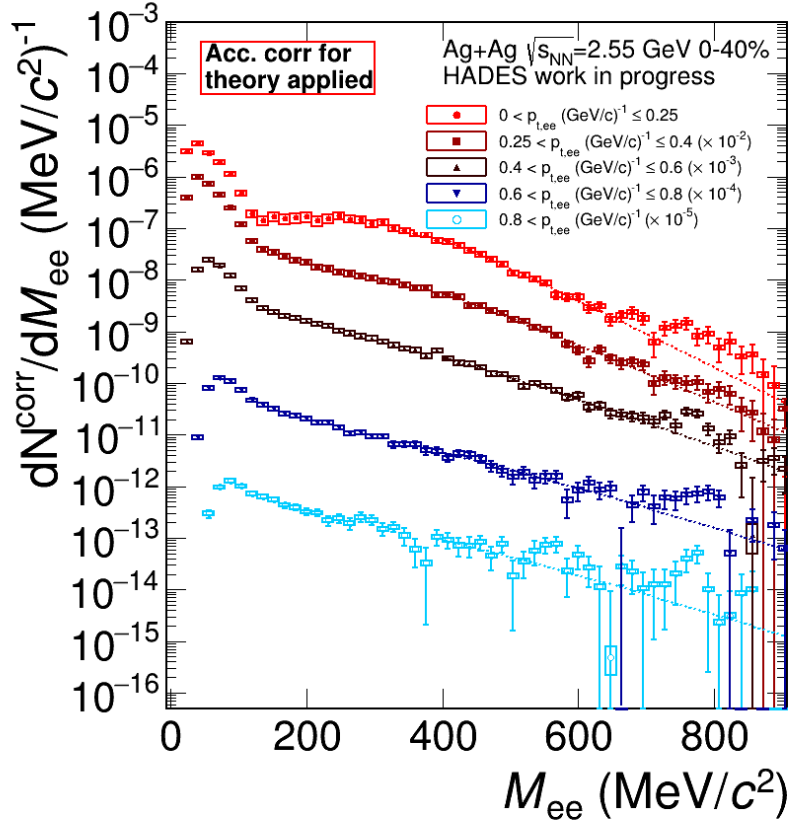


Figure D.15: Dielectron signal in Ag+Ag collisions at $\sqrt{s_{NN}} = 2.55 \text{ GeV}$ in five bins of transverse pair momentum. The data is corrected for efficiency and acceptance losses within the geometric acceptance of HADES

DERIVATION OF THE ONE-LOOP SELF ENERGY

The self energy $\Pi(p^2)$ in one-loop with loop-particles of masses m, M , loop-momentum p and coupling constant $g/\sqrt{2}$ [200] is defined as integral over both particles propagators to

$$\Pi(p^2, M, m) = \frac{g^2}{2} \int dV \frac{1}{M^2 + (p - q)^2} \frac{1}{m^2 + q^2} d^4q. \quad (\text{E.1})$$

We derive the integral analytically in spherical coordinates with angles $\Theta_1, \Theta_2, \Theta_3$. Therefore the volume element writes as

$$dV = \frac{q^3}{(2\pi)^4} \sin \Theta_2 \sin^2 \Theta_3. \quad (\text{E.2})$$

Performing the substitution $\cos \Theta_3 = x$, the self energy simplifies to

$$\begin{aligned} \Pi(p^2, M, m, \Lambda) &= \frac{g^2}{2} \int_0^\Lambda \int_0^{2\pi} \int_0^\pi \int_{-1}^1 \frac{q^3}{(2\pi)^4} \sin(\Theta_2) \\ &\quad \sqrt{1-x^2} \cdot \frac{1}{M^2 + p^2 + q^2 - 2p \cdot q \cdot x} \cdot \frac{1}{m^2 + q^2} d\Theta_1 d\Theta_2 dx dq \quad (\text{E.3}) \end{aligned}$$

introducing the cutoff Λ . Solving the integral in Θ_1, Θ_2, x , we derive

$$\begin{aligned} \Pi(p^2, M, m, \Lambda) &= \frac{g^2}{2} \int_0^\Lambda \frac{q (M^2 + p^2 + q^2)}{16p^2 \pi^2 (m^2 + q^2)} \\ &\quad \cdot \left(-1 + \sqrt{1 - \frac{4p^2 q^2}{(M^2 + p^2 + q^2)^2}} \right) dq. \quad (\text{E.4}) \end{aligned}$$

The integral is of lengthy form, but can be derived easily using e.g. the software tool Mathematica. We are interested in the renormalized self-energy $\Pi_R(p^2) = \Pi(p^2) - \Pi(0)$. Calculation of $\Pi(0)$ is performed in an Taylor expansion in λ evaluated in the limit $p \rightarrow 0$,

$$\Pi(0, M, m, \Lambda) = \lim_{p \rightarrow 0} T_{\Pi(\Lambda; \infty)}. \quad (\text{E.5})$$

Divergences of $\Pi_R(p^2)$ in Λ do not depend on the loop momentum p and can therefore be absorbed. As result for the renormalized one-loop self energy we obtain

$$\begin{aligned}
\Pi_R(p^2, M, m) = & \frac{g^2}{64p^2\pi^2} \left((M^2 - m^2) \log\left(\frac{M^2}{m^2}\right) \right. \\
& - 2\sqrt{M^4 - 2M^2(m^2 - p^2) + (m^2 + p^2)^2} \\
& \cdot \left(\operatorname{arctanh}\left(\frac{M^2 - m^2 + p^2}{\sqrt{M^4 - 2M^2(m^2 - p^2) + (m^2 + p^2)^2}}\right) \right. \\
& \left. \left. + \operatorname{arctanh}\left(\frac{m^2 - M^2 + p^2}{\sqrt{M^4 - 2M^2(m^2 - p^2) + (m^2 + p^2)^2}}\right) \right) \right) \\
& + \frac{g^2}{32\pi^2} \left(1 + \frac{(M^2 + m^2) \log\left[\frac{M}{m}\right]}{(M^2 - m^2)} \right). \quad (\text{E.6})
\end{aligned}$$

In the case of both loop particles having the same mass m , equation E.6 simplifies to

$$\Pi_R(p^2, M = m) = -g^2 \sqrt{\frac{4m^2 + p^2}{p^2}} \frac{\operatorname{arctanh}\left[\frac{p}{\sqrt{4m^2 + p^2}}\right]}{16\pi^2} + g^2 \frac{1}{16\pi^2}. \quad (\text{E.7})$$

BIBLIOGRAPHY

- [1] J. I. Breidenbach M.and Friedman, H. W. Kendall, E. D. Bloom, D. H. Coward, H. C. DeStaebler, J. Drees, L. W. Mo, and R. E. Taylor. "Observed behavior of highly inelastic electron-proton scattering." In: *Phys. Rev. Lett.* 23 (1969), pp. 935–939. DOI: [10.1103/PhysRevLett.23.935](https://doi.org/10.1103/PhysRevLett.23.935).
- [2] H. W. Kendall. "Deep inelastic scattering: Experiments on the proton and the observation of scaling." In: *Rev. Mod. Phys.* 63 (3 1991), pp. 597–614. DOI: [10.1103/RevModPhys.63.597](https://doi.org/10.1103/RevModPhys.63.597). URL: <https://link.aps.org/doi/10.1103/RevModPhys.63.597>.
- [3] M. Gell-Mann. "A Schematic Model of Baryons and Mesons." In: *Phys. Lett.* 8 (1964), pp. 214–215. DOI: [10.1016/S0031-9163\(64\)92001-3](https://doi.org/10.1016/S0031-9163(64)92001-3).
- [4] G. Zweig. "An SU(3) model for strong interaction symmetry and its breaking. Version 2." In: *DEVELOPMENTS IN THE QUARK THEORY OF HADRONS. VOL. 1. 1964 - 1978*. Ed. by D. B. Lichtenberg and S. P. Rosen. 1964.
- [5] A. B. Arbuzov. "Quantum Field Theory and the Electroweak Standard Model." In: (2017). Ed. by Martijn Mulders and Giulia Zanderighi. DOI: [10.23730/CYRSP-2017-004.1](https://doi.org/10.23730/CYRSP-2017-004.1). arXiv: [1801.05670 \[hep-ph\]](https://arxiv.org/abs/1801.05670).
- [6] P.A. Zyla et al. "Review of Particle Physics." In: *PTEP* 2020.8 (2020), p. 083C01. DOI: [10.1093/ptep/ptaa104](https://doi.org/10.1093/ptep/ptaa104).
- [7] P. A. M. Dirac. "Quantum theory of emission and absorption of radiation." In: *Proc. Roy. Soc. Lond. A* 114 (1927), p. 243. DOI: [10.1098/rspa.1927.0039](https://doi.org/10.1098/rspa.1927.0039).
- [8] E. Fermi. *Nuclear Physics - A Course Given by Enrico Fermi at the University of Chicago*. Midway Reprint. ISBN: 9780226243658.
- [9] O. W. Greenberg. "Color: From baryon spectroscopy to QCD." In: *Baryons '92*. 1992. arXiv: [hep-ph/9301207](https://arxiv.org/abs/hep-ph/9301207).
- [10] R. P. Feynman. "Space-Time Approach to Quantum Electrodynamics." In: *Phys. Rev.* 76 (6 1949), pp. 769–789. DOI: [10.1103/PhysRev.76.769](https://doi.org/10.1103/PhysRev.76.769). URL: <https://link.aps.org/doi/10.1103/PhysRev.76.769>.
- [11] S. Chatrchyan et al. "Observation of a new boson at a mass of 125 GeV with the CMS experiment at the LHC." In: *Physics Letters B* 716.1 (2012), pp. 30–61. ISSN: 0370-2693. DOI: <https://doi.org/10.1016/j.physletb.2012.08.021>. URL: <https://www.sciencedirect.com/science/article/pii/S0370269312008581>.

- [12] G. Aad et al. "Observation of a new particle in the search for the Standard Model Higgs boson with the ATLAS detector at the LHC." In: *Physics Letters B* 716.1 (2012), pp. 1–29. ISSN: 0370-2693. DOI: <https://doi.org/10.1016/j.physletb.2012.08.020>. URL: <https://www.sciencedirect.com/science/article/pii/S037026931200857X>.
- [13] F. Englert and R. Brout. "Broken Symmetry and the Mass of Gauge Vector Mesons." In: *Phys. Rev. Lett.* 13 (9 1964), pp. 321–323. DOI: [10.1103/PhysRevLett.13.321](https://doi.org/10.1103/PhysRevLett.13.321). URL: <https://link.aps.org/doi/10.1103/PhysRevLett.13.321>.
- [14] Peter W. Higgs. "Broken Symmetries and the Masses of Gauge Bosons." In: *Phys. Rev. Lett.* 13 (16 1964), pp. 508–509. DOI: [10.1103/PhysRevLett.13.508](https://doi.org/10.1103/PhysRevLett.13.508). URL: <https://link.aps.org/doi/10.1103/PhysRevLett.13.508>.
- [15] G. S. Guralnik, C. R. Hagen, and T. W. B. Kibble. "Global Conservation Laws and Massless Particles." In: *Phys. Rev. Lett.* 13 (20 1964), pp. 585–587. DOI: [10.1103/PhysRevLett.13.585](https://doi.org/10.1103/PhysRevLett.13.585). URL: <https://link.aps.org/doi/10.1103/PhysRevLett.13.585>.
- [16] P.W. Higgs. "Broken symmetries, massless particles and gauge fields." In: *Physics Letters* 12.2 (1964), pp. 132–133. ISSN: 0031-9163. DOI: [https://doi.org/10.1016/0031-9163\(64\)91136-9](https://doi.org/10.1016/0031-9163(64)91136-9). URL: <https://www.sciencedirect.com/science/article/pii/0031916364911369>.
- [17] A. Arbey and F. Mahmoudi. "Dark matter and the early Universe: a review." In: *Prog. Part. Nucl. Phys.* 119 (2021), p. 103865. DOI: [10.1016/j.pnpnp.2021.103865](https://doi.org/10.1016/j.pnpnp.2021.103865). arXiv: [2104.11488](https://arxiv.org/abs/2104.11488) [hep-ph].
- [18] R. S. Ellis. "Gravitational lensing: a unique probe of dark matter and dark energy." In: *Royal Society* 368.1914 (2010), pp. 967–987. ISSN: 1471-2962. DOI: <https://doi.org/10.1098/rsta.2009.0209>. URL: <https://royalsocietypublishing.org/doi/full/10.1098/rsta.2009.0209>.
- [19] S. N. Shore and V. Trimble. "Dark Matter in the Universe." In: *Encyclopedia of Physical Science and Technology (Third Edition)*. Ed. by Robert A. Meyers. Third Edition. New York: Academic Press, 2003, pp. 191–211. ISBN: 978-0-12-227410-7. DOI: <https://doi.org/10.1016/B012-227410-5/00162-9>. URL: <https://www.sciencedirect.com/science/article/pii/B0122274105001629>.
- [20] B. Robson. "The Matter-Antimatter Asymmetry Problem." In: *Journal of High Energy Physics, Gravitation and Cosmology* 04 (2018), pp. 166–178. DOI: [10.4236/jhepgc.2018.41015](https://doi.org/10.4236/jhepgc.2018.41015).
- [21] F. W. Stecker. "The Matter - antimatter asymmetry of the universe." In: *14th Rencontres de Blois on Matter - Anti-matter Asymmetry*. 2002. arXiv: [hep-ph/0207323](https://arxiv.org/abs/hep-ph/0207323).

- [22] T. Mannel. “Theory and Phenomenology of CP Violation.” In: *Nuclear Physics B - Proceedings Supplements* 167 (2007). Proceedings of the 7th International Conference on Hyperons, Charm and Beauty Hadrons, pp. 170–174. ISSN: 0920-5632. DOI: <https://doi.org/10.1016/j.nuclphysbps.2006.12.083>. URL: <https://www.sciencedirect.com/science/article/pii/S0920563206010711>.
- [23] T. Hambye. “CP violation and the matter–antimatter asymmetry of the Universe.” In: *Comptes Rendus Physique* 13.2 (2012). Flavour physics and CP violation / Physique de la saveur et violation de CP, pp. 193–203. ISSN: 1631-0705. DOI: <https://doi.org/10.1016/j.crhy.2011.09.007>. URL: <https://www.sciencedirect.com/science/article/pii/S1631070511001873>.
- [24] J. Goldstone. *Field theories with “superconductor” solutions*. Vol. 19. 1961, pp. 154–164. DOI: <https://doi.org/10.1007/BF02812722>.
- [25] J. Goldstone, A. Salam, and S. Weinberg. “Broken Symmetries.” In: *Phys. Rev.* 127 (1962), pp. 965–970. DOI: [10.1103/PhysRev.127.965](https://doi.org/10.1103/PhysRev.127.965).
- [26] A. Salam and J. C. Ward. “Electromagnetic and weak interactions.” In: *Phys. Lett.* 13 (1964), pp. 168–171. DOI: [10.1016/0031-9163\(64\)90711-5](https://doi.org/10.1016/0031-9163(64)90711-5).
- [27] S. Weinberg. “A Model of Leptons.” In: *Phys. Rev. Lett.* 19 (21 1967), pp. 1264–1266. DOI: [10.1103/PhysRevLett.19.1264](https://doi.org/10.1103/PhysRevLett.19.1264). URL: <https://link.aps.org/doi/10.1103/PhysRevLett.19.1264>.
- [28] R. Keith Ellis, W. James Stirling, and B. R. Webber. *QCD and collider physics*. Vol. 8. Cambridge University Press, 2011. ISBN: 978-0-511-82328-2, 978-0-521-54589-1.
- [29] P. Skands. “Introduction to QCD.” In: *Theoretical Advanced Study Institute in Elementary Particle Physics: Searching for New Physics at Small and Large Scales*. 2012. DOI: [10.1142/9789814525220_0008](https://doi.org/10.1142/9789814525220_0008). arXiv: [1207.2389](https://arxiv.org/abs/1207.2389) [hep-ph].
- [30] E. Schrödinger. “Quantisierung als Eigenwertproblem.” In: *Annalen der Physik* 385.13 (1926), pp. 437–490. DOI: [10.1002/andp.19263851302](https://doi.org/10.1002/andp.19263851302).
- [31] A. Deur, S. J. Brodsky, and G. F. de Teramond. “The QCD Running Coupling.” In: *Nucl. Phys.* 90 (2016), p. 1. DOI: [10.1016/j.ppnp.2016.04.003](https://doi.org/10.1016/j.ppnp.2016.04.003). arXiv: [1604.08082](https://arxiv.org/abs/1604.08082) [hep-ph].
- [32] A. Deur, V. Burkert, Jian-Ping Chen, and W. Korsch. “Experimental determination of the effective strong coupling constant.” In: *Phys. Lett. B* 650 (2007), pp. 244–248. DOI: [10.1016/j.physletb.2007.05.015](https://doi.org/10.1016/j.physletb.2007.05.015). arXiv: [hep-ph/0509113](https://arxiv.org/abs/hep-ph/0509113).
- [33] H. E. Haber and L. Stephenson H. “Supersymmetric Theory and Models.” In: *Theoretical Advanced Study Institute in Elementary Particle Physics: Anticipating the Next Discoveries in Particle Physics*. WSP, 2017. DOI: [10.1142/9789813233348_0006](https://doi.org/10.1142/9789813233348_0006). arXiv: [1712.05926](https://arxiv.org/abs/1712.05926) [hep-ph].

- [34] M. K. Parida and R. Samantaray. “Unification Predictions With or Without Supersymmetry.” In: *Eur. Phys. J. ST* 229.21 (2020), pp. 3243–3262. DOI: [10.1140/epjst/e2020-000024-x](https://doi.org/10.1140/epjst/e2020-000024-x). arXiv: [2002.06869](https://arxiv.org/abs/2002.06869) [hep-ph].
- [35] A. Eichhorn, A. Held, and C. Wetterich. “Predictive power of grand unification from quantum gravity.” In: *JHEP* 08 (2020), p. 111. DOI: [10.1007/JHEP08\(2020\)111](https://doi.org/10.1007/JHEP08(2020)111). arXiv: [1909.07318](https://arxiv.org/abs/1909.07318) [hep-th].
- [36] The ATLAS collaboration. *Searching for natural supersymmetry using novel techniques*. CERN LHC seminar Physics Briefing, 18 Feb 2020.
- [37] A. Canepa. “Searches for supersymmetry at the Large Hadron Collider.” In: *Reviews in Physics* 4 (2019), p. 100033. ISSN: 2405-4283. DOI: <https://doi.org/10.1016/j.revip.2019.100033>. URL: <https://www.sciencedirect.com/science/article/pii/S2405428318300091>.
- [38] W. Heisenberg. “Über den Bau der Atomkerne. I.” In: *Zeitschrift für Physik* 77.1-2 (1932), pp. 1–11. DOI: [10.1007/BF01342433](https://doi.org/10.1007/BF01342433).
- [39] E. Noether. “Invariante Variationsprobleme.” In: *Nachrichten der Königl. Gesellschaft der Wissenschaften zu Göttingen, Math.-phys. Klasse* (1918), pp. 235–257.
- [40] E. Noether. “Invariant variation problems.” In: *Transport Theory and Statistical Physics* 1.3 (1971), pp. 186–207. eprint: <https://doi.org/10.1080/00411457108231446>. URL: <https://doi.org/10.1080/00411457108231446>.
- [41] K. Fukushima and T. Hatsuda. “The phase diagram of dense QCD.” In: *Rept. Prog. Phys.* 74 (2011), p. 014001. DOI: [10.1088/0034-4885/74/1/014001](https://doi.org/10.1088/0034-4885/74/1/014001). arXiv: [1005.4814](https://arxiv.org/abs/1005.4814) [hep-ph].
- [42] N. Cabibbo and G. Parisi. “Exponential Hadronic Spectrum and Quark Liberation.” In: *Phys. Lett. B* 59 (1975), pp. 67–69. DOI: [10.1016/0370-2693\(75\)90158-6](https://doi.org/10.1016/0370-2693(75)90158-6).
- [43] O. Philipsen. “Status of Lattice Studies of the QCD Phase Diagram.” In: *Prog. Theor. Phys. Suppl.* 174 (2008). Ed. by T. Kunihiro, K. Fukushima, T. Hirano, K. Iida, M. Kitazawa, M. Tachibana, H. Iida, and T. T. Takahashi, pp. 206–213. DOI: [10.1143/PTPS.174.206](https://doi.org/10.1143/PTPS.174.206). arXiv: [0808.0672](https://arxiv.org/abs/0808.0672) [hep-ph].
- [44] J. Stachel, A. Andronic, P. Braun-Munzinger, and K. Redlich. “Confronting LHC data with the statistical hadronization model.” In: *J. Phys. Conf. Ser.* 509 (2014). Ed. by D. Evans, S. Hands, R. Lietava, R. Romita, and O. Villalobos Baillie, p. 012019. DOI: [10.1088/1742-6596/509/1/012019](https://doi.org/10.1088/1742-6596/509/1/012019). arXiv: [1311.4662](https://arxiv.org/abs/1311.4662) [nucl-th].
- [45] N. Armesto, N. Borghini, S. Jeon, and U. A. Wiedemann, eds. *Proceedings, Workshop on Heavy Ion Collisions at the LHC: Last Call for Predictions: Geneva, Switzerland, May 14 - June 8, 2007*. Vol. 35. 2008, p. 054001. DOI: [10.1088/0954-3899/35/5/054001](https://doi.org/10.1088/0954-3899/35/5/054001). arXiv: [0711.0974](https://arxiv.org/abs/0711.0974) [hep-ph].

- [46] M. Bluhm, P. Alba, W. Alberico, R. Bellwied, V. Sarti, M. Nahrgang, and C. Ratti. “Determination of freeze-out conditions from fluctuation observables measured at RHIC.” In: *Nuclear Physics A* 931 (2014). DOI: [10.1016/j.nuclphysa.2014.08.016](https://doi.org/10.1016/j.nuclphysa.2014.08.016).
- [47] F. Becattini, M. Bleicher, T. Kollegger, T. Schuster, J. Steinheimer, and R. Stock. “Hadron Formation in Relativistic Nuclear Collisions and the QCD Phase Diagram.” In: *Phys. Rev. Lett.* 111 (2013), p. 082302. DOI: [10.1103/PhysRevLett.111.082302](https://doi.org/10.1103/PhysRevLett.111.082302). arXiv: [1212.2431](https://arxiv.org/abs/1212.2431) [nucl-th].
- [48] A. Ayala, A. Bashir, J. J. Cobos-Martinez, S. Hernandez-Ortiz, and A. Raya. “The effective QCD phase diagram and the critical end point.” In: *Nucl. Phys. B* 897 (2015), pp. 77–86. DOI: [10.1016/j.nuclphysb.2015.05.014](https://doi.org/10.1016/j.nuclphysb.2015.05.014). arXiv: [1411.4953](https://arxiv.org/abs/1411.4953) [hep-ph].
- [49] C. Schmidt. “Lattice QCD at finite density.” In: *PoS LAT2006* (2006). Ed. by T. Blum, M. Creutz, C. DeTar, F. Karsch, A. Kronfeld, C. Morningstar, D. Richards, J. Shigemitsu, and D. Toussaint, p. 021. DOI: [10.22323/1.032.0021](https://doi.org/10.22323/1.032.0021). arXiv: [hep-lat/0610116](https://arxiv.org/abs/hep-lat/0610116).
- [50] A. Ayala, A. Bashir, C. A. Dominguez, E. Gutierrez, M. Loewe, and A. Raya. “QCD phase diagram from finite energy sum rules.” In: *Phys. Rev. D* 84 (2011), p. 056004. DOI: [10.1103/PhysRevD.84.056004](https://doi.org/10.1103/PhysRevD.84.056004). arXiv: [1106.5155](https://arxiv.org/abs/1106.5155) [hep-ph].
- [51] B.-J. Schaefer and M. Wagner. “On the QCD phase structure from effective models.” In: *Prog. Part. Nucl. Phys.* 62 (2009). Ed. by A. Faessler, pp. 381–385. DOI: [10.1016/j.pnpnp.2008.12.009](https://doi.org/10.1016/j.pnpnp.2008.12.009). arXiv: [0812.2855](https://arxiv.org/abs/0812.2855) [hep-ph].
- [52] K. Rajagopal and F. Wilczek. “The Condensed matter physics of QCD.” In: *At the frontier of particle physics. Handbook of QCD. Vol. 1-3*. Ed. by M. Shifman and Boris Ioffe. 2000. DOI: [10.1142/9789812810458_0043](https://doi.org/10.1142/9789812810458_0043). arXiv: [hep-ph/0011333](https://arxiv.org/abs/hep-ph/0011333).
- [53] A. Ayala, A. Bashir, J. J. Cobos-Martinez, Saul Hernandez-Ortiz, and Alfredo Raya. “The effective QCD phase diagram and the critical end point.” In: *Nucl. Phys. B* 897 (2015), pp. 77–86. DOI: [10.1016/j.nuclphysb.2015.05.014](https://doi.org/10.1016/j.nuclphysb.2015.05.014). arXiv: [1411.4953](https://arxiv.org/abs/1411.4953) [hep-ph].
- [54] K. Kashiwa, H. Kouno, M. Matsuzaki, and M. Yahiro. “Critical endpoint in the Polyakov-loop extended NJL model.” In: *Phys. Lett. B* 662 (2008), pp. 26–32. DOI: [10.1016/j.physletb.2008.01.075](https://doi.org/10.1016/j.physletb.2008.01.075). arXiv: [0710.2180](https://arxiv.org/abs/0710.2180) [hep-ph].
- [55] P. Bicudo. “QCD confinement and chiral crossovers, two critical points?” In: *PoS FACESQCD* (2010), p. 015. DOI: [10.22323/1.117.0015](https://doi.org/10.22323/1.117.0015). arXiv: [1102.5531](https://arxiv.org/abs/1102.5531) [hep-lat].
- [56] M. G. Orsaria, G. Malfatti, M. Mariani, I. F. Ranea-Sandoval, F. García, W. M. Spinella, G. A. Contrera, G. Lugones, and F. Weber. “Phase transitions in neutron stars and their links to gravitational waves.” In: *J. Phys. G* 46.7 (2019), p. 073002. DOI: [10.1088/1361-6471/ab1d81](https://doi.org/10.1088/1361-6471/ab1d81). arXiv: [1907.04654](https://arxiv.org/abs/1907.04654) [astro-ph.HE].

- [57] M. Mannarelli. “Color superconductivity and dense quark matter.” In: *PoS CONFINEMENT8* (2008), p. 010. DOI: [10.22323/1.077.0010](https://doi.org/10.22323/1.077.0010). arXiv: [0812.2831](https://arxiv.org/abs/0812.2831) [hep-ph].
- [58] B. Betz. “Jet Propagation and Mach-Cone Formation in (3+1)-dimensional Ideal Hydrodynamics.” Master thesis. 2009. arXiv: [0910.4114](https://arxiv.org/abs/0910.4114) [nucl-th].
- [59] J. Adamczewski-Musch et al. “Probing dense baryon-rich matter with virtual photons.” In: *Nature Physics* 15 (2019), pp. 1040–1045. DOI: [10.1038/s41567-019-0583-8](https://doi.org/10.1038/s41567-019-0583-8). URL: <https://doi.org/10.1038/s41567-019-0583-8>.
- [60] T. Galatyuk. “HADES overview.” In: *Nuclear Physics A* 931 (2014). QUARK MATTER 2014, pp. 41–51. ISSN: 0375-9474. DOI: <https://doi.org/10.1016/j.nuclphysa.2014.10.044>. URL: <https://www.sciencedirect.com/science/article/pii/S0375947414005399>.
- [61] P. Senger. “Probing dense QCD matter in the laboratory—The CBM experiment at FAIR.” In: *Phys. Scripta* 95.7 (2020). Ed. by L. Bravina, S. Kabana, V. Volkova, and V. Ivanovitch Zakharov, p. 074003. DOI: [10.1088/1402-4896/ab8c14](https://doi.org/10.1088/1402-4896/ab8c14). arXiv: [2005.03321](https://arxiv.org/abs/2005.03321) [nucl-ex].
- [62] T. Ablyazimov et al. “Challenges in QCD matter physics –The scientific programme of the Compressed Baryonic Matter experiment at FAIR.” In: *Eur. Phys. J. A* 53.3 (2017), p. 60. DOI: [10.1140/epja/i2017-12248-y](https://doi.org/10.1140/epja/i2017-12248-y). arXiv: [1607.01487](https://arxiv.org/abs/1607.01487) [nucl-ex].
- [63] ALICE homepage. *The heavy ion experiment at the Large Hadron Collider*. URL: <https://alice.cern/>.
- [64] PHENIX homepage. *PHENIX, the Pioneering High Energy Nuclear Interaction eXperiment*. URL: <https://www.phenix.bnl.gov>.
- [65] STAR homepage. *The STAR experiment at Relativistic Heavy Ion Collider, Brookhaven National Laboratory*. URL: <https://www.star.bnl.gov/>.
- [66] P. Braun-Munzinger and B. Dönigus. “Loosely-bound objects produced in nuclear collisions at the LHC.” In: *Nuclear Physics A* 987 (2019). DOI: [10.1016/j.nuclphysa.2019.02.006](https://doi.org/10.1016/j.nuclphysa.2019.02.006).
- [67] D. Kharzeev, C. Lourenco, M. Nardi, and H. Satz. “A Quantitative analysis of charmonium suppression in nuclear collisions.” In: *Z. Phys. C* 74 (1997), pp. 307–318. DOI: [10.1007/s002880050392](https://doi.org/10.1007/s002880050392). arXiv: [hep-ph/9612217](https://arxiv.org/abs/hep-ph/9612217).
- [68] M. Asakawa and T. Hatsuda. “J / psi and eta(c) in the deconfined plasma from lattice QCD.” In: *Phys. Rev. Lett.* 92 (2004), p. 012001. DOI: [10.1103/PhysRevLett.92.012001](https://doi.org/10.1103/PhysRevLett.92.012001). arXiv: [hep-lat/0308034](https://arxiv.org/abs/hep-lat/0308034).
- [69] R. Stock. “Relativistic Nucleus-Nucleus Collisions and the QCD Matter Phase Diagram.” In: (2008). DOI: [10.1007/978-3-540-74203-6_7](https://doi.org/10.1007/978-3-540-74203-6_7). arXiv: [0807.1610](https://arxiv.org/abs/0807.1610) [nucl-ex].

- [70] E. Scomparin et al. "Dimuon and charm production in In+In collisions at the CERN SPS." In: *Nuclear Physics A* 774 (2006), pp. 67–76. DOI: [10.1016/j.nuclphysa.2006.06.030](https://doi.org/10.1016/j.nuclphysa.2006.06.030).
- [71] J. Adams and C. et al. Adler. "Evidence from $d + Au$ Measurements for Final-State Suppression of High- p_T Hadrons in Au + Au Collisions at RHIC." In: *Phys. Rev. Lett.* 91 (7 2003), p. 072304. DOI: [10.1103/PhysRevLett.91.072304](https://doi.org/10.1103/PhysRevLett.91.072304). URL: <https://link.aps.org/doi/10.1103/PhysRevLett.91.072304>.
- [72] C. et al. Alt. "Directed and elliptic flow of charged pions and protons in Pb + Pb collisions at 40A and 158AGeV." In: *Phys. Rev. C* 68 (3 2003), p. 034903. DOI: [10.1103/PhysRevC.68.034903](https://doi.org/10.1103/PhysRevC.68.034903). URL: <https://link.aps.org/doi/10.1103/PhysRevC.68.034903>.
- [73] A. Rustamov. "The Horn, Kink and Step, Dale: from few GeV to few TeV." In: *Central Eur. J. Phys.* 10 (2012), pp. 1267–1270. DOI: [10.2478/s11534-012-0148-2](https://doi.org/10.2478/s11534-012-0148-2). arXiv: [1201.4520](https://arxiv.org/abs/1201.4520) [nucl-ex].
- [74] M. Gazdzicki and D. Rohrlich. "Strangeness in nuclear collisions." In: *Z. Phys. C* 71 (1996), pp. 55–64. DOI: [10.1007/s002880050147](https://doi.org/10.1007/s002880050147). arXiv: [hep-ex/9607004](https://arxiv.org/abs/hep-ex/9607004).
- [75] N. Abgrall. *Report from the NA61/SHINE experiment at the CERN SPS*. Tech. rep. Geneva: CERN, 2014. URL: <http://cds.cern.ch/record/1955138>.
- [76] B. B. Abelev et al. "Multi-strange baryon production at mid-rapidity in Pb-Pb collisions at $\sqrt{s_{NN}} = 2.76$ TeV." In: *Phys. Lett. B* 728 (2014). [Erratum: *Phys.Lett.B* 734, 409–410 (2014)], pp. 216–227. DOI: [10.1016/j.physletb.2014.05.052](https://doi.org/10.1016/j.physletb.2014.05.052). arXiv: [1307.5543](https://arxiv.org/abs/1307.5543) [nucl-ex].
- [77] M. Gazdzicki and M. I. Gorenstein. "On the early stage of nucleus-nucleus collisions." In: *Acta Phys. Polon. B* 30 (1999), p. 2705. arXiv: [hep-ph/9803462](https://arxiv.org/abs/hep-ph/9803462).
- [78] The ALICE collaboration. "Multi-strange baryon production at mid-rapidity in Pb–Pb collisions at $s_{NN}=2.76$ TeV." In: *Physics Letters B* 728 (2014), pp. 216–227. ISSN: 0370-2693. DOI: <https://doi.org/10.1016/j.physletb.2013.11.048>. URL: <https://www.sciencedirect.com/science/article/pii/S0370269313009544>.
- [79] The ALICE collaboration. "Centrality dependence of π , K , and p production in Pb-Pb collisions at $\sqrt{s_{NN}} = 2.76$ TeV." In: *Phys. Rev. C* 88 (4 2013), p. 044910. DOI: [10.1103/PhysRevC.88.044910](https://doi.org/10.1103/PhysRevC.88.044910). URL: <https://link.aps.org/doi/10.1103/PhysRevC.88.044910>.
- [80] K. Aamodt et al. "Strange particle production in proton-proton collisions at $\sqrt{s} = 0.9$ TeV with ALICE at the LHC." In: *Eur. Phys. J. C* 71 (2011), p. 1594. DOI: [10.1140/epjc/s10052-011-1594-5](https://doi.org/10.1140/epjc/s10052-011-1594-5). arXiv: [1012.3257](https://arxiv.org/abs/1012.3257) [hep-ex].

- [81] The STAR collaboration. "Systematic measurements of identified particle spectra in pp , $d + Au$, and $Au + Au$ collisions at the STAR detector." In: *Phys. Rev. C* 79 (3 2009), p. 034909. DOI: [10.1103/PhysRevC.79.034909](https://doi.org/10.1103/PhysRevC.79.034909). URL: <https://link.aps.org/doi/10.1103/PhysRevC.79.034909>.
- [82] The STAR collaboration. "Strange particle production in $p + p$ collisions at $\sqrt{s} = 200$ GeV." In: *Phys. Rev. C* 75 (6 2007), p. 064901. DOI: [10.1103/PhysRevC.75.064901](https://doi.org/10.1103/PhysRevC.75.064901). URL: <https://link.aps.org/doi/10.1103/PhysRevC.75.064901>.
- [83] G. et al. Agakichiev. "Enhanced Production of Low-Mass Electron Pairs in 200 GeV/Nucleon S-Au Collisions at the CERN Super Proton Synchrotron." In: *Phys. Rev. Lett.* 75 (7 1995), pp. 1272–1275. DOI: [10.1103/PhysRevLett.75.1272](https://doi.org/10.1103/PhysRevLett.75.1272). URL: <https://link.aps.org/doi/10.1103/PhysRevLett.75.1272>.
- [84] G. Agakichiev et al. "e+ e- pair production in Pb - Au collisions at 158-GeV per nucleon." In: *Eur. Phys. J. C* 41 (2005), pp. 475–513. DOI: [10.1140/epjc/s2005-02272-3](https://doi.org/10.1140/epjc/s2005-02272-3). arXiv: [nucl-ex/0506002](https://arxiv.org/abs/nucl-ex/0506002).
- [85] G. et al. Agakichiev. "Systematic study of low-mass electron pair production in p-Be and p-Au collisions at 450 GeV/c." In: *The European Physical Journal C - Particles and Fields* 4 (2 1998), pp. 231–247. DOI: [10.1007/PL00021659](https://doi.org/10.1007/PL00021659). URL: <https://doi.org/10.1007/PL00021659>.
- [86] A. Marin et al. "Dilepton measurements with CERES." In: *PoS CPOD07* (2007), p. 034. DOI: [10.22323/1.047.0034](https://doi.org/10.22323/1.047.0034). arXiv: [0802.2679](https://arxiv.org/abs/0802.2679) [[nucl-ex](https://arxiv.org/abs/nucl-ex)].
- [87] *Technical note on the CERES/NA45 upgrade*. Tech. rep. Geneva: CERN, 1996. URL: <http://cds.cern.ch/record/615465>.
- [88] D. Adamova et al. "Modification of the rho-meson detected by low-mass electron-positron pairs in central Pb-Au collisions at 158 AGeV/c." In: *Phys. Lett. B* 666 (2008), pp. 425–429. DOI: [10.1016/j.physletb.2008.07.104](https://doi.org/10.1016/j.physletb.2008.07.104). arXiv: [nucl-ex/0611022](https://arxiv.org/abs/nucl-ex/0611022).
- [89] G.E. Brown and M. Rho. "On the manifestation of chiral symmetry in nuclei and dense nuclear matter." In: *Physics Reports* 363.2 (2002), pp. 85–171. ISSN: 0370-1573. DOI: [https://doi.org/10.1016/S0370-1573\(01\)00084-9](https://doi.org/10.1016/S0370-1573(01)00084-9). URL: <https://www.sciencedirect.com/science/article/pii/S0370157301000849>.
- [90] R. Rapp and J. Wambach. "Chiral symmetry restoration and dileptons in relativistic heavy ion collisions." In: *Adv. Nucl. Phys.* 25 (2000), p. 1. DOI: [10.1007/0-306-47101-9_1](https://doi.org/10.1007/0-306-47101-9_1). arXiv: [hep-ph/9909229](https://arxiv.org/abs/hep-ph/9909229).
- [91] A.L.S. Angelis et al. "Excess of continuum dimuon production at masses between threshold and the J/Ψ in S-W interactions at 200 GeV/c/nucleon." In: *The European Physical Journal C - Particles and Fields* 13 (3 2000), pp. 433–452. DOI: [10.1007/s100520000314](https://doi.org/10.1007/s100520000314). URL: <https://doi.org/10.1007/s100520000314>.

- [92] R Arnaldi et al. "Evidence for the production of thermal-like muon pairs with masses above $1\text{-GeV}/c^2$ in 158-A-GeV Indium-Indium Collisions." In: *Eur. Phys. J. C* 59 (2009), pp. 607–623. DOI: [10.1140/epjc/s10052-008-0857-2](https://doi.org/10.1140/epjc/s10052-008-0857-2). arXiv: [0810.3204](https://arxiv.org/abs/0810.3204) [nucl-ex].
- [93] R. Rapp. "Thermal lepton production in heavy ion collisions." In: *18th Winter Workshop on Nuclear Dynamics*. 2002. arXiv: [nuc1-th/0204003](https://arxiv.org/abs/nuc1-th/0204003).
- [94] H. van Hees and Ralf R. "Comprehensive interpretation of thermal dileptons at the SPS." In: *Phys. Rev. Lett.* 97 (2006), p. 102301. DOI: [10.1103/PhysRevLett.97.102301](https://doi.org/10.1103/PhysRevLett.97.102301). arXiv: [hep-ph/0603084](https://arxiv.org/abs/hep-ph/0603084).
- [95] J. Ruppert, C. Gale, T. Renk, P. Lichard, and J. I. Kapusta. "Low mass dimuons produced in relativistic nuclear collisions." In: *Phys. Rev. Lett.* 100 (2008), p. 162301. DOI: [10.1103/PhysRevLett.100.162301](https://doi.org/10.1103/PhysRevLett.100.162301). arXiv: [0706.1934](https://arxiv.org/abs/0706.1934) [hep-ph].
- [96] R. Arnaldi et al. "NA60 results on thermal dimuons." In: *Eur. Phys. J. C* 61 (2009), pp. 711–720. DOI: [10.1140/epjc/s10052-009-0878-5](https://doi.org/10.1140/epjc/s10052-009-0878-5). arXiv: [0812.3053](https://arxiv.org/abs/0812.3053) [nucl-ex].
- [97] S. Afanasiev et al. "Enhancement of the dielectron continuum in $s(NN)^{1/2} = 200\text{-GeV}$ Au+Au collisions." In: (2007). arXiv: [0706.3034](https://arxiv.org/abs/0706.3034) [nucl-ex].
- [98] A. Adare et al. "Detailed measurement of the e^+e^- pair continuum in $p + p$ and Au+Au collisions at $\sqrt{s_{NN}} = 200$ GeV and implications for direct photon production." In: *Phys. Rev. C* 81 (2010), p. 034911. DOI: [10.1103/PhysRevC.81.034911](https://doi.org/10.1103/PhysRevC.81.034911). arXiv: [0912.0244](https://arxiv.org/abs/0912.0244) [nucl-ex].
- [99] A. et. al. Adare. "Dielectron production in Au + Au collisions at $\sqrt{s_{NN}} = 200$ GeV." In: *Phys. Rev. C* 93 (1 2016), p. 014904. DOI: [10.1103/PhysRevC.93.014904](https://doi.org/10.1103/PhysRevC.93.014904). URL: <https://link.aps.org/doi/10.1103/PhysRevC.93.014904>.
- [100] M. Aizawa et al. "PHENIX central arm particle ID detectors." In: *Nuclear Instruments and Methods in Physics Research Section A: Accelerators, Spectrometers, Detectors and Associated Equipment* 499.2 (2003). The Relativistic Heavy Ion Collider Project: RHIC and its Detectors, pp. 508–520. ISSN: 0168-9002. DOI: [https://doi.org/10.1016/S0168-9002\(02\)01953-8](https://doi.org/10.1016/S0168-9002(02)01953-8). URL: <https://www.sciencedirect.com/science/article/pii/S0168900202019538>.
- [101] M. Anderson et al. "The Star time projection chamber: A Unique tool for studying high multiplicity events at RHIC." In: *Nucl. Instrum. Meth. A* 499 (2003), pp. 659–678. DOI: [10.1016/S0168-9002\(02\)01964-2](https://doi.org/10.1016/S0168-9002(02)01964-2). arXiv: [nuc1-ex/0301015](https://arxiv.org/abs/nuc1-ex/0301015).
- [102] J. Adam et al. "Measurements of Dielectron Production in Au+Au Collisions at $\sqrt{s_{NN}} = 27, 39, \text{ and } 62.4$ GeV from the STAR Experiment." In: (2018). arXiv: [1810.10159](https://arxiv.org/abs/1810.10159) [nucl-ex].

- [103] H. van Hees and R. Rapp. "Dilepton radiation at the CERN super-proton synchrotron." In: *Nuclear Physics A* 806.1 (2008), pp. 339–387. ISSN: 0375-9474. DOI: <https://doi.org/10.1016/j.nuclphysa.2008.03.009>. URL: <https://www.sciencedirect.com/science/article/pii/S0375947408004144>.
- [104] S. Endres, H. van Hees, J. Weil, and M. Bleicher. "Coarse-graining approach for dilepton production at energies available at the CERN Super Proton Synchrotron." In: *Phys. Rev. C* 91 (5 2015), p. 054911. DOI: [10.1103/PhysRevC.91.054911](https://doi.org/10.1103/PhysRevC.91.054911). URL: <https://link.aps.org/doi/10.1103/PhysRevC.91.054911>.
- [105] E.L. Bratkovskaya, W. Cassing, V.P. Konchakovski, and O. Linnyk. "Parton - Hadron - String Dynamics at relativistic collider energies." In: *Nuclear Physics A* 856.1 (2011), pp. 162–182. ISSN: 0375-9474. DOI: <https://doi.org/10.1016/j.nuclphysa.2011.03.003>. URL: <https://www.sciencedirect.com/science/article/pii/S0375947411002181>.
- [106] L. et al. Adamczyk. "Dielectron Mass Spectra from Au + Au Collisions at $\sqrt{s_{NN}} = 200$ GeV." In: *Phys. Rev. Lett.* 113 (2 2014), p. 022301. DOI: [10.1103/PhysRevLett.113.022301](https://doi.org/10.1103/PhysRevLett.113.022301). URL: <https://link.aps.org/doi/10.1103/PhysRevLett.113.022301>.
- [107] J. Wambach R. Rapp and H. van Hees. *Relativistic Heavy Ion Collisions*. Vol. 23. Springer-Verlag, 2010, pp. 1–42.
- [108] L. et al. Adamczyk. "Bulk properties of the medium produced in relativistic heavy-ion collisions from the beam energy scan program." In: *Phys. Rev. C* 96 (4 2017), p. 044904. DOI: [10.1103/PhysRevC.96.044904](https://doi.org/10.1103/PhysRevC.96.044904). URL: <https://link.aps.org/doi/10.1103/PhysRevC.96.044904>.
- [109] G. et al. Agakichiev. "Dielectron Production in $^{12}\text{C} + ^{12}\text{C}$ Collisions at $2A$ GeV with the HADES Spectrometer." In: *Phys. Rev. Lett.* 98 (5 2007), p. 052302. DOI: [10.1103/PhysRevLett.98.052302](https://doi.org/10.1103/PhysRevLett.98.052302). URL: <https://link.aps.org/doi/10.1103/PhysRevLett.98.052302>.
- [110] G. et al. Agakishiev. "Dielectron production in Ar + KCl collisions at $1.76A$ GeV." In: *Phys. Rev. C* 84 (1 2011), p. 014902. DOI: [10.1103/PhysRevC.84.014902](https://doi.org/10.1103/PhysRevC.84.014902). URL: <https://link.aps.org/doi/10.1103/PhysRevC.84.014902>.
- [111] G. Agakishiev et al. "Origin of the low-mass electron pair excess in light nucleus-nucleus collisions." In: *Phys. Lett. B* 690 (2010), pp. 118–122. DOI: [10.1016/j.physletb.2010.05.010](https://doi.org/10.1016/j.physletb.2010.05.010). arXiv: [0910.5875](https://arxiv.org/abs/0910.5875) [nucl-ex].
- [112] J. Staudenmaier, J. Weil, V. Steinberg, S. Endres, and H. Petersen. "Dilepton production and resonance properties within a new hadronic transport approach in the context of the GSI-HADES experimental data." In: *Phys. Rev. C* 98 (5 2018), p. 054908. DOI: [10.1103/PhysRevC.98.054908](https://doi.org/10.1103/PhysRevC.98.054908). URL: <https://link.aps.org/doi/10.1103/PhysRevC.98.054908>.

- [113] S. Endres, H. van Hees, J. Weil, and M. Bleicher. “Dilepton production and reaction dynamics in heavy-ion collisions at SIS energies from coarse-grained transport simulations.” In: *Phys. Rev. C* 92 (1 2015), p. 014911. DOI: [10.1103/PhysRevC.92.014911](https://doi.org/10.1103/PhysRevC.92.014911). URL: <https://link.aps.org/doi/10.1103/PhysRevC.92.014911>.
- [114] T. et al. Galatyuk. “Thermal dileptons from coarse-grained transport as fireball probes at SIS energies.” In: *The European Physical Journal A* 52 (2016), p. 131. DOI: [10.1140/epja/i2016-16131-1](https://doi.org/10.1140/epja/i2016-16131-1). URL: <https://doi.org/10.1140/epja/i2016-16131-1>.
- [115] E. L. Bratkovskaya, J. Aichelin, M. Thomere, S. Vogel, and M. Bleicher. “System size and energy dependence of dilepton production in heavy-ion collisions at 1-2 GeV/nucleon energies.” In: *Phys. Rev. C* 87 (6 2013), p. 064907. DOI: [10.1103/PhysRevC.87.064907](https://doi.org/10.1103/PhysRevC.87.064907). URL: <https://link.aps.org/doi/10.1103/PhysRevC.87.064907>.
- [116] R. Schicker et al. “Acceptance and resolution simulation studies for the dielectron spectrometer HADES at GSI.” In: *Nuclear Instruments and Methods in Physics Research Section A: Accelerators, Spectrometers, Detectors and Associated Equipment* 380.3 (1996), pp. 586–596. ISSN: 0168-9002. DOI: [https://doi.org/10.1016/0168-9002\(96\)00732-2](https://doi.org/10.1016/0168-9002(96)00732-2). URL: <https://www.sciencedirect.com/science/article/pii/0168900296007322>.
- [117] G. Agakishiev et al. “The High-Acceptance Dielectron Spectrometer HADES.” In: *Eur. Phys. J. A* 41 (2009), pp. 243–277. DOI: [10.1140/epja/i2009-10807-5](https://doi.org/10.1140/epja/i2009-10807-5). arXiv: [0902.3478](https://arxiv.org/abs/0902.3478) [nucl-ex].
- [118] S. Spiess. *HADES overview - Recent results from the measurement of Ag + Ag collisions at $\sqrt{s_{NN}} = 2.55$ GeV by the HADES collaboration*. Talk at the online Strangeness in Quark Matter Conference 2021.
- [119] J. Pietraszko, L. Fabbietti, and W. Koenig. “Diamonds as timing detectors for MIP: The HADES proton-beam monitor and start detectors.” In: *Nucl. Instrum. Meth. A* 618 (2010), pp. 121–123. DOI: [10.1016/j.nima.2010.02.113](https://doi.org/10.1016/j.nima.2010.02.113). arXiv: [0911.0337](https://arxiv.org/abs/0911.0337) [nucl-ex].
- [120] A. Rost et al. “Performance of the CVD Diamond Based Beam Quality Monitoring System in the HADES Experiment at GSI*.” In: *Proc. 10th International Particle Accelerator Conference (IPAC'19), Melbourne, Australia, 19-24 May 2019* (Melbourne, Australia). International Particle Accelerator Conference 10. Geneva, Switzerland: JACoW Publishing, 2019, pp. 2507–2509. ISBN: 978-3-95450-208-0. DOI: [doi:10.18429/JACoW-IPAC2019-WEPGW019](https://doi.org/10.18429/JACoW-IPAC2019-WEPGW019). URL: <http://jacow.org/ipac2019/papers/wepgw019.pdf>.
- [121] C. Müntz et al. “The HADES tracking system.” In: *Nuclear Instruments and Methods in Physics Research Section A: Accelerators, Spectrometers, Detectors and Associated Equipment* 535.1 (2004). Proceedings of the 10th International Vienna Conference on Instrumentation, pp. 242–246. ISSN: 0168-9002. DOI: <https://doi.org/10.1016/j.nima.2004.0>

- 7.232. URL: <https://www.sciencedirect.com/science/article/pii/S0168900204016468>.
- [122] H et al. Bokemeyer. "Development of low-mass drift chambers for the HADES spectrometer." In: *Nucl. Instrum. Meth. A* 477 (2002). Ed. by A. Bird, P. R. Hobson, G. Royle, and A. Smith, pp. 397–400. DOI: [10.1016/S0168-9002\(01\)01842-3](https://doi.org/10.1016/S0168-9002(01)01842-3).
- [123] F. Bloch. "Zur Bremsung rasch bewegter Teilchen beim Durchgang durch Materie." In: *Annalen der Physik* 408.3 (1933), pp. 285–320. DOI: <https://doi.org/10.1002/andp.19334080303>. eprint: <https://onlinelibrary.wiley.com/doi/pdf/10.1002/andp.19334080303>. URL: <https://onlinelibrary.wiley.com/doi/abs/10.1002/andp.19334080303>.
- [124] C. Agodi et al. "The HADES time-of-flight wall." In: *Nuclear Instruments and Methods in Physics Research Section A: Accelerators, Spectrometers, Detectors and Associated Equipment* 492.1 (2002), pp. 14–25. ISSN: 0168-9002. DOI: [https://doi.org/10.1016/S0168-9002\(02\)01004-5](https://doi.org/10.1016/S0168-9002(02)01004-5). URL: <https://www.sciencedirect.com/science/article/pii/S0168900202010045>.
- [125] D. Belver et al. "The HADES RPC inner TOF wall." In: *Nuclear Instruments and Methods in Physics Research Section A: Accelerators, Spectrometers, Detectors and Associated Equipment* 602.3 (2009). Proceedings of the 9th International Workshop on Resistive Plate Chambers and Related Detectors, pp. 687–690. ISSN: 0168-9002. DOI: <https://doi.org/10.1016/j.nima.2008.12.090>. URL: <https://www.sciencedirect.com/science/article/pii/S0168900208019633>.
- [126] G. Kornakov et al. "Time of flight measurement in heavy-ion collisions with the HADES RPC TOF wall." In: *Journal of Instrumentation* 9.11 (2014), pp. C11015–C11015. DOI: [10.1088/1748-0221/9/11/c11015](https://doi.org/10.1088/1748-0221/9/11/c11015). URL: <https://doi.org/10.1088/1748-0221/9/11/c11015>.
- [127] G. Kornakov. "Time of Flight calibration and reaction time determination." In: *Talk in the HADES Collaboration Meeting XXVIII, Bratislava, Slovakia* (2014).
- [128] A. Bałanda et al. "The HADES Pre-Shower detector." In: *Nuclear Instruments and Methods in Physics Research Section A: Accelerators, Spectrometers, Detectors and Associated Equipment* 531.3 (2004), pp. 445–458. ISSN: 0168-9002. DOI: <https://doi.org/10.1016/j.nima.2004.05.082>. URL: <https://www.sciencedirect.com/science/article/pii/S0168900204011039>.
- [129] W. Czyzycki et al. "Electromagnetic Calorimeter for HADES." In: (2011). arXiv: [1109.5550](https://arxiv.org/abs/1109.5550) [nucl-ex].
- [130] O Svoboda et al. "Electromagnetic calorimeter for the HADES@FAIR experiment." In: *Journal of Instrumentation* 9.05 (2014), pp. C05002–C05002. DOI: [10.1088/1748-0221/9/05/c05002](https://doi.org/10.1088/1748-0221/9/05/c05002). URL: <https://doi.org/10.1088/1748-0221/9/05/c05002>.

- [131] A. Rost. “Design, installation and commissioning of new read-out electronics for HADES ECAL and diamond detectors for To-reconstruction and beam diagnostics.” In: *PhD Thesis* (2020). DOI: <https://doi.org/10.25534/tuprints-00012235>.
- [132] J. Michel et al. “The upgraded HADES trigger and data acquisition system.” In: *Journal of Instrumentation* 6.12 (2011), pp. C12056–C12056. DOI: [10.1088/1748-0221/6/12/c12056](https://doi.org/10.1088/1748-0221/6/12/c12056). URL: <https://doi.org/10.1088/1748-0221/6/12/c12056>.
- [133] The HADES collaboration. “HADES Logbook.” In: (). URL: https://hades-db.gsi.de/pls/hades_webdbs/hades_oper.hlogbook2.form_selection?p_exp_id=MAR19.
- [134] Geant4 Collaboration. “Introduction to Geant4 - Release 10.7.” In: (2020). URL: <https://geant4-userdoc.web.cern.ch/UsersGuides/IntroductionToGeant4/fo/IntroductionToGeant4.pdf>.
- [135] S. A. Bass et al. “Microscopic models for ultrarelativistic heavy ion collisions.” In: *Prog. Part. Nucl. Phys.* 41 (1998), pp. 255–369. DOI: [10.1016/S0146-6410\(98\)00058-1](https://doi.org/10.1016/S0146-6410(98)00058-1). arXiv: [nucl-th/9803035](https://arxiv.org/abs/nuc1-th/9803035).
- [136] I. Fröhlich et al. “Pluto: A Monte Carlo Simulation Tool for Hadronic Physics.” In: *PoS ACAT* (2007), p. 076. DOI: [10.22323/1.050.0076](https://doi.org/10.22323/1.050.0076). arXiv: [0708.2382](https://arxiv.org/abs/0708.2382) [[nucl-ex](https://arxiv.org/abs/nuc1-ex)].
- [137] C. A. Mead. “Quantum Theory of the Refractive Index.” In: *Phys. Rev.* 110 (2 1958), pp. 359–369. DOI: [10.1103/PhysRev.110.359](https://doi.org/10.1103/PhysRev.110.359). URL: <https://link.aps.org/doi/10.1103/PhysRev.110.359>.
- [138] M. Adinolfi et al. “Performance of the LHCb RICH detector at the LHC.” In: *Eur. Phys. J. C* 73 (2013), p. 2431. DOI: [10.1140/epjc/s10052-013-2431-9](https://doi.org/10.1140/epjc/s10052-013-2431-9). arXiv: [1211.6759](https://arxiv.org/abs/1211.6759) [[physics.ins-det](https://arxiv.org/abs/physics.ins-det)].
- [139] Hamamatsu. *Flat panel type multianode PMT assembly H12700 series/-H14220 series*. 2019. URL: https://www.hamamatsu.com/resources/pdf/etd/H12700_H14220_TPMH1379E.pdf.
- [140] A. Weber. *The HADES RICH upgrade within the FAIR Phase-0 program*. Quark Matter, poster presentation. 2019.
- [141] C. Pauly et al. “Upgrade of the HADES RICH photon detector with H12700 MAPMTs.” In: *Nuclear Instruments and Methods in Physics Research Section A: Accelerators, Spectrometers, Detectors and Associated Equipment* 876 (2017). The 9th international workshop on Ring Imaging Cherenkov Detectors (RICH2016), pp. 164–167. ISSN: 0168-9002. DOI: <https://doi.org/10.1016/j.nima.2017.02.067>. URL: <https://www.sciencedirect.com/science/article/pii/S0168900217302632>.
- [142] J. Adamczewski-Musch et al. “Wavelength shifting films on multi-anode PMTs with UV-extended window for the CBM RICH detector.” In: *Nucl. Instrum. Meth. A* 766 (2014). Ed. by T. Sumiyoshi, G. Hallewell, W. Hofmann, T. Iijima, E. Nappi, and P. Krizan, pp. 180–182. DOI: [10.1016/j.nima.2014.05.011](https://doi.org/10.1016/j.nima.2014.05.011).

- [143] P. Koczon A. Braem C. Joram P. Solevi M. Dürr and C. Höhne. "Wavelength-shifting materials for the use in RICH detectors - p-terphenyl and tetraphenyl-butadiene revisited." In: *Technical Report CERN Geneva* (2010).
- [144] J. Adamczewski-Musch et al. "Efficiency and temporal response of p-terphenyl based wavelength shifting films on H12700 multi anode photomultipliers." In: *Nuclear Instruments and Methods in Physics Research Section A: Accelerators, Spectrometers, Detectors and Associated Equipment* 952 (2019). DOI: [10.1016/j.nima.2019.01.093](https://doi.org/10.1016/j.nima.2019.01.093).
- [145] Paul C. Hough V. "Method and means for recognizing complex patterns." In: 3069654 (1962). URL: <https://www.freepatentsonline.com/3069654.html>.
- [146] S. A. Lebedev and G. A. Ososkov. "Fast algorithms for ring recognition and electron identification in the CBM RICH detector." In: *Phys. Part. Nucl. Lett.* 6 (2009), pp. 161–176. DOI: [10.1134/S1547477109020095](https://doi.org/10.1134/S1547477109020095).
- [147] R. Haas. Analyse von blobartigen Strukturen in der MAPMT Photodetektorebene des HADES-RICH Detektors in Ag+Ag Kollisionen bei 1,58 AGeV Strahlenergie. Bachelor Thesis 2019.
- [148] The HADES collaboration. "Centrality determination in AgAg." In: *HADES Foswiki, Work-in-progress figures* (2021). URL: <https://hades-wiki.gsi.de/foswiki/bin/view/Physics/AgagEventChara>.
- [149] J. Adamczewski-Musch et al. "Centrality determination of Au + Au collisions at 1.23A GeV with HADES." In: *Eur. Phys. J. A* 54.5 (2018), p. 85. DOI: [10.1140/epja/i2018-12513-7](https://doi.org/10.1140/epja/i2018-12513-7). arXiv: [1712.07993 \[nucl-ex\]](https://arxiv.org/abs/1712.07993).
- [150] J. Foertsch. *RICH alignment and performance using multiple scattering correction*. Talk in the IV HADES Analysis meeting, June 2021.
- [151] J.-H. Otto. *Dielectron reconstruction in Ag+Ag at $\sqrt{NN} = 2.55$ GeV*. Talk in the HADES Dielectron meeting, 08.06.2021.
- [152] HADES RICH group. RICH analysis results, FOSWIKI. 2021. URL: <https://hades-wiki.gsi.de/foswiki/bin/view/RICH/RichAnalysis>.
- [153] J.-H. Otto. *Dielectron reconstruction in Ag+Ag at $\sqrt{NN} = 2.55$ GeV*. Talk in the III HADES Analysis meeting, June 2020.
- [154] J. et. al. Adamczewski-Musch. "The RICH detector of the CBM experiment." In: *Nuclear Instruments and Methods in Physics Research Section A: Accelerators, Spectrometers, Detectors and Associated Equipment* 876 (2017). DOI: [10.1016/j.nima.2017.01.052](https://doi.org/10.1016/j.nima.2017.01.052).
- [155] *Technical Design Report for the CBM Ring Imaging Cherenkov Detector*. Tech. rep. 2013, 215 p. URL: <https://repository.gsi.de/record/65526>.
- [156] S. Harabasz. "Reconstruction of virtual photons from Au+Au collisions at 1.23 GeV/u." en. PhD thesis. Darmstadt: Technische Universität, 2017. URL: <http://tuprints.ulb.tu-darmstadt.de/6605/>.

- [157] M. Nabroth. talk at the HADES collaboration meeting. 2022-23-03.
- [158] J.-H. Otto. *4 electron in Ag+Ag at $\sqrt{NN} = 2.55$ GeV*. Talk in the HADES RICH meeting, Mai 2022.
- [159] J. Förtsch. *Meson reconstruction with photon conversion method: From sim to data*. Talk in the HADES Analysis meeting, July 2022.
- [160] HADES collaboration. *Proposal for experiments at SIS18 during FAIR Phase-0*. 2017. URL: <http://repository.gsi.de/record/220071/files/HADES%20Proposal%20to%20G-PAC%202017.pdf>.
- [161] S. Spies. *K_s^0 mass peak investigations*. Talk in the HADES Analysis meeting, July 2022.
- [162] R. Averbeck, R. Holzmann, V. Metag, and R. S. Simon. “Neutral pions and η mesons as probes of the hadronic fireball in nucleus-nucleus collisions around 1A GeV.” In: *Phys. Rev. C* 67 (2 2003), p. 024903. DOI: [10.1103/PhysRevC.67.024903](https://doi.org/10.1103/PhysRevC.67.024903). URL: <https://link.aps.org/doi/10.1103/PhysRevC.67.024903>.
- [163] R. Averbeck et al. “Contribution of π^0 and η Dalitz decays to the dilepton invariant-mass spectrum in 1A GeV heavy-ion collisions.” In: *Phys. Rev. C* 56 (6 1997), R2920–R2923. DOI: [10.1103/PhysRevC.56.R2920](https://doi.org/10.1103/PhysRevC.56.R2920). URL: <https://link.aps.org/doi/10.1103/PhysRevC.56.R2920>.
- [164] M. Kohls. talk at the HADES collaboration meeting. 2022-23-03.
- [165] M. Lorenz. “Vector meson production in p+Nb reactions and statistical particle production in Ar+KCl collisions.” PhD thesis. Frankfurt, Germany: Johann Wolfgang Goethe-Universitaet, 2012.
- [166] O. Buss, T. Gaitanos, K. Gallmeister, H. van Hees, M. Kaskulov, O. Lalakulich, A. B. Larionov, T. Leitner, J. Weil, and U. Mosel. “Transport-theoretical Description of Nuclear Reactions.” In: *Phys. Rept.* 512 (2012), pp. 1–124. DOI: [10.1016/j.physrep.2011.12.001](https://doi.org/10.1016/j.physrep.2011.12.001). arXiv: [1106.1344](https://arxiv.org/abs/1106.1344) [hep-ph].
- [167] *The Giessen Boltzmann-Uehling-Uhlenbeck Project*. <https://gibuu.hepforge.org/trac/wiki>. Accessed: 2022-09-03.
- [168] W. Botermans and R. Malfliet. “Quantum transport theory of nuclear matter.” In: *Physics Reports* 198.3 (1990), pp. 115–194. ISSN: 0370-1573. DOI: [https://doi.org/10.1016/0370-1573\(90\)90174-Z](https://doi.org/10.1016/0370-1573(90)90174-Z). URL: <https://www.sciencedirect.com/science/article/pii/037015739090174Z>.
- [169] J.-H. Otto. talk at the weekly JLU transport meeting. 2020-01-10.
- [170] A. B. Larionov, U. Mosel, and L. von Smekal. “Dilepton production in microscopic transport theory with in-medium ρ -meson spectral function.” In: *Phys. Rev. C* 102.6 (2021), p. 064913. DOI: [10.1103/PhysRevC.102.064913](https://doi.org/10.1103/PhysRevC.102.064913). arXiv: [2009.11702](https://arxiv.org/abs/2009.11702) [nucl-th].

- [171] G. Agakishiev et al. "Origin of the low-mass electron pair excess in light nucleus-nucleus collisions." In: *Phys. Lett. B* 690 (2010), pp. 118–122. DOI: [10.1016/j.physletb.2010.05.010](https://doi.org/10.1016/j.physletb.2010.05.010). arXiv: [0910.5875](https://arxiv.org/abs/0910.5875) [nucl-ex].
- [172] N. Schild. talk at the HADES collaboration meeting. 2022-24-03.
- [173] G. Agakishiev et al. "First measurement of proton-induced low-momentum dielectron radiation off cold nuclear matter." In: *Physics Letters B* 715.4 (2012), pp. 304–309. ISSN: 0370-2693. DOI: <https://doi.org/10.1016/j.physletb.2012.08.004>. URL: <https://www.sciencedirect.com/science/article/pii/S0370269312008398>.
- [174] B. Friman, C. Höhne, J. Knoll, S. Leupold, J. Randrup, R. Rapp, and P. Senger. *The CBM Physics Book: Compressed Baryonic Matter in Laboratory Experiments*. Vol. 814. 2011. ISBN: 978-3-642-13292-6. DOI: [10.1007/978-3-642-13293-3](https://doi.org/10.1007/978-3-642-13293-3).
- [175] private communication with K. Gallmeister. 2022-05-07.
- [176] private communication with L. von Smekal. 2022-05-07.
- [177] C. Jung, J.-H. Otto, R.-A. Tripolt, and L. von Smekal. "Self-consistent $O(4)$ model spectral functions from analytically continued FRG flows." In: (2021). arXiv: [2107.10748](https://arxiv.org/abs/2107.10748) [hep-ph].
- [178] L. D. McLerran and T. Toimela. "Photon and dilepton emission from the quark-gluon plasma: Some general considerations." In: *Phys. Rev. D* 31 (3 1985), pp. 545–563. DOI: [10.1103/PhysRevD.31.545](https://doi.org/10.1103/PhysRevD.31.545). URL: <https://link.aps.org/doi/10.1103/PhysRevD.31.545>.
- [179] F. Jüttner. "Das Maxwell'sche Gesetz der Geschwindigkeitsverteilung in der Relativtheorie." In: *Annalen der Physik* 339.5 (1911), pp. 856–882. DOI: <https://doi.org/10.1002/andp.19113390503>. eprint: <https://onlinelibrary.wiley.com/doi/pdf/10.1002/andp.19113390503>. URL: <https://onlinelibrary.wiley.com/doi/abs/10.1002/andp.19113390503>.
- [180] J. Sakurai. "Theory of strong interactions." In: *Annals of Physics* 11.1 (1960), pp. 1–48. ISSN: 0003-4916. DOI: [https://doi.org/10.1016/0003-4916\(60\)90126-3](https://doi.org/10.1016/0003-4916(60)90126-3). URL: <https://www.sciencedirect.com/science/article/pii/0003491660901263>.
- [181] R. Rapp and H. van Hees. "Thermal dileptons as fireball thermometer and chronometer." In: *Physics Letters B* 753 (2016), pp. 586–590. ISSN: 0370-2693. DOI: <https://doi.org/10.1016/j.physletb.2015.12.065>. URL: <https://www.sciencedirect.com/science/article/pii/S0370269315010138>.
- [182] V. V. Ezhela, S. B. Lugovsky, and O. V. Zenin. "Hadronic part of the muon $g-2$ estimated on the $\sigma^{*2003}(\text{tot})(e^+ e^- \rightarrow \text{hadrons})$ evaluated data compilation." In: (2003). arXiv: [hep-ph/0312114](https://arxiv.org/abs/hep-ph/0312114).

- [183] C. A. Dominguez and K. Schilcher. “Chiral sum rules and duality in QCD.” In: *Phys. Lett. B* 448 (1999), pp. 93–98. DOI: [10.1016/S0370-2693\(99\)00028-3](https://doi.org/10.1016/S0370-2693(99)00028-3). arXiv: [hep-ph/9811261](https://arxiv.org/abs/hep-ph/9811261).
- [184] R.-A. Tripolt, C. Jung, L. von Smekal, and J. Wambach. “Vector and axial-vector mesons in nuclear matter.” In: *Phys. Rev. D* 104.5 (2021), p. 054005. DOI: [10.1103/PhysRevD.104.054005](https://doi.org/10.1103/PhysRevD.104.054005). arXiv: [2105.00861](https://arxiv.org/abs/2105.00861) [hep-ph].
- [185] R.-A. Tripolt, L. von Smekal, and J. Wambach. “Spectral functions and in-medium properties of hadrons.” In: *Int. J. Mod. Phys. E* 26.01n02 (2017), p. 1740028. DOI: [10.1142/S0218301317400286](https://doi.org/10.1142/S0218301317400286). arXiv: [1605.00771](https://arxiv.org/abs/1605.00771) [hep-ph].
- [186] H. Gies. “Introduction to the functional RG and applications to gauge theories.” In: *Lect. Notes Phys.* 852 (2012), pp. 287–348. DOI: [10.1007/978-3-642-27320-9_6](https://doi.org/10.1007/978-3-642-27320-9_6). arXiv: [hep-ph/0611146](https://arxiv.org/abs/hep-ph/0611146).
- [187] B.-J. Schaefer and J. Wambach. “Renormalization group approach towards the QCD phase diagram.” In: *Phys. Part. Nucl.* 39 (2008), pp. 1025–1032. DOI: [10.1134/S1063779608070083](https://doi.org/10.1134/S1063779608070083). arXiv: [hep-ph/0611191](https://arxiv.org/abs/hep-ph/0611191).
- [188] K. G. Wilson. “Renormalization group and critical phenomena. 2. Phase space cell analysis of critical behavior.” In: *Phys. Rev. B* 4 (1971), pp. 3184–3205. DOI: [10.1103/PhysRevB.4.3184](https://doi.org/10.1103/PhysRevB.4.3184).
- [189] K. G. Wilson and J. Kogut. “The renormalization group and the ϵ expansion.” In: *Physics Reports* 12.2 (1974), pp. 75–199. ISSN: 0370-1573. DOI: [https://doi.org/10.1016/0370-1573\(74\)90023-4](https://doi.org/10.1016/0370-1573(74)90023-4). URL: <https://www.sciencedirect.com/science/article/pii/0370157374900234>.
- [190] C. S. Fischer. “QCD at finite temperature and chemical potential from Dyson–Schwinger equations.” In: *Prog. Part. Nucl. Phys.* 105 (2019), pp. 1–60. DOI: [10.1016/j.pnpnp.2019.01.002](https://doi.org/10.1016/j.pnpnp.2019.01.002). arXiv: [1810.12938](https://arxiv.org/abs/1810.12938) [hep-ph].
- [191] R. Alkofer and L. von Smekal. “The Infrared behavior of QCD Green’s functions: Confinement dynamical symmetry breaking, and hadrons as relativistic bound states.” In: *Phys. Rept.* 353 (2001), p. 281. DOI: [10.1016/S0370-1573\(01\)00010-2](https://doi.org/10.1016/S0370-1573(01)00010-2). arXiv: [hep-ph/0007355](https://arxiv.org/abs/hep-ph/0007355).
- [192] C. Wetterich. “Exact evolution equation for the effective potential.” In: *Physics Letters B* 301.1 (1993), pp. 90–94. ISSN: 0370-2693. DOI: [https://doi.org/10.1016/0370-2693\(93\)90726-X](https://doi.org/10.1016/0370-2693(93)90726-X). URL: <https://www.sciencedirect.com/science/article/pii/037026939390726X>.
- [193] T. Appelquist and J. Carazzone. “Infrared singularities and massive fields.” In: *Phys. Rev. D* 11 (10 1975), pp. 2856–2861. DOI: [10.1103/PhysRevD.11.2856](https://doi.org/10.1103/PhysRevD.11.2856). URL: <https://link.aps.org/doi/10.1103/PhysRevD.11.2856>.

- [194] T. R. Morris. “The Exact renormalization group and approximate solutions.” In: *Int. J. Mod. Phys. A* 9 (1994), pp. 2411–2450. DOI: [10.1142/S0217751X94000972](https://doi.org/10.1142/S0217751X94000972). arXiv: [hep-ph/9308265](https://arxiv.org/abs/hep-ph/9308265).
- [195] R.-A. Tripolt. “Spectral Functions and Transport Coefficients from the Functional Renormalization Group.” In: *PhD Thesis* (2015).
- [196] K. Kamikado, N. Strodthoff, L. von Smekal, and J. Wambach. “Real-time correlation functions in the $O(N)$ model from the functional renormalization group.” In: *Eur. Phys. J. C* 74.3 (2014), p. 2806. DOI: [10.1140/epjc/s10052-014-2806-6](https://doi.org/10.1140/epjc/s10052-014-2806-6). arXiv: [1302.6199](https://arxiv.org/abs/1302.6199) [hep-ph].
- [197] D. F. Litim. “Optimized renormalization group flows.” In: *Phys. Rev. D* 64 (2001), p. 105007. DOI: [10.1103/PhysRevD.64.105007](https://doi.org/10.1103/PhysRevD.64.105007). arXiv: [hep-th/0103195](https://arxiv.org/abs/hep-th/0103195).
- [198] B.-J. Schaefer and J. Wambach. “The Phase diagram of the quark meson model.” In: *Nucl. Phys. A* 757 (2005), pp. 479–492. DOI: [10.1016/j.nuclphysa.2005.04.012](https://doi.org/10.1016/j.nuclphysa.2005.04.012). arXiv: [nucl-th/0403039](https://arxiv.org/abs/nucl-th/0403039).
- [199] A. Kurganov and E. Tadmor. “New High-Resolution Central Schemes for Nonlinear Conservation Laws and Convection–Diffusion Equations.” In: *Journal of Computational Physics* 160.1 (2000), pp. 241–282. ISSN: 0021-9991. DOI: <https://doi.org/10.1006/jcph.2000.6459>. URL: <https://www.sciencedirect.com/science/article/pii/S0021999100964593>.
- [200] A. K. Das. *Finite temperature field theory*. World Scientific, 1997.